



**THE UNIVERSITY OF QUEENSLAND**  
AUSTRALIA

**Wideband Microwave Imaging Systems for the Diagnosis of Fluid Accumulation  
in the Human Torso**

Sasan AHDI REZAEIEH

B.Sc. (Telecommunications Eng.), M.Sc. (Telecommunications Eng.)

*A thesis submitted for the degree of Doctor of Philosophy at  
The University of Queensland in 2016*

School of Information Technology and Electrical Engineering



## **Abstract**

According to the World Health Organization (WHO), cardiovascular diseases (CVDs) are the leading causes of death worldwide, with one third of deaths attributed to CVDs in 2012. Pulmonary oedema and pleural effusion are the most apparent symptoms of many diseases categorized under CVDs such as heart failure and lung cancer, at which fluid (mainly with high water content) is accumulated in or around the lungs. Therefore, constant monitoring of fluid levels inside the lungs is one of the most efficient ways of early detection of CVDs. Chest X-Rays and computational tomography (CT)-scans are the most widely used devices for fluid detection; however, they suffer from lack of sensitivity and ionizing radiation, respectively, that makes them unsuitable for long term monitoring purposes. Currently, magnetic resonance imaging (MRI) is the most reliable device that can be utilized for fluid accumulation detection. However, considering the fact that more than 75% of the CVDs occur in countries with low or middle income, it is not widely available. Moreover, due to their bulky structures, the abovementioned devices lack the capability of being used in mobile emergency units such as ambulances or clinics at rural areas. To that end, this thesis is dedicated to design and fabrication of a low cost, portable and non-invasive device that can be used as an initial decision making tool for medical staff to pursue further investigations to define the exact cause of the oedema.

First chapter of the thesis is allocated to introduction of the cardiovascular diseases and their effects on the dielectric properties of the tissues inside the lungs. A complete literature review on various alternative methods for replacing the conventional devices is performed. The obtained results by these systems and their advantages as well as their limitations are discussed. Microwave imaging technique is then presented in chapter two as a robust method which can both provide information about the presence and location of the accumulated fluid. This is specifically of great importance for cases where biopsy is required to remove or take sample of the accumulated fluid for saving the life of the patient. Chapter two is also allocated to the introduction of microwave-based medical diagnostic and monitoring systems for different applications such as breast cancer detection and brain imaging. A prospect of the possible realizable systems is investigated and existing scanning approaches are discussed. The main contributions of the thesis that are the design of several complete platforms, design of novel and unidirectional microwave sensors (antennas), promotion of novel scanning and detection methods are clarified in these chapters.

In chapter three, firstly the optimum operating frequency for torso imaging is defined. By applying a circuit model that models different layers of torso as circuit elements, it is shown that a wide operating bandwidth at lower ultra-high frequency (UHF) band provides a reasonable

compensation between the resolution of the obtained images and signal penetration inside the body. It is explained that due to the limited allowed microwave power for safety considerations unidirectional antennas are required. Then, it is explained that due to the large wavelengths at lower UHF band the sizes of the prospective antennas are expected to be large. To that end, novel miniaturization techniques are proposed to reduce the sizes of the conventional antennas in chapters three and four. These antennas are categorized under three dimensional (3-D) and planar structure. A folding technique is introduced and used in the proposed 3-D structures and it is shown that by using this technique both size and directivity/back radiation suppression is improved. 3-D slot-antenna and cubic monopole-fed antennas are also proposed that wide operating bandwidth is achieved using slot impedance transformer, and multiple resonance-merging techniques, respectively. Regarding the planar structures that are presented in chapter four, it is shown that by combining the loop-dipole modes, both wide-operating bandwidth and directivity enhancement is achievable. Capacitive-loading of a loop antenna is the other proposed technique in which a loop antenna is partially and/or non-uniformly loaded with capacitors in the forms of simple slots and mu-negative (MNG) metamaterial-unitcells that help miniaturizing the size of the antenna by lowering its first resonance frequency.

In chapters five and six, several platforms using single and multiple antennas with linear and circular configurations are presented and the utilized imaging technique for data processing is explained. The platforms are presented in a systematic progressive manner in which each system is covering the limitations of its previous prototype. Two final clinical platforms in the shape of clinical bed and doughnut-shaped chamber are proposed and the obtained test results on artificial phantom, animal lungs and human tests are presented. Based on the obtained results on healthy human beings it is shown that the scattered-field from torso of people with different body sizes vary in a reasonably limited range that is a welcoming result for building a global-database to define a threshold for healthy range.

Chapter seven concludes the discussions made throughout the thesis and explains future works that can be carried out to further improve the reported systems.

## **Declaration by author**

This thesis is composed of my original work, and contains no material previously published or written by another person except where due reference has been made in the text. I have clearly stated the contribution by others to jointly-authored works that I have included in my thesis.

I have clearly stated the contribution of others to my thesis as a whole, including statistical assistance, survey design, data analysis, significant technical procedures, professional editorial advice, and any other original research work used or reported in my thesis. The content of my thesis is the result of work I have carried out since the commencement of my research higher degree candidature and does not include a substantial part of work that has been submitted to qualify for the award of any other degree or diploma in any university or other tertiary institution. I have clearly stated which parts of my thesis, if any, have been submitted to qualify for another award.

I acknowledge that an electronic copy of my thesis must be lodged with the University Library and, subject to the policy and procedures of The University of Queensland, the thesis be made available for research and study in accordance with the Copyright Act 1968 unless a period of embargo has been approved by the Dean of the Graduate School.

I acknowledge that copyright of all material contained in my thesis resides with the copyright holder(s) of that material. Where appropriate I have obtained copyright permission from the copyright holder to reproduce material in this thesis.



## **Publications during candidature**

1. **S.A. Rezaeieh**, A Zamani, KS Bialkowski, A Mahmoud, AM Abbosh, "Feasibility of using wideband microwave system for non-invasive detection and monitoring of pulmonary oedema," *Nature, Scientific Reports*, No. 14047,2015.
2. **S.A. Rezaeieh**, A. Zamani, K.S. Bialkowski, A.M. Abbosh, "Foam embedded wideband antenna array for early congestive heart failure detection with tests using artificial phantom with animal organs" *IEEE Transactions on Antennas and Propagation*, vol. 63, no. 11, pp. 5138-5143, Nov. 2015.
3. **S.A. Rezaeieh**, A.M. Abbosh, Y. Wang, "Wideband unidirectional antenna of folded structure in microwave system for early detection of congestive heart failure", *IEEE Transactions on Antennas and Propagation*, vol. 62, no. 10, pp. 5375-5381, 2014.
4. **S.A. Rezaeieh**, A. Zamani, K.S. Bialkowski, A.M. Abbosh, "Unidirectional slot-loaded loop antenna with wideband performance and compact size for congestive heart failure detection", *IEEE Transactions on Antennas and Propagation*, 2015, vol. 63, no. 10, pp. 4557-4562, Oct. 2015.
5. **S.A. Rezaeieh**, K.S. Bialkowski, A. Zamani, A.M. Abbosh, "Loop-dipole composite antenna for wideband microwave-based medical diagnostic systems with verification on pulmonary edema detection" *IEEE Antennas and Wireless Propagation Letters*, Accepted on 1<sup>st</sup> September 2015, Available at IEEE Xplore website.
6. **S.A. Rezaeieh**, A. Zamani, A.M. Abbosh,"3-D wideband antenna for head-imaging system with performance verification in brain tumor detection", *IEEE Antennas and Wireless Propagation Letters*, vol. 14, pp.910-914, 2015.
7. **S.A. Rezaeieh**, A.M. Abbosh, A. Zamani, K.S. Bialkowski, "Pleural effusion detection system using wideband slot-loaded loop antenna", *Electronics Letters*, vol. 51, pp. p. 1144–1146, 2015.
8. A Zamani, **S.A. Rezaeieh**, AM Abbosh, "Lung cancer detection using frequency-domain microwave imaging", *Electronics Letters*, vol.51, pp.740-741, 2015.
9. **S.A. Rezaeieh**, K.S. Bialkowski, A. Abbosh, "Three-dimensional open-ended slot antenna for heart failure detection system employing differential technique" *IEEE Antennas and Wireless Propagation Letters*, vol. 13, pp.1753-1756, 2014.
10. **S.A. Rezaeieh**, A. Abbosh, "Wideband and unidirectional folded antenna for heart failure detection system," *IEEE Antennas and Wireless Propagation Letters*, vol. 13, pp.844-847, 2014.
11. **S.A. Rezaeieh**, K.S. Bialkowski, A. Abbosh, "Microwave system for the early stage detection of congestive heart failure", *IEEE Access*, vol. 2, pp. 921-929, 2014.

12. **S.A. Rezaeieh**, A. Abbosh, M.A. Antoniadou, "Compact CPW-fed planar monopole antenna with wide circular polarization bandwidth," *IEEE Antennas and Wireless Propagation Letters*, vol. 12, pp.1295-1298, 2013.
13. **S.A. Rezaeieh**, A. Abbosh, M.A. Antoniadou, "Broadband planar circularly polarized antenna for ultra-high frequency applications," *IET Microwaves, Antennas & Propagation*, vol. 8, no. 4, pp. 263-271, March 18 2014.
14. **S.A. Rezaeieh**, K.S. Bialkowski, A. Abbosh, "Folding method for bandwidth and directivity enhancement of meandered loop uhf antenna for heart failure detection system", *IET Microwaves, Antennas & Propagation*, vol. 8, No. 14, pp. 1218-1227, 2014.
15. **S.A. Rezaeieh**, M.A. Antoniadou, A.M. Abbosh, "Compact wideband loop antenna partially loaded with mu-negative metamaterial unit-cells for directivity enhancement," *IEEE Antennas and Wireless Propagation Letters*, 2016. DOI: 10.1109/LAWP.2016.2542799
16. **S.A. Rezaeieh**, M.A. Antoniadou, A.M. Abbosh, "Bandwidth and Directivity Enhancement of Loop Antenna by Non-Periodic Distribution of Mu-Negative Metamaterial Unit Cells," *IEEE Transactions on Antennas and Propagation*, 2016. DOI: 10.1109/TAP.2016.2574878
17. **S.A. Rezaeieh**, A.M. Abbosh, "Compact Planar Loop-Dipole Composite Antenna with Director for Bandwidth Enhancement and Back Radiation Suppression," *IEEE Transactions on Antennas and Propagation*, 2016. DOI: 10.1109/TAP.2016.2570246.
18. **S. A. Rezaeieh**, A. Abbosh, "Broadband CPW-fed slot antenna with circular polarization for on-body applications at ISM band," *IEEE Asia-Pacific Microwave Conference Proceedings (APMC)*, pages 1184-1186, Dec. 2012.
19. **S. A. Rezaeieh**, Y.-Q. Tan, A. Abbosh, "Design of coupling medium for pulmonary edema microwave detection system," *IEEE Antennas and Propagation Society International Symposium (APSURSI)*, pp.2057-2058, 2013.
20. **S.A. Rezaeieh**, A. Abbosh, M.A. Antoniadou, "Broadband UHF antenna for heart failure detection system," *IEEE Antennas and Propagation Society International Symposium (APSURSI)*, pp.2089-2090, 2013.
21. **S.A. Rezaeieh**, Y.Q. Tan, A. Abbosh, M.A. Antoniadou, "Equivalent circuit model for finding the optimum frequency range for the detection of heart failure using microwave systems," *IEEE Antennas and Propagation Society International Symposium (APSURSI)*, pp.2059-2060, 2013.
22. **S.A. Rezaeieh**, A. Abbosh, M.A. Antoniadou, S. Mustafa, "Dual-band dual-polarized antenna for medical applications," *International Conference on Electromagnetics in Advanced Applications (ICEAA)*, pp.1277-1279, 2013.

23. Y.Q. Tan, **S.A. Rezaeieh**, A. Abbosh, S. Mustafa, "Defining optimum frequency range for heart failure detection system considering thickness variations in human body tissues," *International Conference on Electromagnetics in Advanced Applications (ICEAA)*, pp.1280-1282, 2013.
24. **S.A. Rezaeieh**, A. Abbosh, "Compact UHF wide slot antenna for microwave stethoscope designed for heart failure detection," *Asia-Pacific Microwave Conference Proceedings (APMC)*, pp.1136-1138, 2013.
25. **S.A. Rezaeieh**, A. Abbosh, "Broadband Zigzag Corrugated Taper Slot Antenna for Heart Failure Detection Systems", *International workshop on antennas technology (iWAT)*, pp.177-179, 2014.
26. **S.A. Rezaeieh**, U.T. Ahmet, A. Abbosh, "Unidirectional Antenna with Planar Reflector for Heart Failure Detection Systems", *International workshop on antennas technology (iWAT)*, pp.171-173, 2014.
27. **S.A. Rezaeieh**, K.S. Bialkowski, A. Abbosh, "Effects of Antenna Characteristics on Performance of Microwave Based System Designed for Early Stage Congestive Heart Failure Detection", *1st Australian Microwave Symposium (AMS)* , pp.35-36, 26-27 June 2014.
28. **S.A. Rezaeieh**, K. Sorbello, A. Abbosh, "Specific Absorption Rate in Human Torso from Microwave-based Heart Failure Detection Systems", *IEEE Antennas and Propagation Society International Symposium (APSURSI)*, pp.518-519, 6-11 July 2014.
29. **S.A. Rezaeieh**, A. Abbosh, "Miniaturization Techniques for Antennas Designed for Microwave-based Heart Failure Detection Systems", *IEEE Antennas and Propagation Society International Symposium (APSURSI)*, pp.520-521, 6-11 July 2014.
30. A.M. Abbosh, **S.A. Rezaeieh**, K.S. Bialkowski, "Microwave techniques as diagnostic tool for congestive heart failure", *IEEE MTT-S International Microwave Workshop Series on RF and Wireless Technologies for Biomedical and Healthcare Applications (IMWS-Bio)*, pp.1-3, 8-10 Dec. 2014 (Invited)
31. A. Zamani, **S.A. Rezaeieh**, A.M. Abbosh, "Frequency domain method for early stage detection of congestive heart failure", *IEEE MTT-S International Microwave Workshop Series on RF and Wireless Technologies for Biomedical and Healthcare Applications* pp.1-3, 8-10 Dec. 2014.
32. **S.A. Rezaeieh**, A.M. Abbosh, "Recent developments in antenna design for microwave based congestive heart failure detection systems," *IEEE Antennas and Propagation & USNC/URSI National Radio Science Meeting*, pp. 538-539, 19-24 July 2015.
33. **S.A. Rezaeieh**, A.M. Abbosh, "Review of systems for the detection and monitoring of accumulated fluids in the human torso," *International Symposium on Antennas and Propagation (ISAP2015)*, 9-12th November 2015.

**Publications included in this thesis**

**S.A. Rezaeieh**, A Zamani, KS Bialkowski, A Mahmoud, AM Abbosh, “Feasibility of using wideband microwave system for non-invasive detection and monitoring of pulmonary oedema,” *Nature, Scientific Reports*, No. 14047, 2015. – Various parts of the paper are incorporated to Chapter 1, Chapter 3 and Chapter 6.

Contributor	Statement of contribution
S.A. Rezaeieh (Candidate)	Designed antennas, platform and experiments (70%) Wrote and edited the paper (70%)
A. Zamani	Wrote Imaging Code (100%) Wrote and edited paper (10%)
K.S. Bialkowski	Designed experiments (20%) Wrote and edited the paper (5%)
A. Mahmoud	Wrote and edited the paper (5%)
A.M. Abbosh	Designed experiments/antennas (10%) Wrote and edited the paper (10%)

**S.A. Rezaeieh**, A.M. Abbosh, "Review of Systems for the Detection and Monitoring of Accumulated Fluids in the Human Torso," *International Symposium on Antennas and Propagation (ISAP2015)*, 9-12th November 2015. – This paper is incorporated as Chapter 1.

Contributor	Statement of contribution
S.A. Rezaeieh (Candidate)	Wrote and edited the paper (80%)
A.M. Abbosh	Wrote and edited the paper (20%)

**S.A. Rezaeieh**, Y.Q. Tan, A. Abbosh, M.A. Antoniadis, "Equivalent circuit model for finding the optimum frequency range for the detection of heart failure using microwave systems," *IEEE Antennas and Propagation Society International Symposium (APSURSI)*, pp.2059-2060, 2013. – Various parts of the paper are incorporated in Chapter 1 and Chapter 3.

Contributor	Statement of contribution
S.A. Rezaeieh (Candidate)	Simulations (80%) Wrote and edited the paper (70%)
Y.Q. Tan	Wrote and edited paper (10%)
A. Abbosh	Simulations (20%)

	Wrote and edited the paper (10%)
M.A. Antoniadis	Wrote and edited the paper (10%)

**S.A. Rezaeieh**, A. Abbosh, M.A. Antoniadis, "Broadband planar circularly polarized antenna for ultra-high frequency applications," *IET Microwaves, Antennas & Propagation*, vol. 8, no. 4, pp. 263-271, March 18 2014. – This paper is incorporated in Chapter 1 and Chapter 3.

Contributor	Statement of contribution
S.A. Rezaeieh (Candidate)	Designed antennas, platform and experiments (80%) Wrote and edited the paper (70%)
A.M. Abbosh	Designed experiments/antennas (10%) Wrote and edited the paper (15%)
M.A. Antoniadis	Designed experiments (10%) Wrote and edited the paper (15%)

**S.A. Rezaeieh**, A.M. Abbosh, Y. Wang, "Wideband unidirectional antenna of folded structure in microwave system for early detection of congestive heart failure", *IEEE Transactions on Antennas and Propagation*, vol. 62, no. 10, pp. 5375-5381, 2014. – Various parts of the paper are incorporated in Chapter 1, Chapter 3 and Chapter 5.

Contributor	Statement of contribution
S.A. Rezaeieh (Candidate)	Designed antennas, platform and experiments (70%) Wrote and edited the paper (70%)
A.M. Abbosh	Designed experiments/antennas (10%) Wrote and edited the paper (20%)
Y. Wang	Imaging Code (100%) Designed experiments (20%) Wrote and edited the paper (10%)

**S.A. Rezaeieh**, K.S. Bialkowski, A. Abbosh, "Three-dimensional open-ended slot antenna for heart failure detection system employing differential technique" *IEEE Antennas and Wireless Propagation Letters*, vol. 13, pp.1753-1756, 2014.- Various parts of the paper are incorporated in Chapter 3 and Chapter 5.

Contributor	Statement of contribution
S.A. Rezaeieh (Candidate)	Designed antennas, platform and experiments (70%) Wrote and edited the paper (70%)
K.S. Bialkowski	Designed experiments (20%) Wrote and edited the paper (20%)
A.M. Abbosh	Designed experiments/antennas (10%) Wrote and edited the paper (10%)

**S.A. Rezaeieh**, A. Zamani, K.S. Bialkowski, A.M. Abbosh, “Foam embedded wideband antenna array for early congestive heart failure detection with tests using artificial phantom with animal organs” *IEEE Transactions on Antennas and Propagation*, vol. 63, no. 11, pp. 5138-5143, Nov. 2015.  
– Various parts of the paper are incorporated in Chapter 1, Chapter 3 and Chapter 5.

Contributor	Statement of contribution
S.A. Rezaeieh (Candidate)	Designed antennas, platform and experiments (70%) Wrote and edited the paper (70%)
A. Zamani	Imaging Code (100%) Wrote and edited paper (20%)
K.S. Bialkowski	Designed experiments (20%) Wrote and edited the paper (5%)
A.M. Abbosh	Designed experiments/antennas (10%) Wrote and edited the paper (5%)

**S.A. Rezaeieh**, A. Zamani, K.S. Bialkowski, A.M. Abbosh, “Unidirectional slot-loaded loop antenna with wideband performance and compact size for congestive heart failure detection”, *IEEE Transactions on Antennas and Propagation*, 2015, vol. 63, no. 10, pp. 4557-4562, Oct. 2015. Various parts of the paper are incorporated in Chapter 4 and Chapter 5.

Contributor	Statement of contribution
S.A. Rezaeieh (Candidate)	Designed antennas, platform and experiments (70%) Wrote and edited the paper (70%)
A. Zamani	Imaging Code (100%) Wrote and edited paper (10%)

K.S. Bialkowski	Designed experiments (20%) Wrote and edited the paper (10%)
A.M. Abbosh	Designed experiments/antennas (10%) Wrote and edited the paper (10%)

**S.A. Rezaeieh**, A.M. Abbosh, “Compact Planar Loop-Dipole Composite Antenna with Director for Bandwidth Enhancement and Back Radiation Suppression,” *IEEE Transactions on Antennas and Propagation*, 2015 (*Accepted with Minor Revision*). – This paper is incorporated in Chapter 4.

Contributor	Statement of contribution
S.A. Rezaeieh (Candidate)	Designed antennas and experiments (90%) Wrote and edited the paper (80%)
A.M. Abbosh	Designed experiments/antennas (10%) Wrote and edited the paper (20%)

**S.A. Rezaeieh**, K.S. Bialkowski, A. Abbosh, “Microwave system for the early stage detection of congestive heart failure”, *IEEE Access*, vol. 2, pp. 921-929, 2014. – Various parts of the paper are incorporated in Chapter 1 and Chapter 5.

Contributor	Statement of contribution
S.A. Rezaeieh (Candidate)	Designed antennas, platform and experiments (70%) Wrote and edited the paper (80%)
K.S. Bialkowski	Designed experiments (20%) Wrote and edited the paper (10%)
A.M. Abbosh	Designed experiments/antennas (10%) Wrote and edited the paper (10%)

**S.A. Rezaeieh**, M.A. Antoniadis, A.M. Abbosh, “Bandwidth and Directivity Enhancement of Loop Antenna by Non-Periodic Distribution of Mu-Negative Metamaterial Unit Cells,” *IEEE Transactions on Antennas and Propagation*, 2015 (*Accepted with Minor revision*). – This paper is incorporated as Chapter 4.

Contributor	Statement of contribution
S.A. Rezaeieh (Candidate)	Designed antennas and experiments (70%) Wrote and edited the paper (70%)
M.A. Antoniadis	Design and Theory Analysis (20%)

	Wrote and edited the paper (20%)
A.M. Abbosh	Designed experiments/antennas (10%) Wrote and edited the paper (10%)

**S.A. Rezaeieh**, K.S. Bialkowski, A. Abbosh, “Folding method for bandwidth and directivity enhancement of meandered loop uhf antenna for heart failure detection system”, *IET Microwaves, Antennas & Propagation*, vol. 8, No. 14, pp. 1218-1227, 2014. – This paper is incorporated to Chapter 5.

Contributor	Statement of contribution
S.A. Rezaeieh (Candidate)	Designed antennas, platform and experiments (80%) Wrote and edited the paper (80%)
K.S. Bialkowski	Designed experiments (10%) Wrote and edited the paper (10%)
A.M. Abbosh	Designed experiments/antennas (10%) Wrote and edited the paper (10%)

### **Contributions by others to the thesis**

I acknowledge the contribution by others in this thesis. Assoc. Prof. Amin M. Abbosh as the main supervisor had worked closely on the ideas for the system and antenna designs throughout the thesis. Dr. Konstanty S. Bialkowski as the second supervisor had worked closely on hardware implementation and interfacing of various system elements mainly on configuring switching systems. Assist. Prof. Marco Antoniadis as the third supervisor has contributed in understanding the theory of the different types of antennas. His contribution is specifically acknowledged in providing deep discussions and simulation files on metamaterial antennas. All imaging algorithms utilized and written in the thesis are contributed partly by Dr. Yifan Wang and Dr. Konstanty S. Bialkowski and in a wider scope by Mr. Ali Zamani.

### **Statement of parts of the thesis submitted to qualify for the award of another degree**

“None”



## **Acknowledgements**

Studying Ph.D. is a long journey that comes with its own excitements and frustrations along the way. It takes a lot of effort and patience to complete each step till reaching the final milestone where you submit your findings as a thesis. This is not possible without being surrounded by professional, loving and caring people who would encourage you during this period. First and foremost, I would like to extend my deepest regards and gratitude to my main supervisor Assoc. Prof. A.M. Abbosh for his support, patience and mentorship during my studies. He is not only a great teacher that had technically supported my studies, but also is a close friend who in my opinion had successfully guided me through various problems throughout this long period. I would also like to acknowledge valuable discussions and time that I was privileged to have with my co-advisors, Dr. K.S. Bialkowski and Assist. Prof. M.A. Antoniadis in resolving several technical matters with the designed antennas and the systems. My Ph.D. studies would have not been possible without financial support of Commonwealth of Australia and University of Queensland. I am very grateful for the chance that was given to me to complete my studies. Last but not least, I would like to thank my family for supporting me during my studies and doing whatever they can to provide a calm environment for me to complete my studies. I love you and am so grateful to you.

## **Keywords**

Torso scanner system, fluid accumulation detection, pleural effusion detection, pulmonary oedema detection, heart failure detection, loop-dipole antennas, slot loaded antennas, wideband antennas, unidirectional antennas, three dimensional (3-D) antennas.

## **Australian and New Zealand Standard Research Classifications (ANZSRC)**

ANZSRC code: 100501, Antennas and Propagation, 70%

ANZSRC code: 090399, Biomedical Engineering not elsewhere classified, 30%

## **Fields of Research (FoR) Classification**

FoR code: 0906, Electrical and Electronic Engineering, 70%

FoR code: 0903 Biomedical Engineering, 30%

# Contents

Abstract .....	II
List of Figures .....	XXIII
List of Tables.....	XXX
Abbreviations .....	XXXI
1 Introduction .....	1
1.1 Brief History of Medical Microwave Imaging .....	1
1.2 Pulmonary Oedema and Pleural Effusion .....	3
1.3 Detection Only Techniques .....	5
1.3.1 Standing Wave's Node Monitoring .....	5
1.3.2 Amplitude and/or Phase Analysis.....	5
1.3.3 Acoustic Techniques .....	7
1.3.4 Bioimpedance Spectroscopy .....	8
1.3.5 Ultra-Wideband Radar .....	9
1.3.6 Radiometry.....	11
1.3.7 Permittivity Estimation .....	12
1.4 Detection and Localizing Systems .....	12
1.4.1 Electrical Impedance Tomography .....	13
1.4.2 Radar Based Microwave Imaging.....	14
1.5 Thesis Motivation and Challenges .....	16
1.6 Contributions Proposed in the Thesis .....	18
1.6.1 Antenna Design.....	18
1.6.2 Platform (Data Acquisition Setup) Design .....	19
1.6.3 Detection Approaches .....	19
2 Review of Microwave Imaging Systems and Utilized Detection Algorithms....	20
2.1 Microwave Imaging Systems .....	20
2.2 Monostatic Microwave Imaging Systems .....	21
2.2.1 Rotating Platform Using Single Antenna (Radar) .....	22
2.2.2 Differential Microwave Imaging (Radar).....	23
2.3 Multi Antenna Imaging (Near Field) .....	24

2.4 Multistatic Microwave Imaging Systems.....	25
2.4.1 Multi-Level Imaging System.....	25
2.4.2 Quasi Multistatic System Using Tomography (Radar) .....	26
2.5 Conclusion.....	27
2.6 Thesis Organization.....	27
3 Antenna Designs Part I: Three Dimensional (3-D) Structures .....	29
3.1 Defining Optimum Operating Frequency .....	29
3.2 Antenna Design Criteria.....	31
3.2.1 Designing Wideband Printed Loop Antennas with Back Radiation Suppression Using Folding Technique .....	33
3.2.2 Reducing Size of the Antenna.....	37
3.2.3 Widening the band with Unidirectional Radiation .....	39
3.2.4 Increasing the Operating Bandwidth .....	41
3.2.5 Antenna Test .....	42
3.3 Three-Dimensional Open-Ended Slot Antenna .....	44
3.3.1 Design Criteria and Proposed Antenna Design .....	45
3.3.2 Size Reduction .....	46
3.3.3 Bandwidth Enhancement .....	47
3.3.4 Performance of the Antenna .....	49
3.4 Three Dimensional Meandered Loop Antenna.....	51
3.4.1 Antenna Design.....	51
3.4.2 Further Discussion .....	54
3.5 Cubic Composite Loop-Monopole Antenna.....	55
3.5.1 Antenna Design.....	56
3.5.2 Foam-Embedded Antenna Array .....	58
3.6 Conclusion.....	62
4 Antenna Designs Part II: Planar Structures.....	63
4.1 Loop-dipole Composite Antenna .....	63
4.1.1 Introduction.....	63
4.1.2 Theory .....	63
4.1.3 Antenna Design.....	65
4.1.4 Performance Analysis .....	65
4.1.5 Geometry Analysis.....	71

4.1.6 Position of the Loop Antenna .....	74
4.1.7 Antenna Measurements .....	76
4.2 Non-Uniform Metamaterial Unit-Cell Loaded Loop Antenna .....	79
4.2.1 Introduction .....	79
4.2.2 Theory of MNG Loaded Transmission Lines .....	80
4.2.3 MNG Unit-cell Design .....	82
4.2.4 Antenna Designs .....	84
4.2.5 MZR Antenna .....	85
4.2.6 Unidirectional MZR Antenna .....	88
4.2.7 Wideband and Unidirectional Loaded Loop Antenna .....	89
4.2.8 Antenna Measurements .....	94
4.3 Capacitively Loaded Loop Antenna .....	98
4.3.1 Slot-Loaded Loop Design Analogy .....	98
4.3.2 Design Procedure .....	98
4.3.3 Further Discussion .....	102
4.3.4 Antenna Measurements .....	102
5 Proposed Torso Imaging Systems .....	105
5.1 Torso Phantom .....	106
5.2 Linear Scanning System with Synthetic Aperture Radar Imaging Approach ..	107
5.2.1 Scanning Approach and Data Acquisition Process .....	108
5.2.2 Experimental Results .....	109
5.2.3 Effect of Antenna Characteristics on Imaging Results .....	110
5.3 Automated Linear Scanning System Using Image Subtraction Method .....	112
5.3.1 Introduction .....	112
5.3.2 System Design .....	112
5.3.3 Platform Details .....	113
5.3.4 Data Acquisition .....	114
5.3.5 Data Processing .....	115
5.3.6 System Calibration .....	116
5.3.7 Minimum Detectable Level of Fluid Accumulation .....	118
5.3.8 Fluid Localization .....	120
5.3.9 Detection in the Case of Presence of Fluid in Both Lungs .....	120

5.4 Automated System Employing Two Antennas for Simultaneous Vertical Scanning .....	121
5.4.1 Introduction .....	121
5.4.2 Differential Detection Approach .....	124
5.5 Automated System Utilizing Two Antennas for Simultaneous Horizontal Scanning .....	125
5.5.1 Introduction .....	125
5.5.2 Proposed System .....	125
5.6 Multistatic Torso Imaging System Utilizing Expanding Foam .....	128
5.6.1 Introduction .....	128
5.6.2 System Realization .....	129
5.6.3 Imaging Algorithm .....	129
5.6.4 Results .....	133
5.7 Semi Elliptical/Circular Scanning Platform .....	135
5.7.1 Introduction .....	135
5.7.2 Platform Design .....	135
5.8 Conclusion .....	138
6 Clinical Torso Imaging Systems .....	139
6.1 Torso Imaging System Embedded in a Clinical Bed .....	139
6.1.1 System Introduction .....	139
6.1.2 The Proposed Pre-Clinical System .....	140
6.1.3 Imaging Process .....	141
6.1.4 Experimental Results .....	144
6.2 Microwave Torso Scanner .....	149
6.2.1 Design Consideration .....	149
6.2.2 Proposed System .....	150
6.2.3 System Test Configuration .....	151
6.2.4 Mono-Static Data Acquisition Approach .....	152
6.2.5 Multi-Static Data Acquisition Configuration .....	154
6.2.6 Human Test Results .....	156
7 Conclusion and Future Work .....	158
7.1 Conclusion .....	158
7.2 Future Work .....	160

Bibliography..... 161

# List of Figures

Fig. 1.1. Fluid accumulation inside lungs in early stages of (a) pulmonary oedema and (b) pleural effusion. ....	4
Fig. 1.2. (a) Experimental setup and amplitude and phase variation graphs. ....	6
Fig. 1.3. Schematic view of the stethoscope array and water injection area and (b) experimental setup using actual stethoscopes. ....	8
Fig. 1.4. (a) Schematic view and (b) detailed configuration of a bioimpedance spectroscopy configuration. (c) Impedance variations of thorax for various electrode pairs .....	9
Fig. 1.5. (a) Data acquisition setup. (b) Utilized tissue models in the experiments and (c) obtained pulse responses.....	10
Fig. 1.6. (a) Brightness temperature radiated from the lungs in different pulmonary oedema levels. (b) Radiometer reading in different steps of injecting water inside the lungs .....	11
Fig. 1.7. Operating basis of the permittivity estimation method.....	12
Fig. 1.8 (a) Configuration of an EIT system with electrodes surrounding the area under investigation and (b) obtained image of the utilized phantom within the setup .....	14
Fig. 1.9. (a) Head imaging configuration and (b) detected stroke in a desired location. (c) Breast cancer imaging platform and (d) 2-D image of cancerous cell. ....	16
Fig. 2.1 Measured (a) conductivity in S/m and (b) relative permittivity of different tissues. Top charts represent healthy and bottom charts represent malignant cases. (Numbers inside parentheses represent the number of measurements.) .....	21
Fig. 2.2 A mono-static microwave imaging configuration. ....	22
Fig. 2.3 (a) Scanning system top view (left) and front view (right) and (b) obtained images in three different planes.....	23
Fig. 2.4 (a) Array Setup and (b) obtained images using differential microwave imaging. ....	24
Fig. 2.5 (a) Schematic view and (b) fabricated near field imaging system configuration. ....	25
Fig. 2.6 Multi level multi static microwave imaging system.....	26
Fig. 2.7 Quasi multi static data acquisition system. ....	27
Fig. 3.1. HFSS human model of the torso area. Front view (left) and side view (right).....	30

Fig. 3.2. Circuit model of the human torso. $Z$ refers to the impedance, and $\theta$ refers to the electrical length, subscript $c$ refers to coupling medium, $s$ : skin, $f$ : fat, $m$ : muscle, $l$ : lung.....	30
Fig. 3.3. Variation of signal amplitude at the center of deflated lungs with frequency.....	31
Fig. 3.4. Variation of signal amplitude at the center of deflated lungs with frequency.....	31
Fig. 3.5. Detailed geometry and fabricated prototype of the proposed antenna.....	34
Fig. 3.6. Initial antenna configuration.....	34
Fig. 3.7. (a) Geometry of studied antennas. (b) Real part, and (c) imaginary part of the input impedance of the Reference Antenna, Antenna 0 and Antenna 1.....	35
Fig. 3.8. Design evolution of the UHF antenna.....	35
Fig. 3.9. Simulated $ S_{11} $ variations of Antennas 1, 2 and 3.....	36
Fig. 3.10. (a) Initial folding process (Antenna 1) and (b) final design (Antenna 2)..	38
Fig. 3.11. $ S_{11} $ performance of the antenna considering different values for $G_c$ .....	38
Fig. 3.12. (a) Input impedance and (b) $ S_{11} $ performance of the Antenna1 considering various cases.....	40
Fig. 3.13. Vector electric field distribution (a) before and (b) after connecting metal sheets to Antenna 1 at 750 MHz (y z plane).....	40
Fig. 3.14. (a) $ S_{11} $ performance of Antenna 2. Surface current distribution of Antenna 2 (b) before and (c) after addition of a short-ended slot line.....	42
Fig. 3.15. (a) Fabricated Antenna, (b) measured and simulated $ S_{11} $ , gain and FBR.....	43
Fig. 3.16. Normalized measured radiation patterns of the antenna at (a) 600 MHz, (b) 700 MHz and (c) 950 MHz.....	44
Fig. 3.17. (a) Top and (b) side view of the antenna, and (c) fabricated prototype.....	46
Fig. 3.18. (a) $ S_{11} $ of the proposed antenna with different values of $l_f$ and (b) input impedance of the antenna with and without slot on the feeding line.....	48
Fig. 3.19. (a) Fabricated antennas. (b) $ S_{11} $ and $ S_{22} $ in the presence of another antenna, reflector and phantom, (c) and (d) measured radiation patterns with and without (W/O) reflector at 580 MHz and 920 MHz, respectively. (Scale: -40 dB, division: 10 dB).....	50
Fig. 3.20. Geometry details of the optimum design in a (a) 3-D configuration, (b) top view (Side 1) and (c) right side view (Side 3).....	52
Fig. 3.21 (a) Simulated and measured $ S_{11} $ performance and gain of the optimum design and $ S_{11} $ performance of the antenna during the evolution process. Far-field	

radiation pattern of the optimum antenna at (b) 800 MHz and (c) 950 MHz. (d) Time domain near-field of the antenna across the operating bandwidth.....	54
Fig. 3.22. Fig. 1. Detailed geometry of the antenna. (a) Printed layer and its side view, (b) 3-D view .....	57
Fig. 3.23. (a) $ S_{11} $ of the antenna in different design steps (RP: Resonating U-shaped parasitic patch), and (b) $ S_{11} $ with size of the short-ended slot.....	58
Fig. 3.24 Fabrication process of (a) single element, (b) array, (c) foam spraying and (d) final structure .....	60
Fig. 3.25. Measured vs. simulated (a) S-parameters, (b) gain, and radiation patterns at (c) 750 MHz and (d) 920 MHz. (Scale: 40 dB, division: 10 dB).....	62
Fig. 4.1 Radiation pattern of (a) electric dipole ( $J_e$ ), (b) magnetic dipole ( $J_m$ ) and (c) complementary antenna on E-plane. ....	65
Fig. 4.2 Detailed geometry of the proposed loop-dipole composite antenna. ....	66
Fig. 4.3 (a) $ S_{11} $ , (b) real and (c) imaginary parts of the input impedance (identical legends) throughout the evolution process. (d) Equivalent circuit and (e) Smith chart variations for various positions of the loop.....	68
Fig.4.4 Radiation patterns of the antenna at (a) E-plane and (b) H-plane (maximum radiation is at x-direction) (Scale: dB). ....	69
Fig. 4.5 Surface current distribution at (a) 0.75 GHz and (b) 1 GHz and (c) 1.2 GHz.....	70
Fig. 4.6 Radiation patterns of the antenna at (a) E-plane and (b) H-plane (maximum radiation is at x-direction) (Scale: dB). ....	71
Fig. 4.7 $ S_{11} $ variations with (a) $d_e$ and $s$ . (c) E-plane (left side) and H-plane (right) radiation patterns (Scale: dB) and (d) surface current distribution at $s=7$ mm. ....	73
Fig. 4.8 (a) $ S_{11} $ at different $L$ and $d$ values. (b) Variations of magnitude of surface current with $d$ at sample frequency of 1.05 GHz. E-plane (left side) and H-plane (right side) radiation patterns at (c) $d=5$ mm and (d) $L=80$ mm. (Scale: dB).....	75
Fig. 4.9 Fabricated antenna (a) top view, (b) bottom view. Measured (c) reflection coefficient and (d) gain of the antenna vs. simulated results. ....	77
Fig. 4.10 Measured radiation patterns of the antenna at 0.75 GHz (left column), 0.9 GHz (middle column) and 1.05 GHz (right column). (a) E-plane Co-polarization, (b) H-plane Co-polarization, (c) E-plane Cross polarization and (d) H-plane Cross polarization. (Solid lines: simulated, dashed lines: measured) (Scale: dB).....	78
Fig.4.11 (a) Symmetric distributed and (b) lumped element equivalent circuit of a MNG metamaterial unit-cell. ....	80

Fig. 4.12 Dispersion diagram of a MNG unit-cell for arbitrary lumped element values for a transmission line with width of 10mm and length of 20 mm on FR4 substrate with 0.8 mm thickness. ....	82
Fig. 4.13. (a) Proposed periodic structure of MNG unit-cells, including the equivalent symmetric equivalent circuit, (b) detailed geometry of a single MNG unit-cell employing an interdigital capacitor. (c) Dispersion diagram of the MNG unit-cell shown in (b) for the values presented in Table 4-II. ....	83
Fig. 4.14 (a) Schematic view of antennas with one and four unit-cells.(b) Reflection coefficients, (c) real and (d) imaginary parts of the input impedance of the proposed antennas. ....	87
Fig. 4.15. Surface current distribution of the realized antennas with (a) one and (b) four unit-cells at their respective MZR frequencies of 0.56 GHz and 0.67 GHz. (c) x-y plane radiation pattern of the designed antenna employing four unit-cells with uniform and non-uniform distribution of unit-cells at the sample frequency of 0.67 GHz. (maximum radiation in the x-direction).....	88
Fig. 4.16. (a) Schematic view and (b) surface current distribution of the antenna with non-periodic distribution of the unit-cells.....	90
Fig. 4.17. Surface current distribution of the antenna with (a) non-periodic distribution and (b) equivalent dipole array. Radiation patterns of the non-periodically loaded loop (solid line) vs. dipole array (dashed line) in the (c) x-y plane and (d) y-z plane at the resonance frequency of 0.83 GHz. (maximum radiation in the x-direction) .....	90
Fig. 4.18. (a) Proposed wideband and unidirectional MNG-loaded loop antenna. (b) Reflection coefficient variations with the size of the strip and (c) IDC (Dimensions of Table I) gap variations.....	92
Fig. 4.19. (a) Radiation pattern of the antenna in the x-y plane (left) and y-z plane (right). Magnitude of surface current distribution at (b) 0.68 GHz, (c) 0.83 GHz and (d) 0.95 GHz. (maximum radiation in the x-direction).....	94
Fig. 4.20. (a) Fabricated antenna, (b) measured vs. simulated reflection coefficient and (c) gain of the fabricated antenna. (Identical legends).....	96
Fig. 4.21. Measured x-y plane (left side) and y-z plane (right side) radiation patterns of the antenna at (a) 0.68 GHz, (b) 0.83 GHz and (c) 0.95 GHz. (solid line: Simulated, dashed line: Measured). (Maximum radiation in the x-direction) .....	97
Fig. 4.22. (a) Geometry of the antenna and (b) feeding structure.....	99
Fig. 4.23. (a) Reflection coefficient, (b) imaginary and (c) real parts of the input impedance of the antenna during evolution process (identical legends). ....	101
Fig. 4.24. Reflection coefficient of the antenna for different values of space between dipole arms .....	101

Fig. 4.25 Measured vs. simulated (a) $ S_{11} $ and (b) gain of the antenna. Measured radiation patterns of the antenna at (c) 680 MHz, (d) 800 MHz and (e) 1 GHz (maximum radiation: -x-direction) (Scale: 30 dB, division: 10 dB).....	104
Fig. 5.1 Torso X-ray .....	105
Fig. 5.2 Utilized torso phantom in the thesis with the internal organs. ....	106
Fig. 5.3 Proposed imaging system .....	108
Fig. 5.4. Images from a phantom representing (a) healthy case, and (b) early stage heart failure with fluid accumulated at the left lung .....	110
Fig. 5.5 (a) Images using a bidirectional for a healthy case, and (b) images using the proposed antenna with reduced bandwidth for an early heart failure affecting the left lung (black rectangle depicts actual detection of location of water and dashed rectangle shows false detection) .....	111
Fig. 5.6 Block diagram of the system.....	113
Fig. 5.7 Flowchart of data acquisition procedure.....	114
Fig. 5.8 A typical radargram. ....	116
Fig. 5.9 (a) The designed congestive heart failure detection system. Differential scattering profile of (b) measurement error and (c) healthy case. ....	117
Fig. 5.10 Differential scattering profile of lowest detectable fluid compared to healthy cases with identical scaling, (a) 10 mL water, (b) healthy and (c) 4 mL water, (d) healthy. ....	119
Fig. 5.11 Detecting presence and position of water in two cases, (a) water located at middle rear side of phantom and (b) water located at lower front side of the phantom .....	120
Fig. 5.12 Detecting presence and position of fluid in cases of accumulation inside both lungs, (a) water content with 7 mL difference (b) water content with 4 mL difference.....	121
Fig. 5.13 Proposed heart failure detection system using two identical antennas on an automated scanning platform .....	122
Fig. 5.14 Radargrams of received signals from both sides of the torso.....	123
Fig. 5.15 Differential scattering profile of (a) healthy (R-L), and unhealthy cases with fluid accumulated at (b) lower front (R-L), (c) top rear (L-R), where R denotes the right lung and L denotes the left lung. ....	124
Fig. 5.16 Proposed system for CHF detection. ....	126
Fig. 5.17. (a) Reflection coefficient samples of the antenna for healthy and unhealthy cases. Obtained images for (b) healthy and (c) unhealthy cases. (Black rectangle shows the location of the inserted fluid inside a lung).....	127

Fig. 5.18. (a) Proposed system, and (b) measured dielectric properties of lamb lungs vs human lungs (dashed line: human data, solid line: measured lamb) .....	130
Fig. 5.19 Incident and scattering electric fields in the investigation area.....	131
Fig. 5.20. Images for (a) healthy case, (b) 2 mL water injected in right lung. ....	134
Fig. 5.21. Images for (a) healthy case, (b) 2 mL water injected in right lung and, (c) water injected on both lungs with difference of 2 mL .....	134
Fig. 5.22 System configuration with quasi-elliptical antenna array .....	136
Fig. 5.23. Reconstructed images for (a) healthy case, and pulmonary edema cases using (b) artificial phantom, (c) lamb lungs and (d) Zubal phantom (simulations). ....	137
Fig. 6.1 Proposed preclinical microwave imaging system of the torso for fluid accumulation detection.....	141
Fig. 6.2 Diagram of the utilized torso imaging domain .....	144
Fig. 6.3 (a) The artificial phantom used in the tests. Images from using 8×2 array configuration on artificial phantom: (b) healthy and (c) unhealthy (1 mL inserted water). Images from using 4×2 array configuration: (d) healthy and (e) unhealthy ( 1 mL inserted water).....	146
Fig. 6.4 (a) The phantom used in the tests: Lamb lungs inside an artificial torso. Images from using 8×2 array configuration on that phantom: (b) healthy lamp and (c) lamb with 1 mL injected water.....	147
Fig. 6.5 Example of the obtained torso images of healthy volunteers. The high intensity area indicates the location of the heart. ....	148
Fig. 6.6 Statistical properties of the field intensity over the subjects. ....	148
Fig.6.7. (a) Dismantled presentation of the proposed torso scanner installed on a wall. (b) Measurement setup with human subject inside the scanner .....	151
Fig. 6.8. Scattering signal acquisition in (a) mono static and (b) multistatic configurations. ....	152
Fig. 6.9 Reconstructed image of the upper and lower regions of the torso in (a) healthy case and (b) unhealthy case with accumulated fluid inside the thorax area. Subtracted images of the upper and lower regions at three different positions; front side of the torso (left), behind ribs (middle) and deep inside thorax (right) with (c) 10 mL and (d) 3 mL injected water. (e) Scattering field intensity variation diagram for 10 mL and 3 mL inserted water compared to the healthy threshold. ....	154
Fig. 6.10. (a) Switching configuration for multi-static data acquisition. (b) Subtracted images of the upper and lower regions at three different positions; front side of the torso (left), behind ribs (middle) and deep inside thorax (right) with 3 mL injected water. (e) Scattering field intensity variation diagram in case of 3 mL inserted water compared to the healthy threshold. ....	155

Fig. 6.11. (a) Reconstructed images for top and bottom regions of the torso of one of the tested healthy subjects. (b) Scattering field intensity variation range for top and bottom regions for all of the six cases..... 157

# List of Tables

Table 3-I: Geometry details in (mm) of the reference antenna.....	44
Table 3-II: Effects of different parameters on the resonances and bandwidth (—: small or no effect). .....	49
Table 3-III: Geometrical details in (mm) of the optimum design.....	55
Table 4-I: Comparison between the area occupied by the proposed antenna and state of art unidirectional planar antennas.....	76
Table 4-II: Detailed Geometric Values of the Utilized Unit-cell.....	84
Table 4-III: Estimated and simulated resonant frequencies for a unit-cell with dimensions presented in Table 4-II, and achieved antenna size with respect to MZR resonance frequency and conventional loop resonance .....	87
Table 4-IV: Theoretical Estimation Of the Series Loading Capacitor Value, MZR resonance and simulated results for a unit-cell with different gap sizes.....	93
Table 4-V: Final dimensions of the proposed antenna.....	96
Table 4-VI: Geometrical details of the final design.....	102

# Abbreviations

HFSS	High Frequency Structure Simulator
ADS	Advanced Design System
PO	Pulmonary Oedema
PE	Pleural Effusion
CVD	Cardiovascular Disease
CPW	Coplanar Waveguide
MTM	Metamaterial
TL	Transmission Line
MNG	Mu-Negative
MZR	Mu-Zero Resonance
NRI	Negative Refractive Index
3-D	Three Dimensional
2-D	Two Dimensional
VNA	Vector Network Analyzer
BW	Bandwidth
FBR	Front to Back Ratio
FB	Fractional Bandwidth
RF	Radio Frequency
FCC	Federal Communications Committee
WGS	White Gaussian Noise
EIT	Electrical Impedance Tomography
S-parameters	Scattering Parameters
L-D Mode	Loop-Dipole Mode
IDC	Interdigital Capacitors
CPS	Coplanar Strip-Line
SAR	Specific Absorption Rate
CT	Computed Tomography
MRI	Magnetic Resonance Imaging
IOS	In-home Operating System
DD	Differential Detection
PC	Personal Computer

# Chapter 1

## Introduction

With the improvement of economical revenues in the past century, there has been extensive efforts to increase the quality of life and life expectancy of the citizens as main factors in which countries are categorized and assessed. To that end, there has been great research on finding new detection solutions and treatments to the diseases which has been unknown or complex to the medical society and industry. Medical imaging is inevitably one of the breakthroughs of the century that has provided a valuable visual guide to the medical staff and research industry to better understand and treat the diseases.

### **1.1 Brief History of Medical Microwave Imaging**

Studying the history of medical imaging [1]-[2] reveals that its roots traces back to 1895 where X-ray was discover by Wilhelm Roentgen, a German scientist, who performed the first X-ray of the history by imaging his wife's hand. This technology started to being widely used by the end of 1896. However, its ionizing nature and lack of sensitivity in detection of certain types of malignancies such as accumulation of small amounts of fluids inside human torso are of the limitations of this technology.

Ultrasound imaging was invented in 1955 which enabled doctors to see a live image of inner organs of the body. This technology uses sound waves which are out of the range of the human ears and can only be detected using ultrasound devices. The greatest advantage of this device is the fact that it is not ionizing and can be safely used as many times as required for precise detection and monitoring purposes. However, it suffers from the fact that it is in need of specialized medical staff to perform the test and interpret the obtained results in addition to lack of sensitivity in diagnosing tissues behind bones.

In, 1960, Endoscopy, a minimally invasive technique, was started to being used to examine the inner organs of the body by physically sending a tube inside the holes/cavities of the body such as stomach. Despite its unpleasant experience for the patients, it provided valuable visual data in areas of body which were not possible to be imaged by the existing technologies at the time.

By the development and convenience of accessibility and use of computers in the late 1960's, computed tomography (CT)-scan technology was proposed in 1967. This method utilizes computational techniques to analyse several X-ray images and produce a more accurate image of the

investigated area of the body. It was firstly used in 1971 to image the brain of a human being that was a breakthrough in detection of presence and actual position of tumours. However, despite its impressive performance in terms of providing clear images, there are serious concerns regarding its safety as it imposes rays that are extremely higher than conventional X-rays and therefore, cannot be safely used by certain types of patients such as pregnant women. Moreover, due to similar safety issues and limited allowable exposed dose, it cannot be used frequently. This is a drawback considering the fact that a monitoring tool is needed in rehabilitation process for certain types of diseases such as monitoring the progress of fluid level in patients with congestive heart failure.

The latest and most exciting breakthrough in the field of medical imaging which lead to the winning of several Nobel prizes for the researchers in the field is the invention of magnetic resonance imaging (MRI). This technique is based on the nuclear magnetic resonance (NMR) method which was first proposed by Felix Bloch and Edward Purcell in 1946. It was used to show the potential of the technique in differentiating the cancerous and normal cells based on their resonance responses in 1971. MRI device use complex computations to produce images from the NMR responses and produce a high quality image of the desired area of the body. However, due to the very complex structure of computation and also high price of the utilized coils for creating electromagnetic field, the overall size and price of the device are large and expensive, respectively.

Therefore, while the conventional imaging devices have come a long way and evolved from very simple images such as X-ray to the very complex ones similar to that of a MRI, each associate with limitations in the modern demanding society where high sensitivity is required to be accompanied with mobility for the medical diagnosis and imaging tools. To that end, there has been an immense amount of research conducted by various organizations and universities to introduce alternative and or supplementary tools which could be easily employed at any location, e.g. a remote village, or by first aid units in an ambulance.

Studying the literature reveals that there are a wide variety of techniques and devices that has been proposed and fabricated, respectively, for two major diseases; breast cancer and brain stroke. However, according to World Health Organization (WHO) [3], cardiovascular (CVD) related diseases, specifically heart failure, are the predominant cause of mortality in the world. Analysing the statistics released by WHO in January 2015, around 17.5 million people have lost their lives due to CVDs that is about 31% of the deaths in the world. Based on these published data, more than 75% of these mortalities are taking place in middle or low income countries. This report suggests that besides exercising a healthy life, people need early diagnosis. One of the common symptoms of these diseases is the accumulation of fluid in the torso (inside or around the lungs). Therefore, early stage detection and monitoring of the lungs is the key to early medical intervention to prevent health deterioration or even death. This aim is of great importance for the welfare of the society, and is

essential to relieve the associated burden from the healthcare system. Yet, investigating the existing literature, reveals that there has been limited success in building a fully operational system that can be tested in realistic and clinical scenarios to verify the reliability of the system for early stage detection of fluid as a sign of many chronic heart diseases and cancers. This thesis aims at filling this gap by thoroughly studying the symptoms of these diseases and how they can be detected using various system configurations, and finally proposing a clinical device which can be easily used in clinics, remote and/or mobile emergency units. To that end, the following sections are contributed to the introduction of the symptoms of these diseases and a complete review of the proposed techniques.

## **1.2 Pulmonary Oedema and Pleural Effusion**

Pulmonary oedema is the common manifestation of various diseases, such as hypertension, pulmonary infections, acute heart failure and respiratory distresses that some are among the leading causes of fatality worldwide. As an example, the early pulmonary manifestation of the acute phase of decompensated heart failure is the congestion of the vascular bed due to increased capillary hydrostatic pressure that results in the accumulation of fluids (cardiac pulmonary oedema) inside the air sacs in the lungs as depicted in Fig. 1.1 (a) [4]. When the heart fails to supply enough blood, pressure increases in the blood vessels near the lungs. This results in a gradual leakage of blood into air sacs of the lungs. Accumulation of blood increases the pressure in the capillaries, which are the tiniest blood vessels in the body and consequently causes leakage of fluid (mainly water) inside the lungs, known as cardiac pulmonary oedema.

On the other hand, as shown in Fig. 1.1 (b) pleural effusion is the accumulation of fluid around the lungs between outer layer of the lungs and the chest wall, which reduces the area of lung expansion and hence weakens the breathing and causes chest pains. It can be caused by various diseases such as cancer, liver failure and heart failure. Through invasive monitoring systems of pulmonary pressure, it has been shown that acute heart failure has a relatively long incubation period, up to two weeks, during which pulmonary oedema can be identified before the appearance of clinical signs [5], [6]. Therefore, if that accumulated fluid is detected and monitored early when it is small in volume, it allows a timely treatment to avoid further complications such as volume overload and worsening cardiac function. Previous research and current guidelines indicate the importance of monitoring volume overload and timely treatment to reduce hospitalization [7]-[9].

Ultrasonic tests, CT-scan and chest X-ray are the most widely used diagnostic tools for lungs' fluid detection. However, ionization nature and lack of sensitivity prevents their use as an early stage diagnostic and long-term monitoring tool. To overcome the disadvantageous, there has been intensive research to realize a portable non-invasive device for lung fluid diagnosis and monitoring in the past

four decades [10]-[31] The realized systems can be classified under two main categories; 1) detection only systems [10]-[21] and 2) detection and localization ones [22]-[31]. The first category aims at monitoring the level of accumulated fluids in the torso by observing certain aspects of reflected or transmitted signals, and linking the presence of the fluid to any sensible changes in those quantities. The second category, on the other hand, aims at detecting the presence of the fluid and defining its approximate or accurate position by creating two or three dimensional images. Those images map the torso, especially lungs, tissues' properties by calculating the intensity of the electromagnetic field or impedance distribution of tissues depending on the utilized imaging algorithm. This section reviews the operating basis of the proposed systems with different modalities and their achieved results.

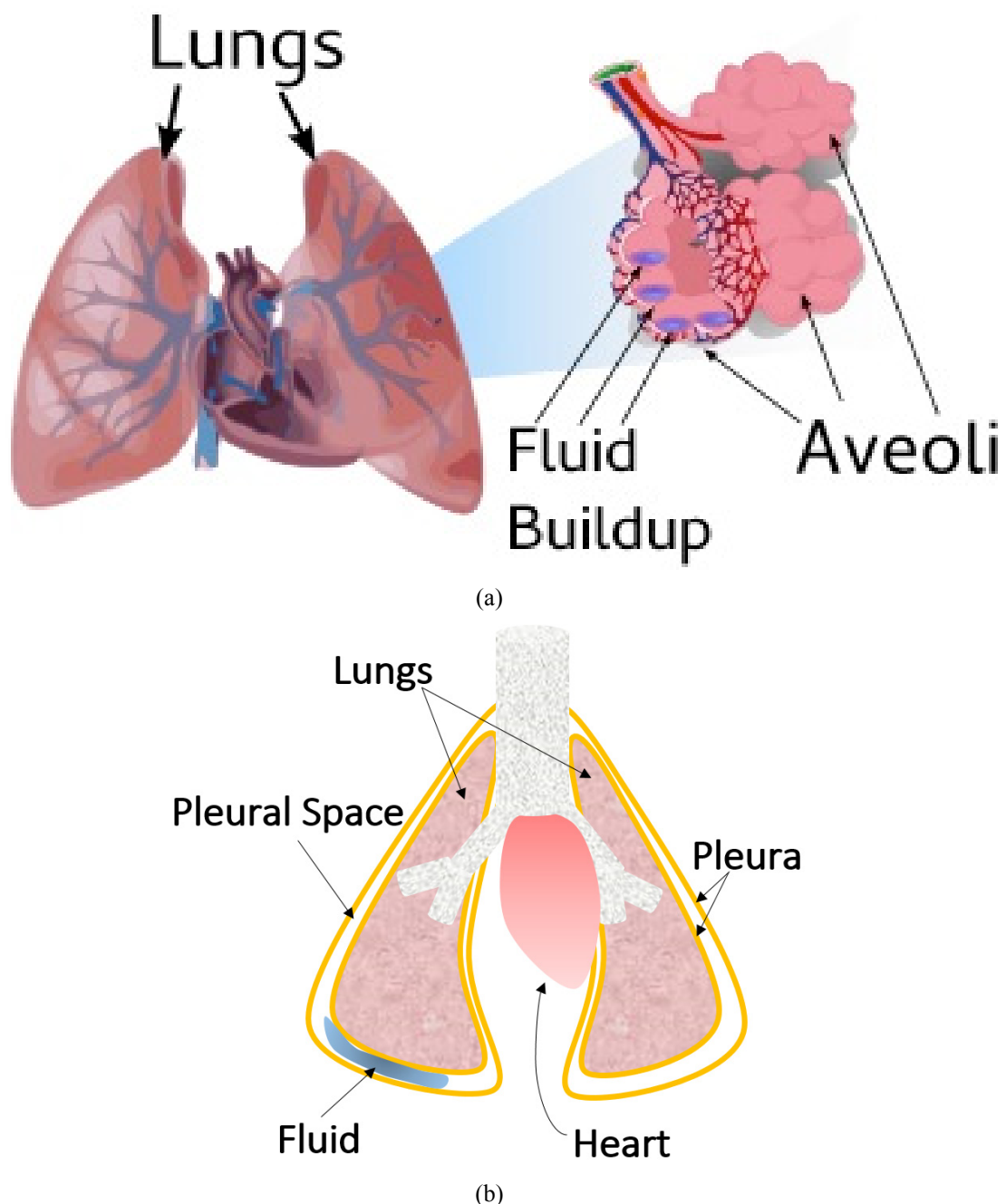


Fig. 1.1 Fluid accumulation inside lungs in early stages of (a) pulmonary oedema and (b) pleural effusion.

### **1.3 Detection Only Techniques**

This section reviews the systems that only aim detecting the presence or absence of fluid (mainly water) inside the torso. The main purpose of those modalities is to provide a preliminary piece of information to help define the required medication to be given by paramedics at the accident scenes encountering lung injuries or beach rescue teams dealing with drown people.

#### **1.3.1 Standing Wave's Node Monitoring**

The feasibility of using microwave signals as a reference for the detection of fluid accumulation inside the lungs was first investigated by Susskind in 1973 [10]. This study revealed that the position of the node of standing wave changes when it encounters water content, and hence it can be used as a measure for monitoring fluid content inside the lungs. In this study, a simple structure that includes a pair of sponges was used to model the lungs. Two transmitting/receiving horn antennas were used at both sides of the sponges, which are sandwiched between two metal sheets and represent the torso shell. The study does not define the best operating frequency, yet, it denotes that the signals above 10 GHz cannot be used due their short wavelengths that limit signal penetration deep inside the torso. The reported results revealed that by gradually inserting water inside the sponges, the node in the standing wave on the source changes and its shift is consistent with the dampness of the sponge.

#### **1.3.2 Amplitude and/or Phase Analysis**

As mentioned above the change in the behaviour of microwave signals in encountering different media is the principle of microwave diagnostic systems that is widely utilized to detect vital signs [32]-[35] and cancerous tumours, which inherently have high water contents [36]-[37]. This fact led to the investigation of the effects of presence of water inside the lungs on the levels of amplitude and phase of the reflected or transmitted signals [11]-[16]. To that end, as shown in Fig. 2, an applicator was directly placed on the chest of a subject under study to record the changes in the amplitude and phase of signals [11]. The applicator was designed to operate at 915 MHz with a power of 50 – 500  $\mu$ W to enhance the required signal penetration. As can be seen from Fig. 1.2 (a), the results showed a 1 dB change in the amplitude and 5 degree variations in the phase of the reflected signal during normal breathing. Further experiments revealed that locating the applicator at the rear side of the torso provides larger variations both in phase and amplitude of the reflected signal. To test the possibility of detecting fluid using potential changes, massive amounts of water was inserted into the lungs of a dog, and it was found that a significant shift, up to 15 times, occurs in the level of the baseline of the amplitude. The same changes in the baseline of the phase were not observed.

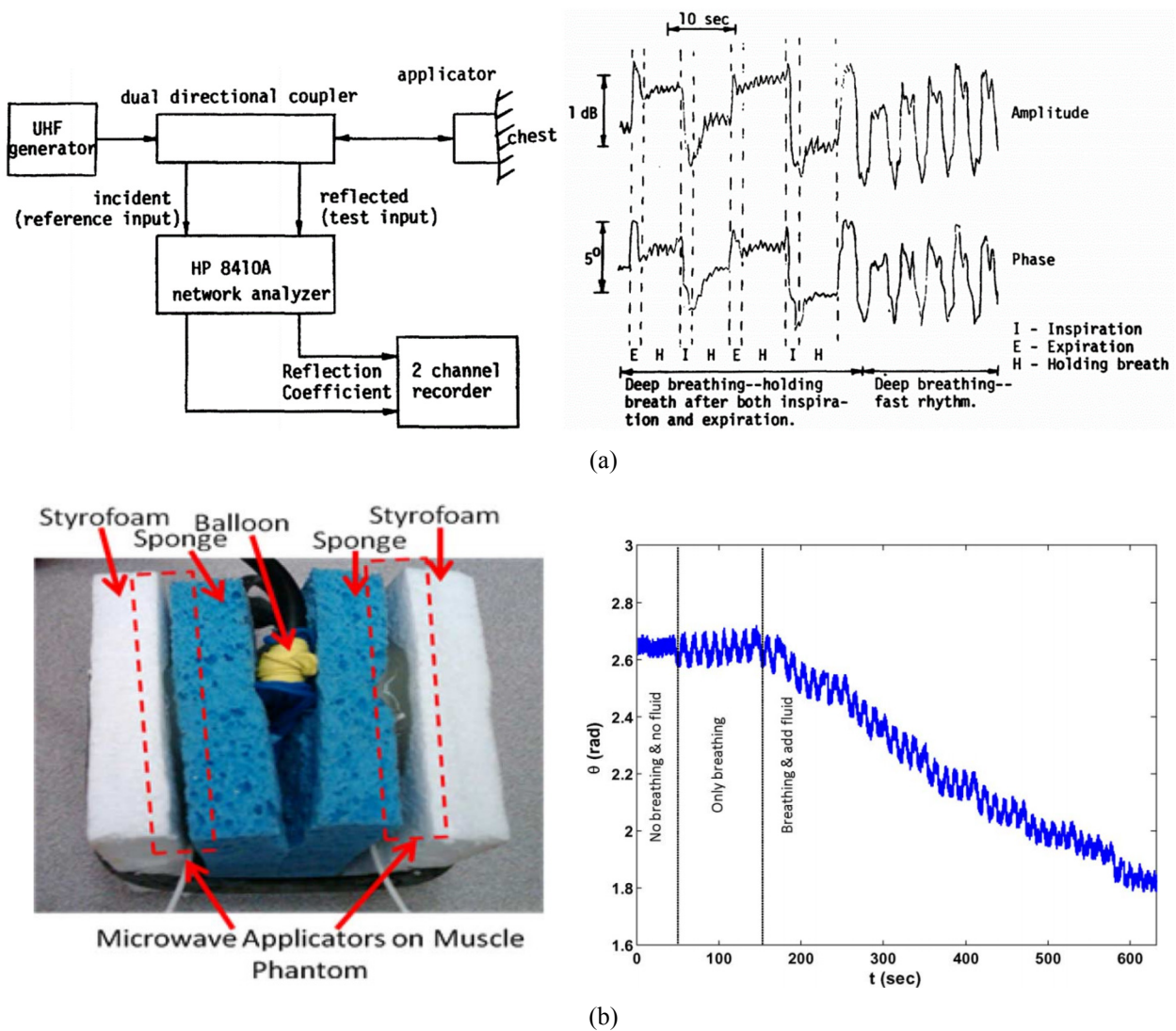
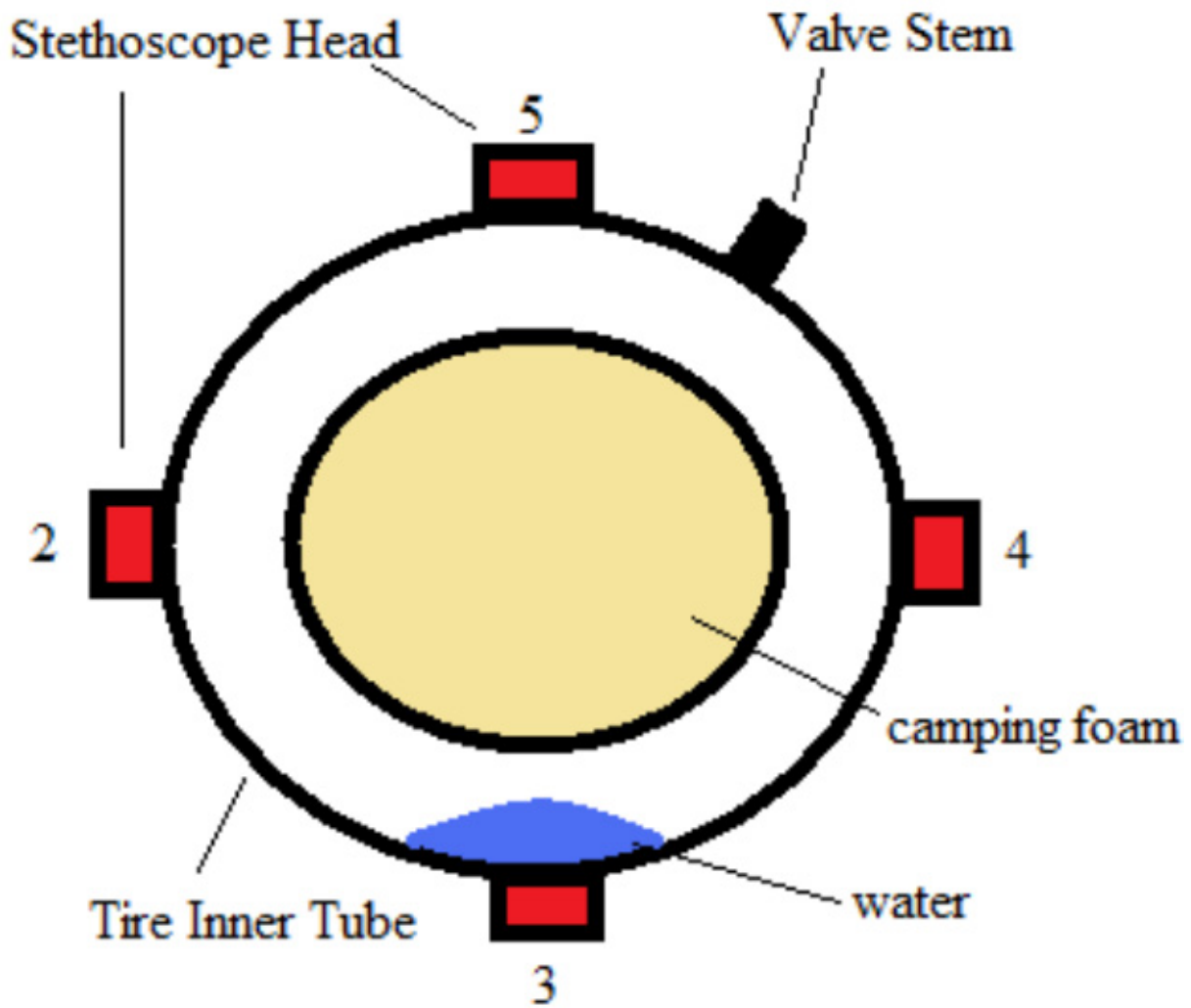


Fig.1.2. (a) Experimental setup and amplitude and phase variation graphs. (Images obtained from [11], [15] © [1976, 2011] IEEE)

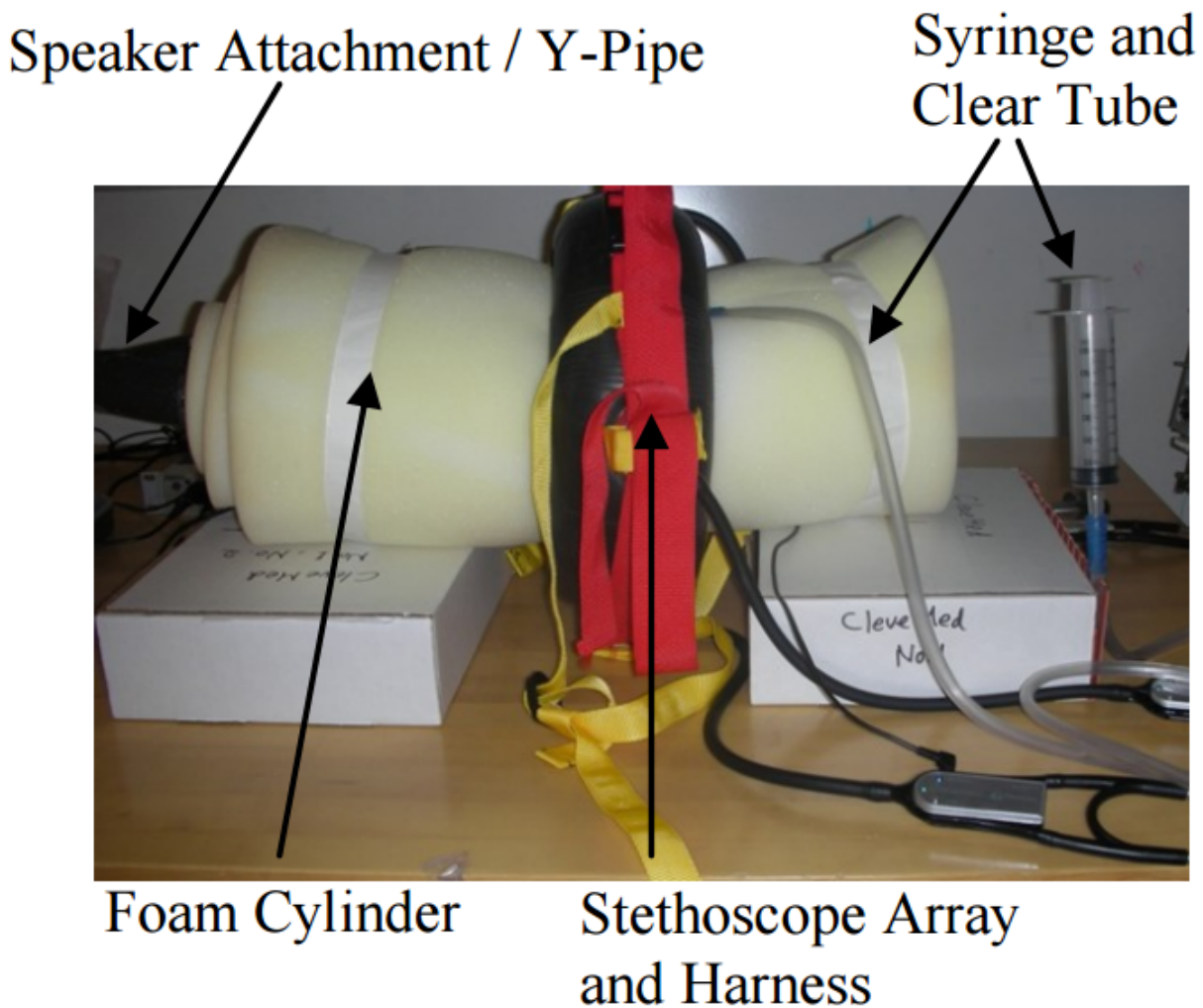
Considering the fact that the transmission coefficient between two sources is determined by the dielectric properties of the medium between them, further studies reported changes in the level of the transmitted signal by increasing the fluid amount inside the lungs [12]. Additional studies concluded that the transmission tests are 50 times more sensitive to changes than the reflection ones [13]. To address the uncertainty between selecting the amplitude, phase or mix of them as the determining criteria for monitoring the fluid level changes, a numerical study in which the lung was divided into three regions was conducted [14]. Different positions for the transmitter and receiver were investigated and the obtained results were compared. It was shown that amplitude variations are more consistent compared to the phase ones. However, as the variations in the amplitude are significantly smaller than the phase one, phase variations were determined as a more robust measure of monitoring changes. This measure is extended to the most recent experiments using reflection coefficients [15]-[16] (See Fig. 2(b)).

### 1.3.3 Acoustic Techniques

By considering the well-known fact that sound travels faster in water compared to air, the possibility of using acoustic system for lung water monitoring was investigated in [17]. To evaluate the usefulness of the abovementioned notion about the speed of water, a White Gaussian Noise (WGN) covering 0 – 4 KHz is used as a source signal that is transmitted into the lungs through a funnel from the mouth (See Fig.1.3 (a)). Four electric stethoscopes were used in the experiment to assess the received signal using adaptive filter processing. By applying the technique on a torso phantom that is made of foam, Fig. 1.3(b), and considering the gravity dependency of the water, it was found that the stethoscopes which is located below the water receives the transmitted signal with the least delay compared to the other ones, and hence detects the presence of fluid.



(a)



(b)

Fig. 1.3. Schematic view of the stethoscope array and water injection area and (b) experimental setup using actual stethoscopes. (Images obtained from [17] ©[2009] IEEE)

### 1.3.4 Bioimpedance Spectroscopy

Modelling human tissues as circuit elements and utilizing the variations of the tissues is another technique which is investigated in bioimpedance spectroscopy (BS) [18]. The basis of this technique operates based on the fact that the thorax of a human body has a certain impedance value, and this value changes by the accumulation of fluid inside the torso. Therefore, monitoring the variations of the impedance value can provide valuable information regarding the changes in the water content of the lungs. However, it is mentioned that the human torso has very small impedance value in the range of 20-50  $\Omega$  and considering the fact that lungs contribute maximum 20% to this value. Therefore, precise positioning of the current sensors for measuring the impedance is crucial. As shown in Fig. 1.4 (a), a set of sensors are used to inject the current into the body and measure the resultant voltage and determine the impedance of the thorax. In this type of measurement, the intracellular or

extracellular water is modelled as resistor and the cellular membrane is modelled as a capacitor due to its lipid layer. As shown in Fig. 1.4(b), by using a set of sensors all around the thorax, injecting the water alters the impedance value that is different in each set of sensors. Nevertheless, this variation can be used as a measure of water content variation inside the lungs.

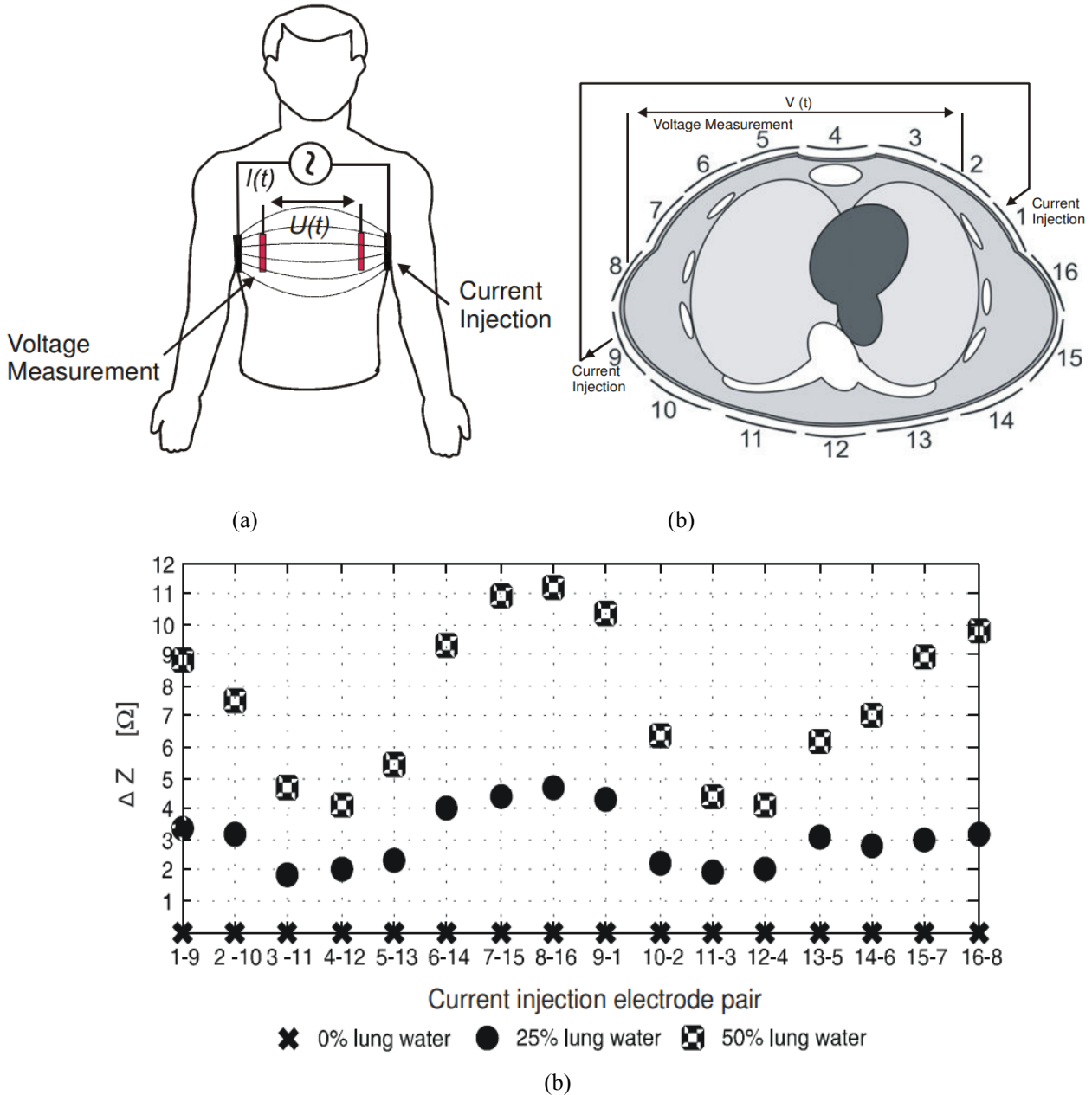


Fig. 1.4. (a) Schematic view and (b) detailed configuration of a bioimpedance spectroscopy configuration. (c) Impedance variations of thorax for various electrode pairs. (Images obtained from [18] © [2007] IEEE)

### 1.3.5 Ultra-Wideband Radar

Ultra-wideband radar is another non-invasive technique that operates based on the fact that the electrical properties of healthy tissues are different from that of a malignant one. Therefore, different pulse responses should be obtained for healthy and unhealthy tissues and this can be used as measure

for detection of fluid inside human body. A typical data acquisition setup for this type of detection is presented in Fig. 1.5(a). As can be seen an UWB antenna is used to transmit pulses towards human torso and a second antenna is used to receive the reflected signals. These signals are then processed using a computer. To test this idea, the case of water accumulation in human bladder was investigated and a tissue model was evolved as shown in Fig. 1.5 (b). The pulse responses in two cases of healthy and unhealthy cases are recorded. The first peak in Fig. 1.5(c) is attributed to the air muscle boundary and the second peak is related to the boundary of muscle/muscle (solid) or muscle/air (dotted). As can be seen, although small, the level of the second peak is higher in the case with presence of water and it can be concluded that a detection is possible using this technique.

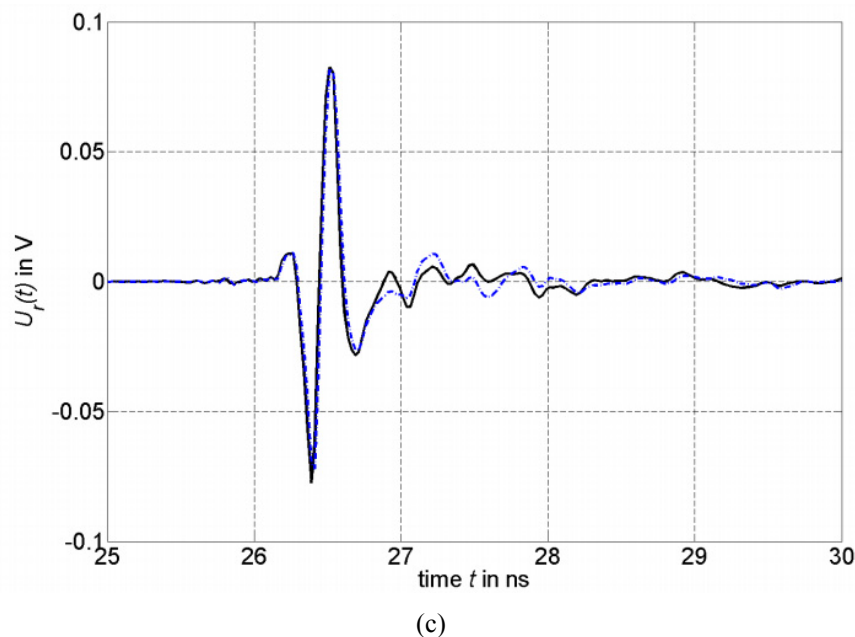
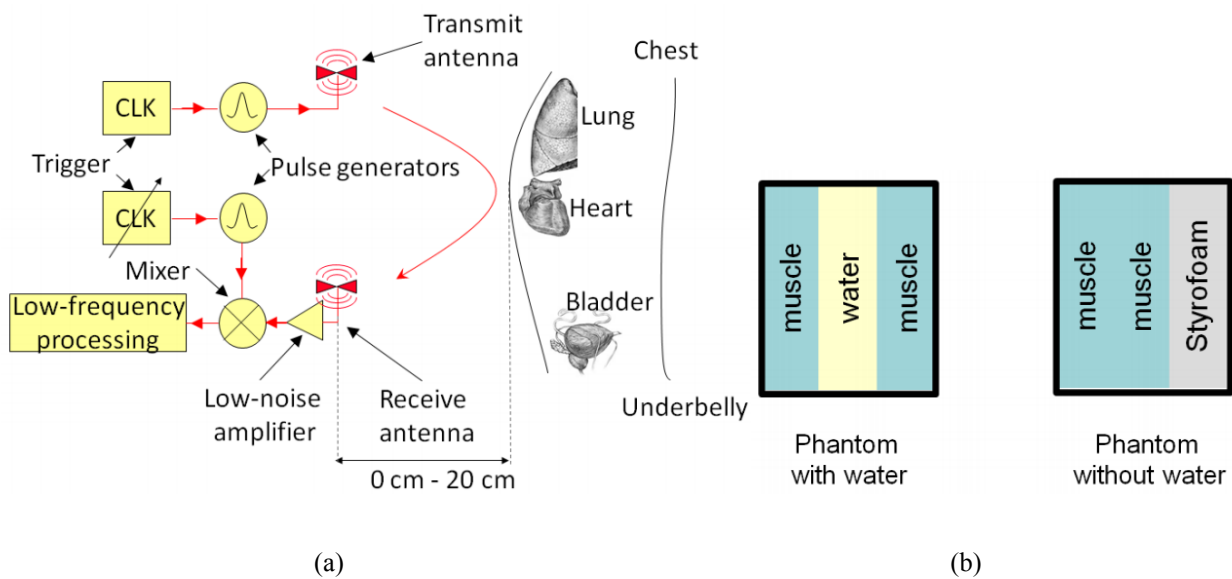
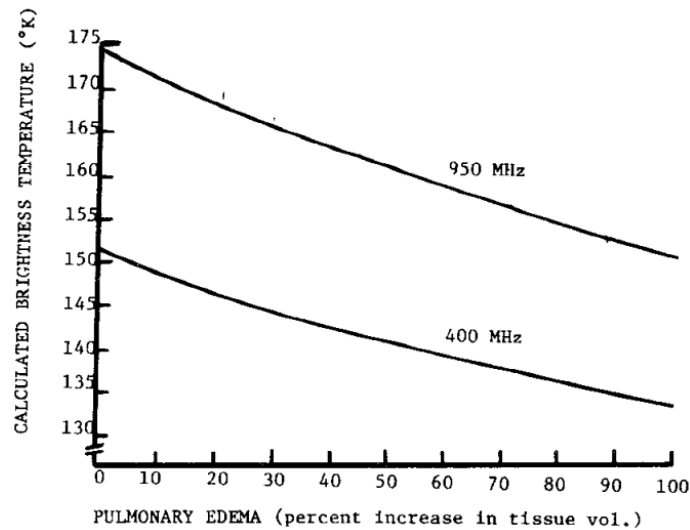


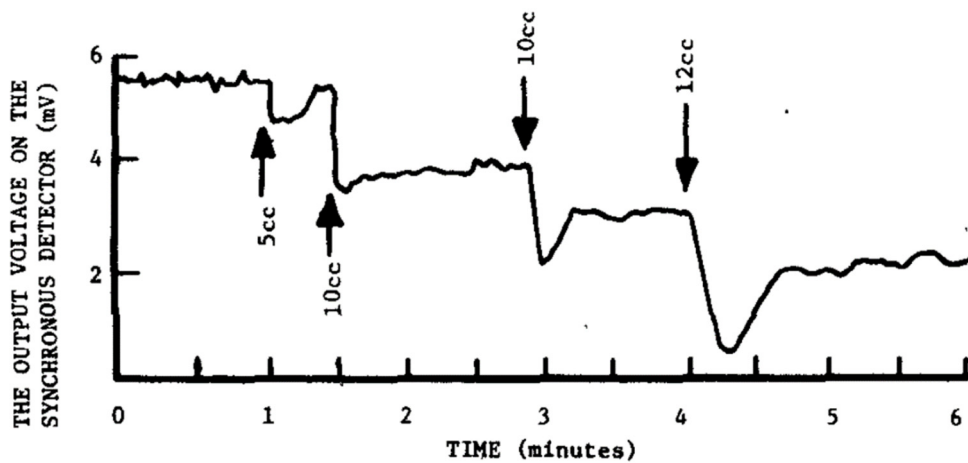
Fig. 1.5. (a) Data acquisition setup. (b) Utilized tissue models in the experiments and (c) obtained pulse responses. (Images obtained from [19] © [2010] IEEE)

### 1.3.6 Radiometry

Using the electromagnetic radiation emission from the body is another approach that is used for detection and monitoring the lung water content [20]. As shown in Fig. 1.6 (a), this value is measured in brightness temperature that relates the emissivity and electrodynamic temperature of the body. By calculating the emissivity of the lungs using the complex dielectric properties of the lungs tissues, blood, air and water, a certain value is obtained. This value changes with different levels of water inside the lungs, and hence alters the emitted electromagnetic radiation from the body. These changes, Fig. 1.6 (b) can be monitored using radiometers that are able to record these emissions. The measurements were conducted at the frequency range of 0.4 – 1 GHz. It was shown that despite the limitations of the radiometers operating at low frequencies, 0.260-K change in the brightness temperature occurs with one percent change in the level of the accumulated water.



(a)



(b)

Fig. 1.6. (a) Brightness temperature radiated from the lungs in different pulmonary oedema levels. (b) Radiometer reading in different steps of injecting water inside lungs. (Images obtained from [20] © [1984] IEEE)

### 1.3.7 Permittivity Estimation

One of the most recent methods in detecting the presence of fluid inside the lungs in the average permittivity estimation. Detecting water accumulation was shown to be possible by estimating the average dielectric properties of the lungs [21]. Considering the fact that when water accumulates inside or around the lungs, it changes the dielectric properties of the lungs' tissues significantly, this method detects the presence of water by monitoring any variations to the obtained value for a healthy lung. In this method, several sensors are involved in the measurements. One of the many sensors that are spread across the chest wall is fed by a 40 MHz radio frequency (RF) signal, whereas the others measure the amplitudes of the reflected signals from the body (See Fig. 1.7). These values are then processed using a weighted sum of the collected signals from the sensors to estimate the average dielectric value. Assuming that the permittivity of the lungs of a healthy case is known, any deviation obtained from the original value is used as a measure of fluid detection. This method has been tested on a phantom with limited layers that only include lungs, muscle and skin and does not include the effect of the ribs and the veins that are carrying blood. It is claimed that with the proposed method, the obtained error between the actual dielectric value of the tissue and the estimated one is less than 11%. This error is reasonably tolerable considering the high contrast between the dielectric constant values of the healthy and unhealthy lungs. However, it is not stated how a reference value can be selected for a person whose average lung properties are not available at the time of measurement.

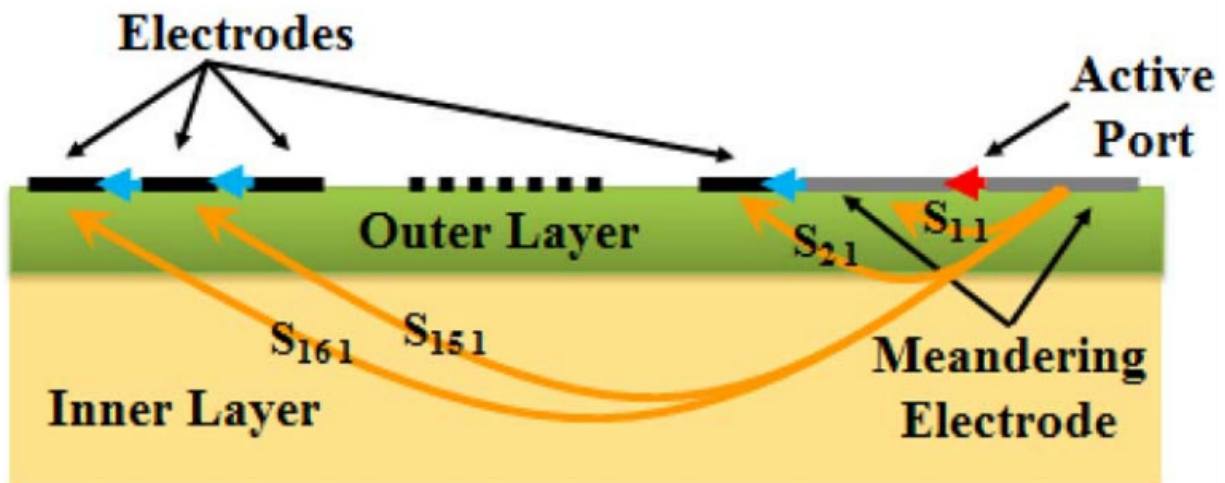


Fig. 1.7. Operating basis of the permittivity estimation method. (Images obtained from [21] © [2014] IEEE)

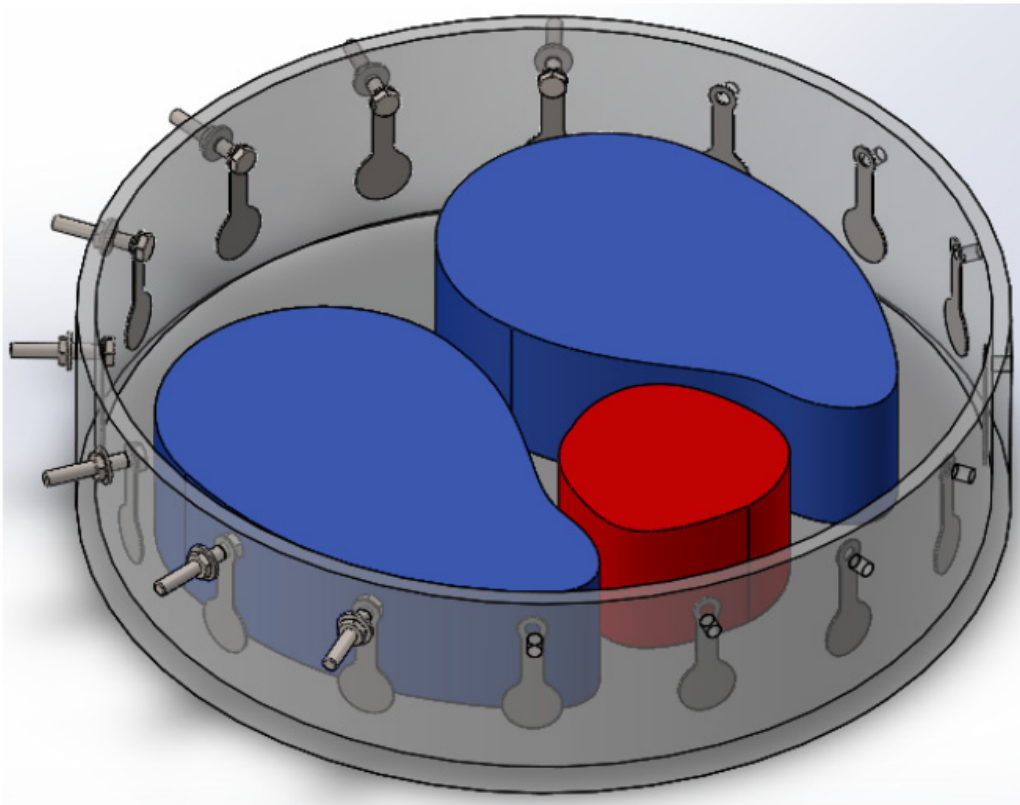
### 1.4 Detection and Localizing Systems

This category of systems provides a more advanced type of diagnosis and focus on both detecting and locating the accumulated fluid. Positioning fluid is of great importance in cases where

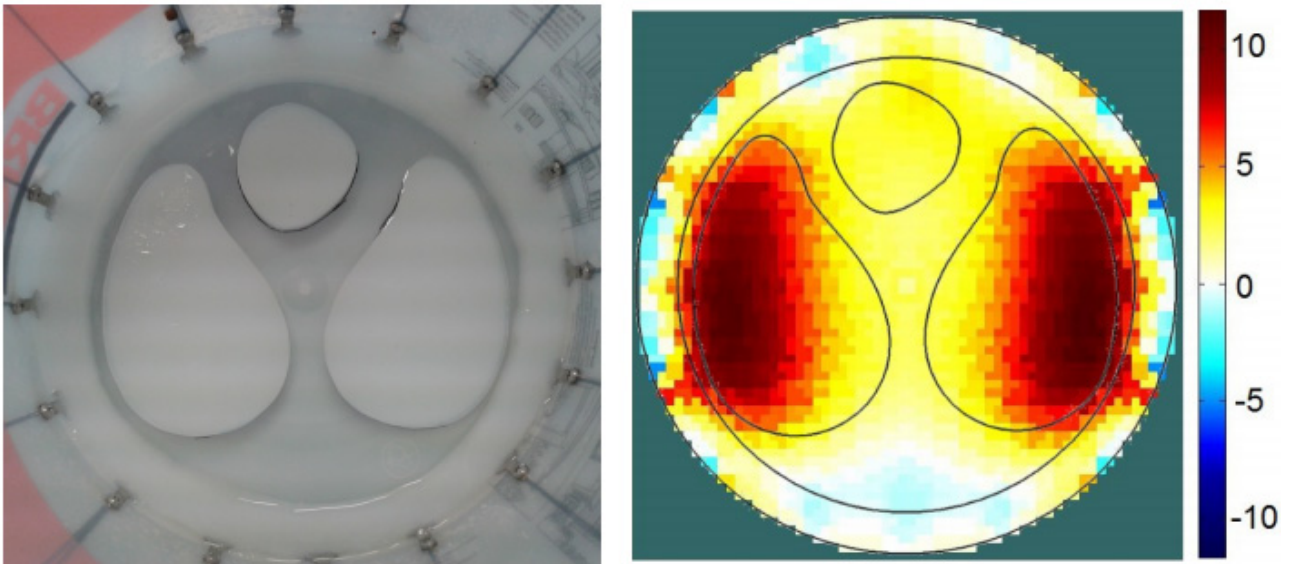
invasive sampling is essential to determine the exact type of the disease causing the oedema, and therefore define the exact medication. To that end, locating the fluid on either sides of the torso accelerates the process while reducing patient's pain and biopsy costs.

### 1.4.1 Electrical Impedance Tomography

One of the relatively new methods in imaging the human body is Electrical Impedance Tomography (EIT). This technique relies on the tissues' bio-impedance properties, which carry important information about the changes that occur inside the body [22]-[23]. In this method, several electrodes are placed around the imaging area (See Fig. 1.8 (a)) and the current is non-invasively injected to the body and the occurred voltage is recorded at receiving electrodes. These systems typically use a range of low and high frequencies of 1 MHz or 20 GHz, respectively. This method models the fluids, such as blood and water, as resistors while modelling the membranes of the cells as capacitors. Considering the fact that different tissues and cells have different sizes, angles and thicknesses, a wide range of impedances are obtained. Tomographic imaging algorithms are then used to image the impedance of each tissue within the imaged area, such as Fig. 1.8 (b). As lungs have extremely different impedances during inhale and exhale due to the air volume, the presence of the water alters the obtained impedance; that variation can be shown as an image [24]-[26][27] .



(a)



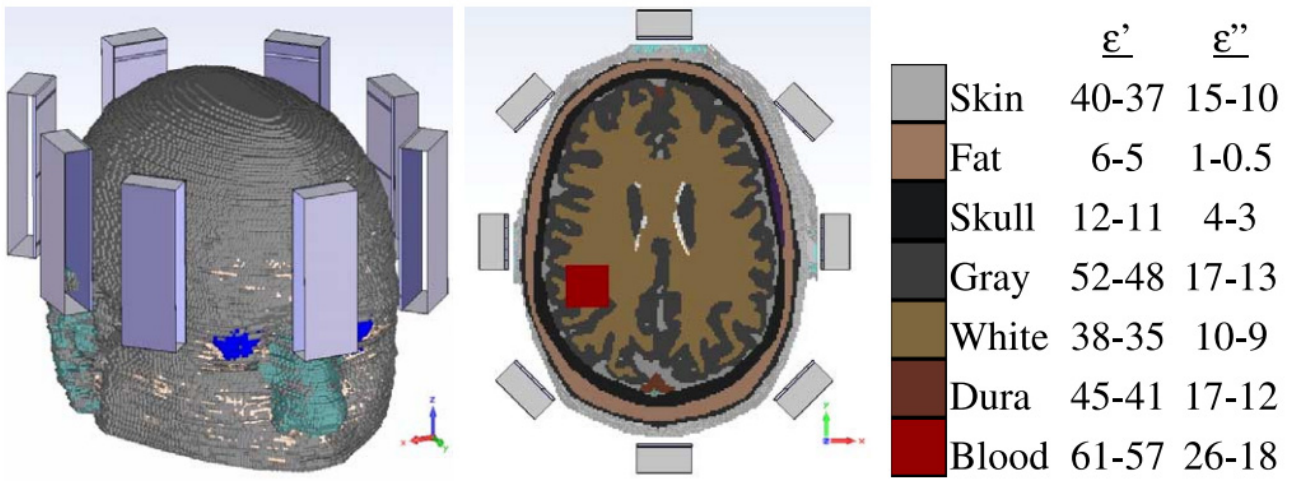
(b)

Fig. 1.8 (a) Configuration of an EIT system with electrodes surrounding the area under investigation and (b) obtained image of the utilized phantom within the setup. (Images obtained from [23] © [2015] IEEE)

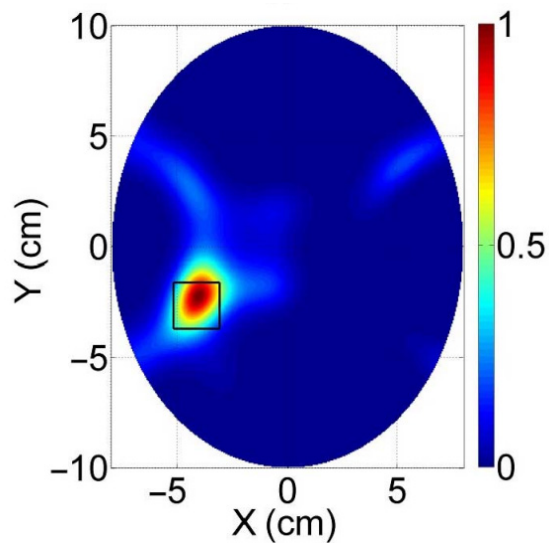
## 1.4.2 Radar Based Microwave Imaging

Radar based microwave imaging has been applied largely for detection and imaging of various kinds of diseases such as cancers and strokes [28]-[30]. These systems operate based on the fact that a higher water content in the unhealthy cells than in normal cells alters the dielectric properties of the cells significantly, and hence the relevant reflected/transmitted microwave signals. These reflections are then processed using different imaging techniques including inverse and direct ones to obtain a two or three dimensional image of the investigated area. The main challenge in this technique is to remove several reflections that occur at the air body interference and mitigate antenna reflections to obtain a clear and meaningful image.

Several preclinical prototypes of such systems have been proposed in the recent decade. As shown in Fig. 1.9 (a) [28], the system is used in the form of several antennas that surround the head of the patient and obtain data from different angles and regions to provide information for the medical staff. Moreover, as can be seen in Fig. 1.9 (b) [29], a test bed is proposed for breast cancer imaging. In this system an antenna is rotated around the breast to obtain data from different slices of the breast to produce a 2-D image which shows any abnormality in the breast tissue.



(a)



(b)



(c)

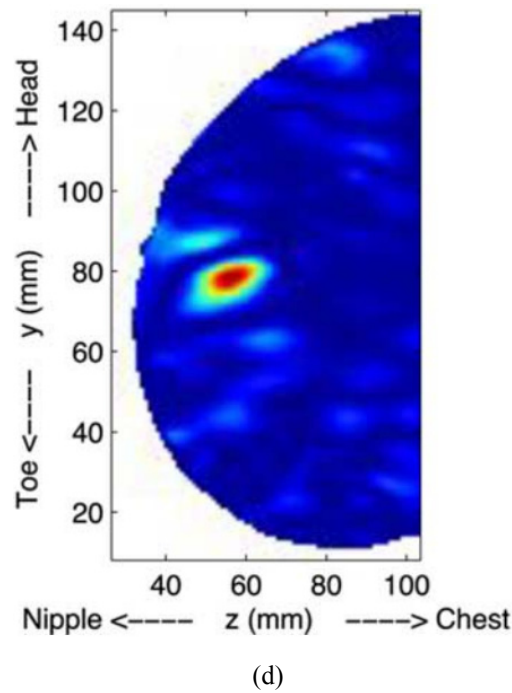


Fig. 1.9. (a) Head imaging configuration and (b) detected stroke in a desired location. (c) Breast cancer imaging platform and (d) 2-D image of cancerous cell. (Images obtained from [28] & [29] © [2015, 2004] IEEE)

## 1.5 Thesis Motivation and Challenges

It can be deduced that a great number of studies and experiments were conducted to replace MRI, CAT and X-Ray equipment with a portable and cost effective system. The only available portable device is proposed by the KYMA Company [31] which claims successful results both on human beings and animals. Ironically, this device is only able to monitor patients with acute heart failure conditions with high water level contents using long periods of time (5 ~ 10 hours). Therefore, it cannot be an option for detection of water accumulation in early stages. Hence, design of a portable, low profile and cost effective device, which is able to detect low water contents at the early stages of pulmonary oedema as a symptom of various diseases can save lives of millions of patients and relief the health care system from the costs of heart failure surgeries and rehabilitation process.

Despite showing a great potential in detecting malignancies such as cancers and strokes in both homogeneous and complex environments, microwave imaging has been less utilized to analyse the fluid levels inside the lungs and monitor its changes. Motivated from this gap, and considering the high contrast between the dielectric properties of water and the tissues present inside the lungs, this thesis is devoted to propose a new prospect in finding a robust solution for diagnosis and monitoring of thoracic fluid accumulation. However, there are several challenges that should be faced before reaching a comprehensive solution that is building a microwave diagnostic system which is portable, low cost, low profile and is capable to detect fluid inside torso area in the early stages of the oedema. The following steps are necessary to realize the objectives of this project:

**1) Operating Frequency:** The basic detection procedure of the current project is dependent on the transmission and reception of the electromagnetic signals by the antennas. Therefore, designing proper types of antennas is the key element in the success of the project. Thus, to prevent a blind process of trial and error along the design process, the optimum frequency range for microwave detection of fluid (mainly water) inside torso should be defined prior to the design of the antennas and defining the types of switches and other microwave components required.

**2) Antenna Requirements:** Antennas are one of the key elements of any microwave based medical diagnostic system and therefore, the success of that system significantly depends on the performance of those antennas. Additionally, the compactness of the system will depend on the size of the designed antennas. Considering the penetration requirements by the system, the optimum frequency range of the microwave detection system is expected to be a sub-band at ultra-high frequency range (UHF). Thus, the antenna is expected, if designed using the conventional methods, to have a large physical and electrical size considering the large wavelengths at this band. Considering the limited allowed microwave power in medical applications for safety reasons, the antenna is required to radiate the power efficiently in the forward direction. Thus, it needs to have a unidirectional radiation. Furthermore, it should possess a wide operating bandwidth to provide an acceptable resolution for the obtained images. An extensive literature review reveals several research articles on unidirectional antennas operating at UHF band [38]-[41]. Various techniques were implemented in order to obtain a unidirectional radiation pattern while not affecting the operating bandwidth of the antenna. The most dominant technique is locating a reflector a quarter wavelength distance from the antenna [38]. However, using such a reflector for antennas operating at the lower UHF frequencies increases their size drastically. Considering their light weight, simple assembly and low fabrication cost, planar end-fire antennas are among the most suitable structures for microwave imaging applications. To achieve wideband performance for that type of antennas, several techniques were utilized, such as loop-dipole composites [42], magneto-electric dipoles [43] and quasi-Yagi structures [44]. However, those techniques result in relatively large sizes that are not suitable for medical applications especially those operating at the UHF band. Recently, a number of compact antennas have been specifically designed for medical applications [45]-[47]. However, they either are in need of matching layers [45], [46] or have narrow operating bandwidths and omnidirectional radiation patterns [47]. Matching layer is a layer with dielectric constant close to that of human skin and is located between antenna and body to reduce the amount of reflections at the air–body boundary. In some cases, this layer is amalgamated as a part of the antenna to reduce its size. However, for non-flat surfaces like human torso, this is not applicable.

**3) Torso Phantom:** One of the main shortcomings of the current research in the field of torso imaging is the use of simple single or limited multilayer structures in the simulation environment.

This issue is of great importance due to the investigation diversity that a realistic phantom provides. It should be noted that by using a realistic model in simulation environment, the effect of various parameters that are exact as the inhale and exhale of lungs can be simulated and studied. Additionally, to test the designed system in the lab, a torso phantom is required. In the present literature, the most complicated phantom that is being used is the single layered homogenous phantoms such as the one from SPEAG, Switzerland [48]. Other phantoms include the use of sponges and rolled foams [17]. While these phantoms mimic the average dielectric constant of the tissues inside the torso, they lack majority of organs including but not limited to lungs, heart, ribs, abdomen, and thorax cage that are extremely influential on the accuracy of the obtained results.

**4) Detection Algorithms:** Studying the proposed methods in the literature, reveals that the utilized algorithms are based on the presumptions that are not practical in clinical environment. As an example, for the techniques that are using phase or amplitude of the reflected or transmitted signal as an indication of detection, it can be seen that it is assumed that the pulmonary oedema starts exactly at the time of examination, and therefore the initiation of the process is marked as the reference, where other variations are compared to. Yet, it is not the case in reality. The lack of a reference point or a global database of healthy cases, where a threshold is defined can be stated as the fundamental weakness of the proposed algorithms.

**5) Platform Design:** The main requirement in building portable medical diagnostic systems is to use simple and lightweight platforms. In the present literature, there are generally two main approaches for building a contact face for medical diagnostic systems. In the first method, the antenna is designed as a part of the system and its performance is characterized accordingly. This usually requires 3D printing of the antenna and the platform or use of matching layers, which yields to fragile and impractical structures, especially for torso scanning purposes.

## **1.6 Contributions Proposed in the Thesis**

By carefully addressing the aforementioned challenges, the following original contributions were obtained that can be classified under three main categories:

### **1.6.1 Antenna Design**

- Defining optimum operating frequency band for fluid detection inside human torso by modelling human tissues as circuit elements using Advanced Design System (ADS) and High Frequency Simulator Software (HFSS) software.
- Introduction of 3-D folding technique for miniaturization and back radiation suppression.
- Theoretical analysis, design, simulation, fabrication and experimental verification of 3-D cubic and bent printed loop antennas.

- Proposal, design and verification of unidirectional loop-dipole composite antennas and eliminate the use of large ground and cavity structures.
- Proposing wideband unidirectional capacitively loaded loop antennas with great size reduction capabilities.
- Theoretical analysis, simulation, and experimental verification of reflector-less metamaterial unit-cell loaded antennas such as non-periodic Mu-Negative loaded loop antennas for the first time in literature.

### **1.6.2 Platform (Data Acquisition Setup) Design**

- Introduction of automated and synchronized simultaneous scanning platforms.
- Design and fabrication of an expanding foam embedded antenna array as a portable platform for torso scanning applications.
- Proposal and realization of a clinical platform that hosts two sets of antenna arrays, which are embedded inside a bed as a non-invasive and innovative tool for clinical trials with tests on animal tissues and actual human beings.
- Design of a concept of doughnut-shape chamber platform for non-invasive scanning of human torso with tests on phantom and human beings.

### **1.6.3 Detection Approaches**

- Using the existing reasonable but not perfect symmetry between the left and right lungs to utilize differential detection technique.
- Utilizing the gravity dependency of the fluid and proposing the horizontal scanning approach to reduce the effect of heart in differential detection.
- Applying frequency domain based algorithms to eliminate problems associated with time domain algorithms.

# Chapter 2

## Review of Microwave Imaging Systems and Utilized Detection Algorithms

To obtain a clear idea of building a microwave imaging system and possible data acquisition/scanning approaches, a review of most predominant microwave imaging systems for medical diagnostic purposes is presented in this chapter. It should be noted that as there are very limited available microwave imaging systems for fluid detection inside human torso, the main objective of this chapter is to mainly introduce the most popular utilized platforms and data acquisition systems regardless of their imaging domain.

### 2.1 Microwave Imaging Systems

Microwave imaging systems are operating based on the fact that there is a certain level of contrast between the dielectric permittivity/conductivity of the malignant or cancerous tissues with the healthy ones [49] (See Fig. 2.1). These changes cause variations in the reflected or transmitted signals and consequently the resultant scattered fields. Therefore, a proper hardware setup is required to acquire the scattered signals and then analyze them using suitable signal processing techniques.

Tissue	Frequency (MHz)									
	50	100	200	300	400	500	600	700	800	900
Colon (21)	0.61	0.62	0.63	0.65	0.68	0.71	0.75	0.80	0.87	0.93
Kidney (6)	0.76	0.77	0.79	0.84	0.90	0.96	1.01	1.08	1.12	1.20
Liver (9)	0.48	0.49	0.52	0.57	0.63	0.70	0.75	0.81	0.88	0.95
Lung (9)	0.61	0.62	0.64	0.70	0.76	0.84	0.92	1.00	1.08	1.16
Mammary (12)	0.11	0.11	0.12	0.12	0.13	0.13	0.14	0.15	0.16	0.18
Muscle (9)	0.61	0.62	0.63	0.64	0.68	0.72	0.75	0.80	0.84	0.92

Tissue	Frequency (MHz)									
	50	100	200	300	400	500	600	700	800	900
Bladder (6)	0.90	0.92	0.95	0.98	1.01	1.06	1.12	1.21	1.32	1.54
Colon (9)	0.73	0.74	0.76	0.80	0.84	0.90	0.94	0.99	1.04	1.08
Kidney (27)	0.74	0.75	0.76	0.80	0.84	0.89	0.95	1.02	1.11	1.20
Liver (15)	0.65	0.66	0.67	0.72	0.77	0.83	0.90	0.96	1.04	1.10
Lung (6)	0.80	0.82	0.84	0.88	0.92	0.96	0.99	1.06	1.14	1.24
Lymph (6)	0.55	0.57	0.61	0.65	0.74	0.79	0.88	0.98	1.15	1.34
Mammary (12)	0.77	0.78	0.79	0.82	0.85	0.90	0.95	1.01	1.08	1.16
Spleen (9)	0.60	0.64	0.72	0.77	0.84	0.96	1.00	1.04	1.08	1.12
Testes (6)	0.82	0.84	0.90	0.95	1.01	1.06	1.12	1.19	1.27	1.34

(a)

Tissue	Frequency (MHz)									
	50	100	200	300	400	500	600	700	800	900
Colon (21)	57.0	52.0	50.0	49.5	49.2	49.0	48.9	48.7	48.6	48.5
Kidney (6)	97.0	72.0	65.0	63.0	62.0	61.8	61.5	61.2	61.1	61.0
Liver (9)	69.0	62.0	55.0	53.0	52.5	52.0	51.5	51.3	51.2	51.1
Lung (9)	99.0	77.0	65.0	62.0	61.5	61.0	60.7	60.5	60.4	60.3
Mammary (12)	21.0	20.5	20.2	20.0	19.0	18.0	17.0	16.5	16.0	15.0
Muscle (9)	73.5	63.0	56.0	53.0	52.6	52.4	52.3	52.2	52.1	52.0

Tissue	Frequency (MHz)									
	50	100	200	300	400	500	600	700	800	900
Bladder (6)	65.0	63.0	59.5	57.0	56.3	55.8	55.4	55.2	55.1	55.0
Colon (9)	67.0	65.0	63.0	60.0	58.3	57.5	57.0	56.5	56.2	56.0
Kidney (27)	85.0	68.0	61.0	59.0	58.5	58.2	58.0	57.8	57.7	57.6
Liver (15)	70.0	66.0	60.0	58.5	58.0	57.6	57.3	57.2	57.1	57.0
Lung (6)	75.0	69.0	61.0	57.2	56.0	55.0	54.5	54.2	54.1	54.0
Lymph (6)	96.0	76.0	62.0	58.0	57.0	56.5	56.2	56.1	56.0	55.9
Mammary (12)	80.0	69.0	60.5	58.2	57.9	57.6	57.4	57.3	57.2	57.1
Spleen (9)	101	82.0	68.0	64.5	63.5	62.8	62.4	62.2	62.1	62.0
Testes (6)	97.0	72.0	61.0	59.0	58.6	58.4	58.3	58.2	58.1	58.0

(b)

Fig. 2.1 Measured (a) conductivity in S/m and (b) relative permittivity of different tissues. Top charts represent healthy and bottom charts represent malignant cases. (Numbers inside parentheses represent the number of measurements.) (Data obtained from [49] ©IEEE [1994])

In general, there are two main types of these configurations; monostatic and multistatic. In the monostatic approach, a single or array of antennas are individually used for transmitting and receiving signals, while in the multistatic setup generally an antenna is used as a transmitter and others are used to collect data. Multistatic configuration requires a more complex hardware configuration, specifically switching systems; however, they provide more information that increases the accuracy of the detection and quality of the obtained image. It should be noticed that mono or multistatic configurations can be used to perform near field or far field (radar based) imaging.

## 2.2 Monostatic Microwave Imaging Systems

A sample configuration of a monostatic microwave imaging system is shown in Fig. 2.2. As can be seen the system is consisted of an antenna that is positioned in a distance from the imaging object. The antenna is connected to a microwave transceiver to send and receive signals through the antenna. The transceiver is connected to a computer, which is at the same time controlling the platform where the imaging object is located. Generally, simple programming is required to provide connection and coherence between the data acquisition by the transceiver and the platform.

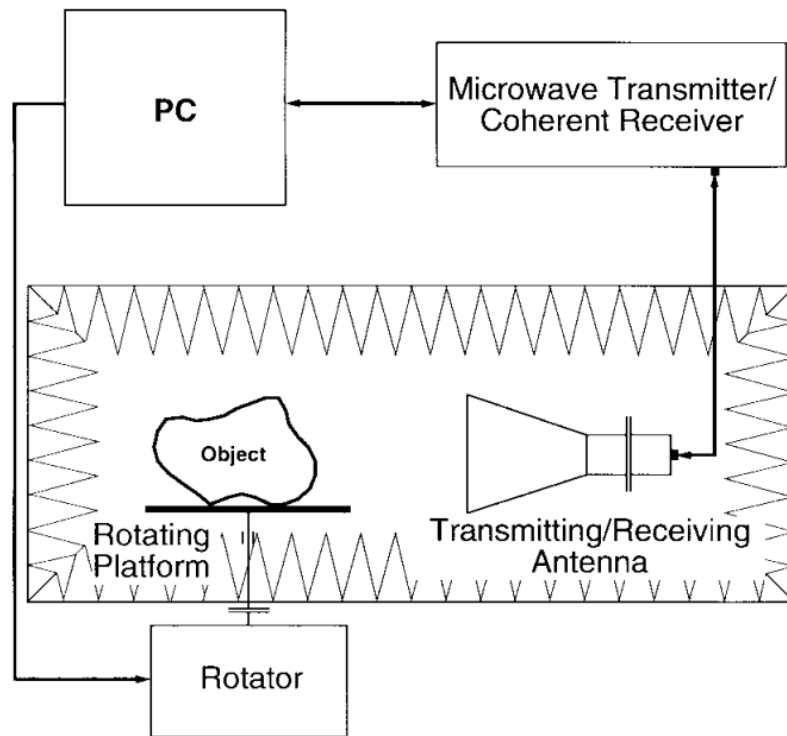


Fig.2.2 A mono-static microwave imaging configuration. (Image obtained from [50] ©IEEE [1999])

### 2.2.1 Rotating Platform Using Single Antenna (Radar-Imaging)

This system is proposed by the research group at the University of Calgary [29] that has a long history of proposing several prototypes of microwave imaging specifically on breast cancer detection. In this system that is shown in Fig. 2.3 (a), a Vivaldi antenna (sensor) is utilized to both transmit and receive the signals toward the breast at the frequency range of 50 MHz-15 GHz. Moreover, a laser scanner is attached besides the antenna and both of them are positioned on an arm that is located on a rotating platform. The main purpose of using a laser beam in this system is to obtain data about the position of the surface of the breast. This system is located under a clinical bed in which a hole is created for breast accommodation. The breast is positioned inside a container that includes canola oil. This oil is used as a matching medium to reduce the skin reflections, and hence enhance the detection process. One of the main advantages of this system is the ability of the platform to move along the breast and scan the breast from the chest wall to the nipple, and hence provide a comprehensive data from all angles and areas of the breast. As a result of such platform three sets of images from all three planes of the breast, shown in Fig. 2.3 (b), can be obtained that is extremely useful in defining the exact position of a potential cancerous cell.

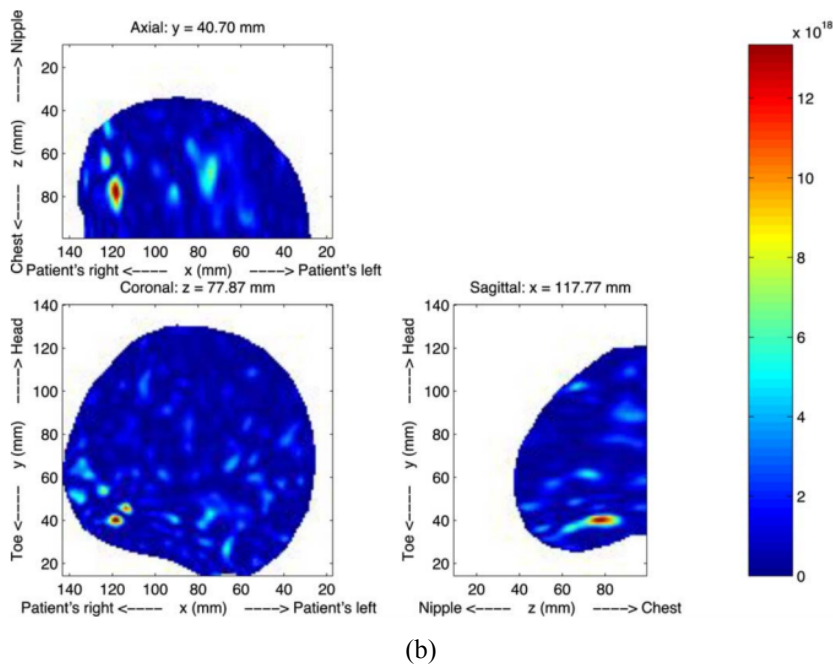
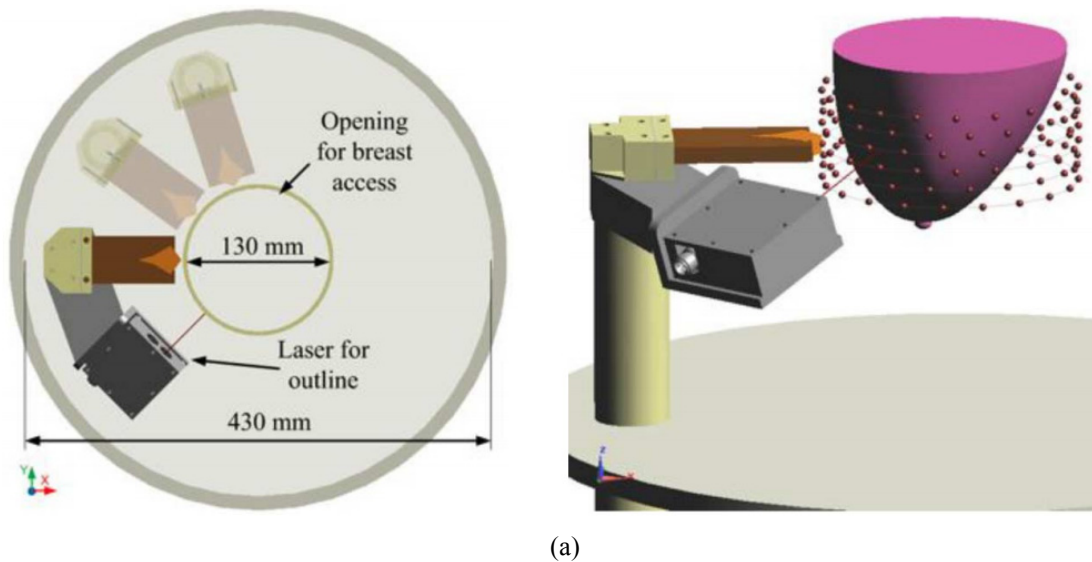


Fig. 2.3 (a) Scanning system top view (left) and front view (right) and (b) obtained images in three different planes. (Images obtained from [29] ©IEEE [2004])

## 2.2.2 Differential Microwave Imaging (Radar-Imaging)

This technique is one of the most recently published approaches that is utilizing the existing symmetry between the left and right side of breasts. This study proposes that based on the available data from different imaging resources, the existing difference between left and right side breasts is less than 3%, and hence this extreme resemblance in tissue structure can be utilized to perform differential detection. While differential detection technique is not novel by itself, yet, the proposed data acquisition setup has not been utilized for this application before. The proposed scanning configuration can be seen in Fig. 2.4 (a). As can be seen in this setup, two arrays of antenna, which are operating at 2.5 – 6 GHz, are utilized in which each array is surrounding the circumference of the

breasts. A reflector is located at a short distance at the back side of the antennas to reduce the back radiation effects on the obtained images. This system is utilizing a monostatic scanning approach and each of antennas send and receive data sequentially. The obtain results reveal that by properly positioning of the antennas and breast to obtain the maximum symmetry, cancerous cells are easily detectable in all three major types of breasts (dense, slightly dense, fatty) by subtracting the left and right hand side images that magnify the presence and position of the cancer (See Fig. 2.3 (b)).

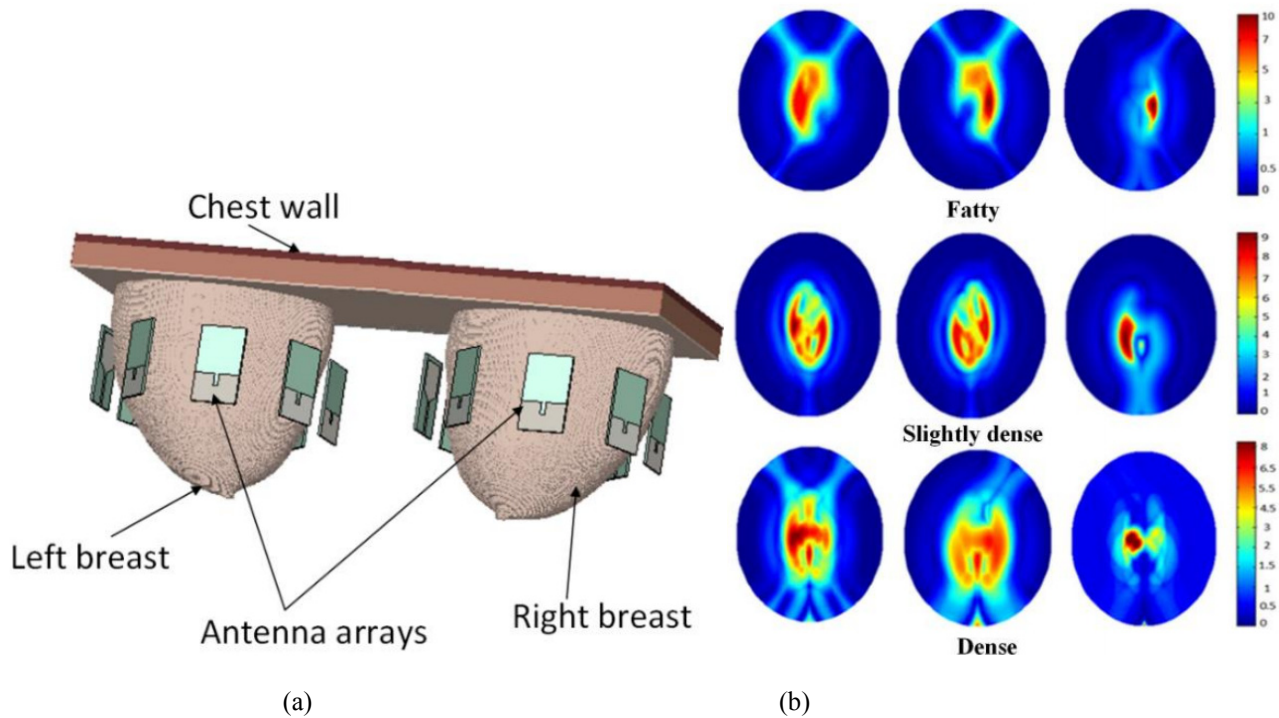


Fig. 2.4 (a) Array Setup and (b) obtained images using differential microwave imaging. (Images obtained from [51] ©IEEE [2016])

## 2.3 Multi Antenna Imaging (Near-Field Imaging)

As discussed before, near field imaging is another technique that is used for creating an image of the domain under investigation. One such system is depicted in Fig. 2.5, where 12 antennas are arranged in a circular configuration and the imaging domain is shielded from surrounding effects using microwave absorbers. The system operates at 2-6 GHz and the utilized antennas are accompanied by TE and TM probes that are collocated with the antennas. In order to reduce the mutual coupling between the antennas and reduce the effect of the probe cables on the results, each Vivaldi antenna is accompanied by a reflector. In this system, one antenna is used to transmit the signal and the closest antenna and probes are utilized to gather the scattered signals. Using probes with different polarizations reduces the phase and environmental errors to a great extent. Moreover, as measurements are done with very short intervals, any similar effect is automatically eliminated. The system is using a conventional vector network analyzer (VNA) for measuring the S-parameters.

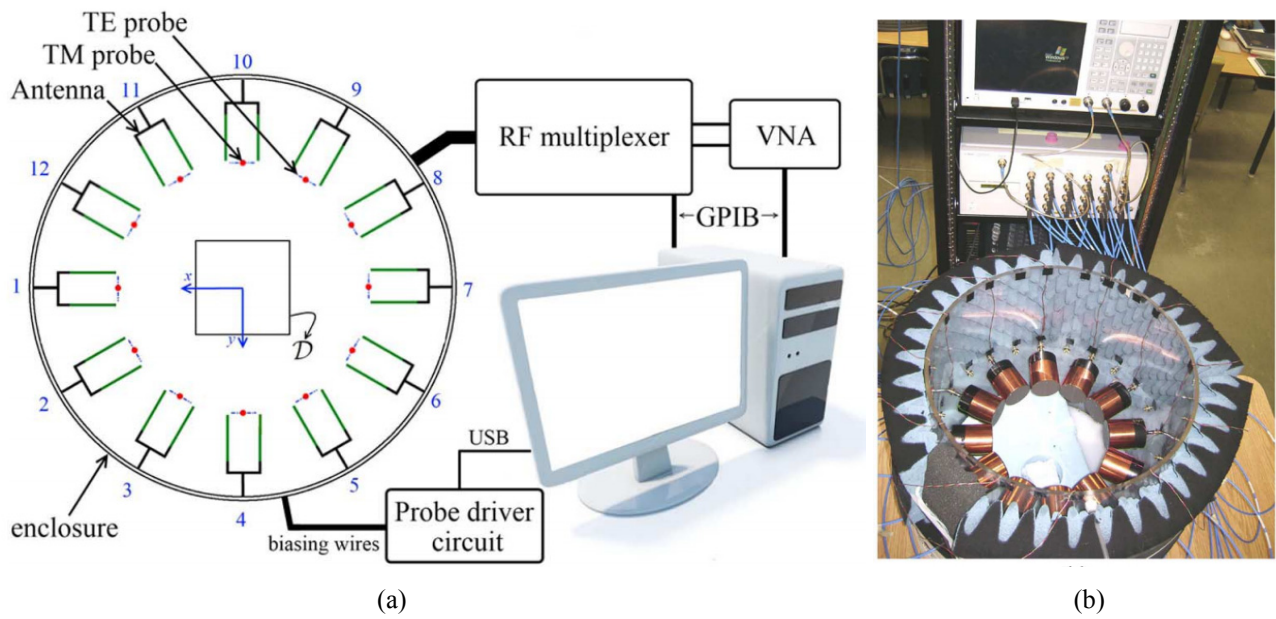


Fig. 2.5 (a) Schematic view and (b) fabricated near field imaging system configuration. (Images obtained from [52] ©IEEE [2013])

## 2.4 Multistatic Microwave Imaging Systems

The second major type of configuration that is used to collect data from an imaging domain is multistatic configuration, where all utilized antennas are actively involved in data acquisition process.

### 2.4.1 Multi-Level Imaging System

As shown in Fig. 2.6 utilizing a multistatic configuration increases the complexity of the system as well as the amount of required cables and switches. However, it provides considerably more data sets that are used to enhance the detection precision and quality of the obtained image. As seen from Fig. 2.6, the proposed system is comprised of 32 monopole antennas that are operating at around 1 GHz, and are arranged in a circular configuration surrounding the imaging domain (breast) in multi-levels to obtain data from all sections of breast. During measurements one antenna acts as transmitter while rest of the antennas receive the scattered signals and this procedure is repeated till all antennas transmit from different angles. The whole antenna system is submerged into a glycerin water that mimics the dielectric constant of breast, and hence allows maximum field coupling into the breast by reducing the skin reflections. The other benefit of using the utilized coupling medium is that it attenuates the reflections by the other antenna elements. Yet, it implies that a network analyzer with a large dynamic range is required.

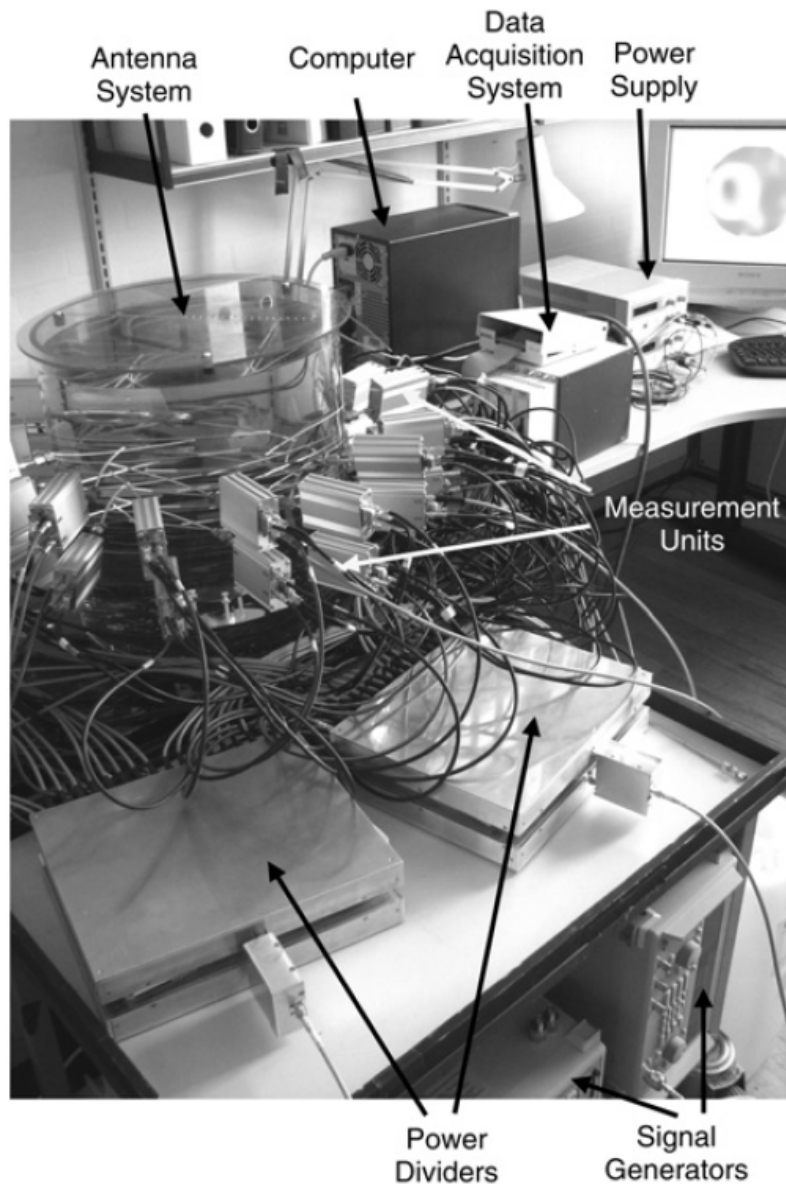


Fig. 2.6 Multi level multi static microwave imaging system. (Images obtained from [53] ©IEEE [2010])

### 2.4.2 Quasi-Multistatic System Using Tomography

There are certain types of configurations that cannot be categorized as a full multistatic system; this is due to the fact that not all of the antennas are used for data acquisition at the same time, and hence these systems are noted as quasi-multistatic. A sample of these systems is presented in Fig. 2.7. This setup is utilized for microwave tomographic imaging of a microwave chamber that is resembling imaging area. The system is comprised of 64 antenna elements that are positioned as shown in Fig. 2.7. Throughout the measurements, one of the emitter antennas is used as transmitter and the rest of receiver antennas are used to collect the scattered signals. This procedure is repeated till a full scan is performed using all antennas. One of the great benefits of using such configuration is the elimination of use of moving platforms that can attribute to system errors such as movement and vibration errors.

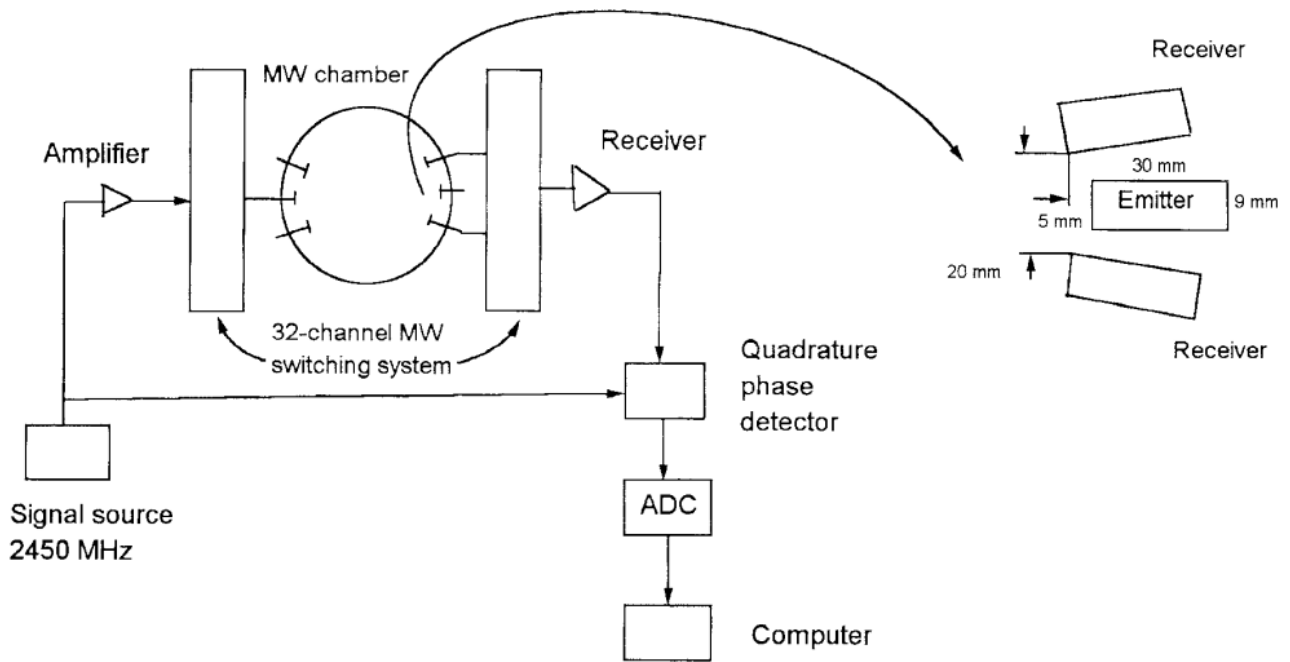


Fig. 2.7 Quasi multi static data acquisition system. (Images obtained from [54] ©IEEE [1996])

## 2.5 Conclusion

Various microwave imaging platforms are introduced and several systems that are mainly designed for breast and head imaging applications are presented. It can be seen that in majority of the cases the proposed setup aims at acquiring data from maximum number of positions to get a better understanding of the imaged area. However, these systems cannot be directly implemented for torso imaging as there are two main obstacles that limits the practicality of these approaches. The first limitation arises from the complexity of the torso structure compared to e.g. breast. This is due to presence of a significant scatterer, heart, which provides a low contrast in terms of dielectric constant compared to accumulated fluid inside the lungs. Secondly, unlike head imaging that has similar physical structure in male and female subjects, torso differs drastically due to the presence of breasts in female subjects. Therefore, several considerations are required to overcome the aforementioned issues when designing a platform and detection algorithms for torso imaging.

## 2.6 Thesis Organization

The rest of the thesis will follow a systematic approach in which firstly one of the most important element of the system, which is the antenna design, will be discussed in chapters three and four. Several innovative approaches and novel designs will be proposed for the torso imaging system. Chapter three is devoted to a thorough investigation of three dimensional antennas and the introduction of folding/bending techniques for bandwidth enhancement and back radiation

suppression. In chapter four, planar antenna designs that are utilizing the theory of loop-dipole composite structures, capacitive loading and metamaterial loading, specifically mu-negative loading, will be discussed.

Chapters five is allocated to step by step introduction of the proposed platforms and their evolution process. Each successive platform is designed to improve the shortcomings from its predecessor. The experiments are conducted on a realistic size human torso phantom with a complex environment that includes majority of cardiovascular organs as well as animal tissues such as lamb lungs that closely mimic the tissue properties of human beings. More specifically, this chapter will be mainly focusing on introduction of linear scanning systems that are utilizing the rear side of the torso due to its analogous structure both in male and female subjects and on measurement setups with circular configurations that are utilizing novel strategies for detection purposes.

Chapter six will be introduction of two preclinical/clinical systems. The first platform is made in the form of an array, which is embedded inside a clinical bed that is built using radio frequency (RF) transparent foam. The second platform is built in a shape of a doughnut shaped chamber that can be used both in standing and lying positions. The clearest advantage of the proposed clinical platforms and the imaging systems to the existing ones is the high sensitivity of the system to the presence of fluid, mobility and low cost of the final product. These systems are designed with an aim of being a complementary and initial detection tools that can assist doctors in fast diagnosis of fluid accumulation inside torso that its early treatment is lifesaving.

# Chapter 3

## Antenna Designs

### Part I: Three Dimensional (3-D) Structures

#### 3.1 Defining Optimum Operating Frequency

As stated in previous chapter, both reflection and transmission measurements of the scattered signals from the torso are the key parameters in diagnosis process as both of these parameters are sensitive to the changes in lung fluid (mainly water) content [10]. The first step in designing a microwave imaging system is to determine the optimum frequency range, which defines the size of the antennas, types of utilized switches, and therefore the size of the system.

In order to quantify the penetration of the electromagnetic energy into the lung region, a simple but effective simulation procedure is applied. From the electrical properties of human tissues in the torso area (skin, fat, muscle, lungs), as depicted in Fig. 3.1, an equivalent circuit model of distributed parameters is derived. This model is imported using voxel data inside HFSS. Each of these layers is represented by a lossy TEM transmission line. The dielectric constant and conductivity of the tissues are used to define the characteristic impedance, electrical length and loss tangent of the equivalent transmission lines. The frequency-dependent properties of the tissues are [55], [56]: Skin: dielectric constant=51, thickness= 2 mm, conductivity= 2 S/m. Fat: dielectric constant=6, thickness= 20 mm, conductivity= 0.2 S/m. Muscle: dielectric constant=55, thickness= 18 mm, conductivity= 1 S/m. Lungs: dielectric constant=53 (deflated), 22 (inflated), thickness= 140 mm, conductivity= 0.7 (deflated), 0.35 (inflated). Note that the thicknesses of the tissues are assumed to be for a standard average person.

A coupling medium with certain properties is assumed at the skin layer. A signal source that represents the microwave signal transmitted from a suitable antenna is connected to the coupling transmission line. The equivalent circuit model is depicted in Fig. 3.2. The termination resistor ( $377\Omega$ ) represents the free-space at the other side of the body. Across the frequency band of interest, the amplitude of the signal that penetrates to the center of the lungs is calculated. To account for the effect of respiration, two scenarios that represent the inflated and deflated lungs are considered. The

results of these calculations are shown in Fig. 3.3 for the deflated lungs and Fig. 3.4 for the inflated lungs.

It is clear from the presented results that the attenuation increases as expected significantly with frequency. However, the slope of attenuation is steeper at frequencies above 1 GHz that is predictable due to the significant reduction in signal penetration. It is noted that the frequencies lower than 500 MHz would provide better penetration, yet, would deteriorate the quality of the obtained image as higher frequencies contribute to the resolution of the image. Therefore, any wide operating bandwidth at 0.5 GHz and 1GHz can provide a compromise between deep penetration of the signal and the high resolution of the obtained image.

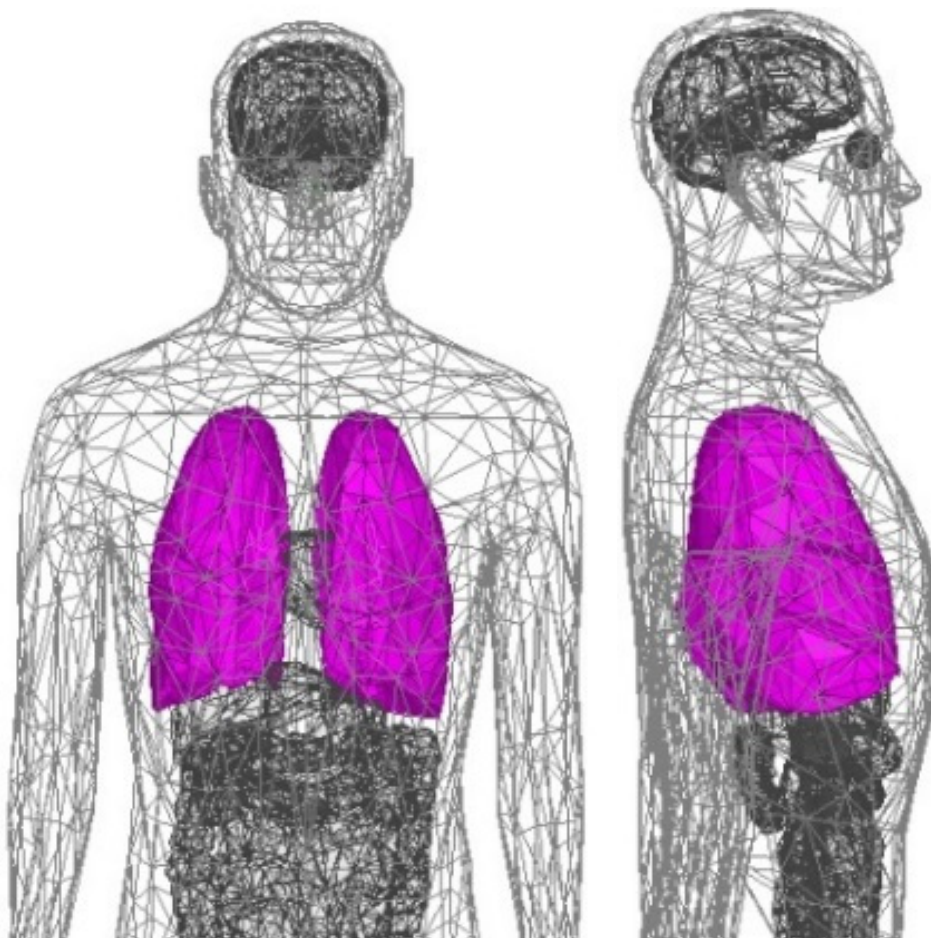


Fig. 3.1. HFSS human model of the torso area. Front view (left) and side view (right).

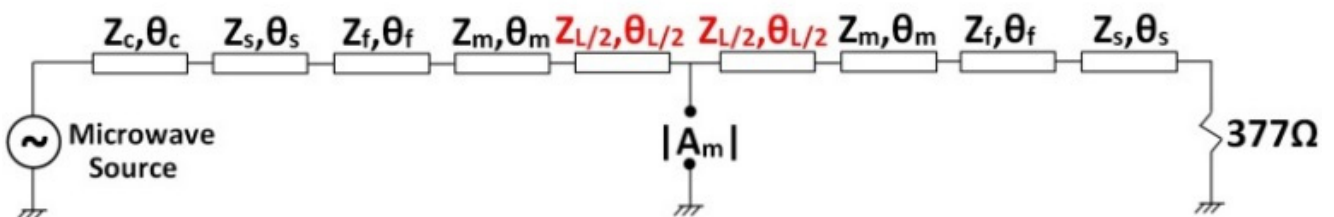


Fig. 3.2. Circuit model of the human torso.  $Z$  refers to the impedance, and  $\theta$  refers to the electrical length, subscript  $c$  refers to coupling medium,  $s$ : skin,  $f$ : fat,  $m$ : muscle,  $l$ : lung.

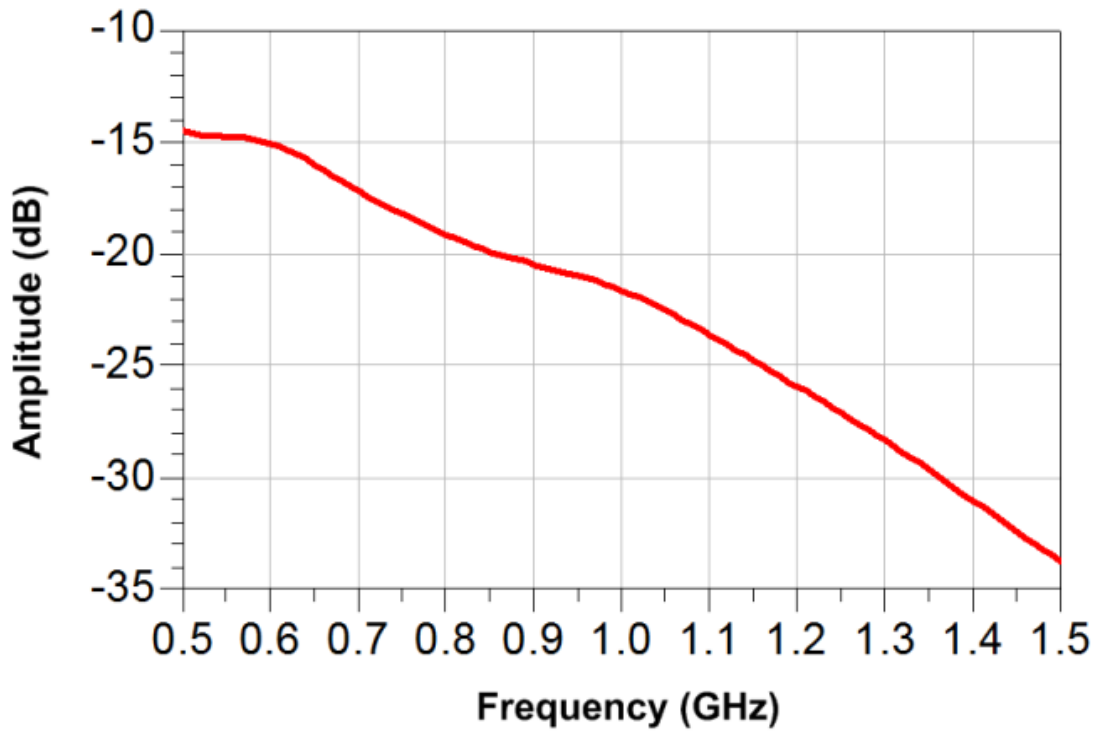


Fig. 3.3. Variation of signal amplitude at the center of deflated lungs with frequency.

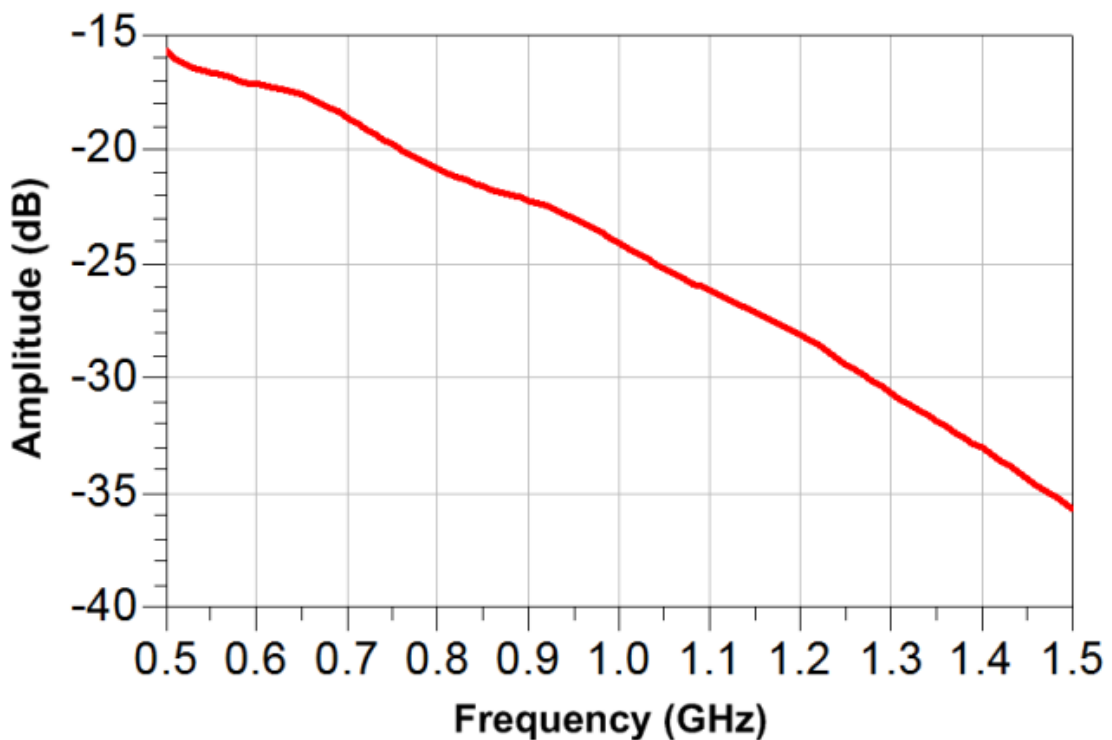


Fig. 3.4. Variation of signal amplitude at the center of deflated lungs with frequency.

### 3.2 Antenna Design Criteria

There are three main requirements from the antennas to be used in microwave-based imaging systems: 1) unidirectional radiation so that the utilized signal is mainly directed towards the human torso with minimum or no interference with nearby objects; 2) wide operational bandwidth to achieve

a reasonable resolution in the image; and 3) compact in size due to the limited available space in the system and to meet the portability requirement of the whole system. While achieving each of the aforementioned requirements separately is possible, combining all of them in a single antenna design is a challenging task that requires certain compromises considering the main priorities of the intended application.

Considering the direct relation between the physical size of any antenna and its operating wavelength, the estimated size of the needed ultra-high frequency (UHF) antennas is physically large if traditional design techniques are used. Early and recent investigations on microwave-based fluid detection use either horn or matched loaded patch antennas [10]. However, they are either large in size [10] or have narrow bandwidth. Investigating available designs of UHF antennas in other applications reveals the use of several techniques, such as fractal [57], loop [58], metamaterial [59] and inverted F-shaped structures [60]. Additionally, folded structures are widely employed to reduce the size of the antennas especially in handset mobile devices [61]–[65]. However, despite achieving a compact size, the aforementioned antennas have narrow bandwidths, and omnidirectional radiation.

To fulfill the antenna requirements of microwave-based torso imaging system, a series of techniques will be proposed in this and following chapter. Since there is no one global solution and single antenna design that can suit all feasible system configurations, this thesis aims at proposing different novel designs to consider certain aspects of a portable torso scanning system for each of those designs. As an example, the compactness and small lateral size of a cubic antenna occupying limited area cannot be compared to the light weight and ease of fabrication of a half-wavelength planar Yagi antenna. Consequently, based on the requirements of the intended detection approach to be devised, a suitable type of the antenna should be selected.

This chapter is focusing on the three dimensional structures and specifically on using folding technique as an effective way of reducing the size of the antenna. This technique starts initially from a planar structure, which is a generally a wideband structure. To make it compact and unidirectional, the design involves defining an optimum folding process for a compact size and a proper input impedance, suppressing the unwanted back radiation and increasing the impedance matching bandwidth. While achieving all three requirements for the antenna design is ideal, there will be compensations that should be made to facilitate building certain scanning platform configurations. Three different antenna topologies will be presented in this chapter. Considering the wide range of antennas that can be designed using folding technique, the main idea will be explained thoroughly by applying it one a planar structure and then similar designs using different topologies will only be introduced.

### 3.2.1 Design of Wideband Printed Loop Antennas with Back Radiation Suppression Using Folding Technique

To explain the design concept, first, the design of a wideband printed loop antenna is explained. The proposed broadband UHF antenna, shown in Fig. 3.5, is designed using Ansoft's HFSS on a RO4003 square substrate, with a side length of  $G = 150$  mm, height of  $h = 0.8$  mm, relative permittivity of 3.55 and loss tangent of 0.0027. The antenna consists of a square loop that is combined with two spiraled monopoles that extend in towards the center of the loop, and which are fed using a common coplanar waveguide (CPW) line. Three conducting rectangles are added to the top right-hand corner of the square loop in order to enhance the impedance matching of the antenna. The average circumference of the loop is initially designed to be one wavelength at 550 MHz, that is,  $\ell_0 = \lambda_1 = 545.5$  mm, as shown in the reference antenna design in Fig. 3.6. In addition, the length of each of the spiraled monopoles is chosen to be a quarter wavelength at the frequencies of 550 and 800 MHz, that is,  $\ell_1 = \lambda_1/4$  at 550 MHz, and  $\ell_2 = \lambda_2/4$  at 800 MHz. In this case, since the substrate is electrically thin and has a relatively low permittivity, the guided wavelength is approximately equal to that of free space.

The antenna utilizes a CPW feed-line that is separated from the ground conductor by a gap of  $g = 0.25$  mm for a  $50 \Omega$  characteristic impedance. To achieve efficient excitation of the structure and good impedance matching, the CPW feed-line is extended into the center of the square loop. Considering the first reference antenna shown in Fig. 3.7 (a), which consists of a simple square loop that is fed using a CPW feed-line, the input impedance exhibits a resonance ( $\text{Im}\{Z_{\text{in}}\} = 0$ ) around 550 MHz. To improve the impedance matching of the loop antenna around the first resonance frequency of  $f_1 = 550$  MHz, a spiraled monopole with a length of  $\ell_1 = \lambda_1/4$  (Monopole #1) is added to the CPW feed-line on the right-hand side, as depicted by Antenna 0 in Fig. 3.7 (a). For this case, the resonant frequency increases to approximately 610 MHz with the addition of the monopole, as shown in Fig. 3.7 (b). Furthermore, to achieve a broader impedance bandwidth, a second spiraled monopole with a length of  $\ell_2 = \lambda_2/4$  at 800 MHz (Monopole #2) is also connected to the CPW feed-line on the left-hand side, as depicted by Antenna 1 in Fig. 3.7 (a). Adding this monopole, a dual-resonance response is achieved at 650 and 800 MHz, albeit with the first resonance being a lot weaker. It can therefore be concluded that the 650 MHz resonance is excited by the combination of the square loop and the right-hand side Monopole #1, while the 800 MHz resonance is excited by the left-hand side Monopole #2. Thus, combining two conventional methods in a proper manner introduces a new and efficient way of increasing the operation impedance bandwidth in a simple way, which is not accessible using any of these techniques alone.

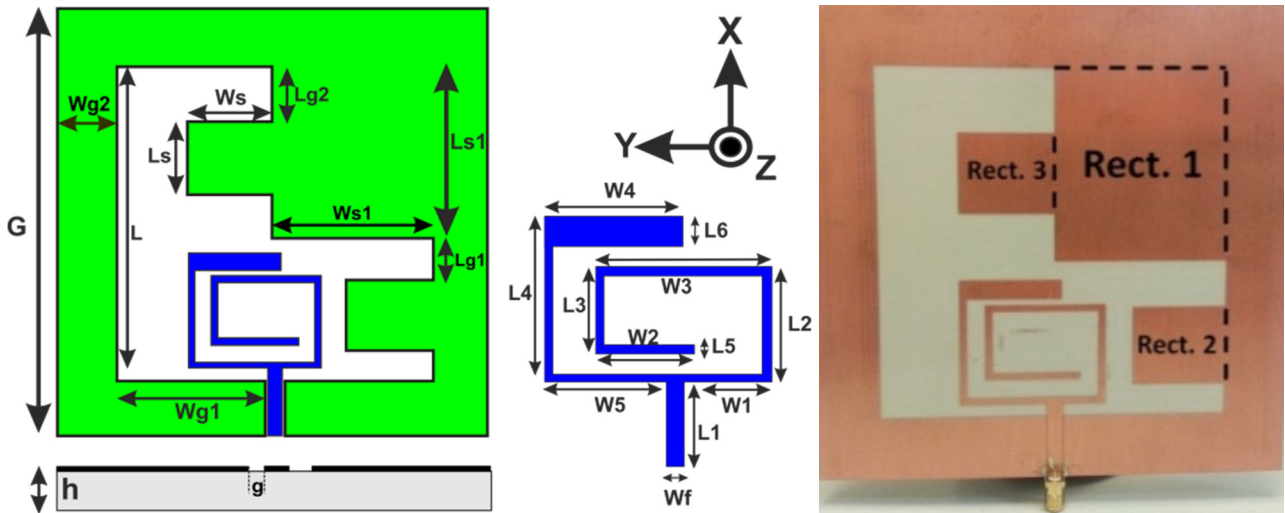


Fig. 3.5. Detailed geometry and fabricated prototype of the proposed antenna

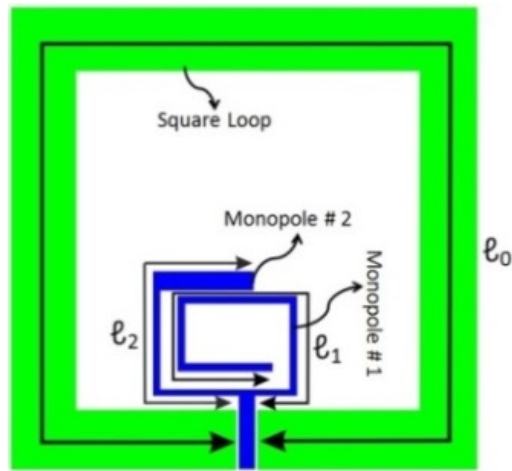
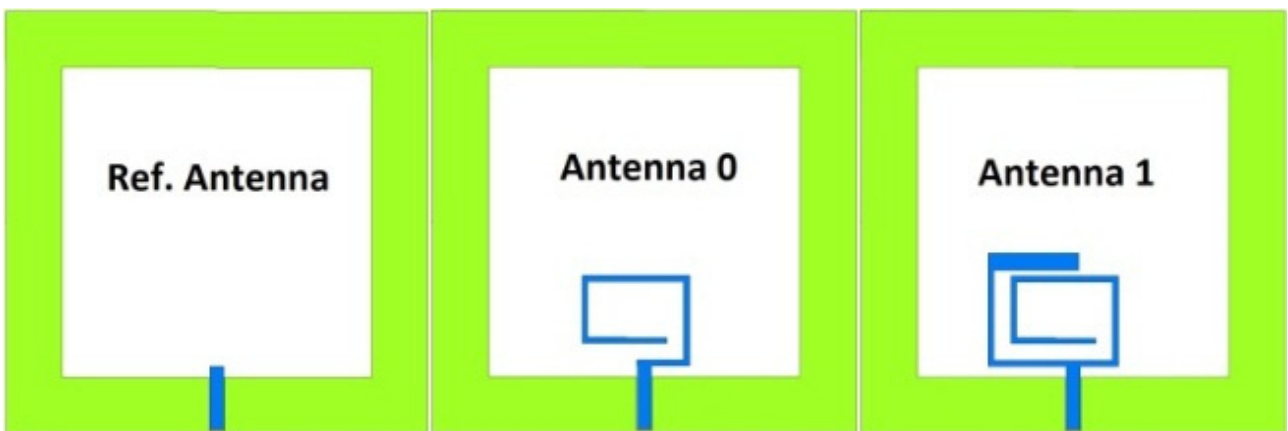


Fig. 3.6. Initial antenna configuration.



(a)

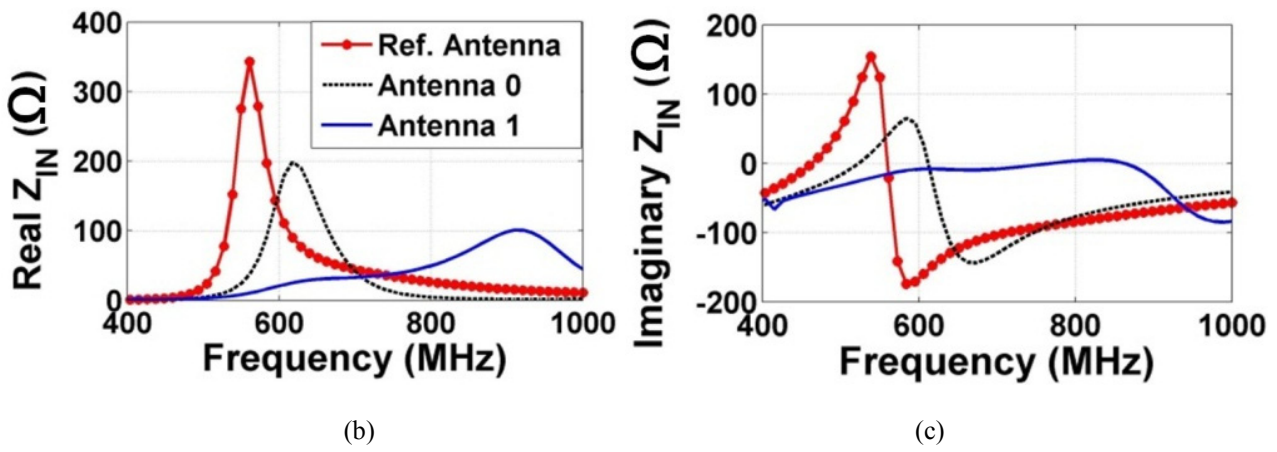


Fig. 3.7. (a) Geometry of studied antennas. (b) Real part, and (c) imaginary part of the input impedance of the Reference Antenna, Antenna 0 and Antenna 1.

The main design goal for this antenna is to achieve broad operating bandwidth. To that end, a rectangular conductor named *Rect. 1*, with dimensions  $W_{s1} \times L_{s1}$ , is added to the loop conductor and designated as Antenna 2 in Fig. 3.8. Adding *Rect. 1* increases the electrical size of the antenna and as a consequence pushes the resonance excited by the square loop and the right-hand monopole down to around 580 MHz again (Fig. 3.9). To widen the impedance bandwidth, two rectangles (*Rect. 2* and *Rect. 3*) with identical dimensions of  $W_s (0.2 G) \times L_s (0.4 G)$  are added to the structure to create Antenna 3, which now consists of a deformed square loop in combination with two spiraled monopoles, fed using a common CPW feed-line. Dimensions of the rectangles are chosen such that the loop antenna ( $\ell_0$ ) resonates at 550 MHz with a widest possible bandwidth.

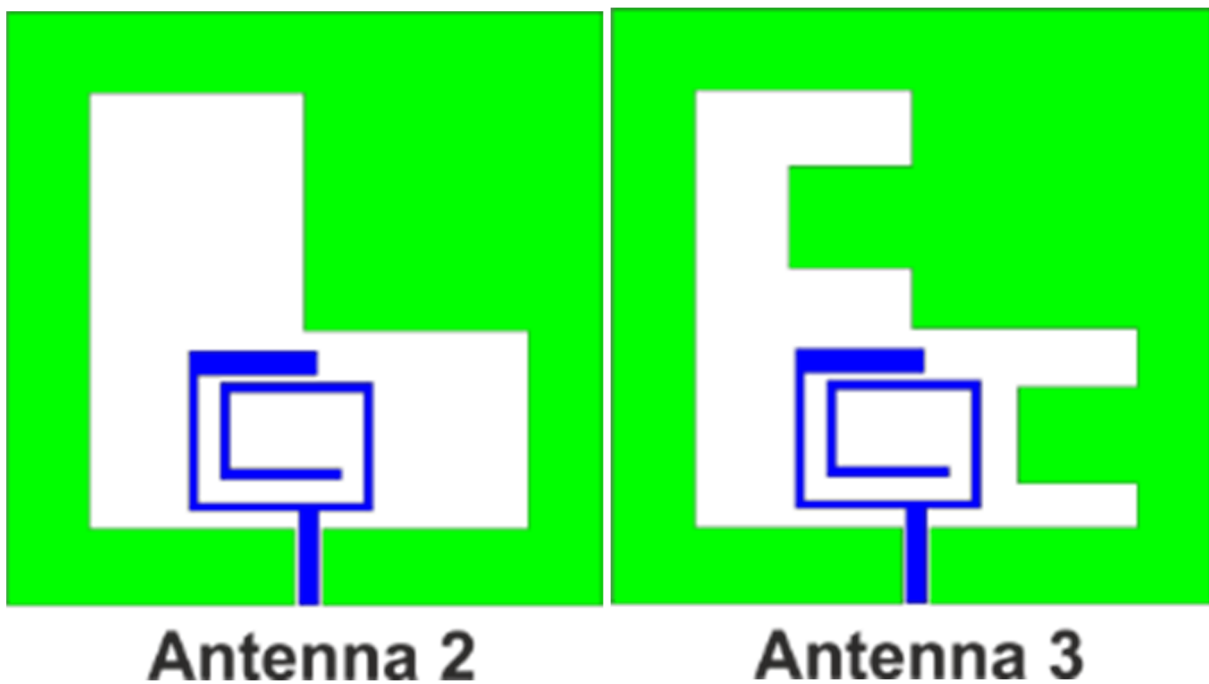


Fig. 3.8. Design evolution of the UHF antenna.

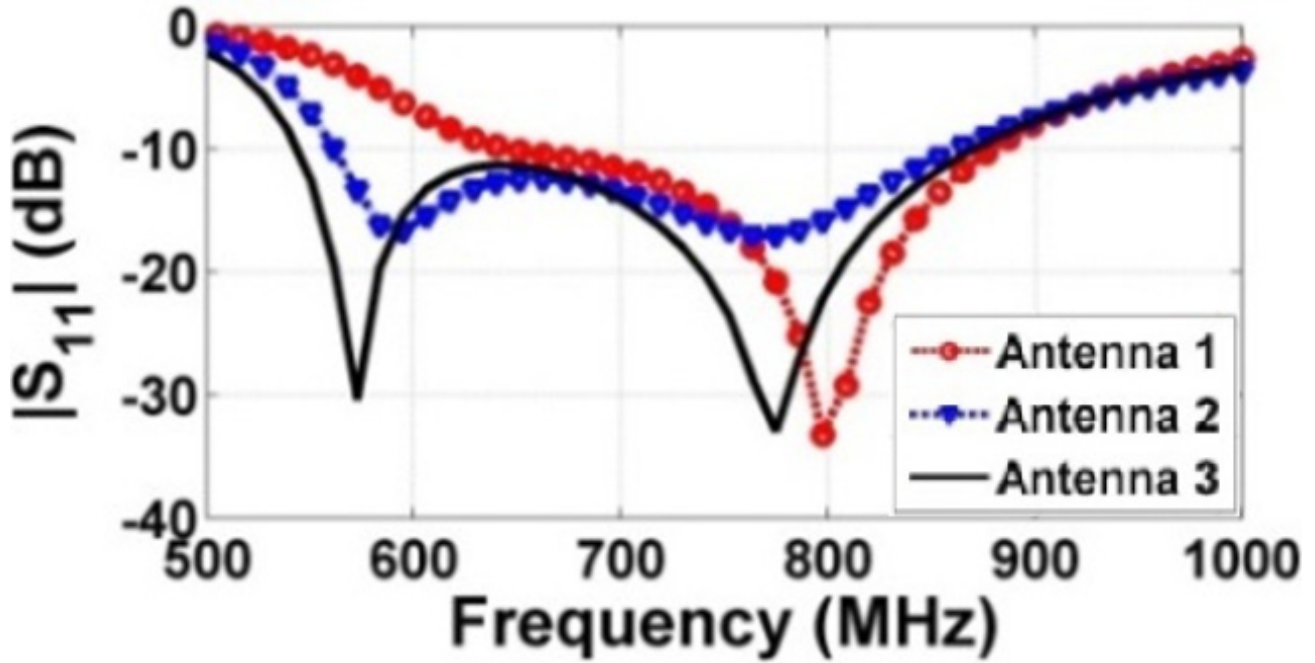


Fig. 3.9. Simulated  $|S_{11}|$  variations of Antennas 1, 2 and 3.

In order to accurately describe the resonant behavior of the antenna, by utilizing the parametric studies the resonant frequencies are related to the dimensions of the antenna loop and monopole elements. As outlined previously, the first resonant frequency,  $f_1$ , of the antenna corresponds to the frequency where the average circumference of the square loop is equal to one wavelength, that is,  $\ell_0 = \lambda_1$ . This also corresponds to the frequency where the total length of the spiral Monopole #1 is equal to  $\ell_1 = \lambda_1/4$ . The first resonant frequency is therefore given as follows in terms of the antenna geometrical parameters shown in Figs. 3.5 and 3.6:

$$f_1 \approx \frac{c}{\lambda_1} = \frac{c}{\ell_0} = \frac{c}{4(W_1+L_2+W_3+L_3+W_2)} \quad (1)$$

Inserting the values of  $W_1$ ,  $L_2$ ,  $W_3$ ,  $L_3$  and  $W_2$  from Table 3-I into equation (1), results in a resonant frequency of  $f_1 = 545$  MHz, which corresponds very well with the initial design frequency of 550 MHz and the final simulated resonant frequency of 580 MHz from Fig. 3.9.

The second resonant frequency,  $f_2$ , corresponds to the frequency where the total length of the spiral Monopole #2 is equal to  $\ell_2 = \lambda_2/4$ . The second resonant frequency is therefore given as follows in terms of the antenna geometrical parameters:

$$f_2 \approx \frac{c}{\lambda_2} = \frac{c}{4(W_5 + L_4 + W_4)} \quad (2)$$

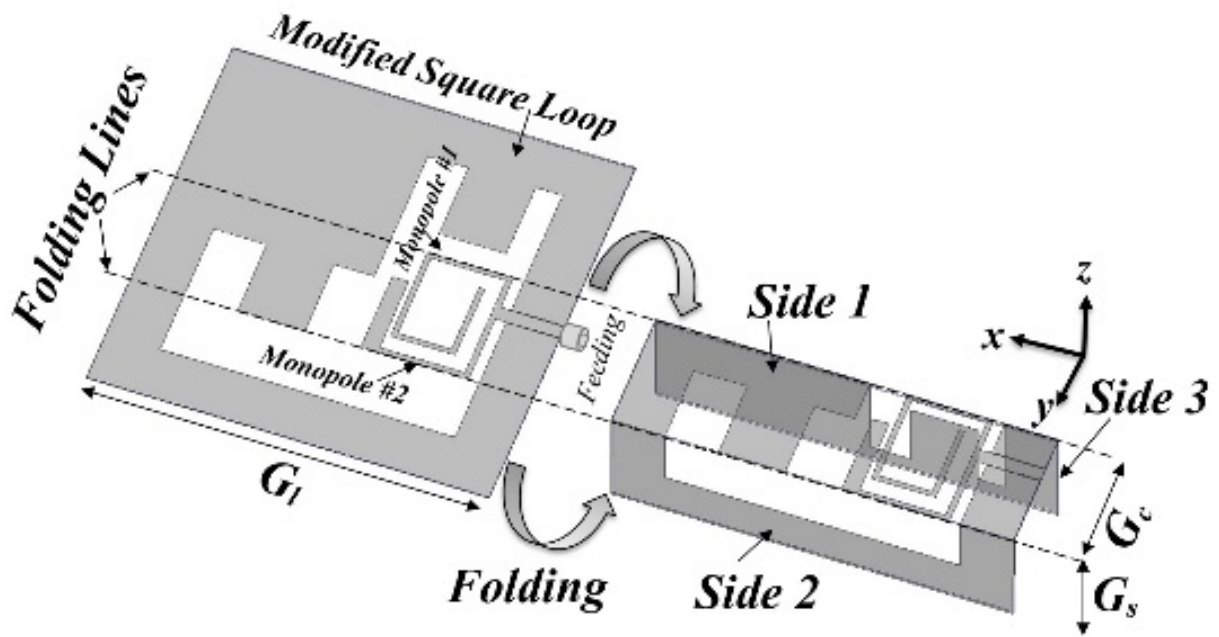
Inserting the values of  $W_5$ ,  $L_4$  and  $W_4$  from Table 3-I into equation (2), results in a resonant frequency of  $f_2 = 754$  MHz, which corresponds very well with the initial design frequency of 800 MHz and the final simulated resonant frequency of 780 MHz from Fig. 3.9.

With the abovementioned configuration, the antenna achieves a relatively wide operating bandwidth of 45% (556 – 882 MHz). However, this antenna, known as *Ref. antenna*, has a large size (150 mm × 150 mm) and possess bidirectional radiation. Thus, the following steps are adopted to obtain a compact, wideband and unidirectional antenna.

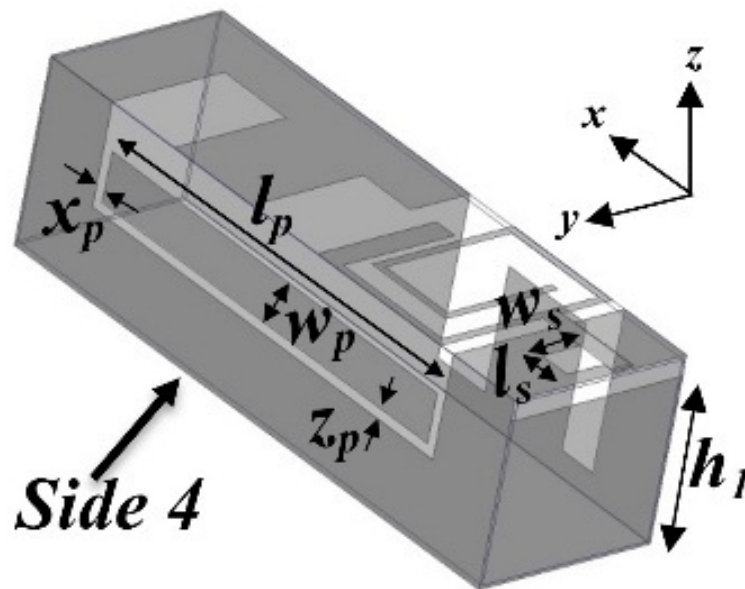
### 3.2.2 Reducing Size of the Antenna

The first step in the design is to reduce the physical size using the methods explained in [64]-[65]. It is known that those methods cannot be applied directly to any arbitrarily structure as they might cause a significant degradation in the antenna's performance. As depicted in Fig. 3.10 (a), the antenna is folded over the indicated lines. To define those folding lines, the minimum possible physical size is calculated. Considering the square structure of the antenna ( $G_l = 150$  mm), the ideal cube size is  $G_l / 4 = 37.5$  mm. However, the folding lines control the current distribution on the antenna's structure, which consequently defines the antenna's radiation properties and bandwidth [66]. Thus, a compromise is required between the optimum bandwidth, size and directivity of the final design.

To avoid disturbing the areas of high current concentration, it is desirable to have minimal folding near the feeder [64]. Therefore, the size of  $G_c$  shown in Fig. 3.10 (b) is used as an initial parameter that needs to be optimized for the best possible performance. Several cases were investigated and the results are presented in Fig. 3.11. As seen from this figure, by bending the antenna, a significant mismatch across the band 530 – 730 MHz occurs at different cases. As per our investigations, the coupling between the loop antenna elements on both sides of the folded structure creates a large capacitive reactance, which in turn degrades the input impedance of the antenna. It also increases the resistance of the antenna at the low frequencies and shifts the first resonance to about 535 MHz.



(a)



(b)

Fig. 3.10. (a) Initial folding process (Antenna 1) and (b) final design (Antenna 2).

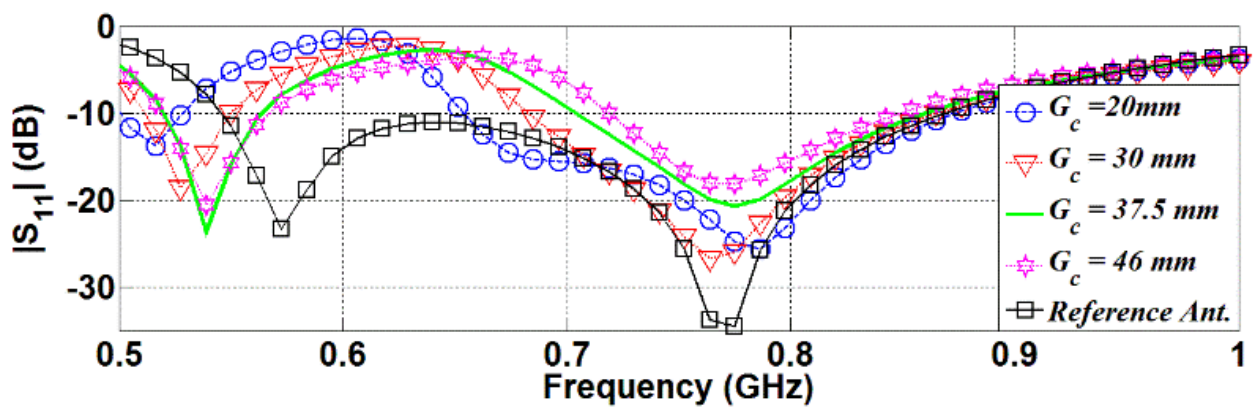


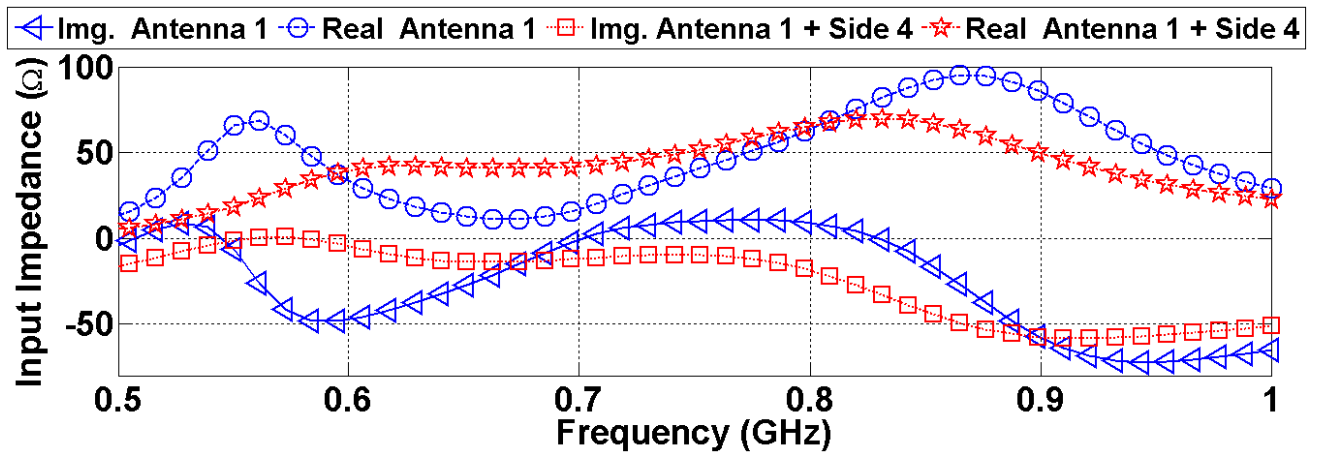
Fig. 3.11.  $|S_{11}|$  performance of the antenna considering different values for  $G_c$ .

### 3.2.3 Widening the band with Unidirectional Radiation

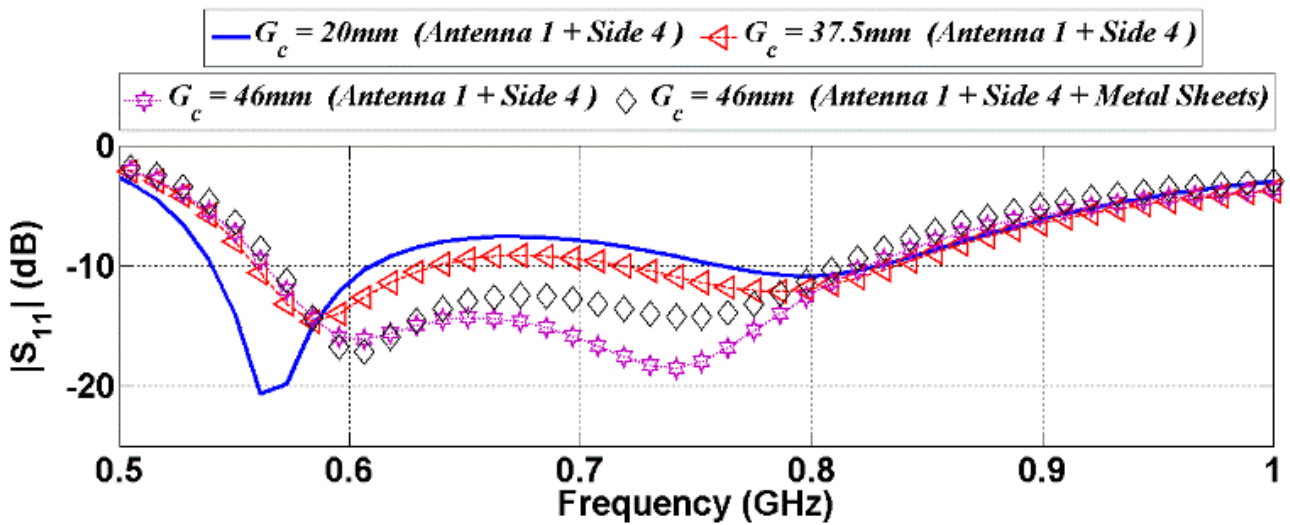
One of the main objectives of the current design is to achieve a unidirectional radiation. However, printed loop antennas, also known as wide slot antennas, have bidirectional radiation patterns [67]. Moreover, the majority of the published three-dimensional antennas have omnidirectional radiation patterns [64], [65]. It is worth mentioning that in telecommunications; the directivity can be enhanced using a large ground near the main radiator [66]. However, that technique is not suitable when wideband coverage in a small physical space is needed as in the current application.

From the image theory, it is expected that locating a conducting ground in the near vicinity of the main horizontal radiating element, cancels the total radiated fields above the radiator, since the image current formed beneath the ground is oppositely directed with respect to the current on the main radiator. This is the main reason that antenna designers generally locate cavities or reflectors at a quarter wavelength distance from the radiator. However, a quarter wavelength distance at the lowest operating frequency of 580 MHz (Ref Antenna) is around 129 mm, which is too large for the target of building a compact structure. To cancel the effect of the large capacitive reactance and reduce the back radiation of the antenna, a conductor is inductively connected as side 4 of the rectangular parallelepiped as shown in Fig. 3.10 (b). As indicated in Fig. 3.12 (a), connecting that conductor reduces the amount of capacitive reactance and increases the resistance in the frequency range 600 – 800 MHz, which in turn improves the input impedance matching of the antenna. At the same time, connecting side 4 reduces the resistance of the antenna at 500 – 600 MHz and thus shifts the resonant frequency to 600 MHz. From Fig. 3.12 (b), the best impedance matching is attained with  $G_c = 46$  mm. However, the overall impedance matching bandwidth of the antenna is decreased by 18% compared to the Reference Antenna. As a compromise between the size and impedance matching, the aforementioned  $G_c$  is selected as the optimum value for side 1 and 4 of the design. To achieve the most compact design,  $G_s$  value for sides 2 and 3 is optimized at 45 mm. The optimization process is not presented for brevity.

The front to back ratio (FBR) of the antenna is also investigated. Antenna 1 with added side 4 achieves a FBR between 3.2 dB and 5.5 dB in the range 600 – 800 MHz. To improve the FBR, two metallic sheets with heights  $h_1$  and  $G_s$  were designed (see Fig. 3.10 (b)). The vector electric field at, say, 750 MHz reveals that prior to adding these sheets, there are strong fields in  $-z$ -direction which result in a low FBR (see Fig. 3.13 (a)). However, as depicted in Fig. 3.13 (b), adding these sheets changes the intensity and direction of the electric field distribution in a way that fields radiating in  $-z$ -direction are weakened in comparison with the fields in  $+z$  direction which in turn enhances the FBR. The optimum heights of these sheets were found to be  $h_1 = 40$  mm and  $G_s = 45$  mm.

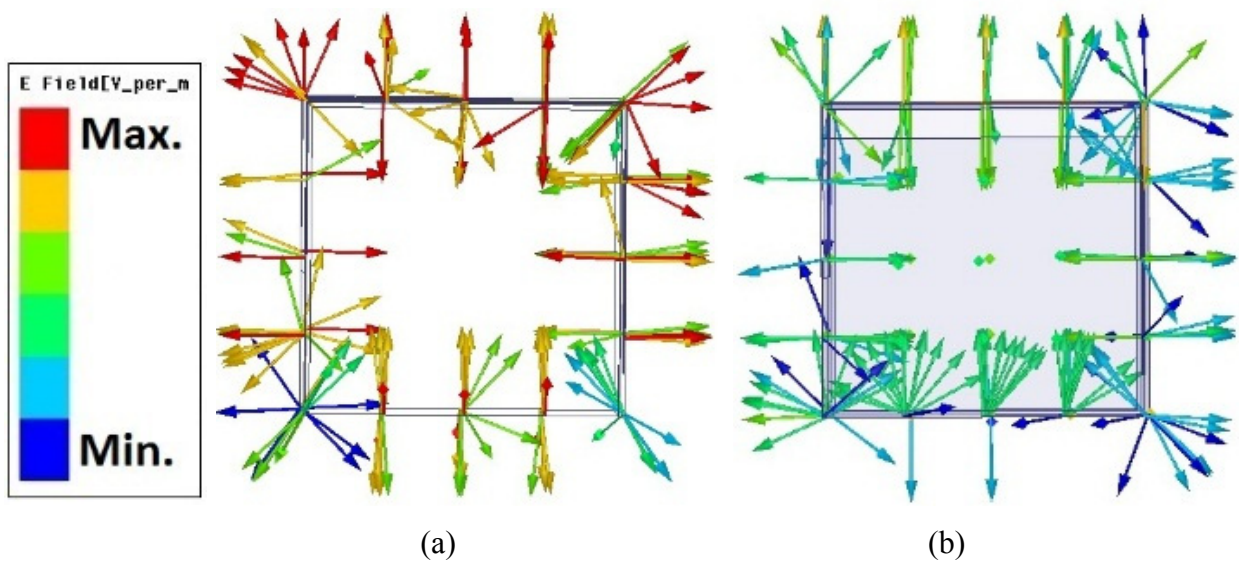


(a)



(b)

Fig. 3.12. (a) Input impedance and (b)  $|S_{11}|$  performance of the Antenna1 considering various cases.



(a)

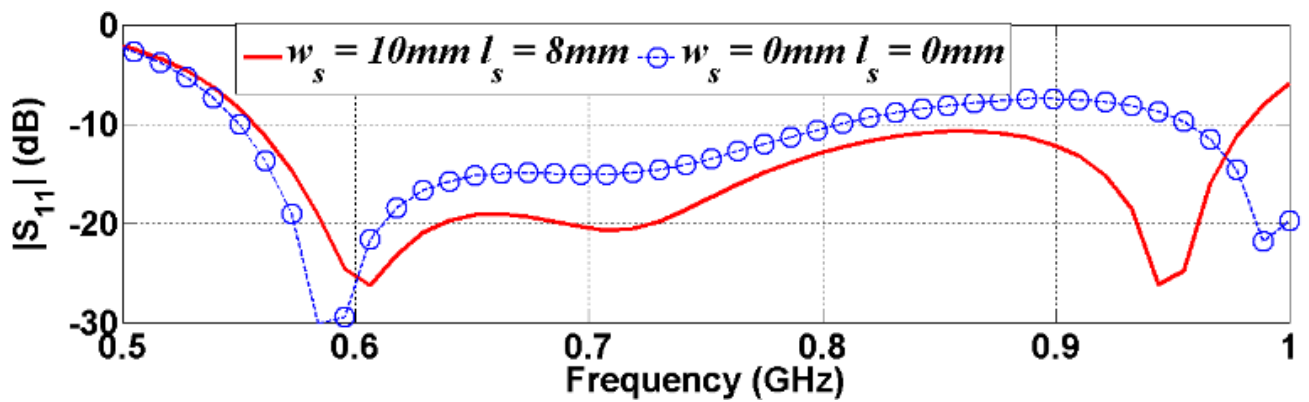
(b)

Fig. 3.13. Vector electric field distribution (a) before and (b) after connecting metal sheets to Antenna 1 at 750 MHz (y-z plane).

### 3.2.4 Increasing the Operating Bandwidth

To extend the impedance matching bandwidth of the antenna up to the frequency 1 GHz as needed for the detection system, a parasitic strip with  $w_p \times l_p$  dimensions is added to the antenna's structure (see Fig. 3.10 (b)). Using HFSS simulator, it was found that the strip's distance from the loop structure is critical to excite a third resonance. A parametric study was conducted to tune the optimum location for the strip. The reflection coefficient of the antenna after adding the strip is presented in Fig. 3.14 (a). Adding the strip creates a current node (minimum current) on monopole #2 and degrades the antenna's performance at 800 – 960 MHz as shown in Fig. 3.14 (b). However, a third resonance is created at 990 MHz. To defy the effect of strip on monopole #2, a rectangular shaped slot with dimensions  $w_s \times l_s$  is created on the loop. This slot acts as a short ended slot line [68]. Its dimensions can be tuned to improve the antenna matching and thus the flow of current from the feeder into the antenna's structure as depicted in Fig. 3.14 (c). As a result, antenna operates over the wide frequency band (565 -988 MHz) which is proportional to a fractional bandwidth of 54.5 %.

The final design of the antenna (Fig. 3.10 (b)) meets the three main design goals of the detection system. Besides the fact that no other available unidirectional antennas covers the required band, the current design is 20% to 80% more compact than the recent unidirectional UHF antennas presented in the literature for different applications [69]-[74]. However, it is worth stating that the design presented in [46] can cover the same band and beyond. However, that antenna requires a matching layer, which is not practical in portable imaging systems aimed at imaging different individuals. The presented antenna has a unidirectional radiation, and has a bandwidth which is wider by more than 20% compared with the designs presented in [72] , [74].



(a)

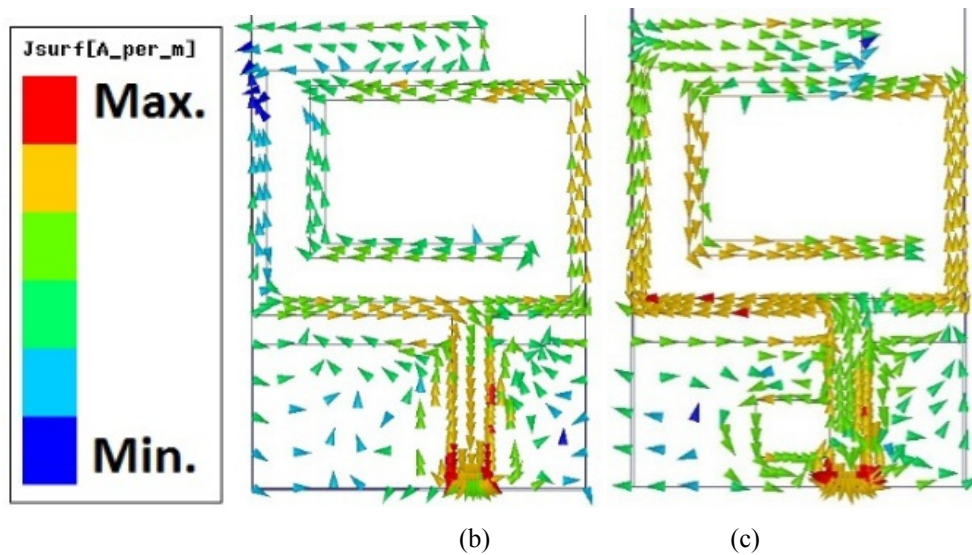
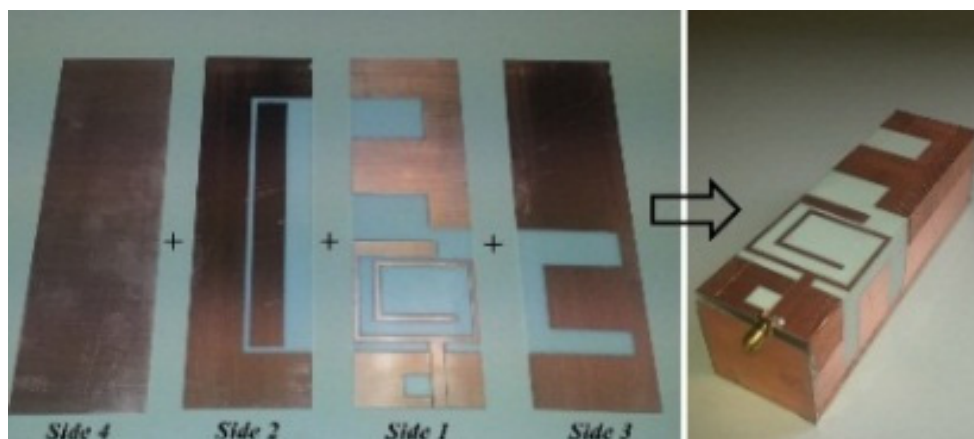


Fig. 3.14. (a)  $|S_{11}|$  performance of Antenna 2. Surface current distribution of Antenna 2 (b) before and (c) after addition of a short-ended slot line.

### 3.2.5 Antenna Test

The optimized antenna design with the dimensions presented in Table 3-I was fabricated (Fig. 3.15 (a)) and its performance was validated. To ease the fabrication process, four sides of the rectangular parallelepiped were carved on a RO4003 substrate using a milling machine. The four pieces were then connected together using copper tapes, while copper sheets were soldered on the sides to close the cubic structure. The antenna was then tested in an anechoic chamber. As presented in Fig. 3.15 (b), the fabricated antenna covers the band estimated in the simulations. However, there is a slight shift of around 15 MHz in the realized operating bandwidth compared with the simulated performance. This slight discrepancy is a result of the imperfect manual connection of the different parts of the antenna. From Fig. 3.15 (b) it can be seen that the measured gain varies between 3 and 5 dBi, whereas the front-to-back ratio varies between 6 dB and 8 dB across the band 580 – 1000 MHz.



(a)

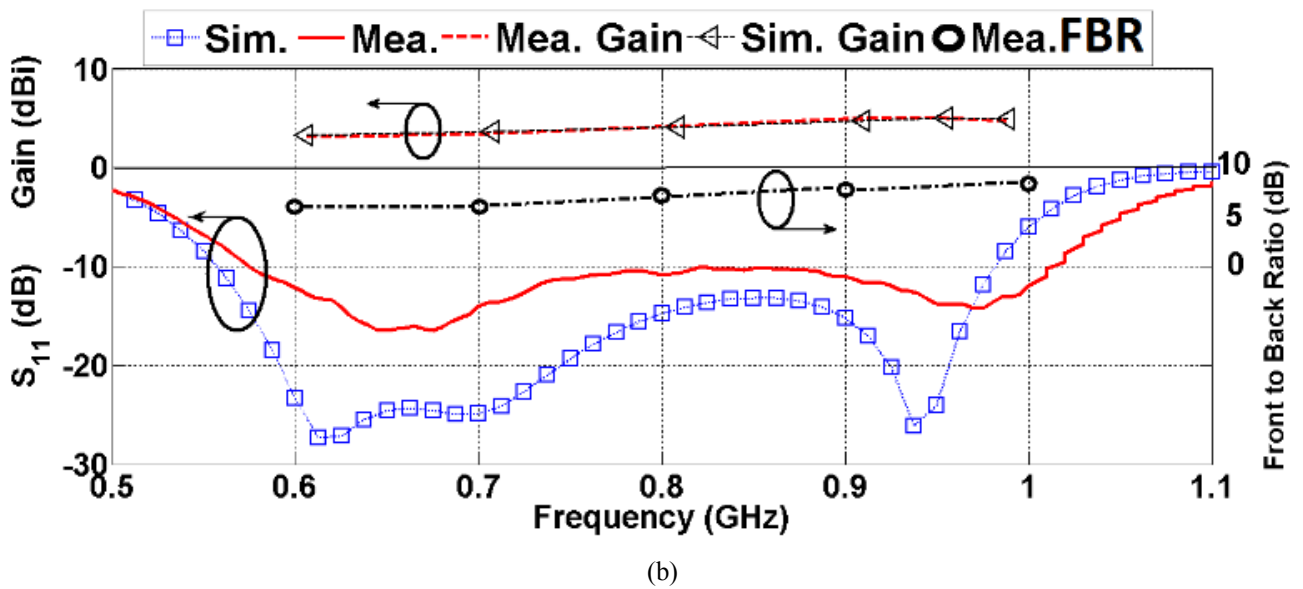
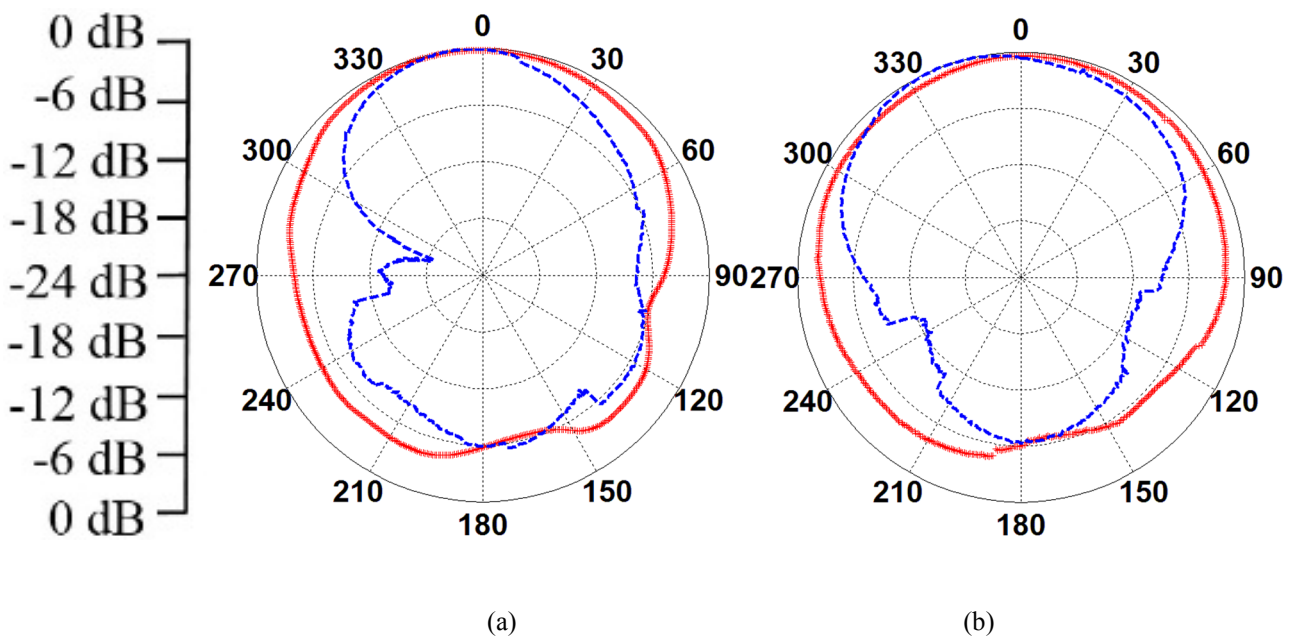


Fig. 3.15. (a) Fabricated Antenna, (b) measured and simulated  $|S_{11}|$ , gain and FBR.

The radiation patterns at the three main resonances of the antenna presented in Fig. 3.16 indicate a unidirectional radiation. The antenna has also a negligible cross-polarization, which is not presented for brevity. The antenna has relatively symmetrical radiation patterns. There are many important advantages of having an antenna with a symmetrical radiation in microwave systems for medical applications: Firstly, due to the identical electric field distributions at all the frequencies, the maximum power direction is radiated at the bore-sight direction, i.e. the target direction, and does not shift to other directions at different frequencies. Secondly, when using this antenna element to build an antenna array, the radiation pattern will be stable across the band of operation.



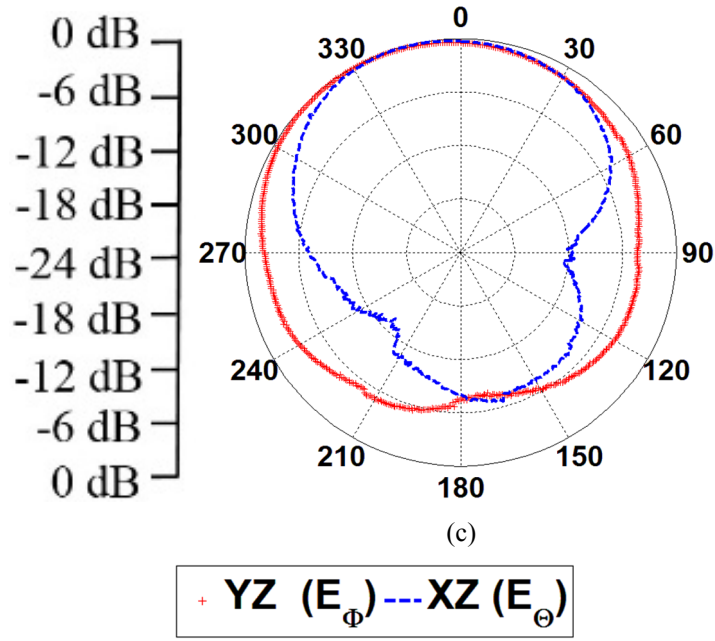


Fig. 3.16. Normalized measured radiation patterns of the antenna at (a) 600 MHz, (b) 700 MHz and (c) 950 MHz.

Since the antenna is designed specifically for a heart failure detection system, the specific absorption rate (SAR) is calculated when using the antenna to image a realistic torso model in HFSS. For all of the following SAR calculations, the antenna is placed in the near vicinity of the torso model in the simulation environment. Following the usual procedure [46], the SAR values are calculated at the single central frequency when using a transmitted power of 1mW on 10 grams of tissue. The calculated maximum SAR value is found to be 0.08 W/Kg, which is well below the standard safe threshold of (0.4 W/Kg) as defined by IEEE [75].

Table 3-I: Geometry details in (mm) of the reference antenna

$L_1$	22	$L_{s1}$	60	$W_5$	27.5	$L_6$	6	$W_3$	38	$W_{s1}$	55
$L_2$	32	$L_{g1}$	15	$W_f$	5	$L_s$	25	$W_4$	32	$h$	0.8
$L_3$	24	$L_{g2}$	20	$W_{g1}$	52.25	$L$	110	$G$	150	$g$	0.25
$L_4$	40	$W_1$	13.5	$W_{g2}$	20	$w_s$	10	$l_s$	8	$w_p$	12
$L_5$	2	$W_2$	30	$W_s$	30	$l_p$	105	$x_p$	2.6	$z_p$	2.5
$G_l$	150	$G_c$	46	$G_s$	45	$h_l$	40	--	--	--	--

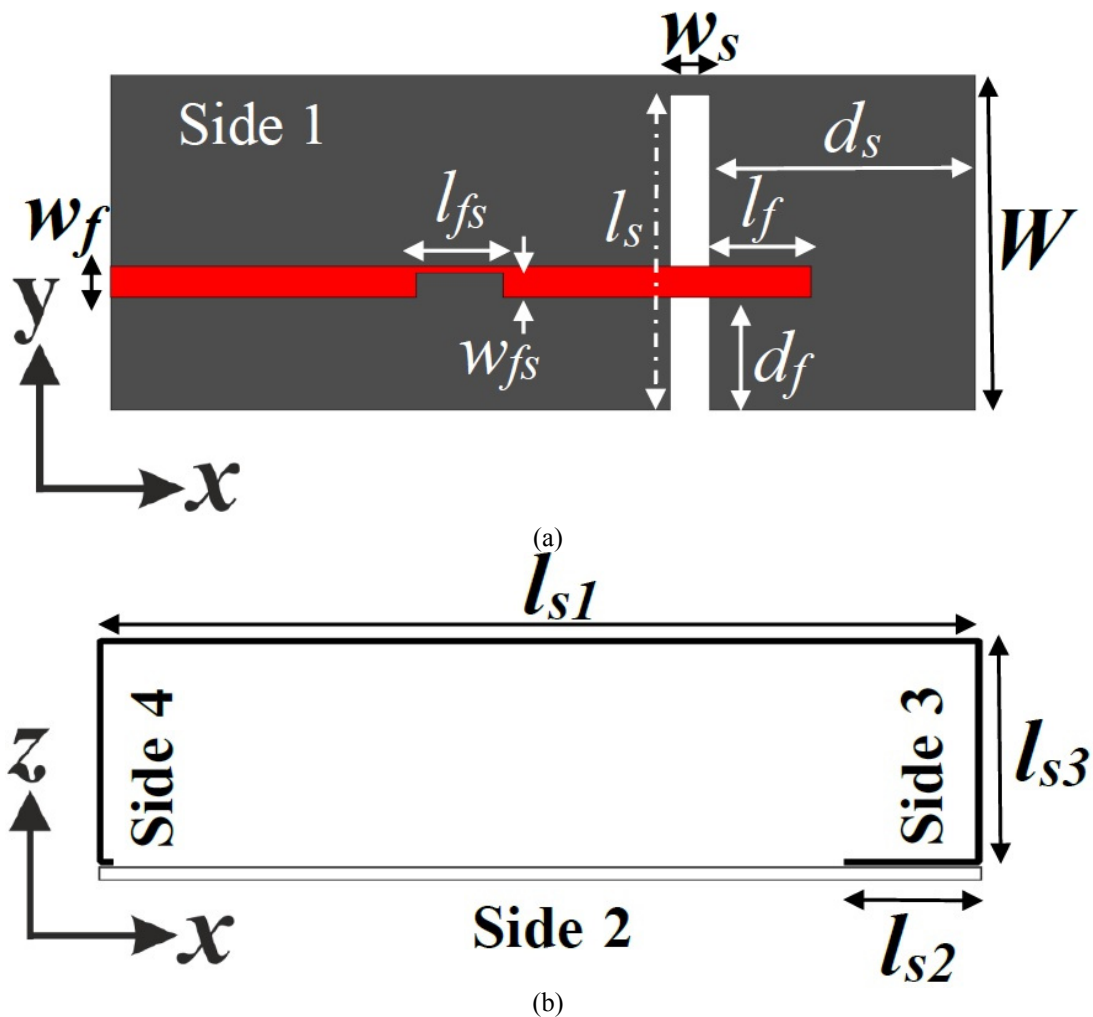
### 3.3 Three-Dimensional Open-Ended Slot Antenna

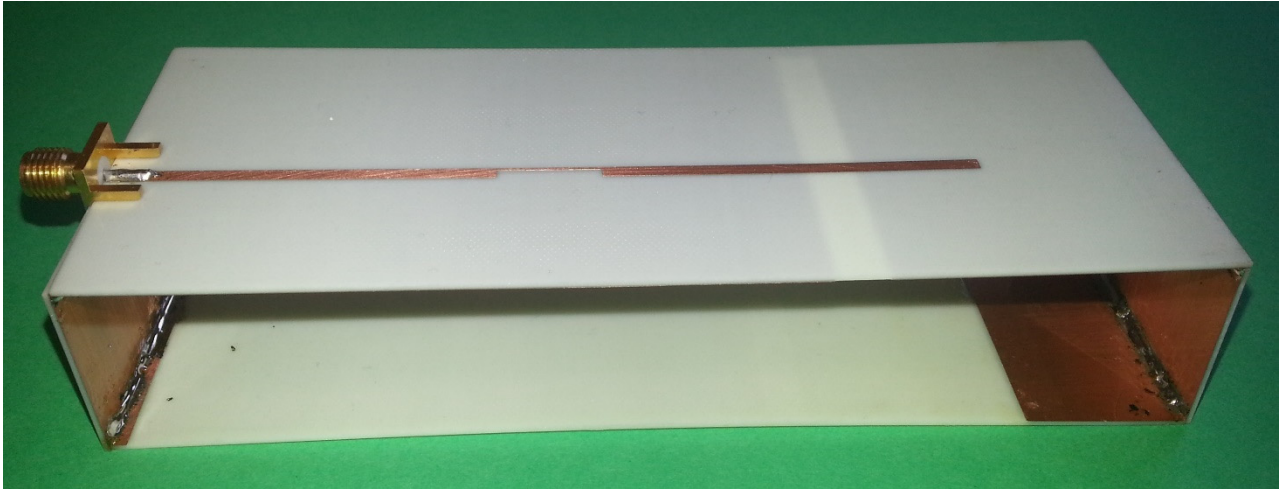
In an attempt to further reduce the size of the antennas and facilitate positioning antennas besides each other for differential detection purposes, a very simple yet effective antenna structure is proposed in this section. This antenna is based on the design of the well-known open ended slot antennas, however, with an extremely condensed size and wider operating bandwidth. It should be

noted that these types of antennas possess a very low front to back ratio, and hence, a reflector should be designed as a compensation of achieving a wide operating bandwidth with a condensed lateral size for the slot design.

### 3.3.1 Design Criteria and Proposed Antenna Design

Considering the differential detection technique as one of the potential applicable approaches for torso imaging, at least two antennas are needed to simultaneously scan the human torso. This approach has shown to be extremely effective in improving the accuracy of measurements and reduce the time of detection. Therefore, antenna's dimensions, mainly parallel to the torso plane, should be as compact as possible. To that end, an antenna design of three-dimensional structure depicted in Fig. 3.17 is designed on RO4003 substrate, with relative permittivity of 3.55, thickness of 0.8 mm and loss tangent of 0.0027. The length of side 1 ( $l_{s1}$ ), and side 2 ( $l_{s2}$ ) are selected as quarter wavelength at the lowest operating frequency, which is equal to 550 MHz in this work. An open-ended rectangle slot with dimensions  $w_s \times l_s$  is carved from the bottom layer of side 1 and is fed using a microstrip line. The height of the antenna,  $l_{s3}$ , is designed to achieve the most compact possible structure.





(c)

Fig. 3.17. (a) Top and (b) side view of the antenna, and (c) fabricated prototype ( $l_{s1} = 130$ ,  $l_{s2} = 20$ ,  $l_{s3} = 25$ ,  $d_s = 40$ ,  $d_f = 19$ ,  $l_f = 105$ ,  $w_f = 1.75$ ,  $w_{fs} = 1.4$ ,  $l_{fs} = 13$ ,  $w_s = 6$ ,  $l_s = 47$ ) (Unit: mm).

### 3.3.2 Size Reduction

Open-ended slot antennas, also known as monopole slots are usually designed to be quarter wavelength at their lowest resonance. That type of antenna is fed using a coupled microstrip line. Miniaturizing techniques, such as matching networks [76], U-shaped [77] and F-shaped slots [78] were used to reduce the physical size of this type of antenna by increasing its effective electrical size. However, those methods mainly result in narrow or multiband operations [76]-[81]. Yet, a wide operating bandwidth is essential to obtain a high-resolution image for medical diagnostic systems [82]. The bandwidth of the planar open-ended slot antenna can be increased and its first resonance frequency can be lowered by increasing its longitudinal dimension [79]. However, due to the limited space available for imaging the human torso, and to avoid the adverse effects of mutual coupling, that method is deemed not suitable for torso imaging application.

To increase the current path on the antenna while maintaining its compact physical size, a three-dimensional structure is adopted in this design. The utilized configuration results in a miniaturized slot length of  $0.08 \lambda_0$  which is 57% smaller than the most recent design [77]. To maintain a wide bandwidth while attaining low resonant frequency, the width is fixed at 6 mm. The antenna's lowest resonance,  $f_l$ , can be roughly predicted as

$$f_l \approx c / [4(2l_s + w_s) \cdot \sqrt{\epsilon_{eff}}] \quad (3)$$

, where  $c$  is the speed of light, and  $\epsilon_{eff}$  is the effective permittivity and can be estimated as  $\epsilon_{eff} \approx (\epsilon_r + 1) / 2$  [77]. Due to the fact that with a fixed slot length, increasing size of the ground plane has no effect on the lowest resonance of the antenna [79], the antenna's width,  $W$ , is kept small at  $0.09 \lambda_0$ , which is the smallest achieved width for open-ended slot antennas compared to other designs [76]-[81].

Although with a fixed slot length, the resonance of the antenna is lowered using a three dimensional structure, there is a limit on the lowest obtainable frequency. This limit is basically applicable on the length of side 2,  $l_{s2}$ . As presented in Table 3-II, increasing this length reduces the lower resonant frequency which consequently increases the operating bandwidth. However, after a certain value ( $l_{s2} = 20$  mm) this pattern is distorted when  $l_{s2}$  gets closer to the slot, which is the high current concentration area. Through parametric studies using HFSS, it was found that optimum results are obtained when the overall ground size ( $l_{s1} + l_{s2} + 2l_{s3}$ ) is around half wavelength at the center frequency 775 MHz.

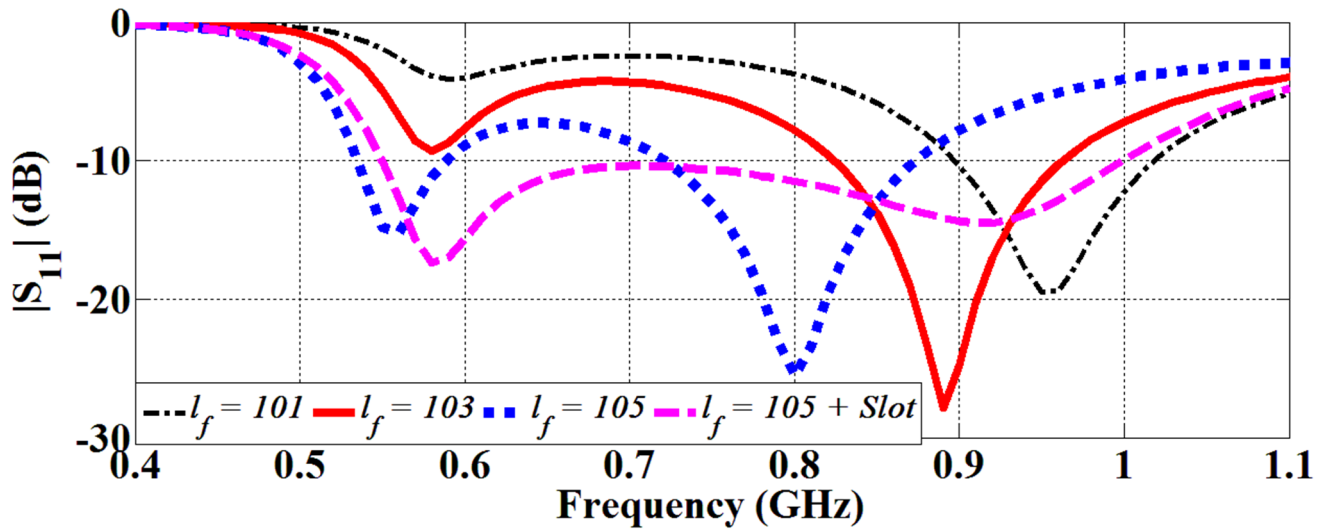
### 3.3.3 Bandwidth Enhancement

When the microstrip line crosses the slot structure, it excites a slot mode through coupling capacitances, which can be used to tune the impedance matching of the antenna [76]. In planar structures, the value of the capacitance varies using two main parameters of the feeder; its length and distance from the edge of the substrate [76]-[81]. As can be realized from Fig. 3.18 (a), the length of the microstrip line,  $l_f$ , mainly defines the second resonance of the antenna. This length is roughly a quarter wavelength at that second resonance. However, due to the fact that in the proposed design, side 2 is located in the vicinity of side 1 to achieve a compact size, an extra capacitive and inductive reactance is imposed on the input impedance.

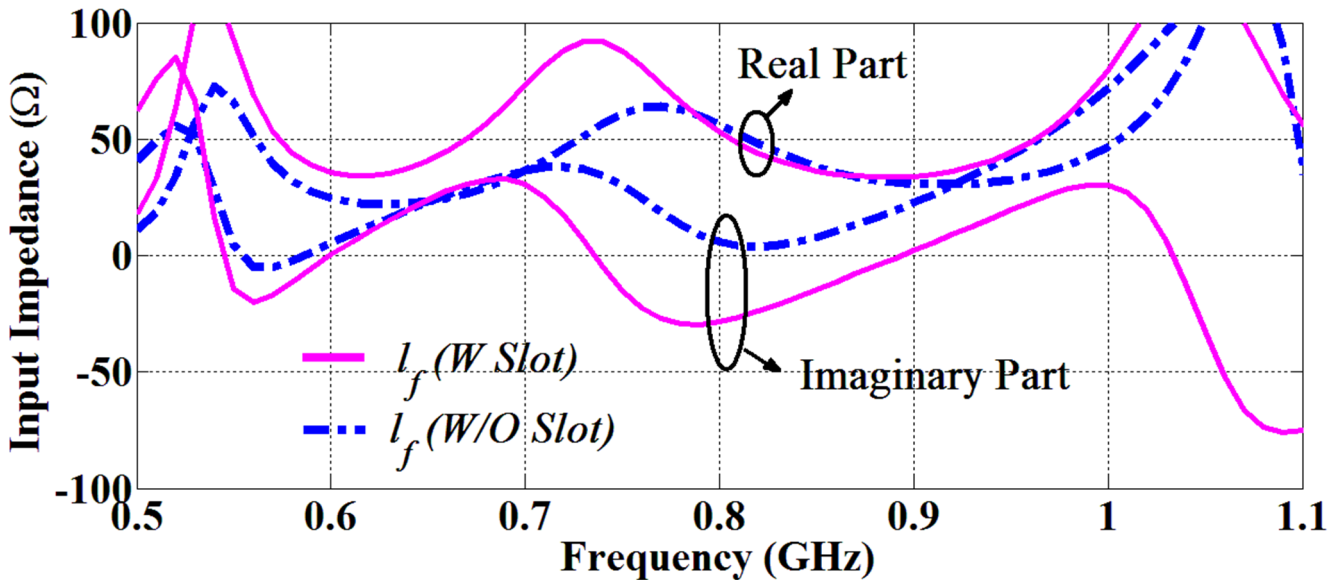
To improve the impedance matching of the antenna, a rectangle shaped slot with dimensions  $w_{fs} \times l_{fs}$  is created in the feeding structure. Effects of the slot's dimensions on the input impedance are summarized in Table 3-II. Fig. 3.18 (a) and (b) show the significant improvement in the input impedance matching of the antenna by the creation of the slot. The high resonance of the antenna,  $f_h$ , can be predicted using by:

$$f_h = c / [2(l_f \sqrt{\epsilon_{eff}})] \quad (4)$$

Effects of the rest of the parameters of the antenna on the resonant frequencies and bandwidth are summarized in Table 3-I for brevity. The optimum design achieves a compact dimension of  $0.24 \lambda_0 \times 0.09 \lambda_0 \times 0.04 \lambda_0$ , which is over 17 % and 50 % smaller than the antennas presented in [82], [83] on x-y and y-z planes, respectively. Also, compared to the most recent 3-D antenna covering similar bandwidth [84], the current design occupies 56 % and 12.5 % less area on x-z and x-y planes, correspondingly.



(a)



(b)

Fig. 3.18. (a)  $|S_{11}|$  of the proposed antenna with different values of  $l_f$  and (b) input impedance of the antenna with and without slot on the feeding line.

Table 3-II: Effects of different parameters on the resonances and bandwidth (—: small or no effect)

	$d_s \uparrow$	$d_f \downarrow$	$w_{sf}$	$l_{sf}$	$l_{s2}$	$l_{s3}$
			$\uparrow$	$\uparrow$	$\uparrow$	$\uparrow$
$f_i$	—	—	—	—	$\downarrow$	$\downarrow$
$f_h$	—	$\uparrow$	$\uparrow$	$\uparrow$	—	—
$BW$	$\uparrow$	$\uparrow$	$\uparrow$	$\uparrow$	$\uparrow$	$\uparrow$

### 3.3.4 Performance of the Antenna

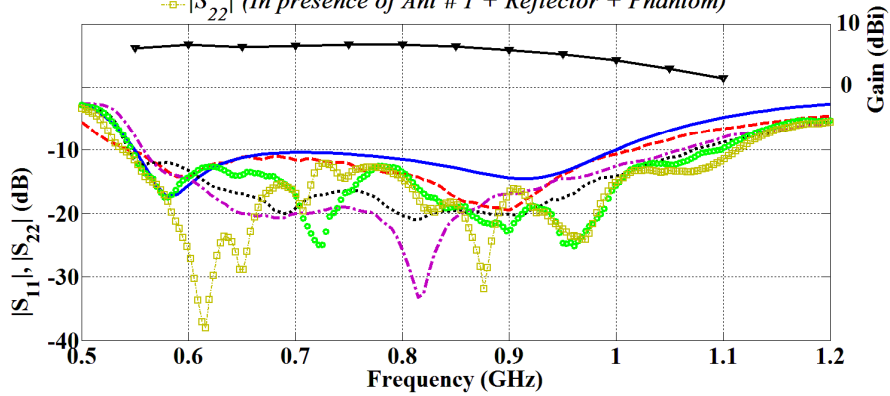
Two prototypes of the designed antenna were fabricated and tested. As shown in Fig. 3.19 (a), there is a good agreement between measured and simulated results in free space. The two antennas were then placed on a foam-based holder ( $\epsilon_r = 1$ ) and attached to platform using a plastic clips. The separation distance between the antennas was 70 mm. A  $50 \times 50 \text{ cm}^2$  metal sheet (reflector) is located at a quarter wavelength distance behind the antennas to reduce the effects of the surrounding environment on the detection results. Antennas' performances were also measured on the platform as well as in the vicinity of the phantom (Fig. 3.19). The two antennas maintain their wide bandwidths in all investigated cases. It is worth mentioning that unlike the antennas designed for communication purposes such as wireless body area networking, which are optimized to maintain their -10 dB for  $|S_{11}|$  in the vicinity of human body, in medical diagnostic systems, the differences in the scattering parameters are the source of data for diagnosis. Hence, variations in  $|S_{11}|$  and  $|S_{22}|$  of the two antennas with respect to free-space values are the key to getting a useful image of the target (torso in this work) using proper signal processing techniques.

As depicted in Fig. 3.19 (c) and (d), the proposed antenna has omnidirectional and donut shaped radiation patterns on y-z and x-y planes, respectively. However, the location of the reflector cancels the antennas' back reflections in  $-y$  direction. With the presence of a large reflector, the antenna achieves a peak measured gain of 7 dBi. The gain and radiation patterns were measured in the presence of the second antenna.

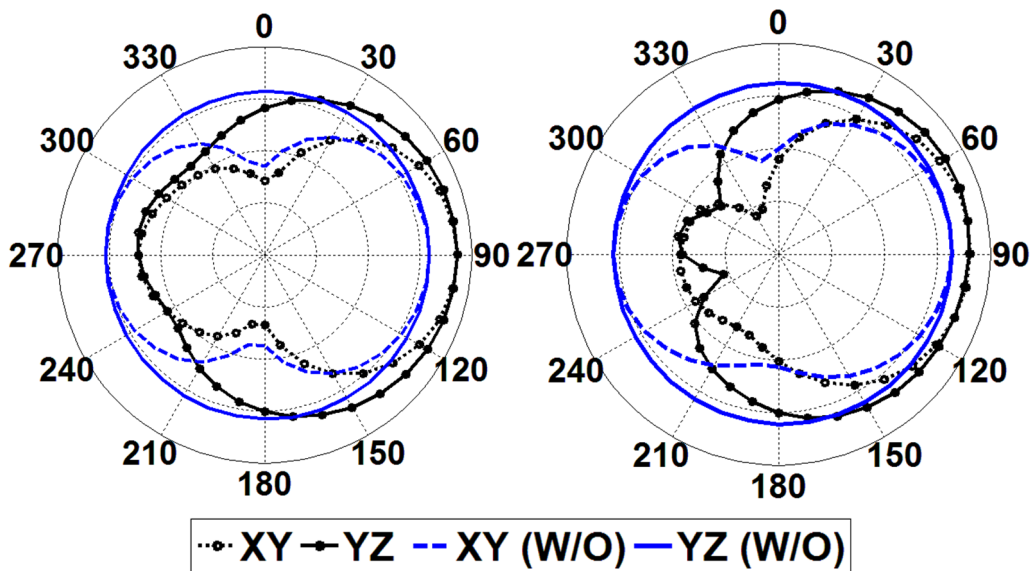


(a)

$\blacktriangleright$  Gain (Mea.)  $- - |S_{11}|$  Free Space (Mea.)  $- |S_{11}|$  Free Space (Sim.)  
 $\dots |S_{11}|$  (In presence of Ant # 2 + Reflector)  $- - |S_{22}|$  (In presence of Ant # 1 + Reflector)  
 $\bullet |S_{11}|$  (In presence of Ant # 2 + Reflector + Phantom)  
 $\square |S_{22}|$  (In presence of Ant # 1 + Reflector + Phantom)



(b)



(c)

(d)

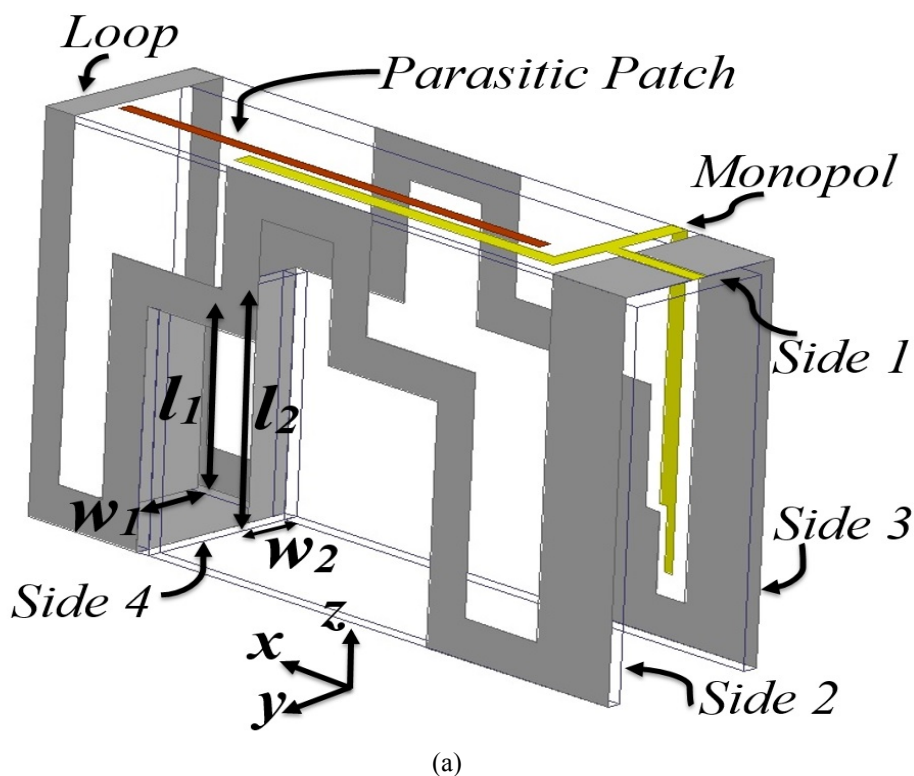
Fig. 3.19. (a) Fabricated antennas. (b)  $|S_{11}|$  and  $|S_{22}|$  in the presence of another antenna, reflector and phantom, (c) and (d) measured radiation patterns with and without (W/O) reflector at 580 MHz and 920 MHz, respectively. (Scale: -40 dB, division: 10 dB).

### 3.4 Three Dimensional Meandered Loop Antenna

The idea of utilizing antennas on both sides can be expanded to the use of multiple antennas on each side of the torso, and the size of the antennas on the rear side of the torso, e.g. x-y plane, defines the maximum number of usable antennas at the constrained area of the torso. Nevertheless, considering the structure of proposed 3-D antennas reveals that the main size reduction occurs only in the x-z and y-z planes. The previously utilized 3-D miniaturization techniques are not effective on the main radiating plane (x-y), which defines the number of antennas to be used to scan the torso, mainly due to the fact that locating the radiating plates in close proximity to each other disturbs the high current concentration areas on the feeding line and the ground plane resulting in the formation of a large capacitive/inductive reactance in the input impedance that makes the impedance matching an extremely challenging task. To overcome the above stated problems, a series of approaches are suggested in this part to propose a more compact antenna.

#### 3.4.1 Antenna Design

The proposed structure, which is depicted in Fig. 3.20 is designed on four FR4 substrates with 1.6 mm thicknesses that have a relative permittivity of 4.4 and loss tangent of 0.02. The printed substrates



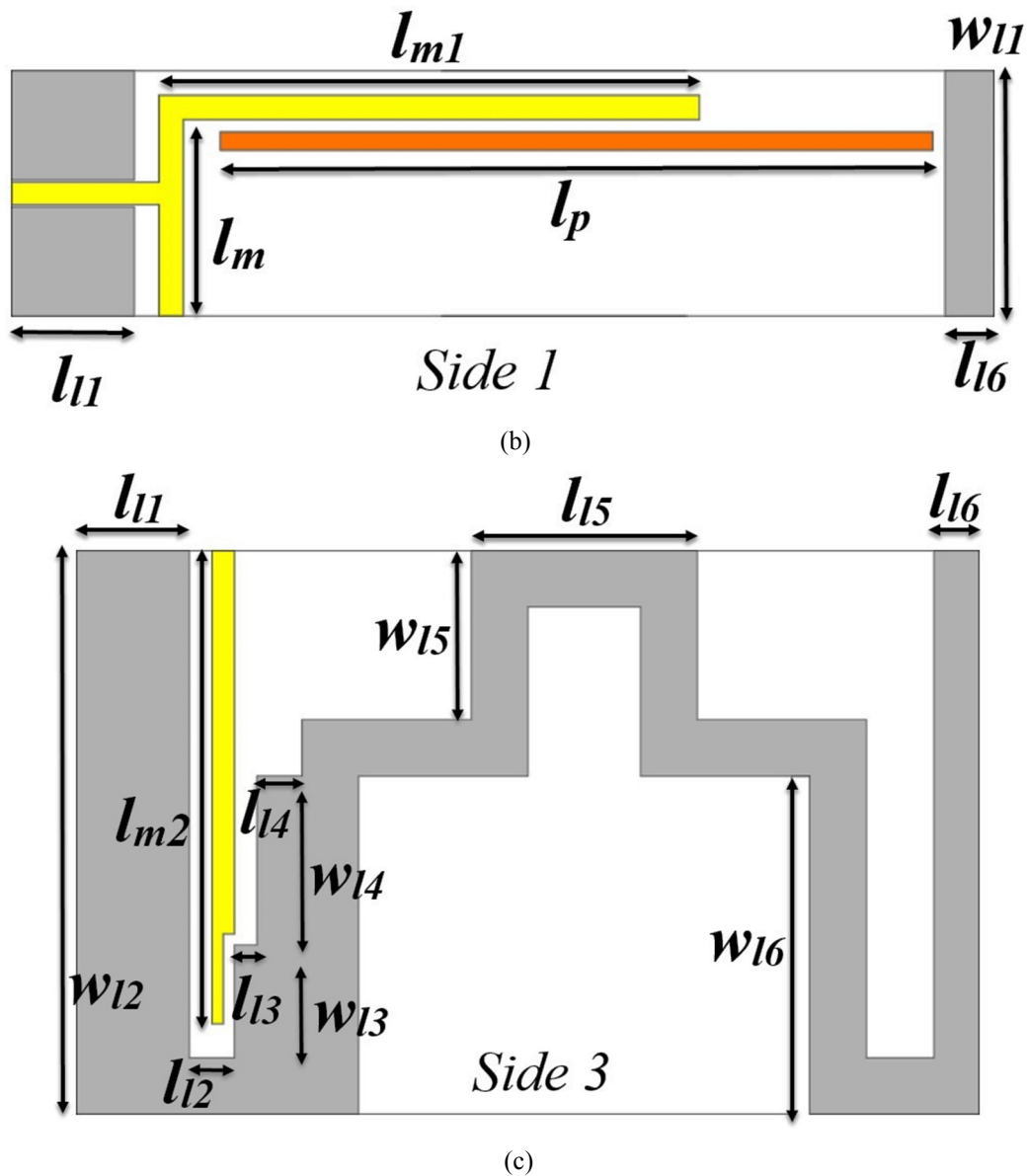
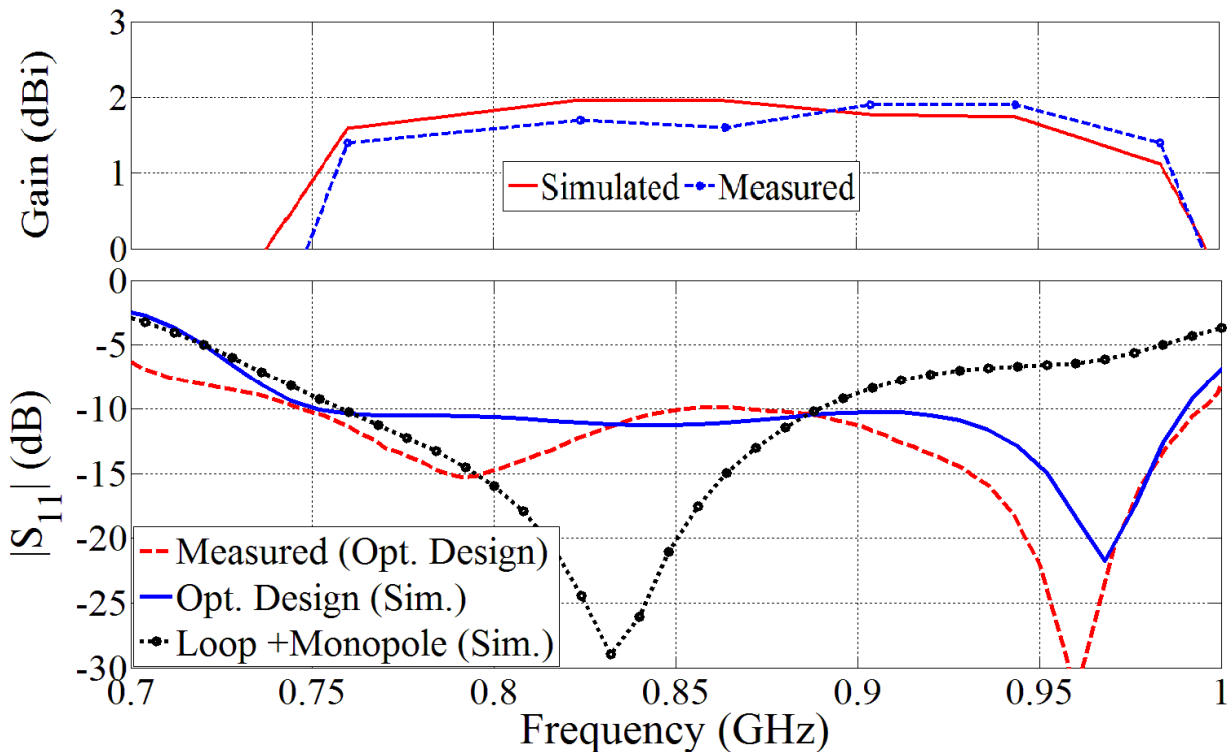


Fig. 3.20. Geometry details of the optimum design in a (a) 3-D configuration, (b) top view (Side 1) and (c) right side view (Side 3).

are connected together to form a three-dimensional structure with the help of solder and copper tape from the outer side of the structure. The antenna is comprised of a meandered loop and an L-shaped monopole antenna in addition to a parasitic patch. The length of a conventional loop is proportional to one wavelength at the resonant frequency. However, to compensate for the intense coupling between the two vertical sides of the design that causes a shift in the resonance to higher frequencies [64], the perimeter of the loop is selected as one wavelength at the low frequency of 0.6 GHz, which is lower than the targeted low frequency of around 0.7 GHz. To accommodate such a large perimeter in a confined structure, a meandering technique is utilized [85]. Besides, two rectangles with dimensions of  $w_1 \times l_1$  and  $w_2 \times l_2$  that are printed on the same substrate with similar thickness are connected to the top portion of the loop structure to alleviate the high capacitive reactance of the input

impedance. The top portions of the sides 2 and 3 are connected to each other using a rectangle patch with dimensions of  $w_{II} \times l_{II}$  to alter the surface current circulation and consequently improve the directivity.

Similar to previous designs, to compensate for the narrow operating bandwidth of the loop structure, an L-shaped monopole element is used to feed the whole structure. The monopole is fed using a CPW line with a length of 12 mm and width of 1.8 mm, which is separated by a gap of 0.2 mm from the loop structure for a  $50 \Omega$  port impedance. The lengths of the monopole ( $l_m + l_{m1} + l_{m2}$ ) is selected as about quarter wavelength at about the center frequency, which is around 850 MHz assuming a band from 700 MHz to 1000 MHz. As depicted in Fig. 3.21 (a), the latter modification expands the 10 dB return loss of the antenna to 760 – 880 MHz. The staircase structure on the monopole and loop antenna at side 3 is used for impedance transformation and tuning purposes [86]. To fulfill the band requirements of a lung fluid detection system, a half wavelength resonating parasitic strip at the upper frequency of 1000 MHz, with 1.5 mm width and length of  $l_p$ , is located at a distance of 1.5 mm from the monopole structure. As a result of proximity coupling, the parasitic patch resonates at 960 MHz, which is slightly less than the targeted value of 1000 MHz, and increases the operating bandwidth of the antenna to 750 – 985 MHz, which is proportional to fractional bandwidth of 27 % as verified by measured results. From the same plot, it can be realized that the antenna has a moderate peak gain of 1.9 dBi in +z direction. It should be noted that the moderate gain of the antenna is the best outcome of the highly miniaturized antenna size.



(a)

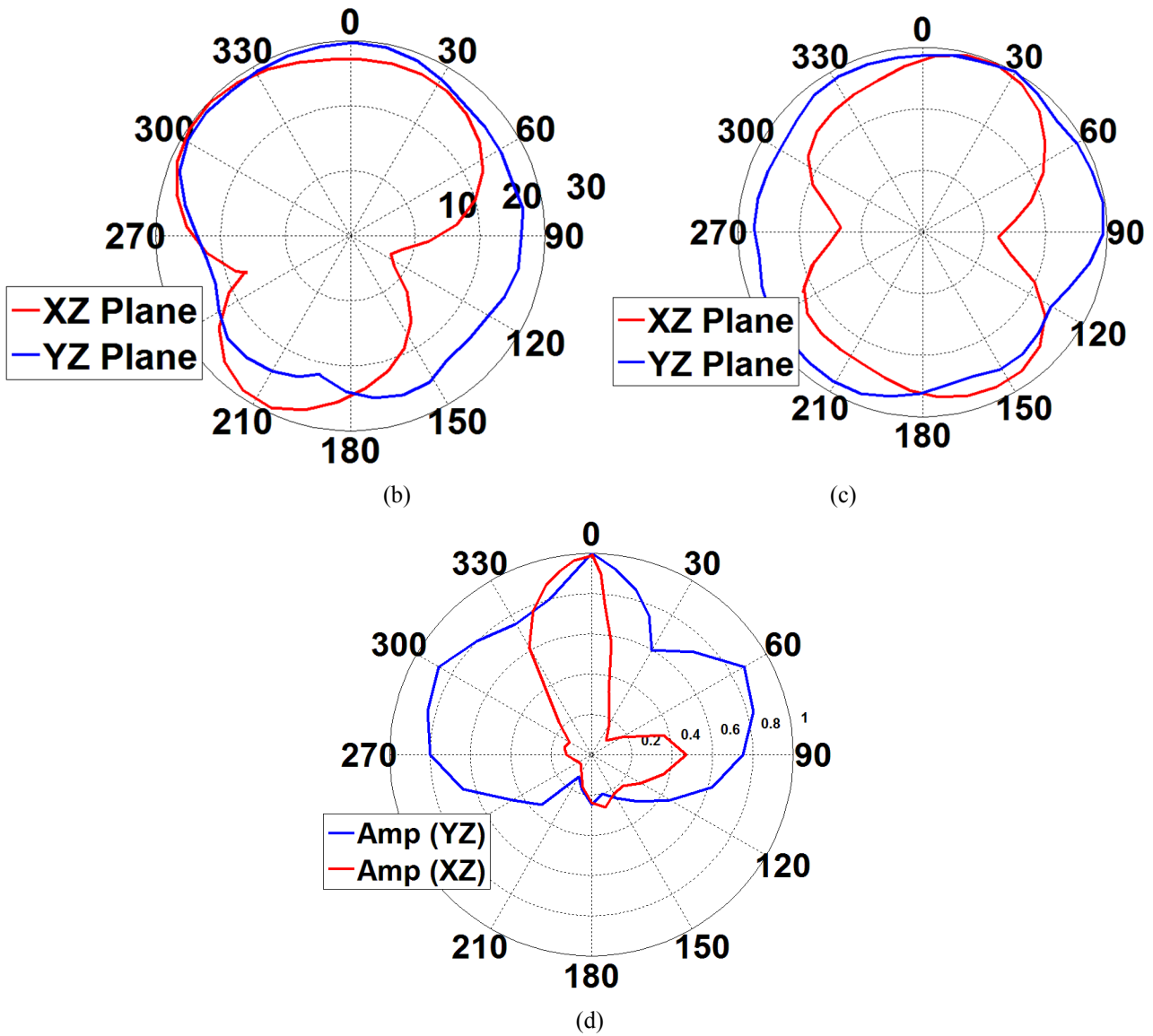


Fig. 3.21 (a) Simulated and measured  $|S_{11}|$  performance and gain of the optimum design and  $|S_{11}|$  performance of the antenna during the evolution process. Far-field radiation pattern of the optimum antenna at (b) 800 MHz and (c) 950 MHz. (d) Normalized time domain near-field of the antenna across the operating bandwidth.

### 3.4.2 Further Discussion

One of the main requirements of the antenna to be used in fluid detection is a unidirectional radiation, i.e. in the forward direction or  $+z$  in this case. In the proposed structure, a unidirectional radiation is achieved by the 3-D structure of the loop antenna. As depicted in Fig. 3.21 (b) and (c), the measured far field radiation patterns of the antenna at the two sample frequencies of 800 MHz and 950 MHz reveals that the antenna has a unidirectional radiation pattern with a reasonable average front to back ratio of 4 dB in the far-field measurements that is considered satisfactory for medical imaging applications [87]. The obtained directivity is the result of phase variations of the antenna's surface currents, which tend to cancel each other at the center of the structure when it is folded [88].

Due to the fact that in the proposed system, the antenna operates at a short distance from the human torso, the near field radiation of the antenna was calculated using the time domain solver of CST microwave studio software. The amplitudes of the fields are calculated using 30 co-polarized electric field probes that are located around the perimeter of the antenna with 12 degree intervals in x-z and y-z planes at a distance of 2 cm with respect to the antenna's surface. The obtained results are depicted in Fig. 3.21 (d). The higher value of the field in the y-z plane of the main lobe of the pattern is due to the fact that the probes are in immediate proximity to the radiating elements on sides 2 and 3, and therefore receive higher values compared to the x-z plane ones. Nevertheless, the calculated time domain front to back ratio of the fields show a value of 4:1 confirming the directive performance of the antenna across its operating band [89]. Additionally, as the antenna is intended to be used in human trials, the specific absorption rate (SAR) in a human body using this antenna was calculated using the simulator HFSS. The antenna was located at a distance of 2 cm from a numerical three-dimensional torso model with 2 mm resolution. As is general practice, the SAR value was calculated on 10 grams of tissue. Using the same microwave power level of the suggested system, i.e. 1 mW (0 dBm), the calculated SAR value was found to be 0.03 (W/Kg), which is well below the specified safe limit for medical applications [90]. With the optimum values presented in Table 3-III, the proposed antenna achieves a compact size of  $0.05 \lambda \times 0.2 \lambda \times 0.12 \lambda$  (where  $\lambda$  is the wavelength at the lowest operating frequency band), which is around half the size of the most compact antennas designed to operate at the same bandwidth on x-y plane [86],[89].

Table 3-III: Geometrical details in (mm) of the optimum design.

$l_1$	$w_1$	$l_m$	$l_{m2}$	$l_{l1}$	$l_{l3}$	$l_{l5}$	$w_{l1}$	$w_{l3}$	$w_{l6}$	$l_2$	$w_2$	$l_{m1}$	$l_p$	$l_{l2}$	$l_{l4}$	$l_{l6}$	$w_{l2}$	$w_{l4}$	$w_{l6}$
8	24	16	42	10	2	20	20	10	15	30	5	44	58	4	4	4	50	15	30

### 3.5 Cubic Composite Loop-Monopole Antenna

In an attempt to realize various configurations for the fluid detection platforms, the idea of using a cubic structure is emerged. The main advantage that is intended to be attained using a compact cubic design is the further increasing of the physical isolation between the antennas at adjacent positions and close proximities, e.g. left and right side lungs.

As mentioned before, one of the prevalent methods in decreasing the size of the antennas is to use three dimensional (3D) structures. This is different from the folding techniques that has been utilized in previous sections. In these configurations, the antenna design is conceptualized to be

accommodated on a 3-D structure rather than folding it from certain positions. However, despite the miniaturization capabilities of existing 3-D antennas, they have narrow bandwidths [64]-[65]. This effect comes from the fact that reducing the size of an antenna with largest dimension of  $a$ , its Q-factor, which is inversely proportional to  $(ka)^3$  (where  $k$  is the wave number), increases and thus, its impedance matching bandwidth reduces according to  $1/Q$  [91]. Therefore, to overcome the present limitations on the size of the antenna, *Chu limit* [92] and efficiency of the antenna (*Wheeler method*) [93], and hence, enhance the impedance matching of the design while maintaining its compact size, three different elements are deployed in the suggested design.

### 3.5.1 Antenna Design

The proposed three dimensional antenna is depicted in Fig. 3.22. It consists of four sides that are united in a square cube arrangement. One side of the antenna is printed on a square RO4003 substrate with thickness of 0.8 mm, whereas the other sides are designed as suspended structures that are made of copper connected to the printed side. To meet the optimum frequency range defined for torso imaging the antenna is designed using three different sets of loop, monopole and parasitic patch structures. The wide operating bandwidth of the antenna is obtained by merging the resonances of these elements. This can be clearly seen from the HFSS simulated performance in Fig. 3.23.

The lowest resonance of the antenna is defined by the perimeter of the loop structure,  $L_l$ , which is roughly proportional to one wavelength at the lowest operating frequency of the antenna at 700 MHz. It should be noted that by increasing  $L_l$ , the resonance can be further lowered. However, considering a confined cubic structure, increasing  $L_l$  is proportional to decreasing  $l_d$  which in turn disturbs the current distribution on the loop and consequently causes an input impedance mismatch. The final dimension of  $L_l$  is calculated as a compromise between achieving the lowest required frequency and the smallest realizable 3-D structure. As it can be seen from Fig. 3.23 (a), the loop structure inherits a relatively narrow operating bandwidth. Hence, its bandwidth is enhanced by introducing a monopole structure with  $\lambda/8$  length ( $l_m$ ) with respect to the resonance at an adjacent frequency of 800 MHz. The monopole is fed by a coplanar waveguide (CPW) line with a length of  $l_f$  and width of  $w_f$  that is separated from the loop structure by a gap of  $g$  to maintain a  $50 \Omega$  input impedance. In that regard, the side pins of the Sub-Miniature version A (SMA) connector are connected to the loop structure, whereas the central pin is connected to the monopole. From Fig. 3.23(a), it can be seen that the latter modification shifts the main resonance frequency of the antenna down by 40 MHz to 740 MHz mainly due to the coupling between the loop and monopole structures. Yet, the fractional bandwidth increases from 6% (680 -725 MHz) to 12.9% (725-820 MHz).

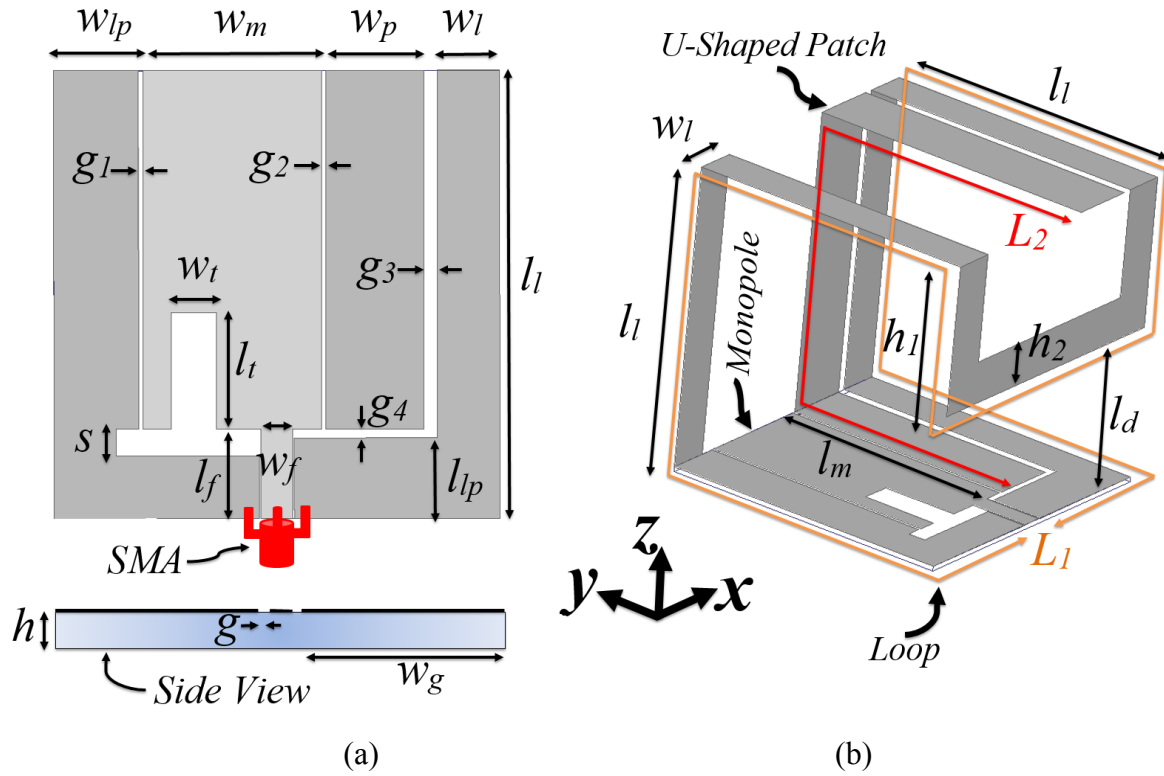
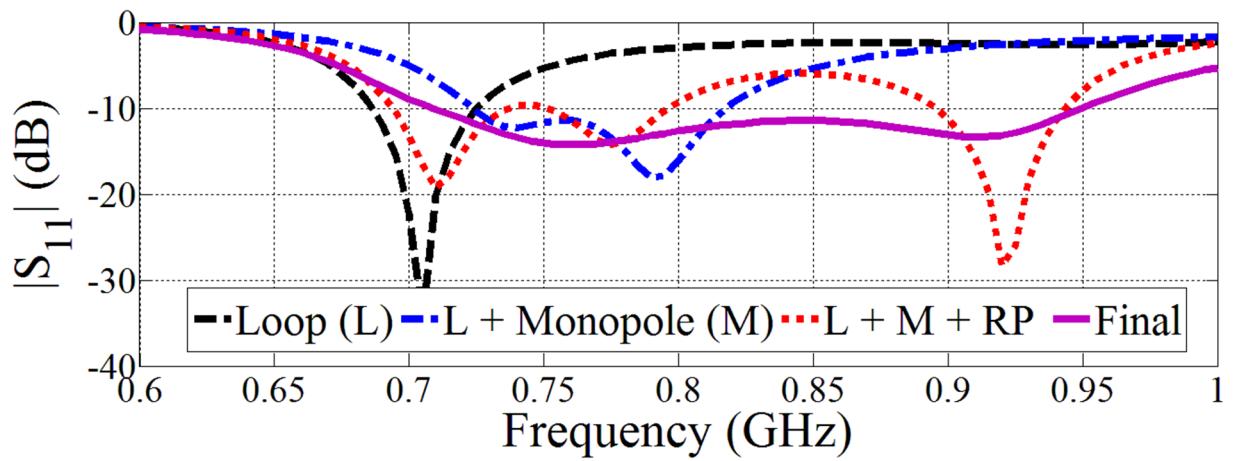


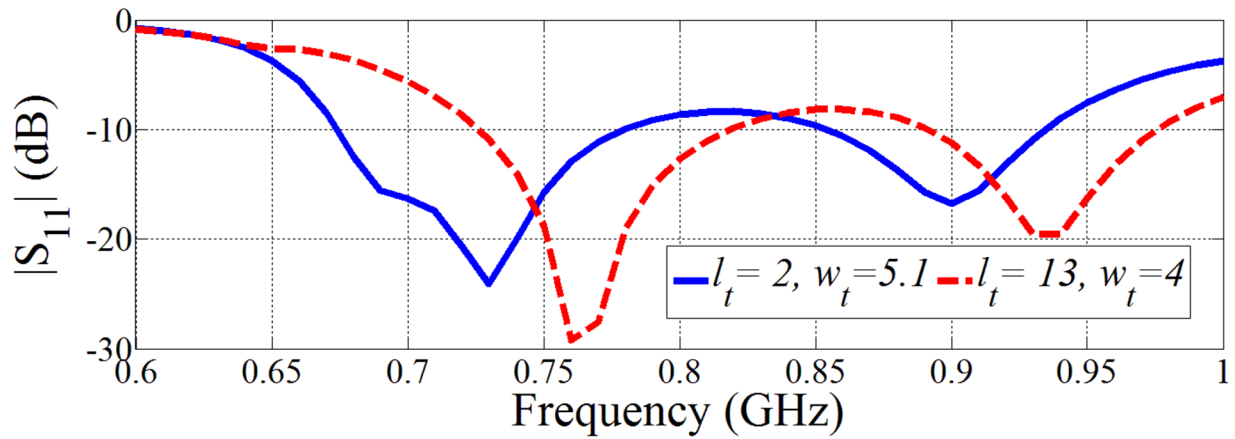
Fig. 3.22. Fig. 1. Detailed geometry of the antenna. (a) Printed layer and its side view, (b) 3-D view.  $l_f=10$ ,  $l_{lp}=7.28$ ,  $l_l=50$ ,  $l_t=12.9$ ,  $l_m=40$ ,  $w_t=5.25$ ,  $w_f=3.5$ ,  $w_g=23$ ,  $w_{lp}=9.5$ ,  $L_1=446$ ,  $w_m=20$ ,  $w_p=11$ ,  $w_l=7$ ,  $l_d=25$ ,  $L_2=140$ ,  $g=0.2$ ,  $g_1=0.5$ ,  $g_2=0.5$ ,  $g_3=1.5$ ,  $g_4=1$ ,  $s=3$ ,  $h=0.8$ ,  $h_1=25$ ,  $h_2=7$ . (Unit: mm)

However, the radar-based microwave imaging requires wider operating bandwidths for fine resolution. One of the most effective ways of increasing the operating bandwidth of the loop antenna is to load parasitic patches to its vicinity to excite new resonant frequencies [82]. But, due to the high capacitive/inductive coupling capacitance of the parasitic patch in a 3-D structure, it is not always a straight forward method and needs further considerations in terms of impedance matching. To that end, a half wavelength U-shaped parasitic patch ( $L_2 = l_m + 2l_l$ ) that is separated by  $g_2$  from the monopole and  $g_3$  from the loop structure and resonates at an adjacent frequency of 920 MHz is used. The main reason behind selecting close resonant frequencies is to keep the structure simple while broadening the bandwidth.

Ideally, decreasing the perimeter of the parasitic patch should result in wider impedance matching as it shifts the higher resonance without affecting the lower one. However, there is a limit where any additional decrease in  $L_2$  creates an undesired coupling between the monopole and loop and creates a mismatch at 800 – 900 MHz (See Fig. 3.23 (a)). This is basically due to the fact that the whole structure is mainly fed by a  $\lambda/8$  structure that is half a standard quarter wavelength monopole and consequently has high capacitive reactance [94]. Therefore, a short ended slot line with  $w_t \times l_t$  dimensions is carved from the monopole structure to improve the input impedance.



(a)



(b)

Fig. 3.23. (a)  $|S_{11}|$  of the antenna in different design steps (RP: Resonating U-shaped parasitic patch), and (b)  $|S_{11}|$  with size of the short-ended slot.

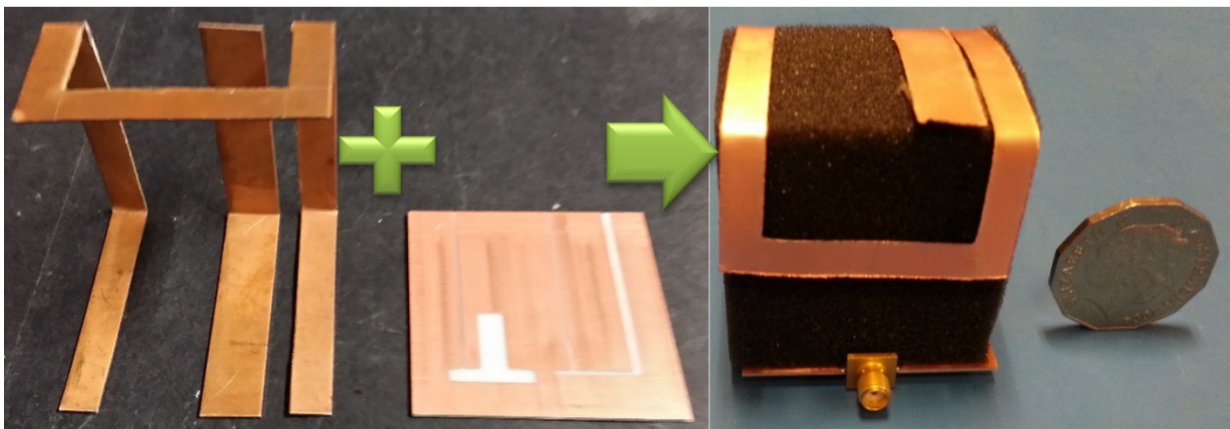
The effect of changing the dimensions of this parameter is depicted in Fig. 3.23 (b) in two extreme cases where width and lengths of the slot line are altered. With proper dimensions of the tuning slot line, the antenna achieves a wide fractional bandwidth of 29% at 710 – 950 MHz. The final antenna design has the compact dimension of  $0.11\lambda \times 0.11\lambda \times 0.11\lambda$  which is smaller by 50 % and 16 % of the area along x-y plane and the volume, respectively, than the most compact design operating at the same low microwave frequency.

### 3.5.2 Foam-Embedded Antenna Array

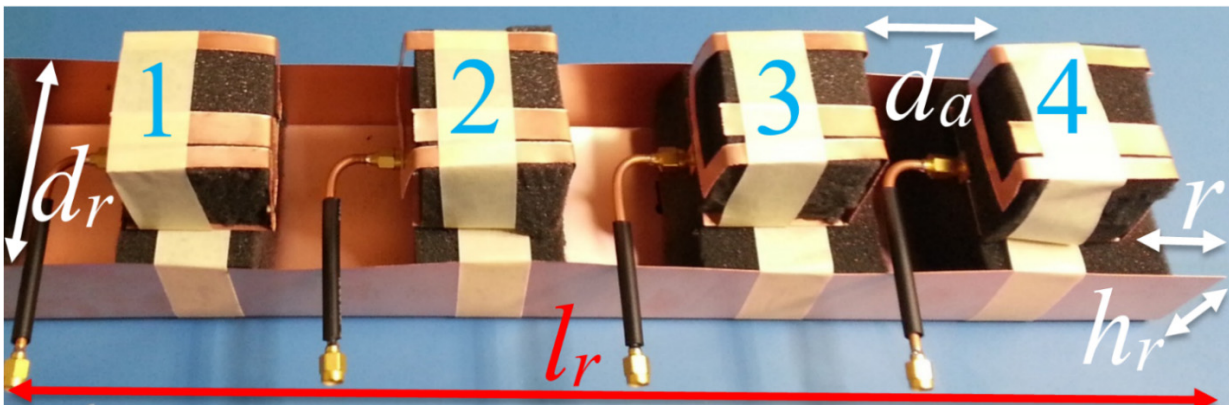
The main requirement in building portable medical diagnostic systems is to use simple and lightweight platforms. The majority of hardware constraints on system designs arise from the fact that present radar based microwave imaging systems are either in need of a large number of antennas [95], a moving platform [86], or a long scanning time [16]. To use smaller number of antennas without

sacrificing detection accuracy, multi-static and differential techniques can be utilized instead.

To that end, an array of four antenna elements with the fabricated sample element depicted in Fig. 3.24 (a), are considered for building the system. This number of elements is selected as a compromise between the number of deployable antennas in the limited space covering rear side of an average human torso and reasonably low mutual coupling between the antennas (See Fig. 3.24 (b)). To reduce the effect of surrounding environment on the detection process, a reflector is located at 5 cm distance behind the array. The shape and size of the reflector,  $h_r$  and  $d_r$ , were designed to maintain the compact size of the system and cancel the back radiation while minimizing its effect on the impedance matching of the antennas. The reflector has small effect on the reflection coefficient of the antennas (not shown for brevity), that is compensated mainly by the size of the slotted line  $w_r$  and  $l_r$ , on the monopole structure (final sizes presented in Fig. 3.22). As it can be seen from Fig. 3.24 (b), the antenna elements are located at a 75 mm distance with respect to each other and 45 mm distance from two ends of the reflector with a length of 515 mm. The antennas' feeding points are prolonged using coaxial extensions to facilitate the excitation of the system. It is noted that there is not a substantial manufacturing tolerance that is of significant impact on the performance of the antenna.



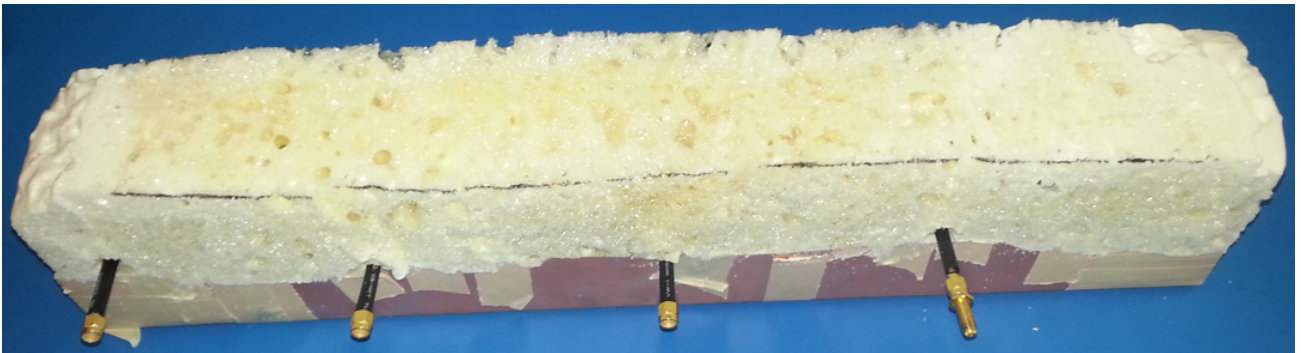
(a)



(b)



(c)



(d)

Fig. 3.24 Fabrication process of (a) single element, (b) array, (c) foam spraying and (d) final structure, ,  $h_r = 50$ ,  $d_r = 80$ ,  $d_a = 75$ ,  $r = 45$ ,  $l_r = 515$  (Unit: mm).

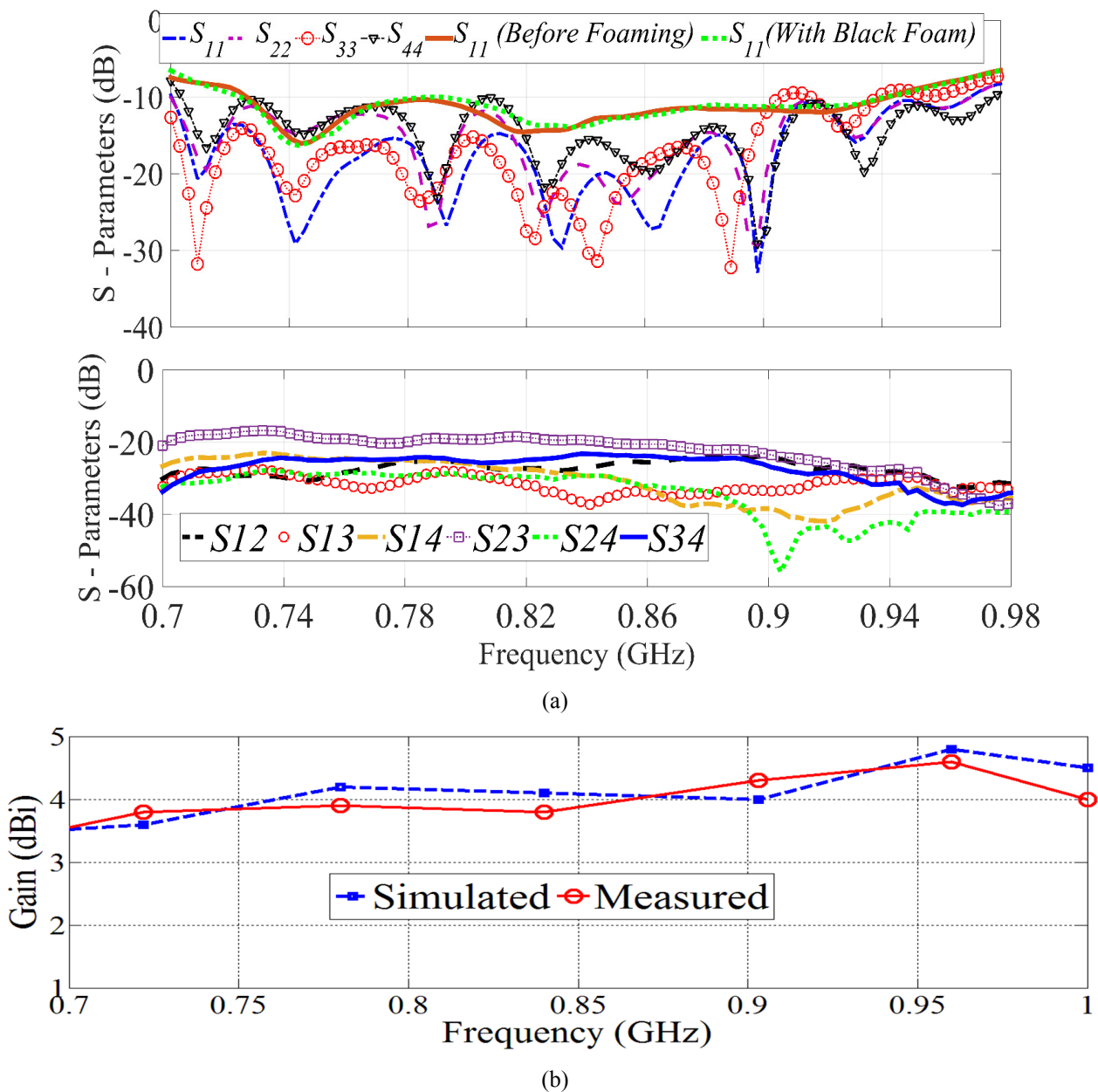
Radio frequency (RF) transparent foam (black color), which has minimal effect on the amplitude or phase of the electromagnetic wave, is used to support the antennas' structure as well as their positions on the reflector. As depicted in Fig. 3.24 (c), to facilitate the stability of the whole structure and achieve lightweight, the whole system is sprayed using a commercially available polyurethane based Sika Boom-AP expanding foam [96] and then is trimmed to form a rectangular shape (See Fig. 3.24(d)). This method is proposed as a simple approach that avoids utilizing a matching medium and fabricating heavy and bulky stands.

The performance of the antennas within the array is tested before and after foaming and the  $S$ -parameter of an arbitrary element,  $S_{11}$ , is depicted in Fig. 3.25 (a). As it can be seen, foaming strengthens the resonances due to the interaction between the injected foam and the antenna elements. The  $S$ -parameters of all antennas after foaming are also depicted in Fig. 3.25 (a). The difference between the performances of the antennas is due to the uneven density of the foam, effects of coaxial extensions and fabrication errors. Nevertheless, all of the antennas maintain their wide bandwidth with maximum 5 % shift at either ends of the operating band, and the mutual coupling between the antenna elements is more than 17 dB in all cases, which means that coupled signals are lower than

the expected reflections from any water content in the lungs.

The maximum gain and radiation patterns of each element are also simulated and measured and the obtained results for an arbitrary element are depicted in Fig. 3.25. As shown in Fig. 3.25 (b), each element of the array inside the foam achieves a modest gain between 3.5 and 4.5 dBi. The radiation patterns are measured in an anechoic chamber and the results for two sample frequencies of 750 MHz and 920 MHz are presented in Fig. 3.25 (c) and (d). As the antenna is not used here for on- or off-body communication, the patterns are presented only to confirm that the antenna radiates majority of its energy towards +z direction with an average front-to-back ratio of 8 dB. The observed discrepancies are due to the imperfect fabrication of the 3-D array and foaming process.

As the fabricated array is designed for medical application, the safety issue is to be verified. The obtained SAR value is 0.026 (W/Kg) which is much lower than IEEE safe limit.



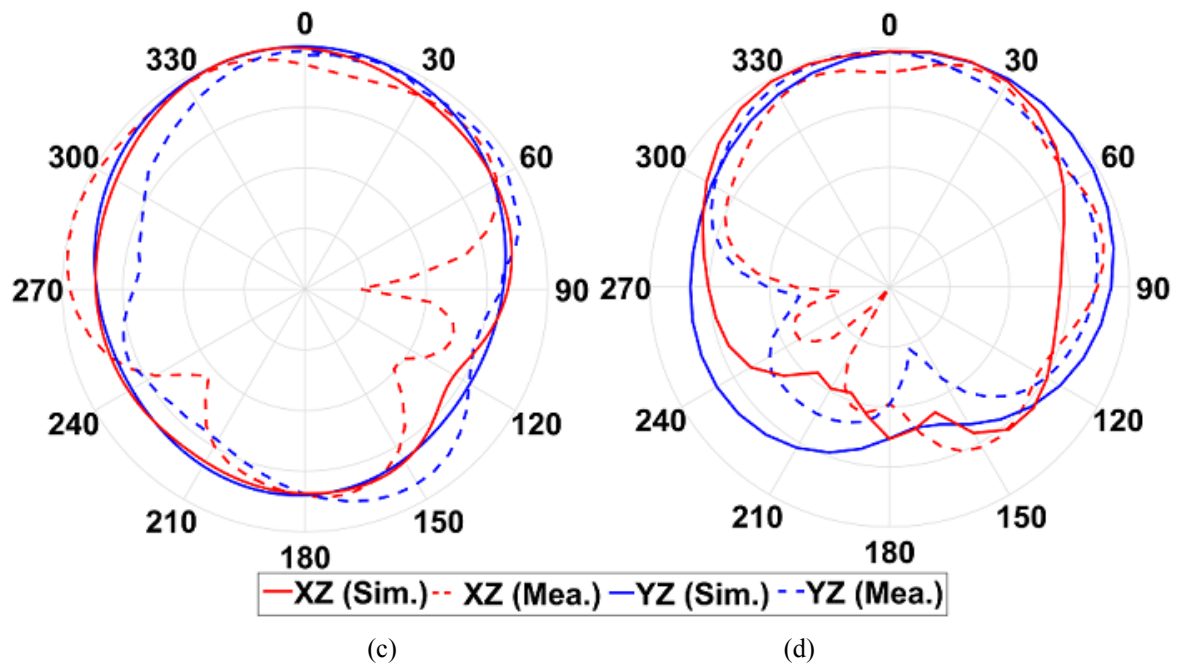


Fig. 3.25. Measured vs. simulated (a) S-parameters, (b) gain, and radiation patterns at (c) 750 MHz and (d) 920 MHz. (Scale: 40 dB, division: 10 dB).

### 3.6 Conclusion

Folding technique is introduced in this chapter and its ability in achieving most of the main requirements of an antenna for a torso imaging system that are compact size, wideband performance at the UHF band and unidirectional radiation is proven. Several antenna designs based on the folding technique were proposed as a proof of concept. It has also shown that designing an antenna using a 3-D configuration can also be a successful approach in reducing its profile such as height and occupied area. Several techniques, such as utilizing a combination of conventional techniques were proposed to overcome the narrow operating bandwidth of compact cubic antennas. It is noted that the proposed antennas are the smallest proposed wideband three dimensional antennas at the lower end of UHF band and their sizes would define the type of the configuration and detection algorithms that is going to be used for the imaging system.

# Chapter 4

## Antenna Designs

### Part II: Planar Structures

Considering different possible configurations for imaging systems that has been thoroughly investigated in chapter 3, it can be realized that while having excellent compact structures, 3-D antenna structures cannot be used in large numbers, e.g., when a circular platform is required. This is due to the fact that the side conductors that are utilized for building the structure participate in antenna radiation, and hence utilizing them in the vicinity of each other creates a great amount of mutual coupling that in turn alters the original operating band and radiation beam of the antenna. This is a great disadvantage considering the fact that increasing the number of antennas in a system that utilizes a proper signal processing technique improves the quality of the obtained image as a result of additional data received by the added antennas. On the other hand, considering their light weight, simple assembly and low fabrication cost, planar end-fire antennas are among the most suitable structures for microwave imaging applications. To achieve wideband performance for that type of antennas, several techniques were utilized, such as loop-dipole composites, magneto-electric dipoles and quasi-Yagi structures. However, those techniques in their conventional configurations result in relatively large electrical sizes of up to half wavelength with respect to the lowest operating frequency of the antenna that is not suitable for medical applications due to resultant large physical size at the UHF band.

To overcome the abovementioned issues, this chapter will be focusing on the introduction and novel utilization of three well-known techniques to miniaturize the size of the planar structures while attaining wide operating bandwidth and a moderate unidirectional radiation. These techniques are summarized as loop-dipole composite structure utilizing an offset broadside coupling feeding technique, capacitive loading of a loop antenna that utilizes a meandering technique for bandwidth enhancement rather than size reduction, and introduction of a unidirectional loop antenna by non-periodic loading of mu-negative metamaterial unit-cells. Similar to the previous chapter, the band of interest for the antenna design for fluid accumulation detection purposes is 0.5-1 GHz.

## 4.1 Loop-Dipole Composite Antenna

As the first attempt to realize a compact planar structure, the theory of loop-dipole composite structures is introduced and the proposed design is presented in this section.

### 4.1.1 Introduction

Magneto-electric dipole and loop-dipole composite antennas have been studied widely due to their unidirectional radiation. The performance of that type of antennas is a result of combining the radiation of electric and magnetic dipoles [97]-[102]. The main challenges in designing those antennas are their feeding structure and how to realize an effective magnetic dipole. The most utilized feeding technique consists of the differential [97], vertical meandered polygon-shaped probe [98] and coaxial feeding [99]. Also, several modifications on an electric dipole, such as using a vertical straight [97], meandered patches [98], [101]-[102], or substrate integrated patches [99], are utilized for the realization of a magnetic dipole. Despite the excellent impedance matching or unidirectional radiation achieved by the aforementioned designs, there are still several major obstacles in applying them for practical portable wireless applications. Those obstacles include using bulky three-dimensional (3-D) structures [103],[104],[105], [98], large planar dimensions [106]-[108], having narrow operational bandwidth [102], complicated fabrication process [97]-[100] or unstable gain [101], [42].

### 4.1.2 Theory

The loop-dipole antenna, like magneto-electric dipole antenna, operates based on the theory of complementary antenna feeding proposed by Chlavin in 1954 [42]. According to that theory, if a magnetic and an electric dipole are excited at the same time with equal amplitude and phase, identical E-plane and H-plane radiations are achievable [97]. Moreover, the combined radiation has a cardiac shape with suppressed back radiation. This can be easily understood from Fig. 4.1[100], where the 8-shaped radiation pattern of the electric dipole and the O-shaped pattern of the magnetic dipole at E-plane are combined. The loop structure does not have the perfect omnidirectional radiation of the magnetic dipole, but it does have a quasi-omnidirectional radiation across wider band. Thus, the design in this section presents a composite loop-dipole antenna for stable wideband radiation.

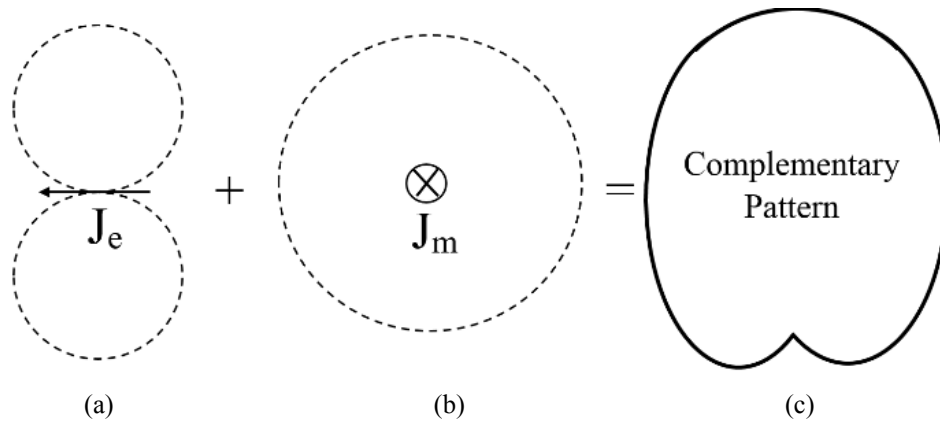


Fig. 4.1 Radiation pattern of (a) electric dipole ( $J_e$ ), (b) magnetic dipole ( $J_m$ ) and (c) complementary antenna on E-plane.

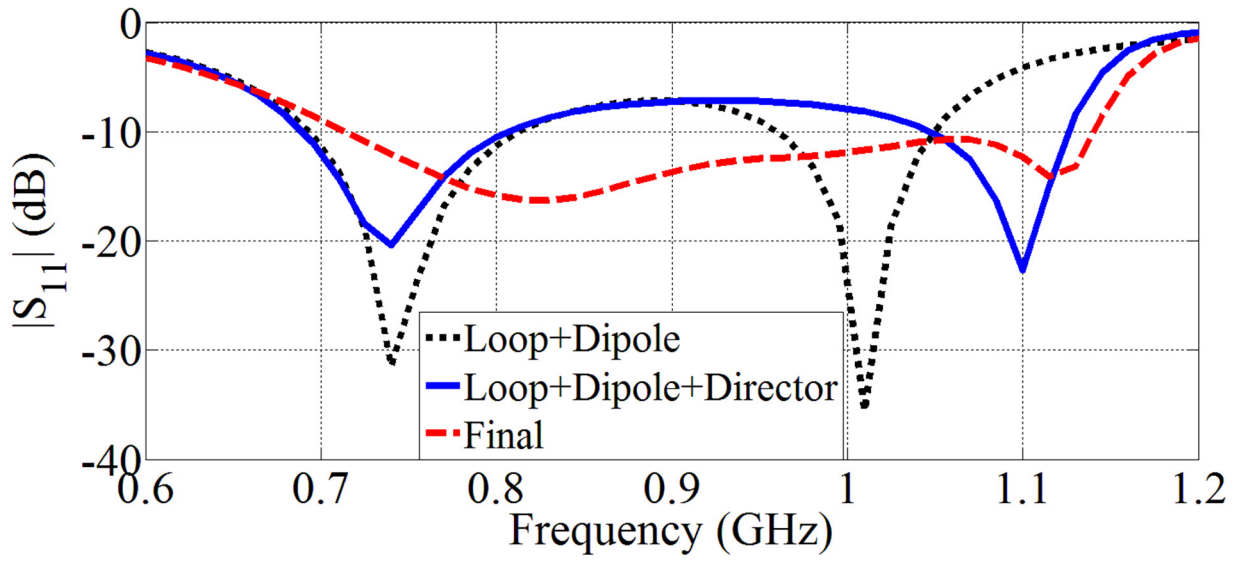
### 4.1.2 Antenna Design

The geometry of the proposed design is presented in Fig. 4.2. The antenna is comprised of a dipole, which operates at its half wavelength,  $f_{dipole} = \lambda/2 = 2(l_{d2} + l_{d1})$ , at the top layer of the substrate, and a loop that resonates at one-wavelength,  $f_{loop} = \lambda = 4l$ , and a nearby parasitic strip (director) that operates at quarter wavelength,  $f_{patch} = \lambda/4 = L$ , at the bottom layer.  $\lambda$  is the wavelength at the desired design resonance frequency. The optimum values for these parameters are obtained using parametric simulations in HFSS. The utilized substrate is a square epoxy FR4 (0.8 mm thickness, dielectric constant of 4.4, and loss tangent of 0.02). The antenna is fed using a coaxial cable that is connected to the two arms of the dipole. To utilize a wide operating bandwidth and control the radiation of the antenna elements individually, the loop is fed through its coupling with the dipole. The intended operating frequency of the antenna is selected to cover the UHF band (0.7-1.2 GHz), which is also the assigned band for industrial, scientific and medical (ISM) applications.

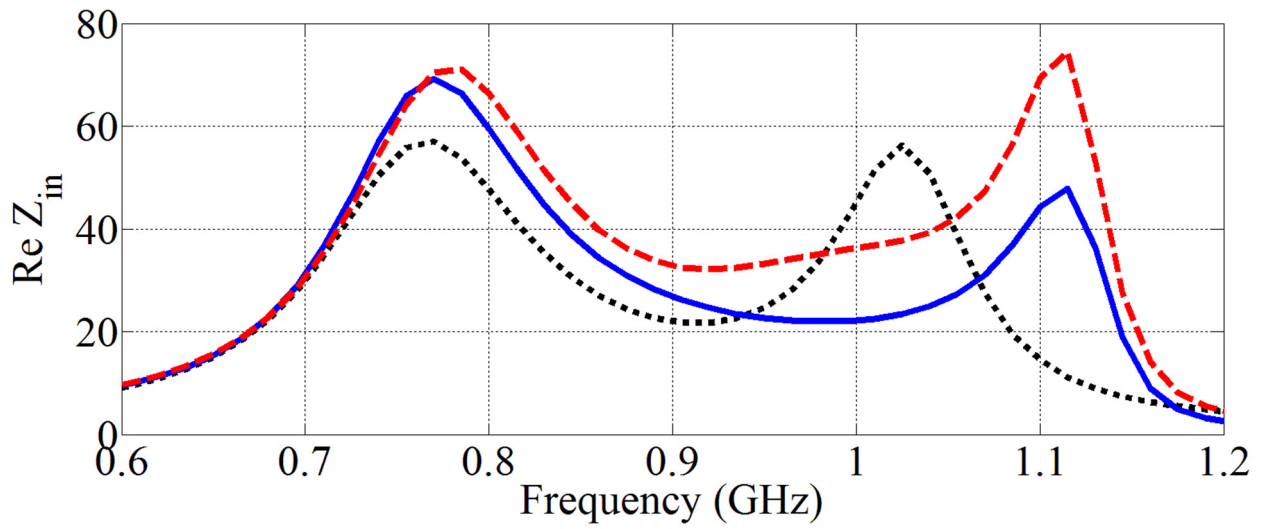
### 4.1.3 Performance Analysis

The reflection-coefficient as well as real and imaginary parts of the input impedance of the antenna throughout the evolution process, which are simulated using HFSS, are depicted in Fig. 4.3(a)-(c). As can be seen, two main resonances are excited by the dipole and loop resulting in a dual-band performance centered at 0.74 GHz and 1.02 GHz, respectively. To keep the size of the antenna as compact as possible, the dipole is folded by 90 degrees towards the center of the substrate from each side. To compensate for the negative effect of the folding on the amount of coupling, its length on x-direction ( $l_{d2}$ ) is selected to be longer than the standard half-wavelength dipole. Nevertheless, this increase in length does not increase the overall size of the structure. Then, the location of the loop is adjusted to obtain the desired resonances for the loop and dipole.

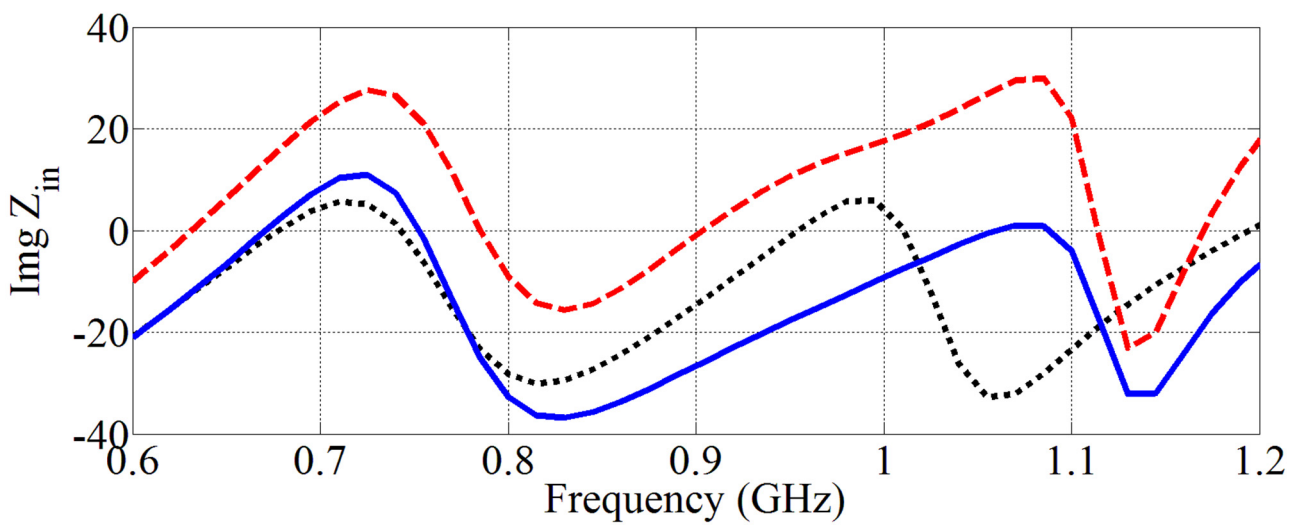




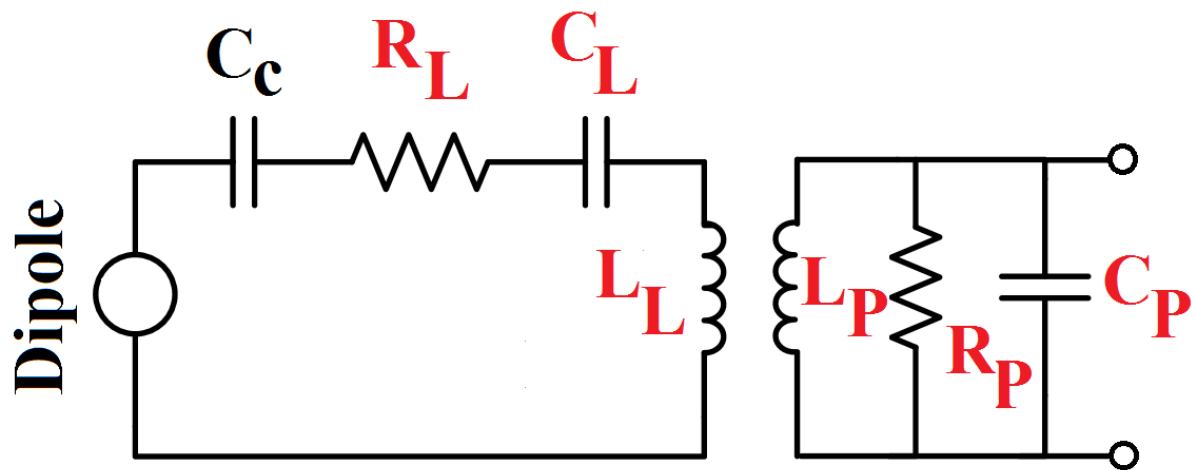
(a)



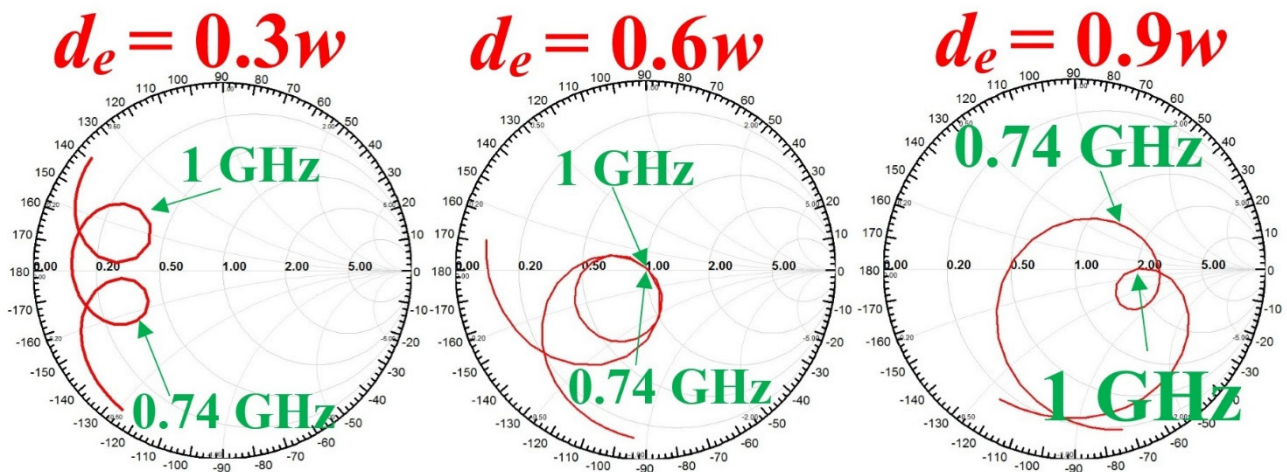
(b)



(c)



(d)



(e)

Fig. 4.3 (a)  $|S_{11}|$ , (b) real and (c) imaginary parts of the input impedance (identical legends) throughout the evolution process. (d) Equivalent circuit and (e) Smith chart variations for various positions of the loop.

Based on the theory of loop-dipole antennas, the complementary antenna radiates directionally when both of the electric and magnetic dipoles are simultaneously excited. To analyze the radiation characteristics of the proposed composite antenna, its radiation patterns are presented in two sample frequencies in Fig. 4.4. As can be seen, the antenna has low and moderate FBR values at 0.75 GHz and 1 GHz, respectively. The reason behind this behavior can be explained using the surface current distribution of the antenna shown in Fig. 4.5. By evaluating the current distribution at lower frequencies, e.g. 0.75 GHz, the majority of the strong currents, except for the coupling area with the loop, flow on the dipole (Fig. 4.5 (a)). Thus, the radiation pattern of the antenna is mainly determined by the dipole. However, at higher frequencies, e.g. 1 GHz, both of the loop and dipole antennas have strong currents. Considering the dipole's current nodes that are defined by the black circles in Fig. 4.5 (b), it can be seen that it operates at its higher mode, while the current distribution on the loop

operates at its main resonance. Thus, the resultant pattern is a combination of the loop-dipole modes [101], and a decent FBR value of 10 dB is attained. It should be noted that as the one-wavelength loop does not have perfect omnidirectional radiation in E-plane, the achieved E- and H-planes are not identical. The reason behind not using a small/smaller-loop as a proper magnetic dipole is its high reactance, which makes it extremely difficult to achieve wide operating bandwidth. Nevertheless, an acceptable FBR value is attainable in both of the aforementioned planes.

Apart from the antennas that use cavities or reflectors to provide unidirectional radiation, the abovementioned variations of the FBR at different frequencies is the main drawback of wideband planar loop-dipole composite antennas [101], [42]. This is due to the fact that loop-dipole mode occurs in narrow range of frequencies, and hence cannot be utilized across wide-band. Therefore, while achieving very large impedance bandwidth [42], the radiation characteristics are not consistent and thus gain variations up to 3-dB are experienced [100], which makes the design undesirable for applications that require a stable radiation across the operating band. To alleviate this inconsistency, a large ground plane is usually added to the antenna, but this solution increases the size of the antenna to around half-wavelength [42], which is not desired especially for systems operating at a low UHF band.

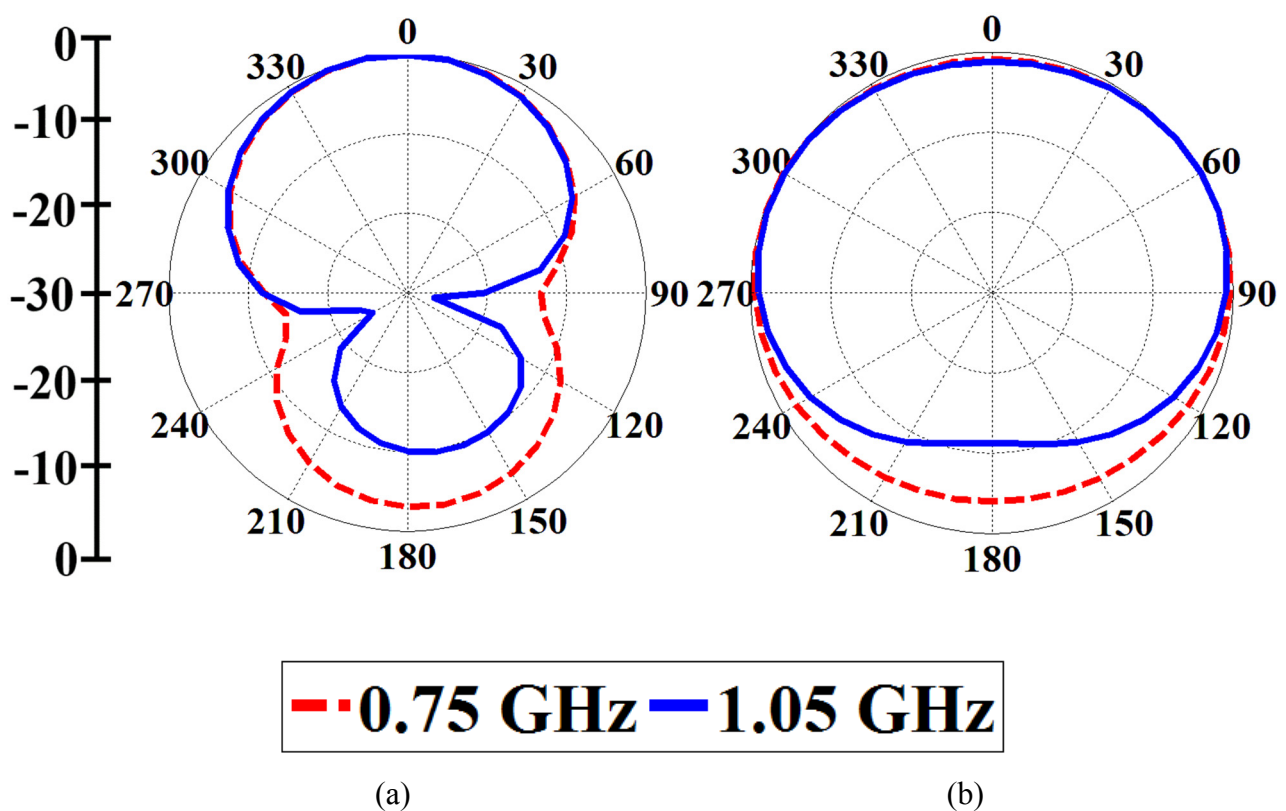


Fig.4.4 Radiation patterns of the antenna at (a) E-plane and (b) H-plane (maximum radiation is at x-direction) (Scale: dB).

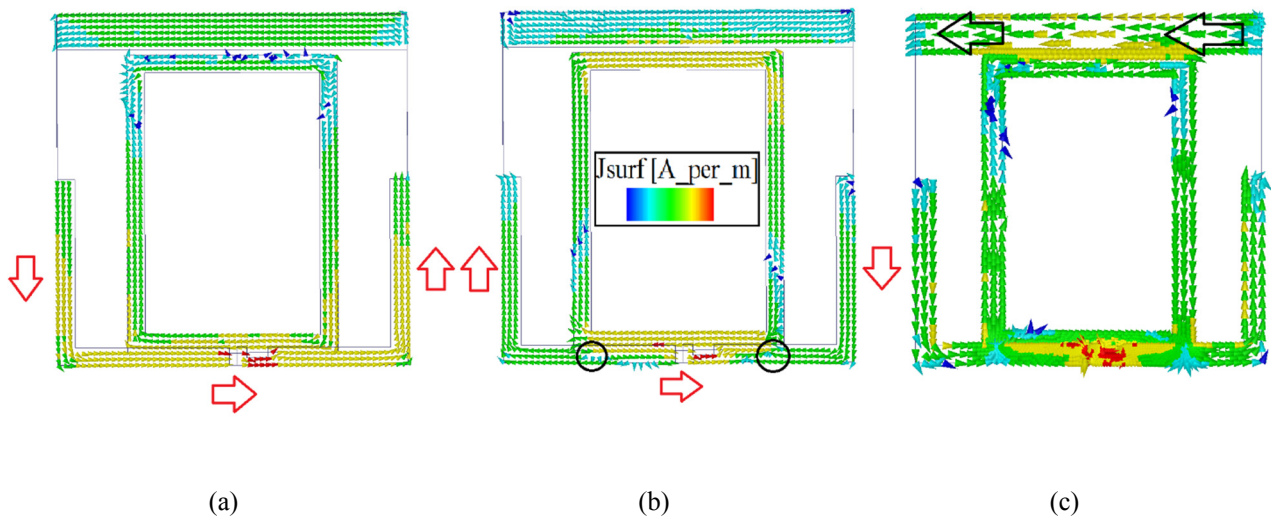


Fig. 4.5 Surface current distribution at (a) 0.75 GHz and (b) 1 GHz and (c) 1.2 GHz.

To solve the aforementioned problem, a configuration based on a conventional technique to increase the FBR of the antenna while keeping its size intact is utilized. To that end, a parasitic strip is added to the upper side of the antenna. The strip is located at less than quarter wavelength distance with respect to the lowest operating frequency from the dipole, and in the vicinity of the loop structure. Moreover, to increase the operating bandwidth of the antenna, a rectangular area is carved from the right arm of the dipole. This area, which acts as a short-ended slot line, is used to tune the resistance as well as capacitance/inductance of the input impedance. It thus helps to achieve a wide operating bandwidth covering 0.71-1.15 GHz (See Fig. 4.1(a)-(c)).

The radiation patterns of the antenna at three sample frequencies are depicted in Fig. 4.6. As can be seen, the addition of the director increases the FBR of the antenna to a great extent across the whole band. It should be noted that the nearby frequencies show similar radiation performance but are not depicted for brevity. By adding the director, the radiating mechanism of the antenna can be analyzed as a quasi-Yagi antenna at the lower and higher frequencies where the dipole and loop, respectively, operate as the driver, whereas the strip acts as the director. This can be realized from the radiation pattern which has a minimum FBR value of 11-dB at the low and high end of the band. The presented patterns indicate that the radiation from the loop-dipole mode is shifted towards central frequencies. This can be explained by the down-shift in the loop's resonance frequency due to the capacitive coupling of the director. Moreover, the additional radiation from the director enhances the FBR to 27 dB at these frequencies.

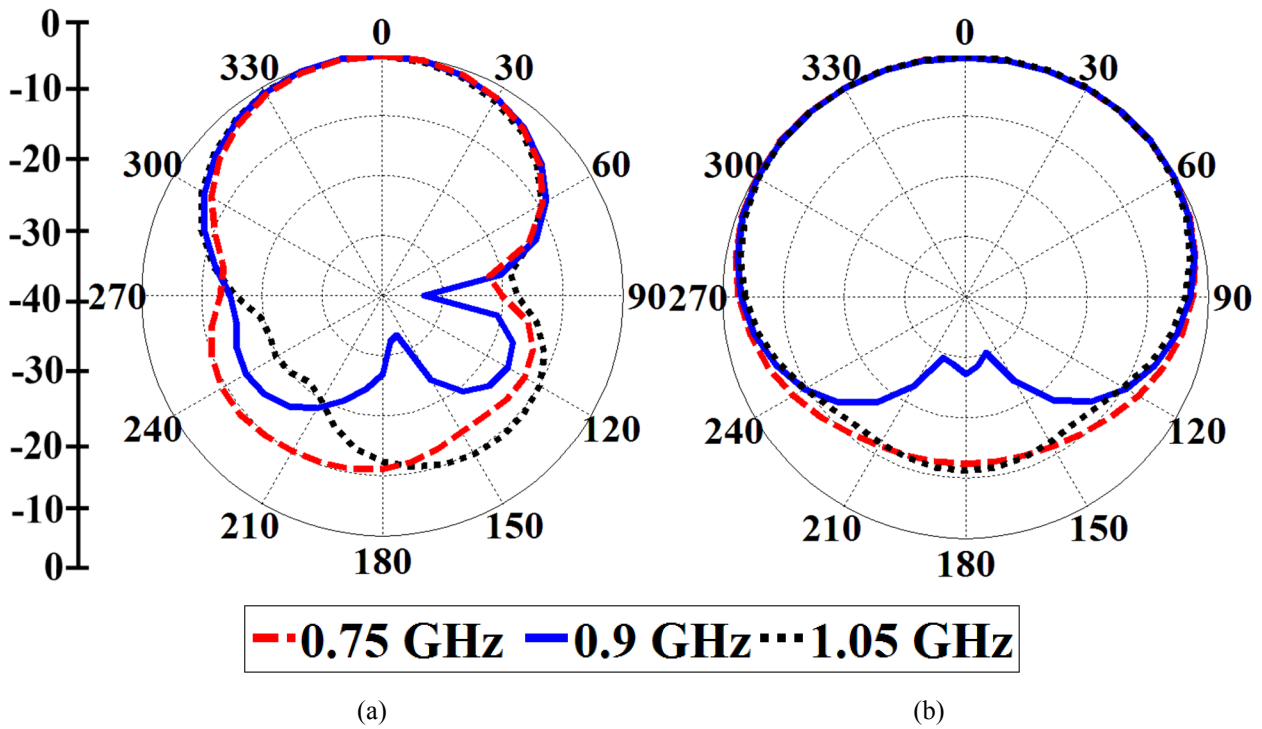


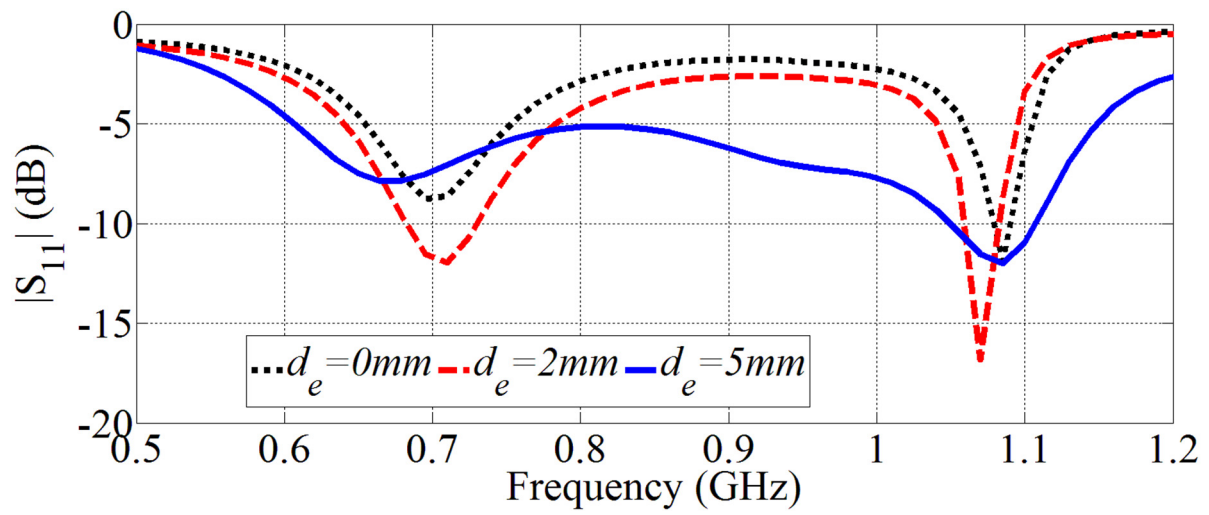
Fig. 4.6 Radiation patterns of the antenna at (a) E-plane and (b) H-plane (maximum radiation is at x-direction) (Scale: dB).

#### 4.1.4 Geometry Analysis

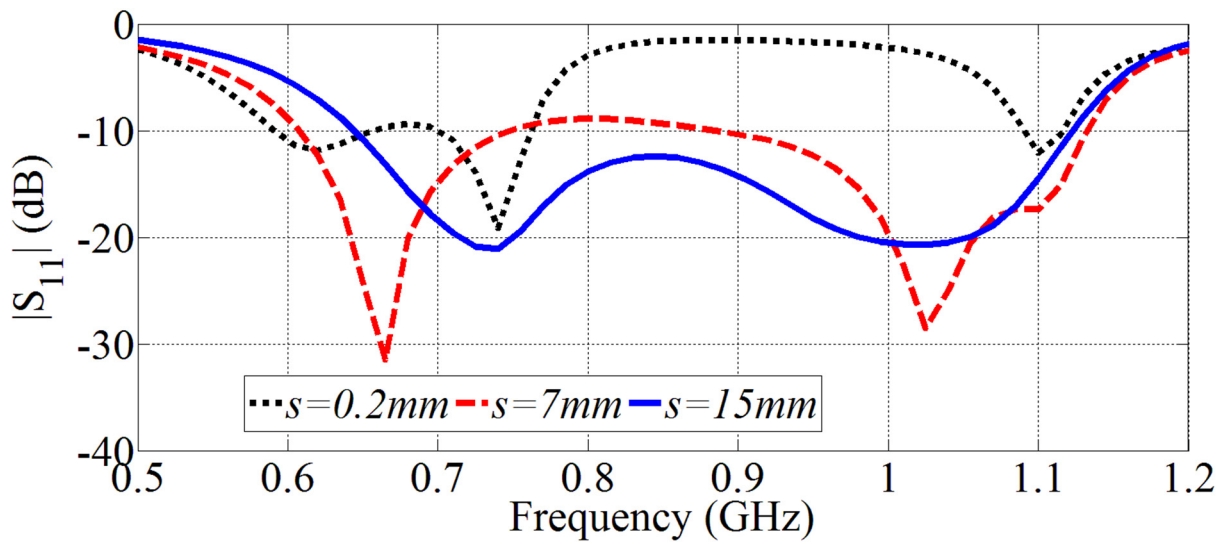
A geometry analysis is conducted on the effect of the size and position of the design elements of the loop and director on the input impedance and FBR of the antenna. To differentiate between the effects of different parameters, only one parameter is varied and its effect is studied at each stage.

#### 4.1.5 Position of the Loop Antenna

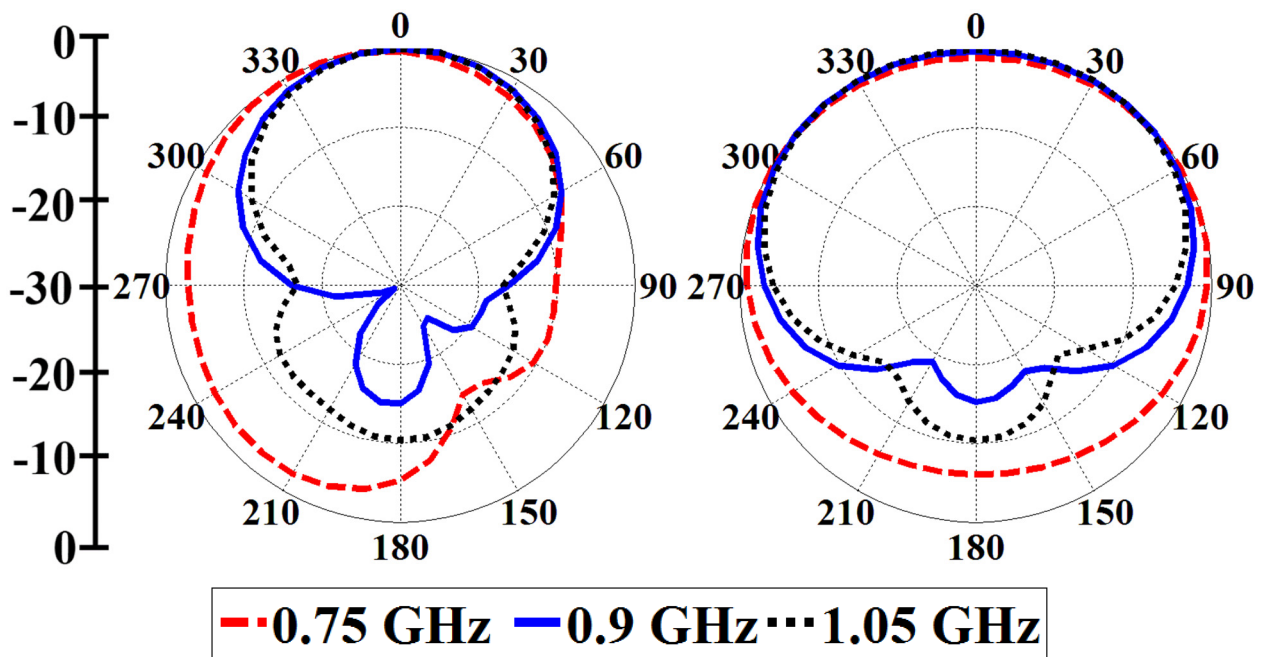
The effects of changing the size and location of the loop on the input impedance and radiation performance of the antenna are presented in Fig. 4.7. The impedance matching of the antenna is sensitive to the vertical (x-direction) position of the loop,  $d_e$ . As can be seen from Fig. 4.7 (a), the input impedance changes with  $d_e$  due to the broad-side coupling feeding which requires a proper coupling between the directly fed dipole at the top layer and the loop at the bottom layer. For optimum vertical position ( $d_e$ ), if the antenna is displaced horizontally ( $s$ ) along the y-direction, the antenna resonates at lower frequencies at the cost of lower FBR. This is one of the main advantages of broad-side coupling which allows higher degree of freedom in controlling the antenna's parameters.



(a)



(b)



(c)

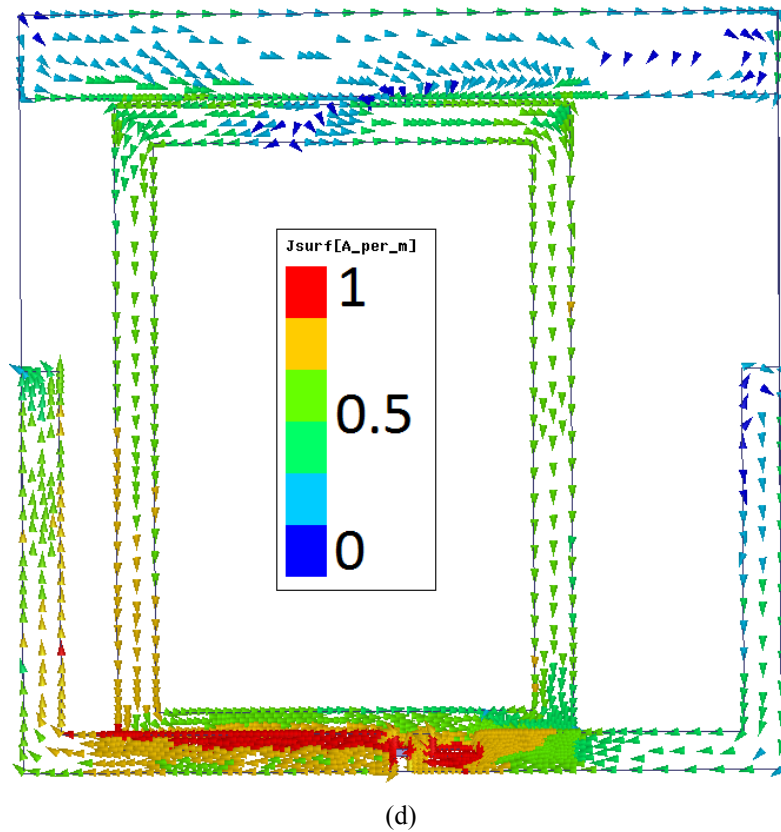


Fig. 4.7  $|S_{11}|$  variations with (a)  $d_e$  and  $s$ . (c) E-plane (left side) and H-plane (right) radiation patterns (Scale: dB) and (d) surface current distribution at  $s=7$  mm.

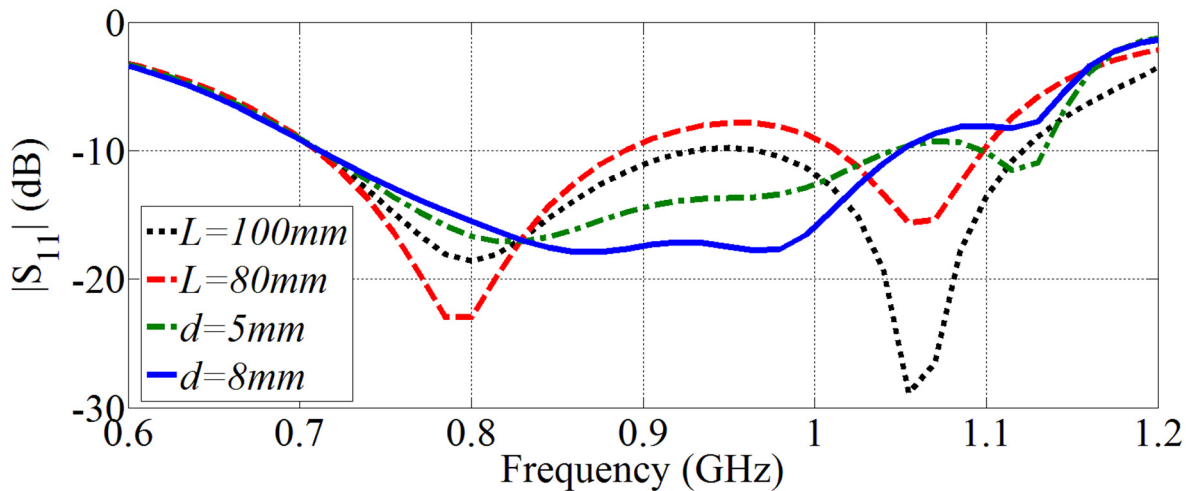
Referring to the reflection coefficient performance depicted in Fig. 4.7 (b), reducing the distance between the vertical arm of the dipole and the loop increases the capacitive coupling between them; thus, the resonance frequencies shift towards lower frequencies. However, it should be noted that there is a limit on reducing the resonance frequency while maintaining wide operating bandwidth. Beyond a certain distance value,  $s = 7$  mm, the created capacitive coupling has an adverse effect on the input impedance and resulting in impedance mismatches, e.g.  $s=0.2$  mm.

Regarding the radiation characteristics of the antenna, as depicted in Fig. 4.7 (c), the antenna achieves a lower FBR value, especially at low frequencies. It is mainly due to the fact that by changing the position of the loop, the current amplitude gets stronger on the coupled arm of the dipole (Fig. 4.7(d)), and hence its radiation, especially on E-plane, is stronger compared to the other arm (See Fig. 4.7(c)). Considering the fixed location of the director, a proper center to center positioning of director-radiator configuration is not attained, and hence FBR value is reduced. Nevertheless, in systems where lower FBR values are tolerable, such as microwave medical imaging, this configuration can be used to further reduce antenna's size.

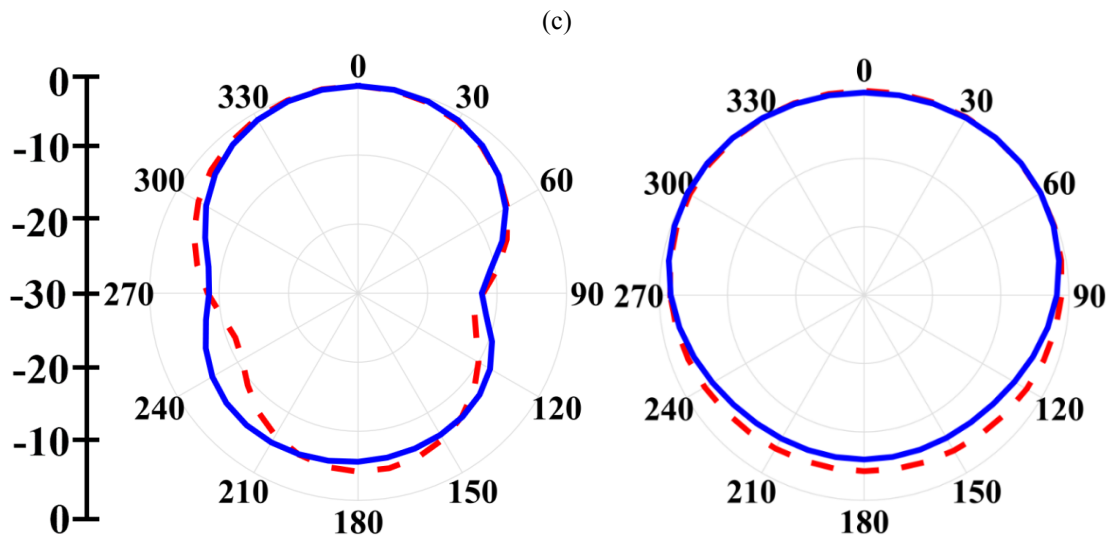
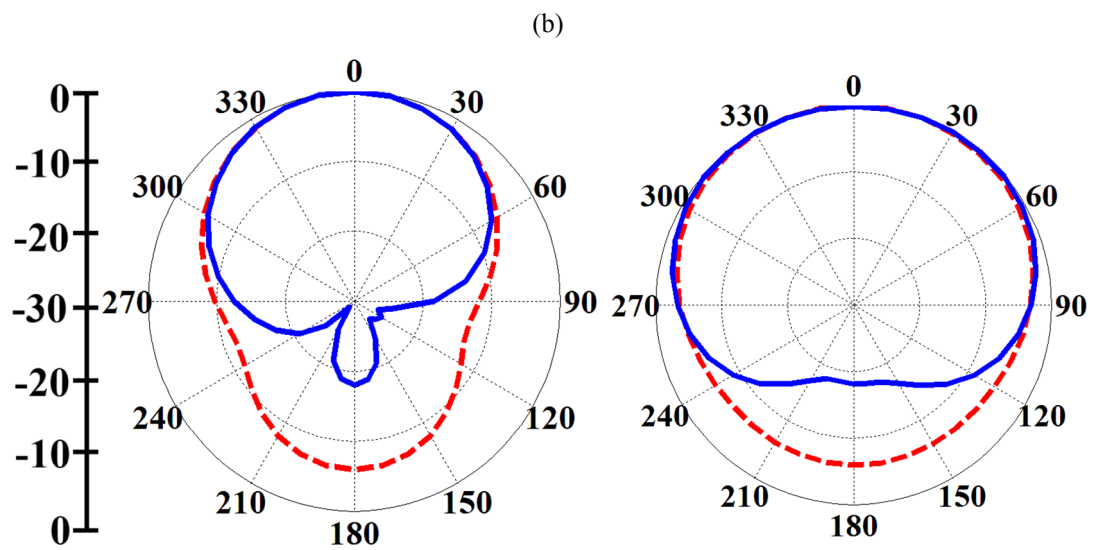
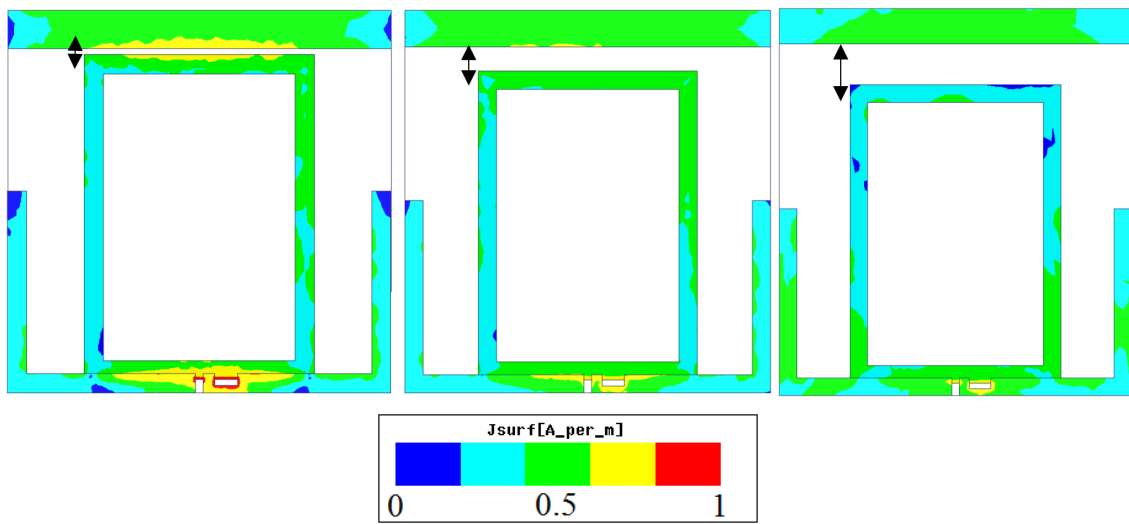
#### 4.1.6 Size and Position of the Director

Considering the fact that the director plays a key role in maintaining the input impedance matching and increasing FBR of the antenna, effects of changing its parameters, such as size and location, are investigated and the results are depicted in Fig. 4.8. As depicted in Fig. 4.8(a), the distance between the director and the loop,  $d$ , has a significant effect on the impedance matching of the antenna. This is mainly due to the alteration in the amount of capacitive coupling created between the loop and the director as shown in Fig. 4.8 (b). As expected, the amount of capacitive coupling between the loop and the director decreases with increasing the separation,  $d$ , and thus the antenna's impedance matching at higher frequencies is undesirably affected. On the other hand, increasing the separation has an adverse effect on the amount of FBR at the lower and higher ends of the band, respectively. As shown in Fig. 4.8 (c) and (d), the FBR is increased at higher frequencies due to the increased distance between the director and the driver (loop), while it is decreased at lower frequencies due to excessive separation between the dipole (driver) and the director. The same analysis is true for the impedance matching changes with the size of the director, e.g. its length,  $L$ , which defines the amount of coupling and affects the input impedance (See Fig. 4.8 (a)) and FBR values (Fig. 4.8 (d)). The detailed values of the final antenna design for a wide bandwidth, high FBR and stable gain are presented in Fig. 4.2.

To present the significance of achieved size reduction, a comparison between the proposed antenna and the most recent unidirectional planar ones is carried out and presented in Table 4-I. As can be seen, the proposed antenna achieves the most compact size (size reduction of 42-583%), while retaining the least gain variation. It should be noted that the obtained size reduction and wide operating bandwidth are of significant importance, especially for array designs in UHF systems, where the physical size of the antenna defines the size and weight of the system.



(a)



- - 0.75 GHz — 1.05 GHz

Fig. 4.8 (a)  $|S_{11}|$  at different  $L$  and  $d$  values. (b) Variations of magnitude of surface current with  $d$  at sample frequency of 1.05 GHz. E-plane (left side) and H-plane (right side) radiation patterns at (c)  $d=5$  mm and (d)  $L=80$  mm. (Scale: dB)

Table 4-I: Comparison between the area occupied by the proposed antenna and state of art unidirectional planar antennas

Ref	Size ( $\lambda_0$ )	Type	Gain Var.	Structure	Size Red. (Area) by Proposed Antenna (%)
107	$0.42 \times 0.35 \times 0.002$	56	2.5	Planar	89
108	$0.36 \times 0.41 \times 0.001$	105	3	Planar	89
99	$0.6 \times 0.6 \times 0.06$	18.7	1.5	Stacked	361
100	$0.73 \times 0.73 \times 0.04$	36	3.5	Wearable	583
101	$0.35 \times 0.31 \times 0.002$	73	3	Planar	42
42	$0.63 \times 0.28 \times 0.01$	129	2	Planar	126
102	$0.37 \times 0.3 \times 0.01$	7.4	2	Planar	42
Prop.	$0.28 \times 0.28 \times 0.001$	51	1.7	Planar	↶↷

#### 4.1.7 Antenna Measurements

Using the detailed parameters presented in Fig. 4.2, the final design was fabricated and tested. Fig. 4.9 (a) and (b) depict the top and bottom views of the fabricated antenna, which is fed using a coaxial cable. It should be noted that the antenna can be fed using various types of balanced to unbalanced (balun) designs. However, to maintain the small size of the antenna, and prevent the balun's spurious radiation, which causes pattern distortions at higher frequencies [101], [42], Richco© ring split core ferrite beads are used instead to reduce the effect of coaxial cable on the measurements.

The measured reflection coefficient of the antenna presented in Fig. 4.9 (c) indicates a band from 0.7 – 1.15 GHz with a good agreement with the simulated results.

The gain of the antenna is measured at  $\varphi=0$  and  $\theta=90$  degrees, and the obtained results are depicted in Fig. 4.9 (d). The antenna achieves maximum gain of 4.7 dBi at 1.11 GHz, while maintaining a stable gain of more than 3 dBi across the operating bandwidth. Those values correspond to a maximum gain variation of 1.5 dBi, which is up to 50% better compared to similar planar designs (See Table 4-IV).

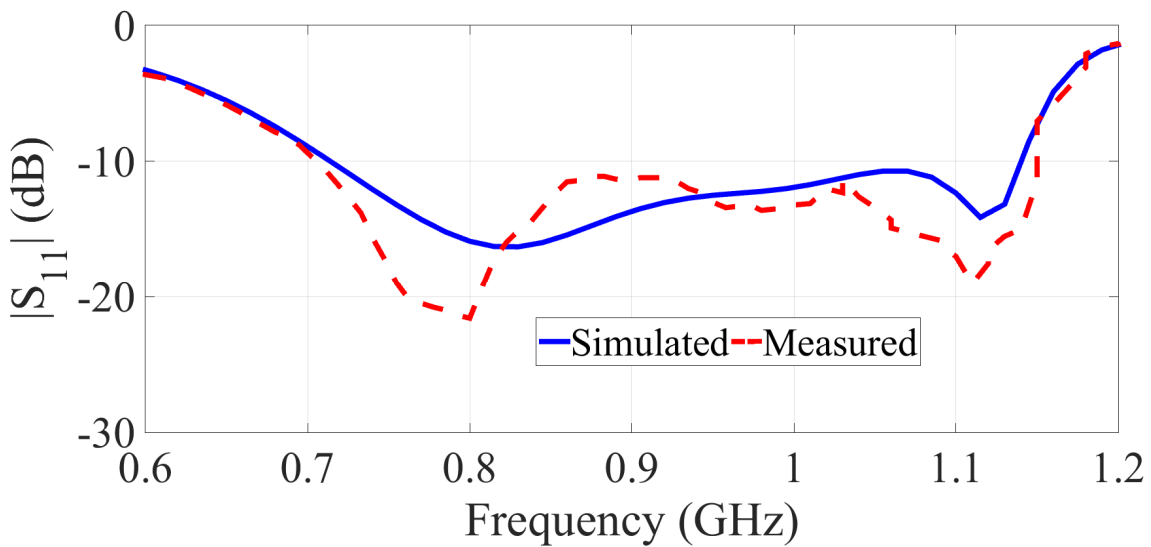
The normalized radiation patterns of the antenna at the two main radiation planes are measured and presented in Fig. 4.10. The measured results at the E- and H-planes are in a good agreement with the simulated ones. It can be realized that the minimum and maximum obtained FBRs are around 11 dB at 0.75 GHz and 20 dB at 0.9 GHz. Considering the cross polarization variations presented at the right side of Fig. 4.10, it can be realized that the cross polarization levels are about 19 dB lower than the co-polarization ones at the maximum radiation direction of the antenna (x-

direction). The main reason behind a generally higher cross-polarization at 0.75 GHz is the radiation from the bulky soldered coaxial cable that is prolonged from the edge of the substrate due to compact size of the dipole. This problem can be easily solved using more delicate cables and soldering techniques. Nevertheless, this value is lower or equal to the cross-polarization levels of printed antenna designs that do not use cavities or reflectors.

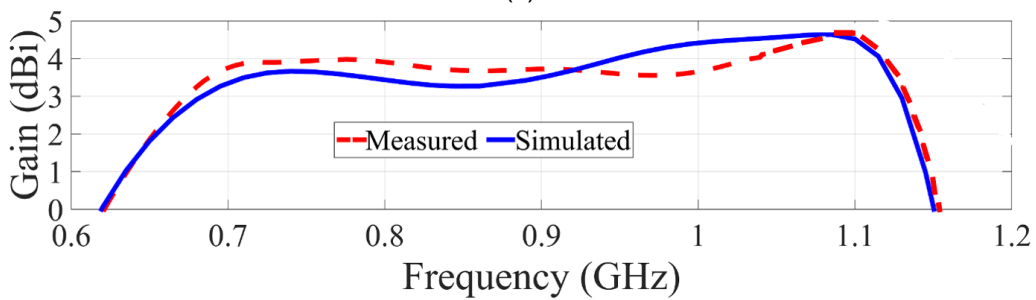


(a)

(b)



(c)



(d)

Fig. 4.9 Fabricated antenna (a) top view, (b) bottom view. Measured (c) reflection coefficient and (d) gain of the antenna vs. simulated results.

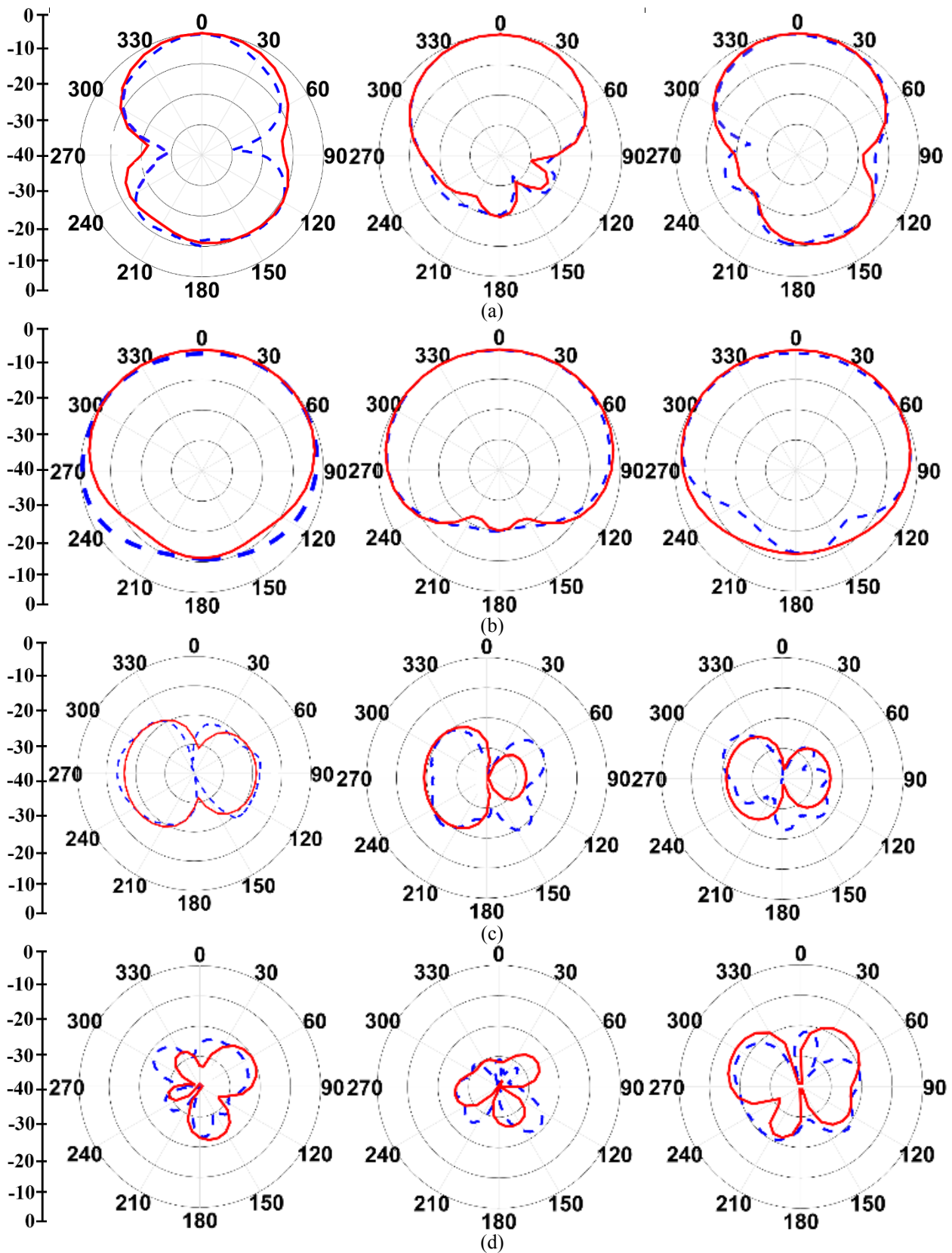


Fig. 4.10 Measured radiation patterns of the antenna at 0.75 GHz (left column), 0.9 GHz (middle column) and 1.05 GHz (right column). (a) E-plane Co-polarization, (b) H-plane Co-polarization, (c) E-plane Cross polarization and (d) H-plane Cross polarization. (Solid lines: simulated, dashed lines: measured) (Scale: dB)

## 4.2 Non-Uniform Metamaterial Unit-Cell Loading

This section is focused on utilizing metamaterial structures to further reduce the size of the antenna while maintain the desired unidirectional radiation and wide operating bandwidth. Unlike any other printed metamaterial antenna, the proposed structure is using a non-periodic distribution of the unit-cells along the host transmission line, which enables controlling its radiation mechanism.

### 4.2.1 Introduction

With the introduction of metamaterials in recent years, several types of compact antennas have been designed [111]-[115]. It has been shown that by loading conventional antennas with periodic structures, unusual properties, such as backward wave propagation and infinite wavelength, are attainable [113]. These antennas use the theory of negative-refractive-index transmission-line (NRI-TL) metamaterials in which the host transmission line is loaded with series capacitors and shunt inductors to create tailored wave propagation characteristics that are non-existent in nature. Utilizing these unique properties has led to the design of antennas and radio frequency devices that are size independent, and hence great degrees of miniaturization are attained [114]-[115]. Besides their miniaturization capabilities, it has been shown that the radiation characteristics of the antennas can also be engineered such that a uniform current distribution with a zero phase difference along the loaded structure can be created [112], [116].

Considering the difficulties associated with implementing both capacitors and inductors, especially in their lumped chip element forms, new types of metamaterials that only support zero and positive wave mode numbers, such as epsilon negative (ENG) and mu-negative (MNG), are introduced [116]-[119]. These structures utilize either shunt-loaded inductors [115] or series-loaded capacitors [116]-[119] to achieve an infinite wavelength or a zeroth-order resonance. However, despite their excellent size reduction capabilities, the aforementioned techniques suffer from narrow/multi-narrow bandwidths and omnidirectional radiation characteristics that limit their practicality in applications requiring wide operating bandwidths and unidirectional radiation for torso imaging.

This section aims at addressing the aforementioned limitations by introducing a new unit-cell arrangement along the host transmission line besides utilizing combinations of conventional techniques with the ones from metamaterial theory.

## 4.2.2 Theory of MNG Loaded Transmission Lines

In this section, the theory of MNG-loaded transmission lines is explained and the related formulas for obtaining various resonant modes are presented. As stated before, MNG-loaded transmission lines are a sub-category of NRI-TL metamaterials in which the metamaterial structure is constructed by loading the host transmission line with only a series capacitor. The symmetric-distributed and lumped-element equivalent circuit of a MNG unit cell is depicted in Fig. 4.11.

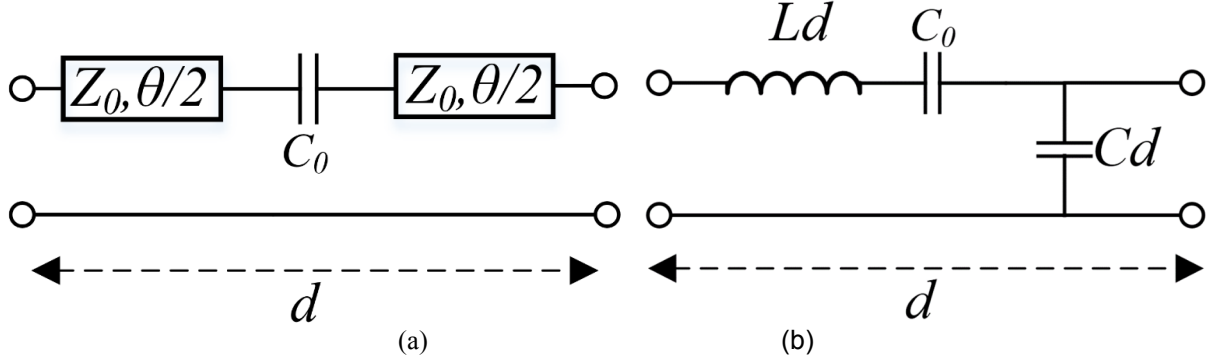


Fig.4.11 (a) Symmetric distributed and (b) lumped element equivalent circuit of a MNG metamaterial unit-cell.

By applying periodic boundary conditions, the dispersion relation for the presented equivalent circuit of Fig. 4.11 can be written as [120]:

$$\cos(\beta d) = \cos(\theta) + \left(\frac{1}{2\omega C_0 Z_0}\right) \sin(\theta) \quad (1)$$

Equation (1) can be simplified to (2) assuming effective medium conditions of  $\theta \ll 1$  and  $\beta d \ll 1$ .

$$\cos(\beta d) \approx 1 - \frac{1}{2} \left( \omega^2 L C d^2 - \frac{L d}{C_0} \right) \quad (2)$$

In these equations,  $C_0$  is the series loading capacitor,  $\beta$  is the propagation constant,  $Z_0$  is the characteristics impedance and  $\theta$  is the electric length of the host transmission line. Moreover, the effective propagation constant of the MNG structure can be written as [120]:

$$\beta_{MNG} = \omega \sqrt{L_{eff} C_{eff}} = \omega \sqrt{\left[ L - \frac{1}{\omega^2 C_0 d} \right] C} = \sqrt{\omega^2 L C - \frac{C}{C_0 d}} \quad (3)$$

From (3), it can be realized that by selecting appropriate values for the series loading capacitor,  $C_0$ , the effective series inductance, which is the combination of the series inductor,  $L_d$ , and the loading

series capacitor,  $C_0$ , can be equated to zero which in turn creates a propagation constant of zero and consequently zeroth order resonance. Moreover, considering the fact that the effective permittivity and permeability of an MNG-TL are obtained using (4) [121], at the point where the value of  $C_0$  is engineered to cancel the effective inductance the permeability equals to zero, which is the notion behind naming the structure mu-zero (MZR).

$$\varepsilon = C, \mu = L - \frac{1}{\omega^2 C_0} \quad (4)$$

Using the expression presented in (1), the dispersion diagram of the MNG-TL depicted in Fig. 4.11, is derived and presented in Fig. 4.12. The presented values are arbitrarily selected as a proof of concept. As can be seen from Fig. 4.12, the MNG-TL supports a zero wave mode number, which supports an infinite wavelength, as well as positive mode numbers. The resonance modes of a MNG-TL can be predicted using the following expression [120]-[122]:

$$\beta_{MNG} d = \frac{n\pi}{N} \quad ; n = 0, 1, 2 \dots (N-1) \quad (5)$$

where  $N$  is the number of unit-cells that results in an overall structure size of  $L_{tot} = Nd$ . The MZR frequency can be estimated using the calculated input impedances at the open and short ended boundary conditions for conventional transmission lines [119], [121]-[122]:

$$\begin{aligned} Z_{in}^{open} &= -jZ_0 \cot(\beta_a L) \approx -jZ_0 \frac{1}{\beta_a L} = \frac{1}{NY} \quad (\beta_a \rightarrow 0) \\ Z_{in}^{short} &= jZ_0 \tan(\beta_a L) \approx jZ_0 \beta_a L = NZ \quad (\beta_a \rightarrow 0) \end{aligned} \quad (6)$$

Applying these conditions to the equivalent circuit of the MNG-TL presented in Fig. 4.11 results in [119], [121]-[122]:

$$Z_{in}^{open} = \frac{1}{j\omega N C d} \quad (7)$$

$$Z_{in}^{short} = \frac{N}{j\omega C_0} + j\omega N L d \quad (8)$$

Therefore, to obtain MZR resonance, the short-ended condition should be selected, and the MZR frequency can be written as [121]

$$\omega_{MZR} = \frac{1}{\sqrt{LC_0}} \quad (9)$$

which is independent of the overall length of the resonator,  $L_{tot}$ .

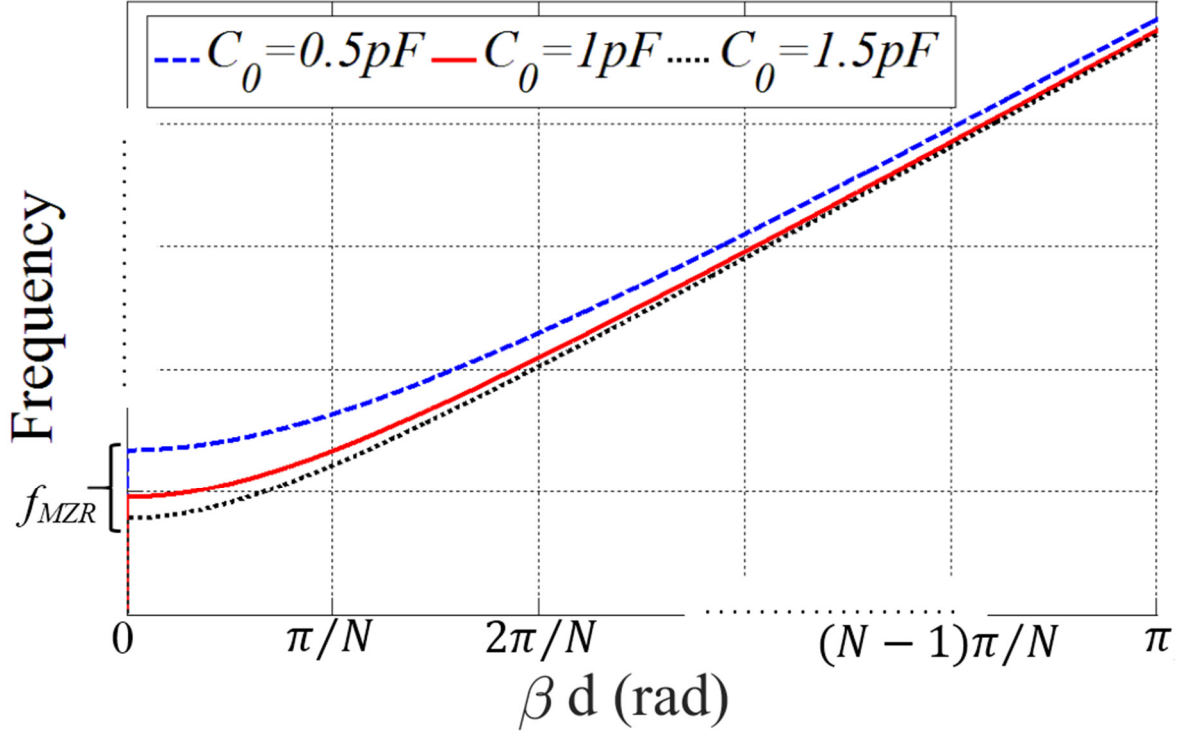


Fig. 4.12 Dispersion diagram of a MNG unit-cell for arbitrary lumped element values for a transmission line with width of 10mm and length of 20 mm on FR4 substrate with 0.8 mm thickness.

### 4.2.3 MNG Unit-cell Design

In order to create a loading capacitor, there are several approaches, such as using lumped chip capacitors [112], gaps [123] and interdigital capacitors [121]. To avoid the tolerance inaccuracies associated with lumped chip elements and limited attainable capacitance values using simple gaps, inter-digital capacitors (IDCs) are selected to create the loading capacitor. The geometry of the proposed periodic structure is depicted in Fig. 4.13 (a). It consists of a two-conductor coplanar strip transmission line loaded with a pair of asymmetric IDCs. The whole structure is designed on an epoxy FR-4 substrate with dielectric constant of 4.4, loss tangent of 0.02 and thickness of 0.8 mm. The equivalent circuit of the proposed MNG-TL is depicted in Fig. 4.13(a), where the IDC is modeled as a loading capacitor. The symmetric coplanar strip-line (CPS) model of the unit-cell in the form of a TL and lumped elements can be simplified to that of Fig. 4.11.

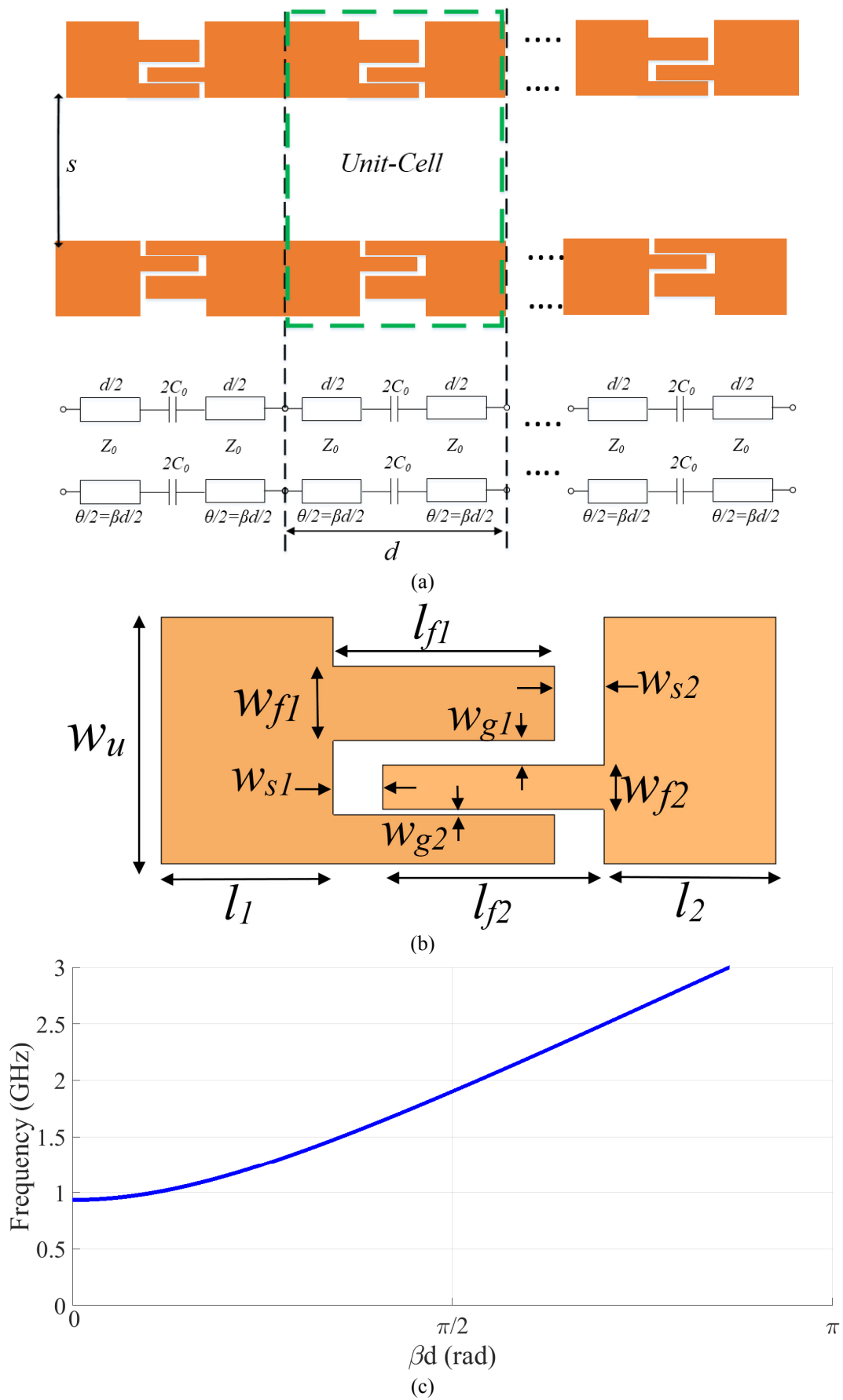


Fig. 4.13. (a) Proposed periodic structure of MNG unit-cells, including the equivalent symmetric equivalent circuit, (b) detailed geometry of a single MNG unit-cell employing an interdigital capacitor. (c) Dispersion diagram of the MNG unit-cell shown in (b) for the values presented in Table 4-II.

To calculate the obtained capacitance from the proposed unit-cell, the characteristics impedance and phase of the unit-cell is calculated using Keysight's ADS Momentum. Then, by forming a two port network circuit model, the  $C_0$  value is calculated using:

$$C_0 = \frac{Im(-Y_{12})}{\omega} \quad (10)$$

where  $Y_{12}$  is the transfer admittance of the network. To plot the dispersion diagram using (1),  $\theta$  should be expressed as a function of  $\omega$  by:

$$\theta = \omega\sqrt{LC}d \quad (11)$$

Using the aforementioned formula and the well-known relation of (12), the value of  $\theta$  at the desired frequency is attainable.

$$Z_0 = \sqrt{L/C} \quad (12)$$

It should be noted that individual values of  $L$  and  $C$  are obtainable by substituting their equivalent formulas from (12) into (11). Therefore, by following the abovementioned analysis steps, the proposed periodic structure can be engineered to obtain the desired MZR frequency. It is noted that in the proposed structure, the gap between the fingers is used to control the capacitance as well as to tune the impedance matching. As an example, the dispersion diagram of the antenna for the proposed values in Table 4-III is presented in Fig. 4.13(c), where the MZR frequency is at 0.96 GHz for a unit-cell with length of 20 mm and a loading capacitor value of  $C_0 = 0.44$  pF.

Table 4-II: Detailed geometric values of the utilized unit-cell

$W_u$	10	$W_{g1}$	1	$W_{f2}$	1.8	$l_{f1}$	9	$W_{s2}$	2	$l_1$	4.5
$W_{f1}$	3	$W_{g2}$	0.2	$W_{s1}$	2	$l_{f2}$	9	$l_2$	4.5	$s$	100

#### 4.2.4 Antenna Designs

In this section, several antennas based on the proposed periodic structure are designed and the obtained results are discussed accordingly. These antennas are presented as a proof-of-concept on the effectiveness of the proposed loaded structure in obtaining MZR frequency.

## 4.2.5 MZR Antenna

To satisfy the short-end boundary and to create an additional resonance, a loop antenna is selected as the host structure. As shown in Fig. 4.14 (a), the horizontal arms of the loop in the x-direction are selected to form the periodic structure, the left vertical arm is used to feed the structure and the right side arm is used to fulfil the short-end boundary condition for attaining MZR frequency. In all the discussed designs, the separation between the top and bottom arms,  $s$ , (see Fig. 4.13(a)) is fixed at 100 mm. The antennas are fed using a coplanar-waveguide (CPW) structure, as can be seen in the inset diagram of Fig. 4.14 (a). The size of the feed is optimized to match to  $50 \Omega$  input impedance. The schematic view and reflection coefficients of the realized antennas using different unit-cell numbers are presented in Fig. 4.14(a) and (b), respectively. The Ansys-HFSS software was utilized to perform the full-wave simulations.

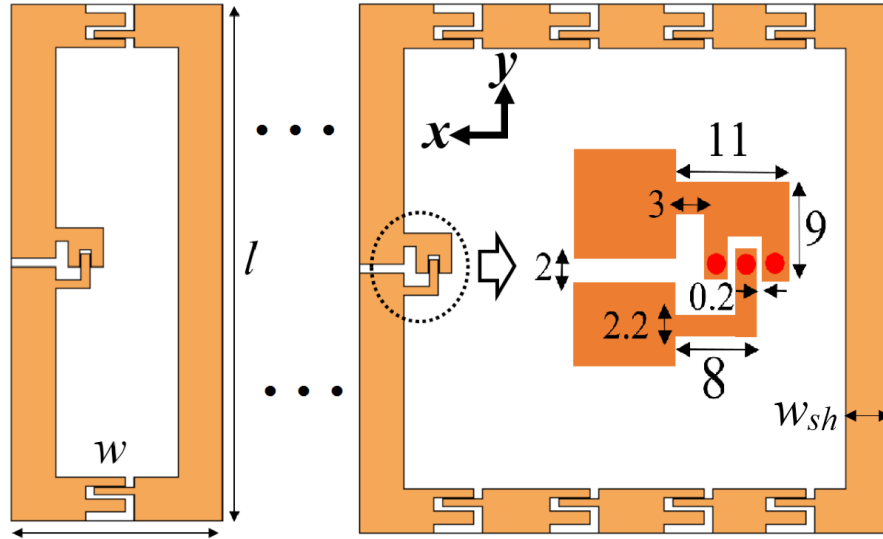
Theoretically, the MZR frequency is independent of the number of unit-cells; however, as can be seen from Fig. 4.14(b)-(d), by increasing the number of unit-cells, the resonance frequency shifts towards higher frequencies and approaches the theoretical value predicted by (9), while its impedance matching improves. This is in contrast with the resonance performance of a conventional unloaded loop, whose resonance frequency decreases with an increase in the loop size. This is firstly due to the fact that the presented equations are obtained by assuming infinite number of unit-cells, and secondly due to the inductive effect of the shortening arm and feeding structure of the loop. To that end, a more accurate MZR frequency can be expressed by [121]:

$$\omega_{MZR} = \sqrt{\frac{N}{C_0(2L_{short} + NL)}} \quad (13)$$

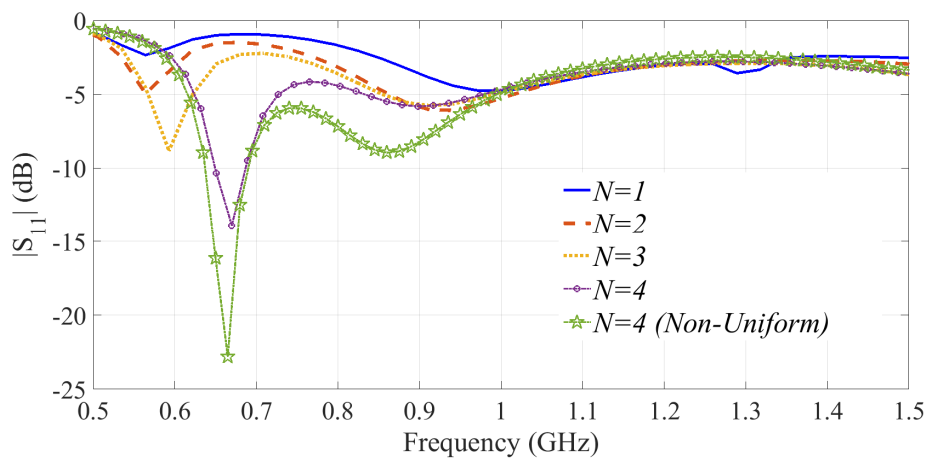
where  $L_{short}$  is the inductance of the shortening arm,  $l$ . As can be seen from Table 4-III, the MZR resonance frequencies predicted by (13) are closer to that of the simulated ones. The reason behind the small deviation between the predicted and simulated results can be attributed to the type of feeding and its length. Furthermore, it can be seen that a second resonance, which is a one-wavelength loop mode, is excited at around 0.8-1 GHz depending on the size of the realized antenna ( $W \times L$ ).

To verify the fact that the lowest obtained resonance is indeed a MZR frequency, the surface current distribution of the antenna, with one and four unit-cells and the electrical sizes presented in Table 4-III, are depicted in Fig. 4.15(a) and (b), respectively. The loop experiences a zero phase shift across its structure, and therefore  $\varphi = -\beta d = 0$ . Consequently, as shown in Fig. 4.15(c), the antenna achieves a relatively symmetrical horizontally polarized quasi-omnidirectional radiation in the x-y plane, which is similar to that of a small-loop or magnetic dipole antenna. By comparing the electrical

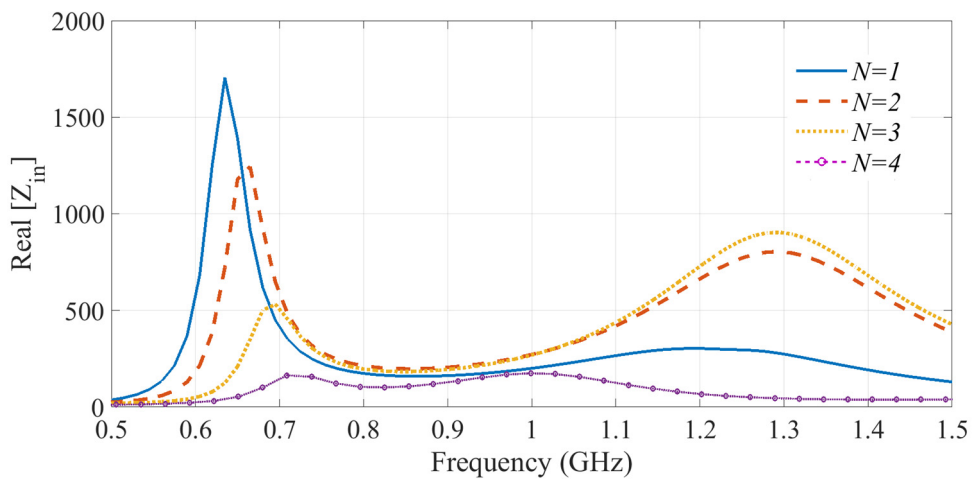
size of the proposed MZR antenna with respect to the conventional loop, it can be seen that minimum size miniaturization of about 50 % is achievable using the proposed periodic structure (See Table 4-III).



(a)



(b)



(c)

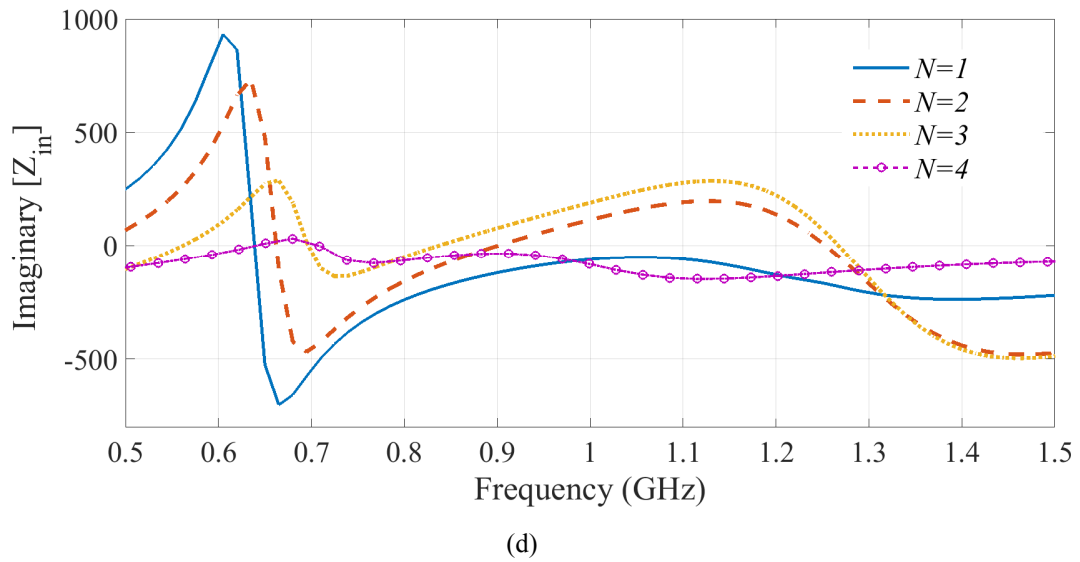
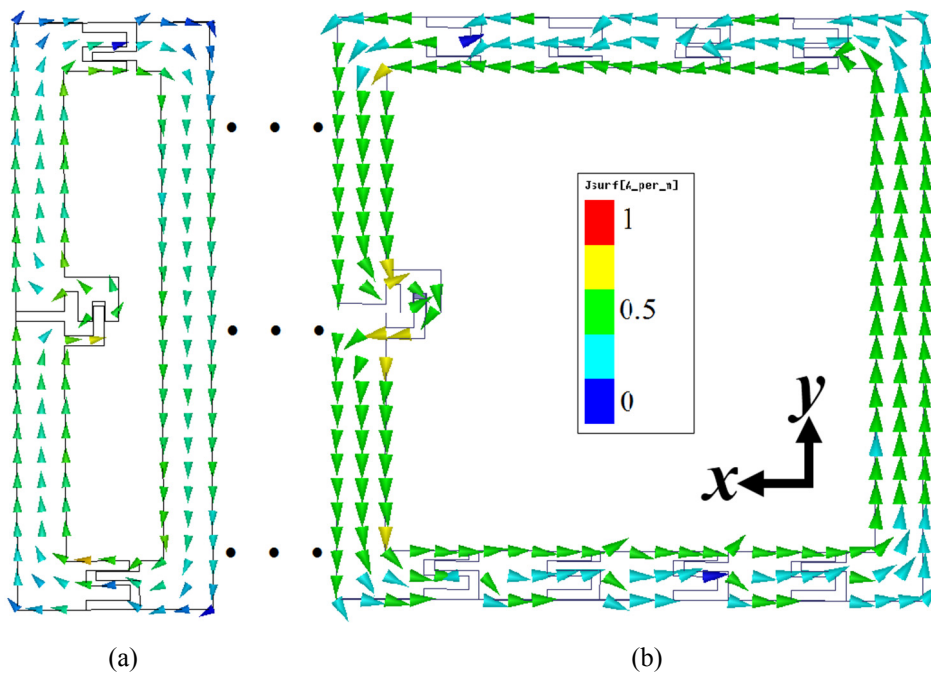


Fig. 4.14 (a) Schematic view of antennas with one and four unit-cells.(b) Reflection coefficients, (c) real and (d) imaginary parts of the input impedance of the proposed antennas.  $W_{sh}=10$  mm,  $l=120$  mm.

Table 4-III: Estimated and Simulated Resonant Frequencies for a Unit-cell with Dimensions Presented in Table 4-II, and Achieved Antenna Size with Respect to MZR Resonance Frequency and Conventional Loop Resonance

N	Eqn.(9) (GHz)	Eqn.(13) (GHz)	Sim. (GHz)	Antenna Size ( $\lambda_0$ @ MZR)	Antenna Size ( $\lambda_0$ @ Loop)	Size Reduction (%)
1	0.96	0.48	0.56	0.07×0.22	0.13×0.4	71
2	0.96	0.68	0.56	0.11×0.22	0.2×0.4	70
3	0.96	0.75	0.59	0.15×0.22	0.24×0.36	61.6
4	0.96	0.79	0.67	0.22×0.26	0.3×0.36	47



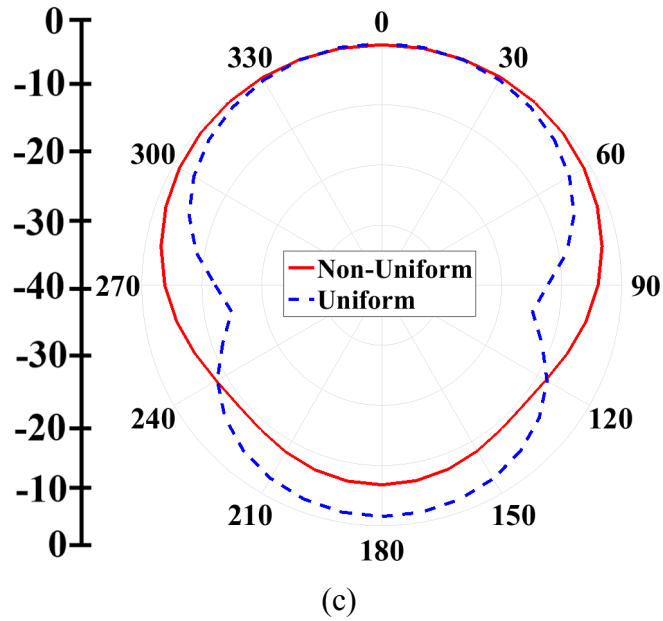


Fig. 4.15. Surface current distribution of the realized antennas with (a) one and (b) four unit-cells at their respective MZR frequencies of 0.56 GHz and 0.67 GHz. (c) x-y plane radiation pattern of the designed antenna employing four unit-cells with uniform and non-uniform distribution of unit-cells at the sample frequency of 0.67 GHz. (maximum radiation in the x-direction)

#### 4.2.6 Unidirectional MZR Antenna

Despite their miniaturization capabilities, the proposed antennas loaded with periodic capacitors require reflectors or cavities to create unidirectional radiation. This is the case for the majority of the metamaterial antennas [112]-[119]. Such a requirement is a significant drawback, especially at lower frequencies in the ultra-high-frequency (UHF) range that hosts a large number of applications such as industrial, scientific and medical (ISM), mobile and television broadcast and short/long range point-to-point communications. To that end, a different approach is proposed. By using a non-periodic positioning of the unit-cells on the host transmission line, a moderate unidirectional radiation can be achieved. It is noted that the effectiveness of non-periodic arrangement of unit-cells has been shown on a leaky wave antenna [124], but has never been studied or applied for other types of antennas. This is due to the fact that with the proposed sinusoidal distribution of unit-cells for a leaky wave antenna, the size of the antenna would be extremely large and impractical, especially at lower frequencies.

With the new proposed arrangement of the unit-cells, the fourth unit-cell is loaded with distance  $S_{uc}$  to the third unit-cell. Consequently, the amplitude of the surface current can be engineered to be higher at certain arm of the loop compared to the other arms, and therefore unidirectional radiation can be achieved. This can be seen in Fig. 4.16 (a) where the unit-cells are positioned non-

periodically along the host transmission line. The surface current distribution of the antenna is presented in Fig. 4.16 (b). As can be realized, despite rearranging the unit-cell positions, the antenna maintains its uniform surface current distribution ( $\varphi = 0$ ). However, studying the amplitude of the surface current reveals that the amplitude of the currents on the left side arm of the loop, near the feeding structure, is higher compared to the other arms and as shown in Fig. 4.15 (c) a unidirectional radiation with moderate front-to-back (FBR) of 7 dB is achieved. The amount of FBR can be adjusted by tuning the distances between the unit-cells. Nevertheless, by utilizing this simple technique a compact and unidirectional MZR antenna is achievable.

With a non-periodic distribution of the unit-cells, unidirectional radiation is obtainable at the second resonance as well. It is a well-known fact that by capacitively loading a loop, its radiation mechanism is divided into a loop and a half-wavelength dipole antenna. For loop structures using a single capacitive loading such as a slot loaded loop, these two frequencies can be easily merged by changing the position of the capacitor on the loop, and hence forming a dipole where its resonance is at the same frequency as the loop antenna. With such a configuration, the loop antenna acts as an array of two dipole antennas that are excited with a 90 degree phase difference and hence creates a cardiac shape radiation pattern which suppresses back radiation [125].

The same performance can be obtained by properly distributing the MNG unit-cells along the host transmission line. The surface current distribution of the proposed non-periodically loaded antenna is depicted in Fig. 4.17 (a) at 0.83 GHz. As can be seen, the resonance of the dipole at this frequency depends on the size of the loop and location of the current node, which defines the size of the dipole at the left side of the structure. The structure can be divided into two folded-dipole antennas, as shown in Fig. 4.17 (b), with their vertical sections located at a quarter-wavelength distance with respect to each other, and hence unidirectional radiation is achievable. To verify the aforementioned notion, an array of two dipole antennas with the exact same configuration and sizes of the proposed antenna that are excited with 90 degree phase difference is designed and shown in Fig. 4.17 (b). As depicted in Fig. 4.17 (a)-(d), similar surface current distributions and radiation patterns are observed.

#### **4.2.7 Wideband and Unidirectional Loaded Loop Antenna**

Based on the above-stated analysis, it can be seen that unidirectional radiation can be obtained by simply rearranging the positioning of the unit-cells. However, similar to the majority of the metamaterial antennas presented in the literature, the proposed antenna designs are either narrowband or exhibit multiple narrowband resonances and can be used for a limited number of applications.

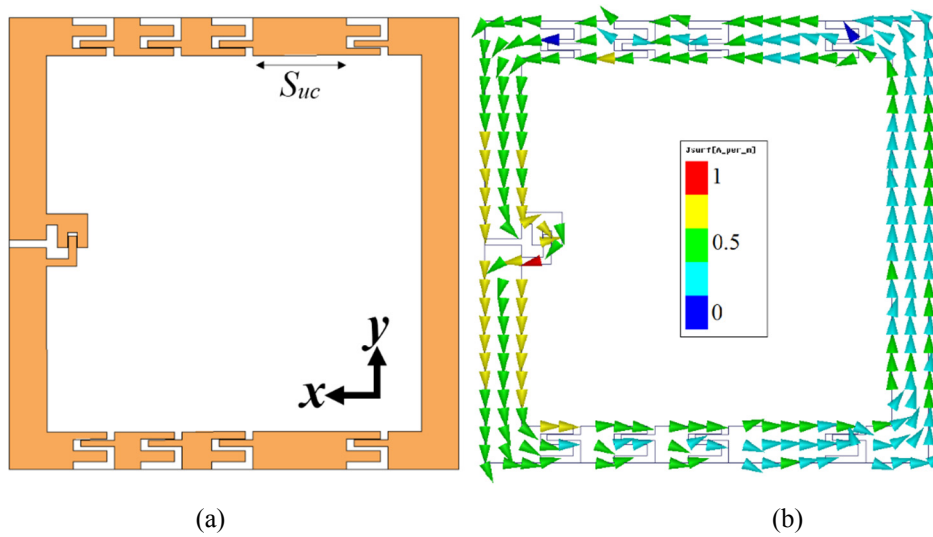


Fig. 4.16. (a) Schematic view and (b) surface current distribution of the antenna with non-periodic distribution of the unit-cells.  $W=120\text{mm}$ , and  $S_{uc}=20\text{ mm}$ .

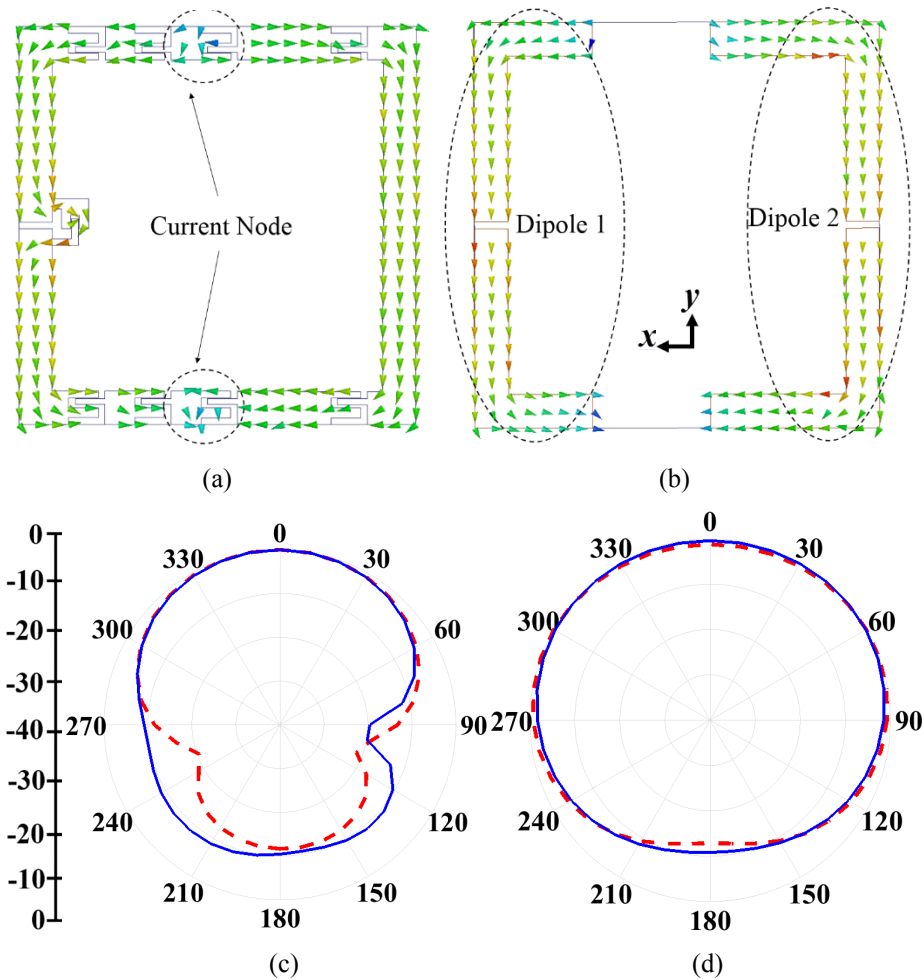


Fig. 4.17. Surface current distribution of the antenna with (a) non-periodic distribution and (b) equivalent dipole array. Radiation patterns of the non-periodically loaded loop (solid line) vs. dipole array (dashed line) in the (c) x-y plane and (d) y-z plane at the resonance frequency of 0.83 GHz. (maximum radiation in the x-direction)

To overcome this limitation, another antenna design is proposed and presented in Fig. 4.18. The antenna utilizes the previously proposed structure with non-periodically positioned MNG unit-cells, together with a strip patch that is positioned in the vicinity of the feeding arm of the loop [40]. To keep the size of the antenna as compact as possible, the width of the feeding arm of the loop is reduced to accommodate the parasitic strip within the same substrate area of the previous design.

Considering the proximity of SMA connector, which is used to feed the antenna, to the strip patch, and its inevitable effect of on the performance of the antenna, it was modeled and included in the simulations. To create a wide operating bandwidth, two steps are devised in the design process. Firstly, a third resonance in addition to the MZR and loop resonances is created using proximity feeding of the strip patch. To that end, the length of the strip was selected to be around a quarter wavelength at 0.95 GHz. Secondly, the distance of the strip from the loop was tuned to obtain the widest achievable bandwidth. As a result of this process, a wide fractional bandwidth of 47% at 0.65-1.05 GHz was obtained (Fig. 4.18(b)). The effect of selecting different strip lengths on the reflection coefficient is also depicted in Fig. 4.18(b). As expected, by choosing shorter strips, the third resonance is excited at higher frequencies, while longer strips resonate close to the loop mode. It can be realized that proper positioning of the strip improves the overall reflection coefficient performance of the antenna due to the capacitive effect of the proximity coupling. Moreover, by increasing the length of the patch more than a limit ( $l_s = s = 90$  mm), a capacitive coupling is created with the unit-cell that downshifts the MZR frequency as shown in Fig. 4.18(b).

One of the main advantages of the proposed antenna is that by keeping the position of the non-periodically distributed MNG unit-cells unchanged, the first and third resonance of the antenna can be adjusted without affecting the second resonance. As mentioned before, the third resonance depends on the size of the strip and can be adjusted in a certain range that is shown in Fig. 4.18 (b). Considering the fact that the first resonance of the antenna is dependent on the amount of capacitive loading, its resonance can be tuned by changing the dimensions of the IDC. To verify the effectiveness of the proposed structure in providing different  $C_0$  values, the gap between the fingers of the IDC is varied, and three sample values are calculated and presented in Table 4-IV. It can be seen that by decreasing the gap between the fingers of the IDC higher capacitor values are achievable. The simulated results verify the theoretical approach and as can be seen in Fig. 4.18(c), the first resonance is shifted towards lower frequencies without greatly affecting the second and third resonances.

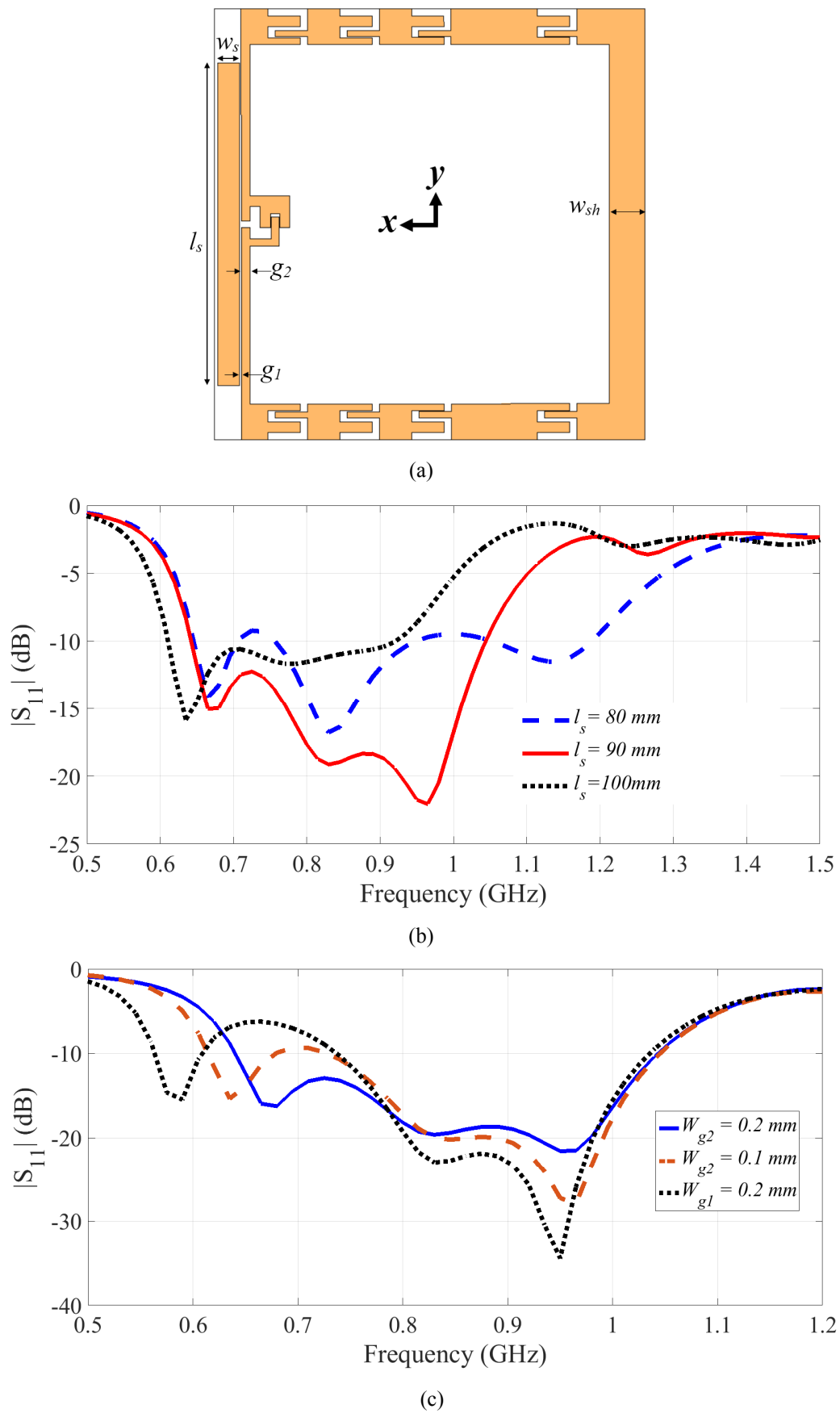
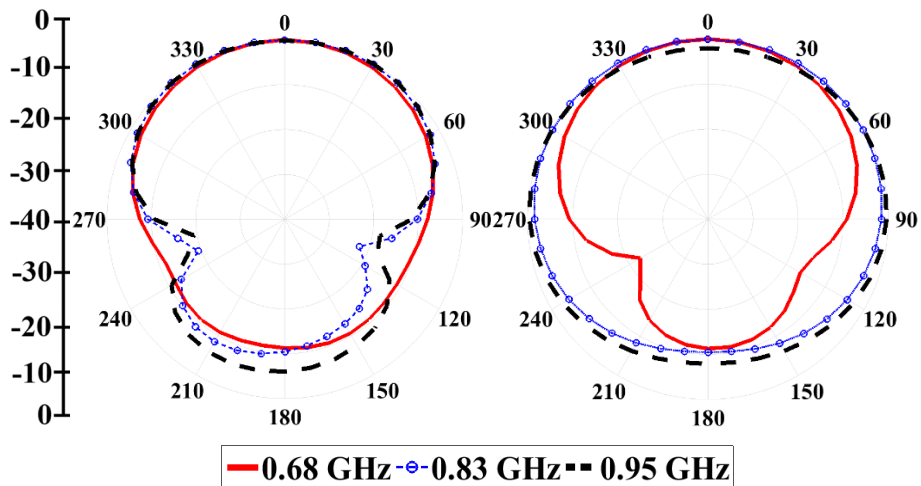


Fig. 4.18. (a) Proposed wideband and unidirectional MNG-loaded loop antenna. (b) Reflection coefficient variations with the size of the strip and (c) IDC (Dimensions of Table I) gap variations.  $l_s = 90$ ,  $g_1 = 0.5$ ,  $g_2 = 2.5$ ,  $w_{sh} = 10$ ,  $w_s = 6$  (unit: mm)

Table 4-IV: Theoretical estimation of the series loading capacitor value, MZR resonance and simulated results for a unit-cell with different gap sizes

	C0 (pF)	Eqn. (13) (GHz)	Sim. (GHz)
$W_{g2}=0.2$	0.44	0.79	0.68
$W_{g2}=0.1$	0.49	0.74	0.63
$W_{g1}=0.1$	0.56	0.7	0.59

To study the radiation characteristics of the antenna, its radiation patterns are presented in Fig. 4.19 (a). The antenna achieves a unidirectional radiation at all its main resonances. It can be noticed that compared to the antenna presented in Fig. 4.16 (a), the FBR is increased at the first resonance to around 12 dB. This is due to the fact that by placing the strip patch in the vicinity of the loop, the amplitude of the current is further enhanced compared to other arms that consequently improves radiation in the x-direction as shown in Fig. 4.19 (b). The FBR at the second resonance is around 12 dB, which is similar to that of the structure with no strips. As can be seen from Fig. 4.19(c), the main resonating elements of the antenna at this frequency are the left and right side arms of the loop that are excited with a 90 degree phase difference. By investigating the radiation pattern in Fig. 4.19 (a), it is realized that the antenna has a unidirectional radiation pattern at its higher resonance as well. By studying the magnitude of the surface current distribution in Fig. 4.19 (d), it can be seen that, at this frequency, the antenna acts as a Yagi antenna, where the feeding arm of the loop acts as the driver and the strip patch acts as the director. As a result, the antenna achieves a moderate FBR of 6 dB. Nevertheless, the antenna presents a unidirectional radiation across its operating bandwidth.



(a)

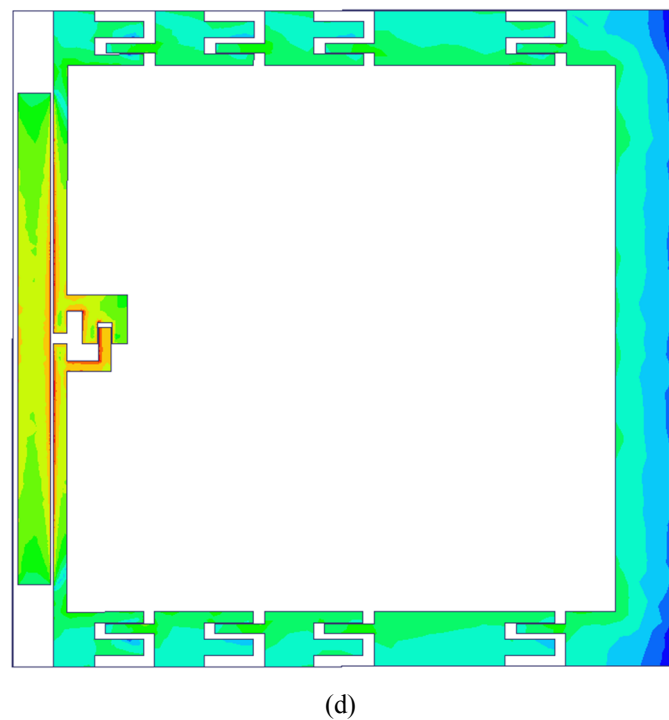
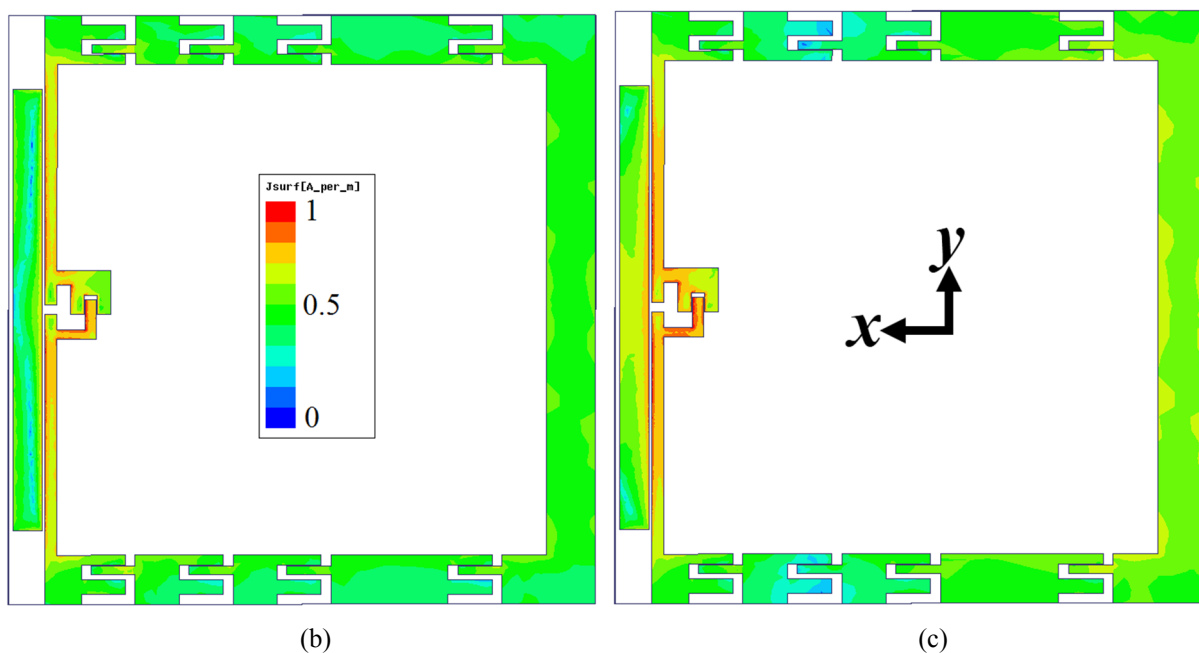


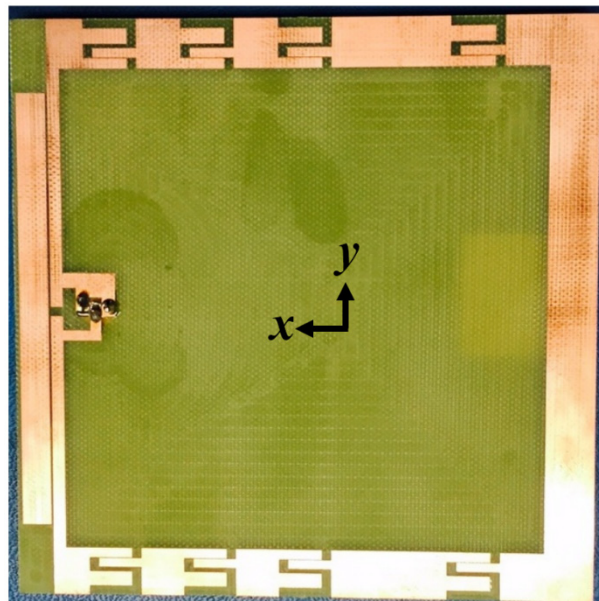
Fig. 4.19. (a) Radiation pattern of the antenna in the x-y plane (left) and y-z plane (right). Magnitude of surface current distribution at (b) 0.68 GHz, (c) 0.83 GHz and (d) 0.95 GHz. (maximum radiation in the x-direction)

### 4.2.8 Antenna Measurements

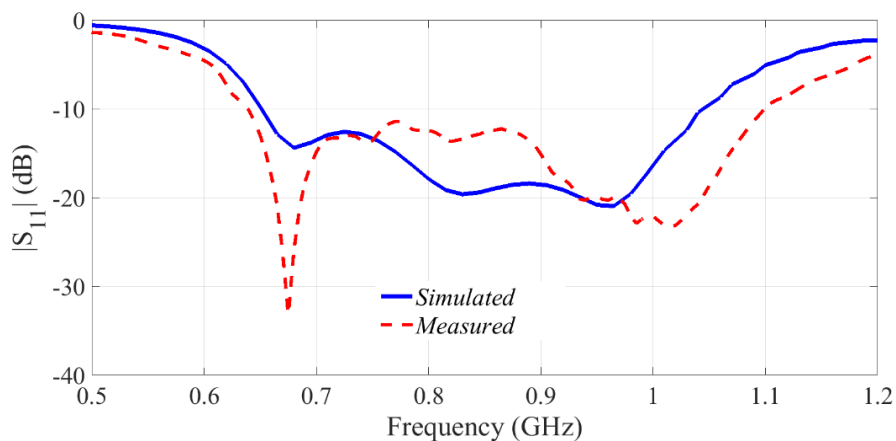
After a full analysis of the proposed antenna designs and considering the ease of fabrication, the antenna with the dimensions presented in Table 4-V was fabricated and is depicted in Fig. 4.20 (a). The antenna was fed using a SMA connector from the opposite side of the substrate using via

holes created on the CPW (red circles in inset of Fig. 4.14(a)). It is noted that the lower pins of the coplanar SMA were cut and removed to accommodate its pin connection through via holes. The central pin was connected to the central arm and the side pins were connected to the side arms, respectively. The measured reflection coefficient, which is in good agreement with the simulations, is presented in Fig. 4.20 (b). The antenna achieves a wide fractional  $-10$  dB bandwidth of 52 %, in the range of 0.64-1.1 GHz. The small shift at the higher resonance frequency is due to the soldering effects and the tolerance of the dielectric constant of the utilized substrate.

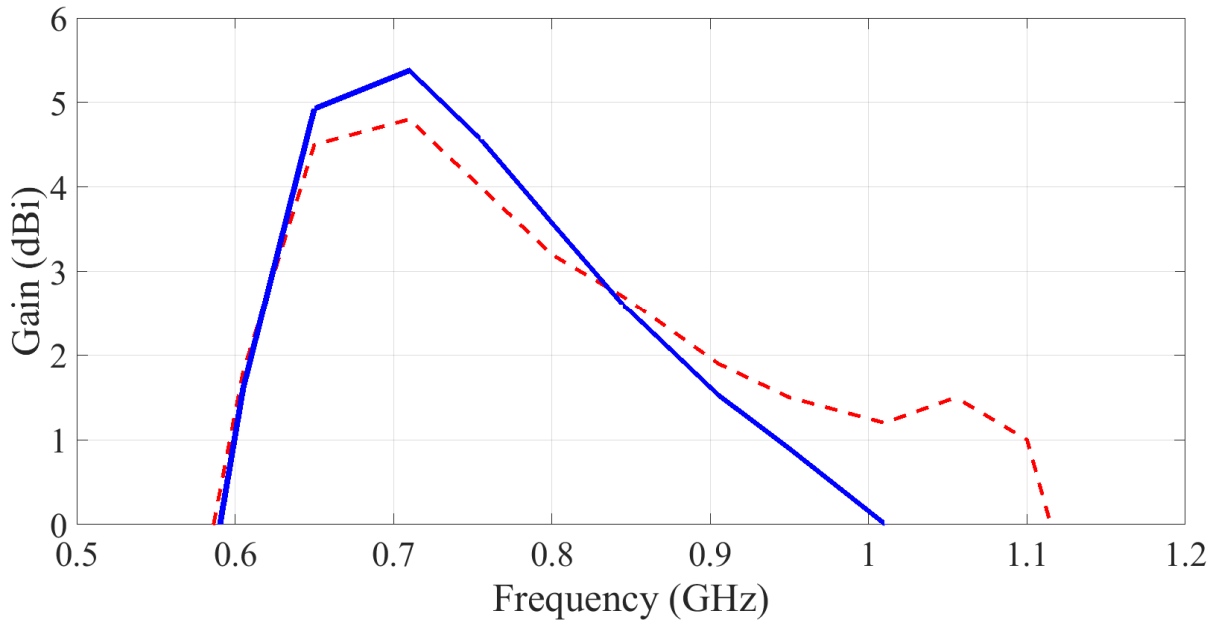
The gain of the antenna is measured in an anechoic chamber and is presented in Fig. 4.20 (c). It should be noted that as discussed previously, the proposed antenna presents a composite design in terms of radiation characteristics, and hence does not follow the general trend where the gain increases with frequency. To that end, the antenna achieves its peak gain of 4.8 dBi at 0.72 GHz, which is around the MZR frequency, and reduces to around 3 dBi at 0.83 GHz. Considering the radiation mechanism at this frequency, it can be seen that while the vertical arms of the equivalent dipoles are



(a)



(b)



(c)

Fig. 4.20. (a) Fabricated antenna, (b) measured vs. simulated reflection coefficient and (c) gain of the fabricated antenna. (Identical legends)

Table 4-V: Final dimensions of the proposed antenna (unit: mm)

$W_u$	10	$W_{g1}$	1	$l_s$	90	$W_{f2}$	1.8	$l_{f1}$	9	$g_2$	2.5	$W_{s2}$	2	$l_1$	4.5	$w_s$	6
$W_{f1}$	3	$W_{g2}$	0.2	$g_1$	0.5	$W_{s1}$	2	$l_{f2}$	9	$w_{sh}$	10	$l_2$	4.5	$s$	100	--	--

positioned at a quarter wavelength distance with respect to each other, the adjacent horizontal arms are in very close proximity to each other, which in turn reduces the amount of forward gain of the antenna. At the highest resonance of the antenna, the measured gain reaches its least value of 1.5 dBi, which is expected considering the very small size of the strip patch. By reconsidering the magnitude of the surface current distribution at 0.95 GHz shown in Fig. 4.19(d), it can be seen that the antenna effectively is radiating through the limited area of the strip. The gain value can be increased either by increasing the width of the strip patch or by adding more directors.

The radiation patterns of the antenna were measured in the two principal x-y and y-z planes and are presented in Fig. 4.21. As can be seen, there is a good agreement with the simulated results. The obtained FBR values, which are 10 dB, 11 dB and 10 dB at 0.68 GHz, 0.83 GHz and 0.95 GHz, respectively, are in a reasonably good agreement with simulated ones, and the experienced deviations can be attributed to the measurement errors. The cross polarization of the antenna is also measured and presented in Fig. 4.21. As can be seen, the antenna achieves a very low cross polarization that is more than 20 dB lower than the co-polarized value in the x-direction, which is the antenna's main radiating direction.

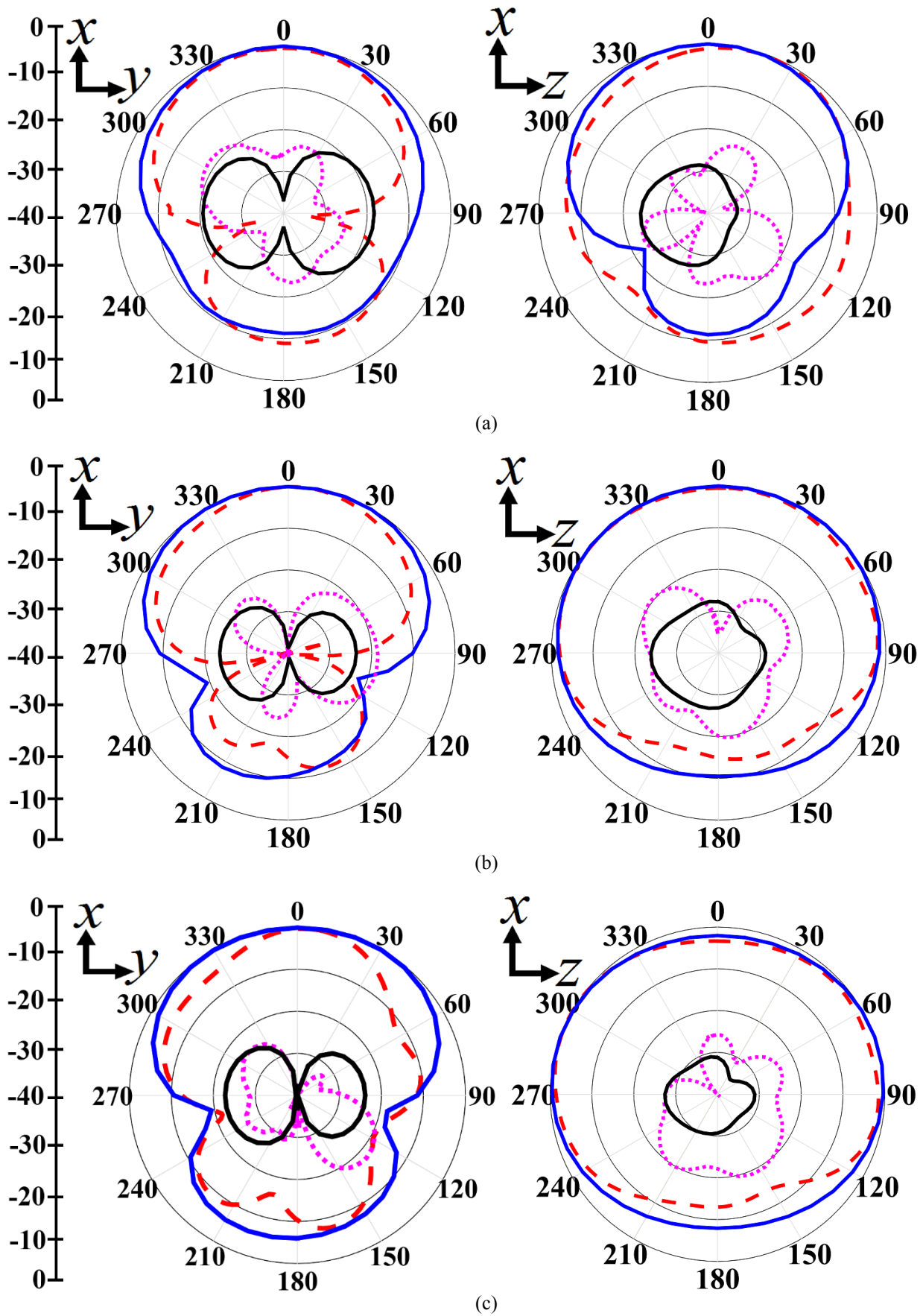


Fig. 4.21. Measured x-y plane (left side) and y-z plane (right side) radiation patterns of the antenna at (a) 0.68 GHz, (b) 0.83 GHz and (c) 0.95 GHz. (solid line: Simulated, dashed line: Measured). (Maximum radiation in the x-direction)

## 4.3 Capacitively Loaded Loop Antenna

In a continuing effort to further reduce the size of the antenna while maintain wide operating bandwidth, a capacitively loaded loop antenna is introduced in this section. To lower the resonance of the antenna and maintain its wide operating bandwidth within a compact size, capacitive loading and meandering techniques are utilized, respectively. Besides, a parasitic patch is utilized to enhance the higher frequency bandwidth.

### 4.3.1 Slot-Loaded Loop Design Analogy

The idea of creating slots on a loop antenna was proposed to utilize the generated phase difference for directivity enhancement [125]. The bandwidth of the antenna at higher frequencies was then enhanced by adding a quarter wavelength parasitic patch in the vicinity of the loop [40]. The size of the afore-stated design mainly depends on the perimeter of the one-wavelength loop. However, by including the slot the resonance mechanism of the antenna is divided into two modes: a one-wavelength loop and a half-wavelength dipole. The size of the slot,  $g$ , is adjusted to keep the aforementioned resonances close to each other to simplify the impedance matching process [125], [40]. Furthermore, the upper portion of the loop, which acts as a folded reflector for the folded dipole, is located at a proper distance from the dipole to reduce the amount of loaded capacitance, which is created by the slot, on the antenna's input impedance. Consequently, the end result of that approach is a large antenna that has side lengths comparable to half wavelength at the low operating frequency.

### 4.3.2 Design Procedure

The geometry of the proposed design is shown in Fig. 4.22. The antenna is designed on a square epoxy FR4 substrate with a side length of  $l$ , dielectric constant of 4.4, loss tangent of 0.02 and thickness of 0.8 mm. It is fed using an internal CPW structure that is excited using a surface mount SMA connector. The connector is properly connected to the antenna through holes from the opposite layer of the substrate as clarified in Fig. 4.22. This type of feeding is utilized to create a wide operating bandwidth [40]. The dimensions of the feeder are selected to match the antenna to  $50 \Omega$  input impedance.

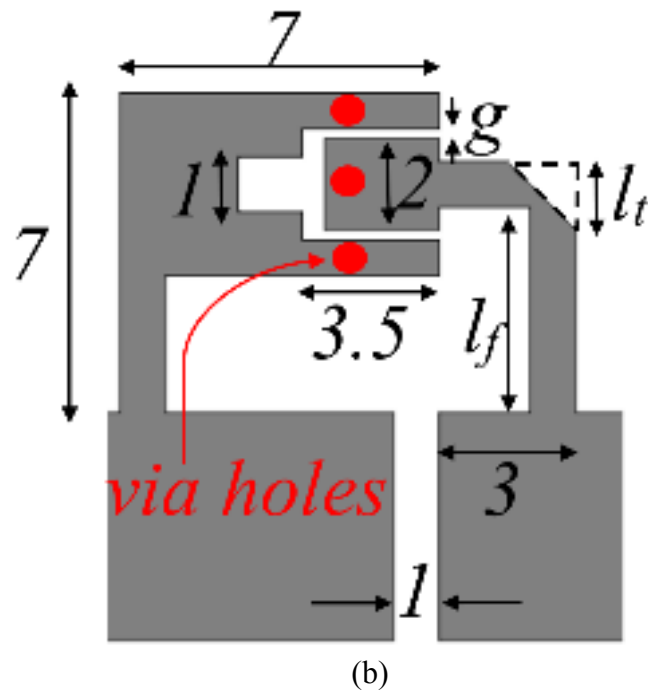
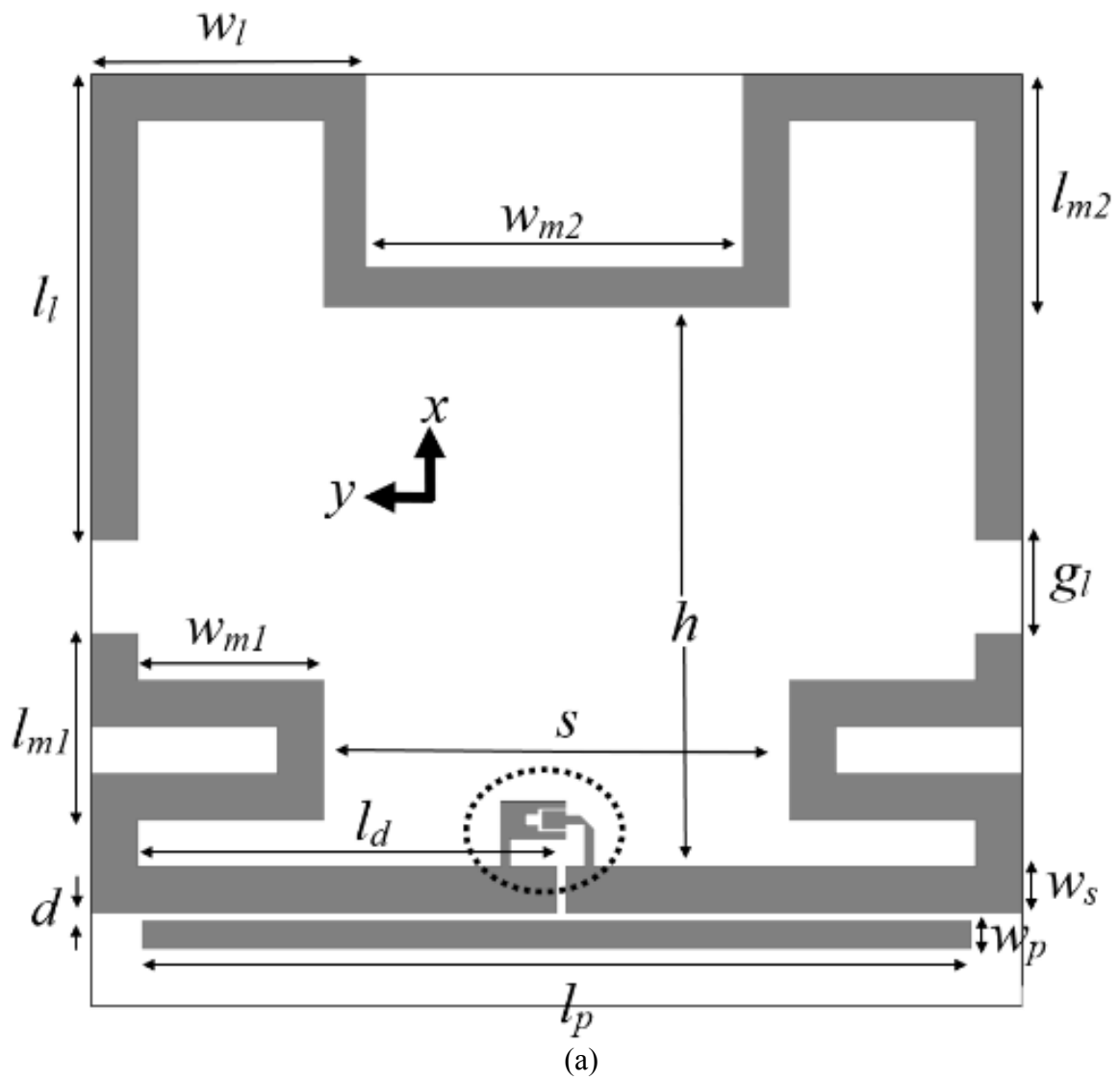
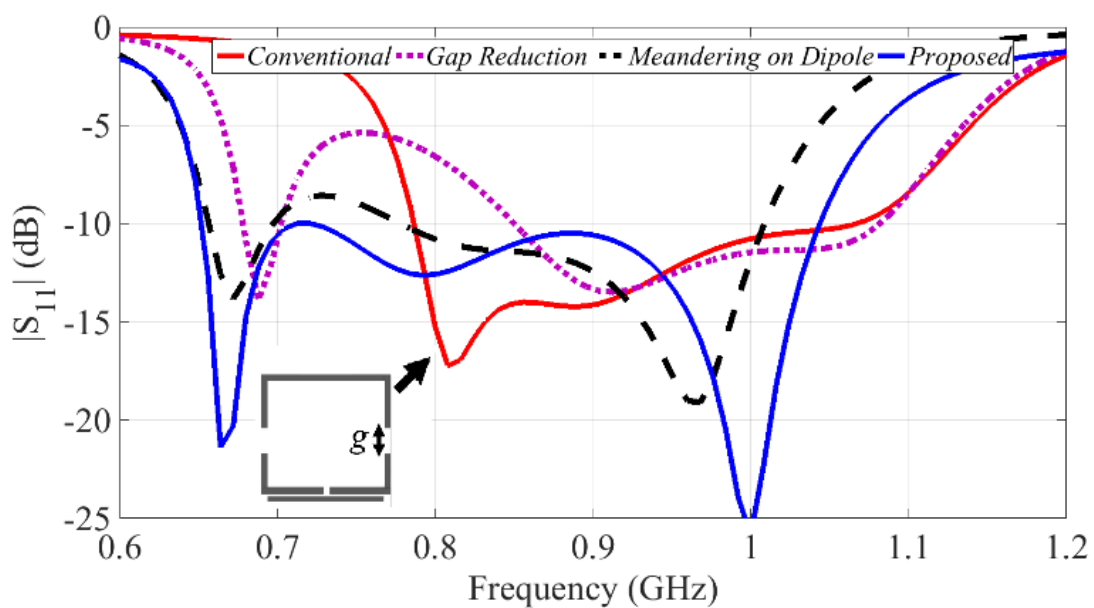


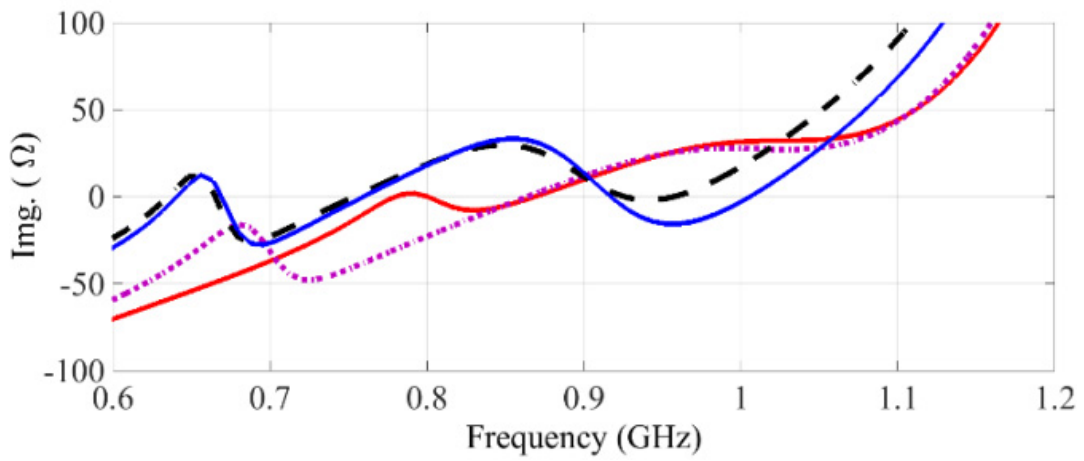
Fig. 4.22. (a) Geometry of the antenna and (b) feeding structure. (Unit: mm)

Firstly, a conventional slot-loaded loop is designed using the procedures proposed in [40] (See Fig. 4.23 (a)). The antenna is formed on a square substrate with 100 mm side length. This value is calculated as the maximum allowable size for locating two antennas at a quarter wavelength separation at the lowest operating frequency (700 MHz) on the back side of an average human torso. The obtained results using HFSS simulator show that the first resonance of the loop occurs at 810 MHz. Considering the wavelength of the lowest operating frequency, the antenna occupies an area of  $0.3 \lambda \times 0.3 \lambda$ , which is large for congestive heart failure (CHF) detection application operating at around 700 MHz. To lower the first resonance without increasing the substrate area, the size of the slot,  $g$ , is amended. As can be seen from Fig. 4.23 (a), by reducing the slot size to  $g_l = g/2$ , the first resonance of the antenna is lowered by 125 MHz without increasing the size of the loop. This can be explained using the input impedance of the antenna depicted in Fig. 4.23 (b) and (c). However, reducing the size of the slot increases the capacitive reactance of the antenna and splits the resonance modes of the loop and dipole, and consequently creates a mismatch at 680 – 850 MHz.

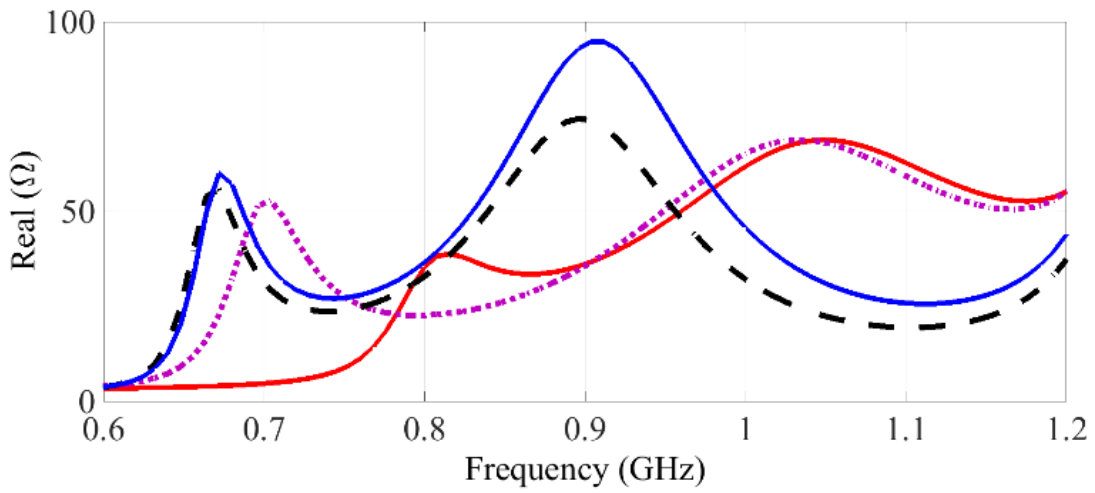
It is a well-known fact that increasing the length of a printed conductive strip enhances its inductance [127]. Therefore, to both reduce the mismatch and keep the substrate size fixed, the dipole arms' lengths are extended using a meandering approach. However, it should be noted that a capacitive reactance is also created as a result of the meandering process. Yet, this value is considerably small compared to the existing inductance, and hence it has a minimal effect on the input impedance [128]. As can be seen from Fig. 4.23 (a), with the latter modification the dipole's resonance frequency is lowered to 810 MHz and the mismatch between the two successive resonances at 680 MHz and 900 MHz is significantly reduced.



(a)



(b)



(c)

Fig. 4.23. (a) Reflection coefficient, (b) imaginary and (c) real parts of the input impedance of the antenna during evolution process (identical legends).

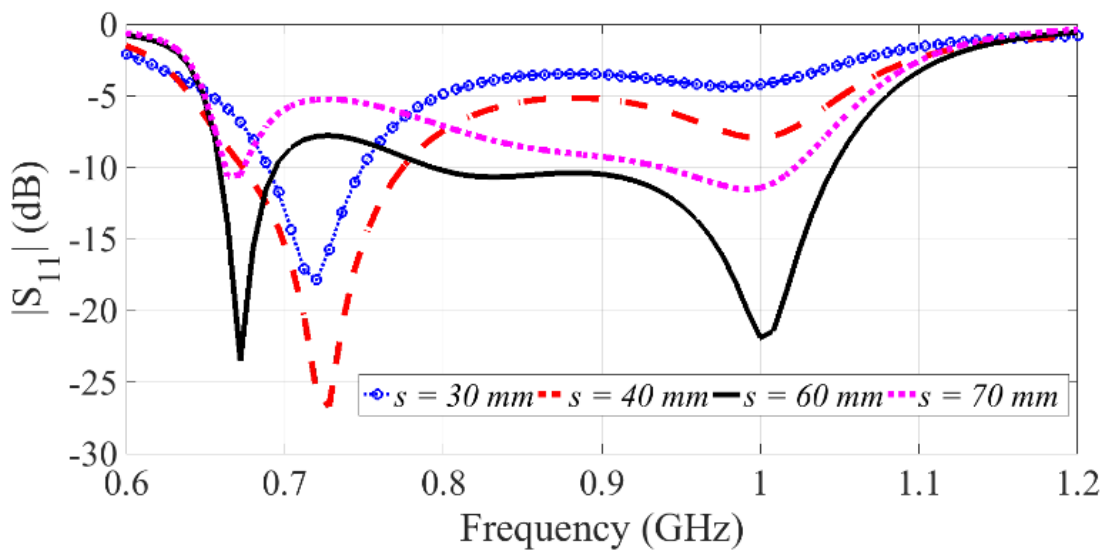


Fig. 4.24. Reflection coefficient of the antenna for different values of space between dipole arms.

Table 4-VI: Geometrical details of the final design in (mm)

$l_p$	89	$l_{m2}$	25	$w_{m1}$	20	$d$	0.8	$l_{m1}$	20	$l_f$	4.5	$w_s$	5	$h$	60	$g$	0.18
$l_d$	45	$l_t$	1.3	$w_{m2}$	40.5	$s$	50	$l_l$	50	$w_l$	29.5	$w_p$	3	$g_l$	10		

### 4.3.3 Further Discussion

Considering the confined substrate area, varying the width of the meandered arms of the dipole,  $w_{m1}$ , changes the distance,  $s$ , between them and has a significant effect on the input impedance. As can be realized from Fig. 4.24, increasing the separation between the arms reduces the created inductance, and hence the mismatch remains at lower frequencies. On the other hand, smaller  $s$  values create a great capacitive coupling between the arms of the dipole, alter the coupling between the dipole and the parasitic patch, and consequently worsen the impedance matching at higher frequencies. Therefore, to create a balance between the required inductance and maintain the wide operating bandwidth, an additional meandering is applied to the top portion of the structure to mitigate the impedance mismatch at 700 – 780 MHz, and improve the coupling between the antenna and the parasitic patch. With this configuration, the simulated results of the final design achieve a wide fractional bandwidth of 50 % (0.65 – 1.05 GHz), which is 20 % wider than the recent counterpart designs [125], [40], [101]. Moreover, its size is reduced by 73 % compared to the similar designs [125], [40]. The optimum sizes of the antenna elements are presented in Table 4-VI.

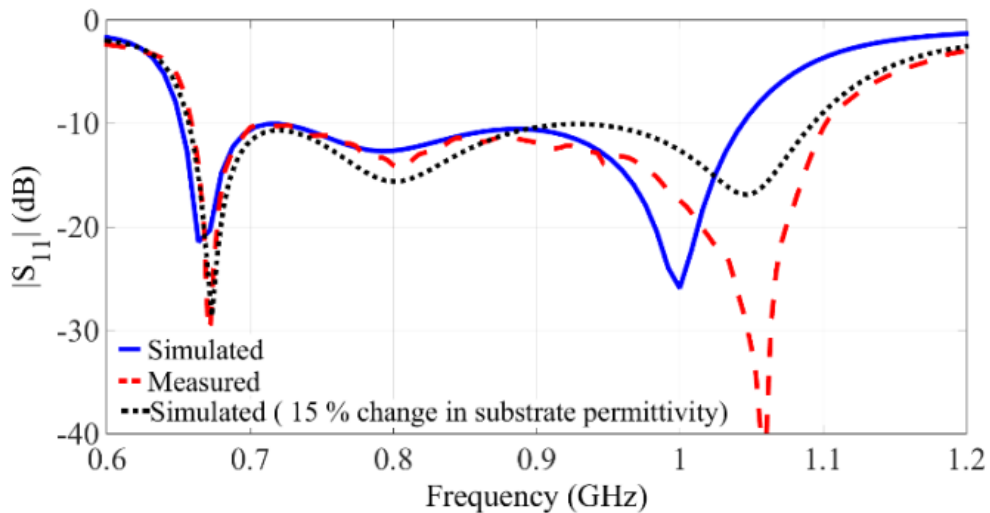
### 4.3.4 Antenna Measurements

The final design was fabricated and its performance was validated by experiments. Ferrite beads were used during the measurements to avoid the effect of coaxial cable. The measured and simulated reflection coefficients of the antenna in free space are presented in Fig. 4.25 (a). As can be seen, the antenna achieves a wide measured fractional bandwidth of 50 % at 660 – 1100 MHz which is in a good agreement with the simulated results. The experienced shift, especially at the higher resonance of the antenna, is due to the dielectric constant variations of the utilized substrate. This was attested in the simulation environment by varying the permittivity of the substrate by 15 % (See Fig. 4.25 (a)).

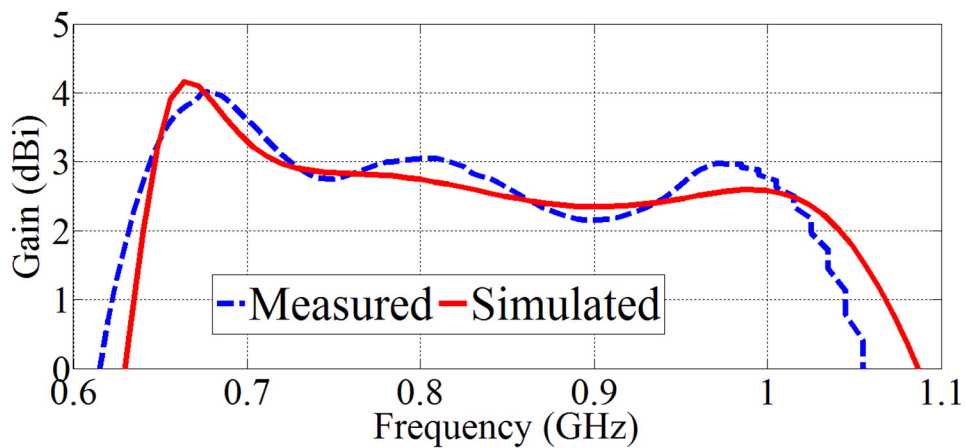
The antenna's gain and radiation patterns were measured in an anechoic chamber and the obtained results are presented in Fig. 4.25 (b). The antenna reaches a peak gain of 4.1 dBi at 665 MHz and achieves a stable gain of more than 2.2 dBi over the intended bandwidth for fluid detection application. The radiation patterns of the antenna at three resonances are depicted in Fig. 4.25 (c)-(e). It should be noted that unlike the antennas that are designed to operate in on-body [129] or off-body

communications [130], the radiation patterns of the proposed antenna in the vicinity of the torso are not of interest, and are only presented to confirm that the maximum radiation is indeed at the desired direction, e.g.  $-x$ -direction.

The antenna has cross-polarization purity better than 17 dB, which is not depicted for brevity. It achieves a front to back ratio (FBR) of 9 dB at 680 MHz. This is due to the fact that the introduction of the slots on the vertical arms of the loop creates 90 degree phase delay between the currents of the horizontal arms of the loop, and therefore acts as two dipole antennas that are excited with different phases and located within a quarter wavelength distance resulting in a significant suppression of the radiation in  $x$ -direction [125]. At 800 MHz and 1050 MHz, the antenna can be analyzed as a quasi-Yagi antenna with a folded dipole driver, a folded reflector and a director; hence, it radiates the accepted power away from the reflector and achieves a front-to-back (FBR) of over 6 dB. By increasing the distance between the top and bottom portions of the design,  $h$ , and adding parasitic strips as directors, the FBR value can be enhanced at higher frequencies. However, considering the essential FBR value of over 4 dB for medical diagnostic applications, the structure is not modified any further.



(a)



(b)

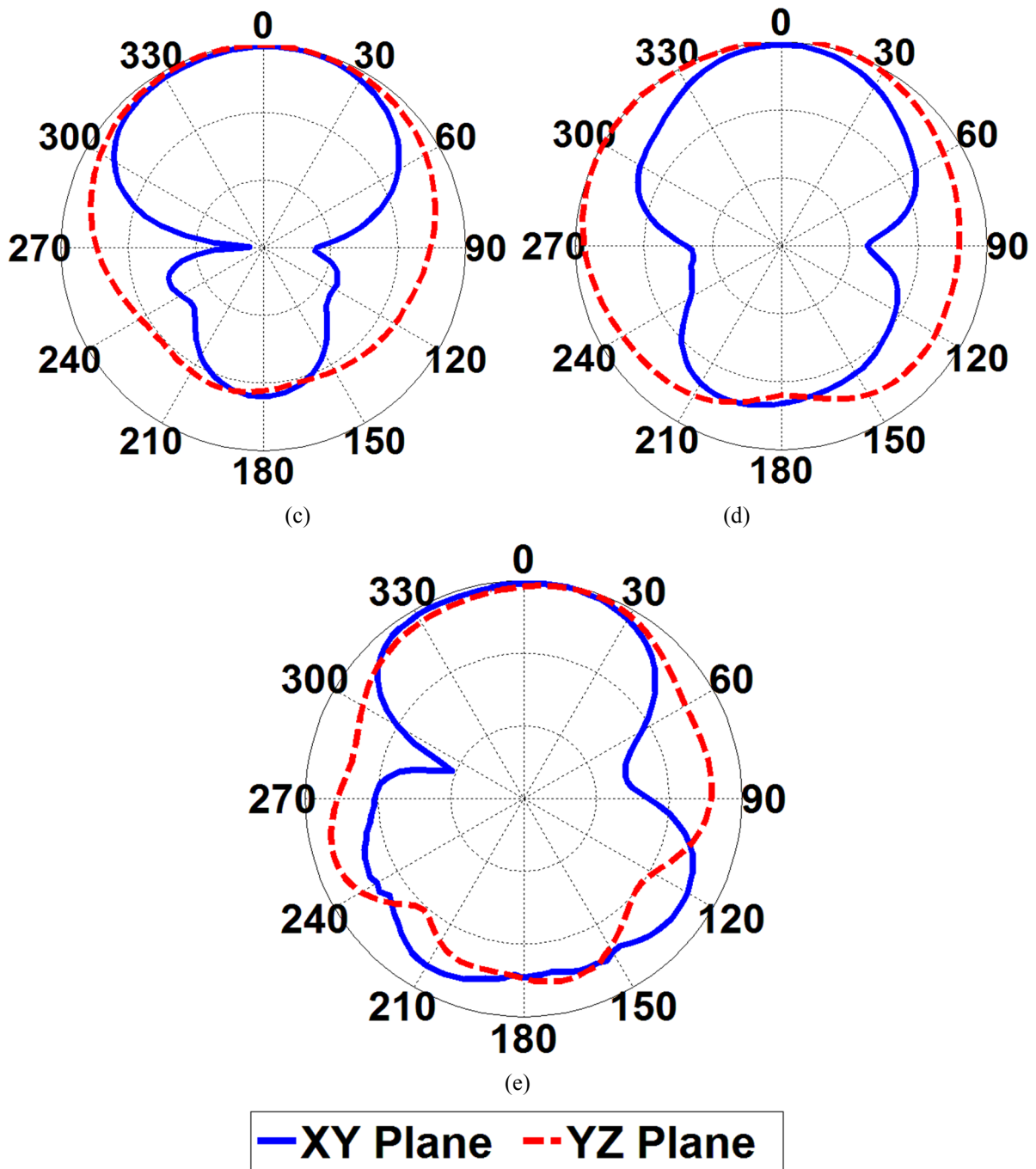


Fig. 4.25 Measured vs. simulated (a)  $|S_{11}|$  and (b) gain of the antenna. Measured radiation patterns of the antenna at (c) 680 MHz, (d) 800 MHz and (e) 1 GHz (maximum radiation: -x-direction) (Scale: 30 dB, division: 10 dB).

As the antenna is designed for medical diagnostic applications, the safe use of the antenna on human subjects is verified. To that end, the specific absorption rate (SAR) for the antenna is calculated using the human model in HFSS that has more than 300 organs with 2 mm resolutions. The SAR for the antenna is calculated as 0.01 (W/kg) over 10 gram of tissue with a transmitted power of 1 mW, which is below the safe range of 0.4 (W/Kg) defined by IEEE for medical applications.

# Chapter 5

## Torso Imaging Systems

This chapter will be introducing different platforms and systems that are built using the designed compact antennas. Different sizes and structures of the antennas brings a great level of freedom in building various types of platforms with different configurations. However, these systems are all based on the fact that there is a reasonable symmetry between left and right side lungs. While not being completely identical, as shown in Fig. 5.1, the left and right side lungs have similar structures except for the fact that part of the heart is inside the left lung. This image, which is obtained using X-ray reveals the possibilities and challenges of designing a platform and detection algorithm that can reduce the effect of heart that has a very high dielectric constant of around 60 and conductivity of 1.17 [S/m]. Therefore, different arrangements of antennas and scanning approaches are proposed. These systems are categorized under linear and circular/cylindrical systems. Linear systems are presented in this chapter and the circular/cylindrical scanning systems are described in chapter 6. Additionally, two clinical ready systems are presented in chapter 7. These systems are tested using phantom, animal tissues and human beings.

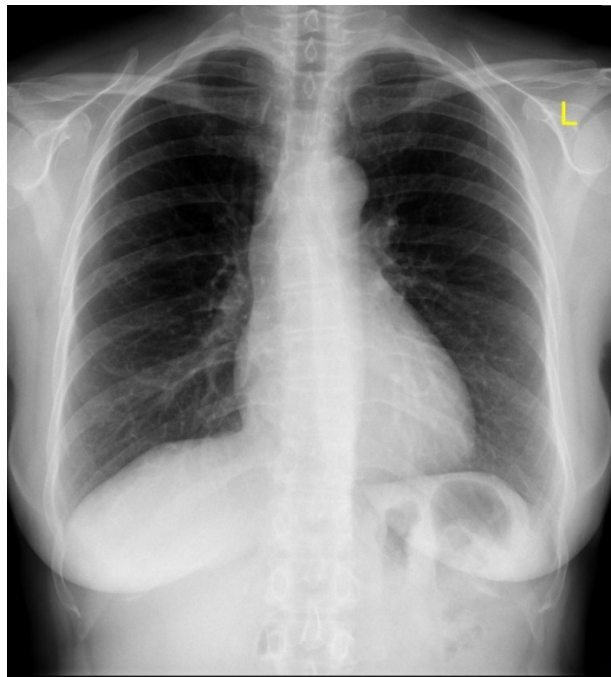


Fig. 5.1 Torso X-ray. (Image obtained from radiopaedia.org, Case courtesy of Dr Henry Knipe, Radiopaedia.org, rID: 31525 [131])

## 5.1 Torso Phantom

To test the designed systems in a realistic environment, a torso phantom is required. In the present literature, single layered homogenous phantoms such as the one from SPEAG, Switzerland, have been used. However, throughout this thesis, a torso phantom with rather complex internal structure is used for testing the system. As depicted in Fig. 5.2, the utilized phantom is an accurate life-size anatomical model of the human torso with  $43 \times 40 \times 48 \text{ cm}^3$ , chest girth of 94 cm and approximate weight of 18 kg [132]. In addition, it also includes the internal tissues and organs, such as ribs, fat, heart, lungs and an abdomen (as a block). The soft tissues are made of polyurethane (gravity 1.06) and synthetic bones are made of epoxy resin. The phantom is originally designed by the company Kyoto Kagako, Japan for testing CT scan systems. In the designed system, the phantom is used for electromagnetic (EM) based imaging, which requires an accurate emulation of the electrical properties of the human torso across the utilized frequency band. The suitability of this phantom was confirmed by testing the electrical properties (permittivity and conductivity) of its parts using Agilent 85070E dielectric probe kit. We found that while the phantom does not fully mimic the electrical properties (permittivity and conductivity) of all the torso human tissues, it has reasonable dispersive properties to test the designed system. Additionally, it provides a complex environment similar to torso, which provides an excellent test environment for the designed system.

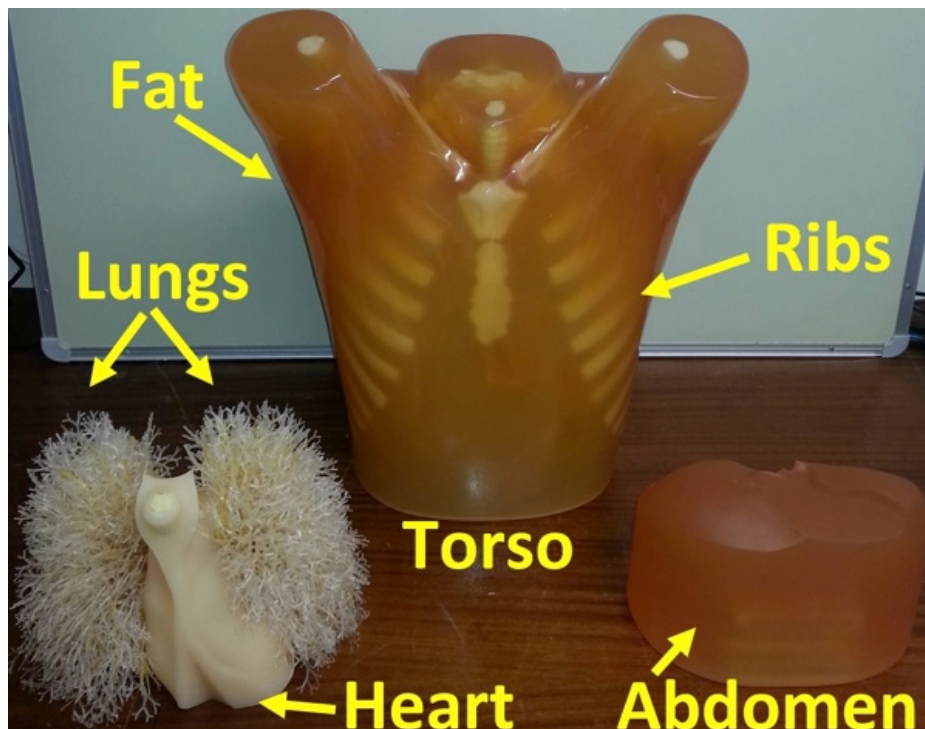


Fig. 5.2 Utilized torso phantom in the thesis with the internal organs.

## 5.2 Linear Scanning System with Synthetic Aperture Radar Imaging Approach

The configuration of the proposed imaging system is depicted in Fig. 5.3. This system is comprised of a wideband and unidirectional antenna explained in section 3.2.1 of the thesis that is mounted on a plastic base and manually adjustable platform. To reduce the cost of the system and provide mobility, the conventional bulky and costly VNA system is replaced with an inexpensive and light N7081 microwave transceiver by Keysight Company [133]. Based on the information that is directly obtained from data sheet [133], the N7081A Microwave Transceiver is a compact vector network analyzer (VNA) that uses a broadband, multi-tone source and broadband receivers to capture the instantaneous S-parameters at multiple tones simultaneously in a faster way than traditional swept frequency VNAs. The device has the broad frequency operation from 100 kHz to 5 GHz with the capability for full 2-port VNA and is controlled by an external PC via USB or LAN using a simple and easy to implement API.

The antenna is connected to this transceiver, which is connected to a laptop via a USB cable and is controlled using a custom programmed software interface. The laptop also includes the imaging algorithm that will be used for post processing of collected scattered signals. The main target of the system is the detection of fluid inside the lungs at its early stages. For signal processing and image reconstruction, the system uses a synthetic aperture focusing technique, which requires one antenna scanning the torso linearly in the vertical direction. The system's architecture and method of signal processing and image reconstruction algorithms are explained hereafter.

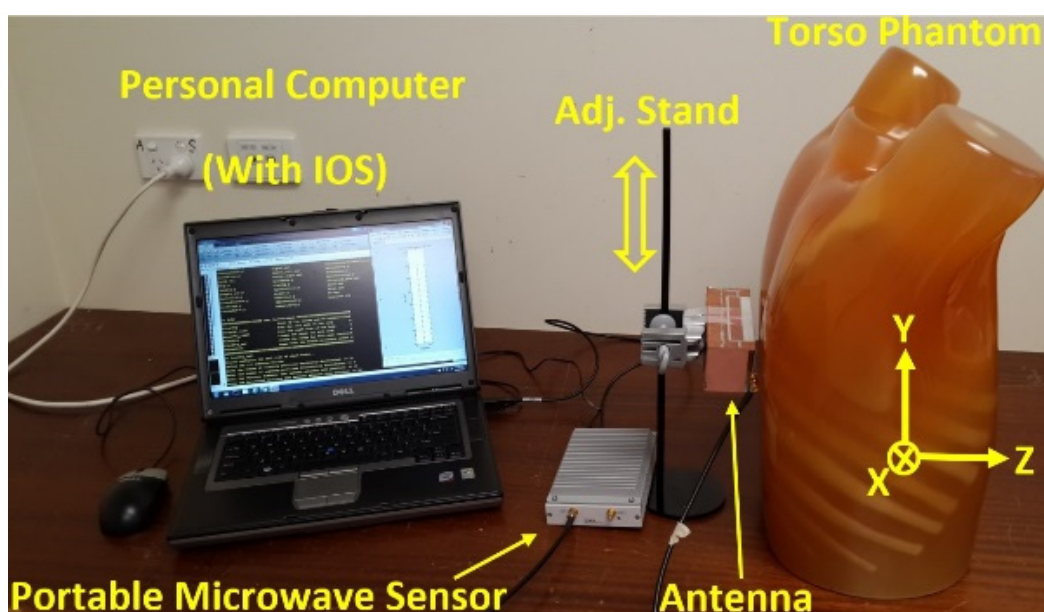


Fig. 5.3 Proposed imaging system.

## 5.2.1 Scanning Approach and Data Acquisition Process

The utilized transceiver sends pulses which occupy the band 0.5-1 GHz via the antenna towards the torso and captures the backscattered signals. Those signals are converted by the same transceiver to digital data and stored in the laptop for processing. An image reconstruction algorithm is used to interpret those stored digital signals and sends the computed two-dimensional image matrix to the display equipment. A synthetic aperture focusing technique, which requires one antenna moving in a vertical direction at the back side of the torso, is utilized. Rear side of the torso is selected due to the similar structure that it provides for male and female subjects. Within the whole hardware infrastructure, all the modules are controlled and synchronized by a laptop equipped with an in-home operation system (IOS), which is coded in MATLAB environment. Its main function is to manage the whole detection process over three scopes: 1) Initializing the microwave transceiver and specifying the frequency band of the transmitted pulse, level of transmitted power, and sampling density of the frequency-domain data, 2) controlling the pre-test calibration procedure and synchronize the data acquisition with user-defined scanning requirement, and 3) conducting the signal processing and image reconstruction.

The detection process is initiated by a two-stage scanning: 1) The fast scan, which collects  $M$  reflection coefficients from individual scan positions by performing electronic sweeping in the frequency domain, and 2) the slow scan, which repeats the process of the fast scan at various antenna positions.

## 5.2.2 Experimental Results

The experiment was conducted in the microwave laboratory at The University of Queensland on the above introduced realistic human torso phantom. In the measurements, the antenna was located at a distance of 15 mm from the phantom and moved manually in steps to scan the torso. In the experiment, 63 scanning positions with step length  $\Delta x = 30 \text{ mm}$  and  $\Delta y = 10 \text{ mm}$  were used. The assumed axes planes are depicted in Fig. 5.3. The transceiver sends a pulse that is formed by 158 frequency samples uniformly distributed within the frequency range from 0.5 to 1.0 GHz.

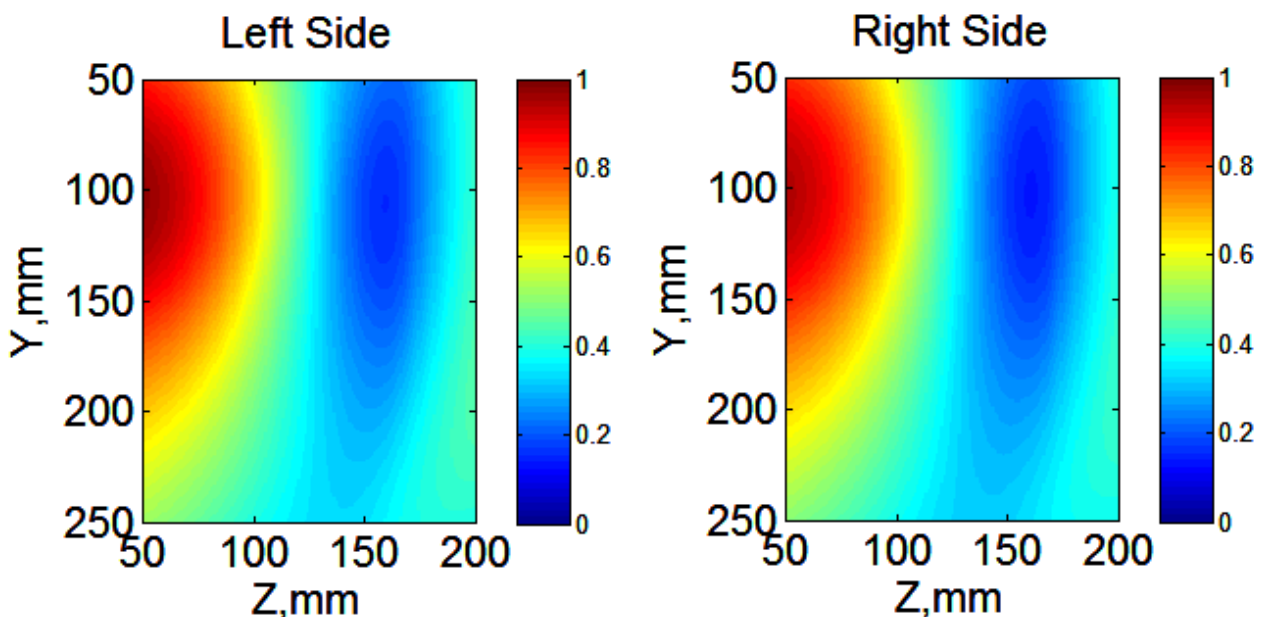
To keep the system compact and avoid the possible adverse effects of mutual coupling, the concept of virtual array is utilized in the detection algorithm. This algorithm proposes a 2-D rectangular synthetic aperture based on the scanning track which involves 3 displacements (6 cm) along X-axis and 21 displacements (20 cm) along Y-axis. The aperture width along X-axis is of significance to sharpen the sensing beam for the sake of achieving better isolation between the

scattered signals from left and right side of the lung, while the aperture height along Y-axis provides a fine resolution to depict the reflection profile distributed vertically.

The collected data is translated into images using the synthetic aperture focusing image reconstruction algorithm [134]. These images show distribution of the scattering profile inside the torso. To magnify the effect of presence of the fluids inside the lungs, similar to X-Ray approaches, the case of inflated lungs was investigated. Due to the large amount of air, the inflated lungs have much lower dielectric constant compared to the deflated ones. Thus, a high contrast can be realized between those lungs and any accumulated fluids. That high contrast is needed for an accurate detection of any early fluid accumulation.

The obtained images for the left and right lungs of a healthy subject (Fig. 5.4 (a)) indicate an acceptable similarity in the distribution of their reflected signals. The dominating scattered signals come from the skin-air interface (located at  $Z=50$  mm) and the ribs. No strong scatterer can be seen inside any of the two lungs located within the  $Z$  range of 100-160 mm.

To emulate a case of fluid accumulation, 50 mL of water is inserted in the left lung. The reconstructed images for this case are shown in Fig. 5.4 (b), which indicate a strong scatterer inside the left lung at the exact position of the fluid (depicted by a black rectangle). Since the utilized antennas do not have a pencil-beam radiation, the added water to the left lung has some effect on the image of the right lung. However, the intensity in the image of the right lung is lower than that of the left lung. The overall visual inspection of the obtained images for the cases representing healthy and sick subjects indicates the feasibility of detection using the proposed system. Moreover, the system can even be used to locate the accumulation of fluids.



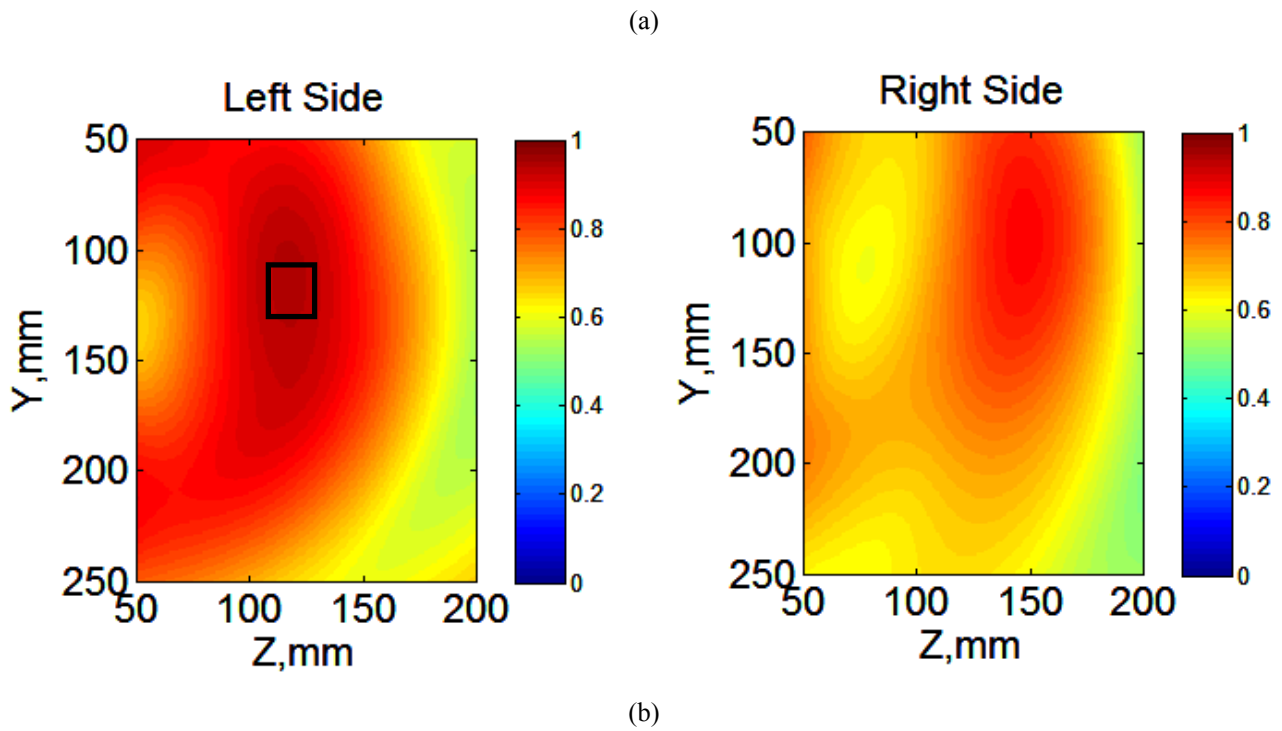
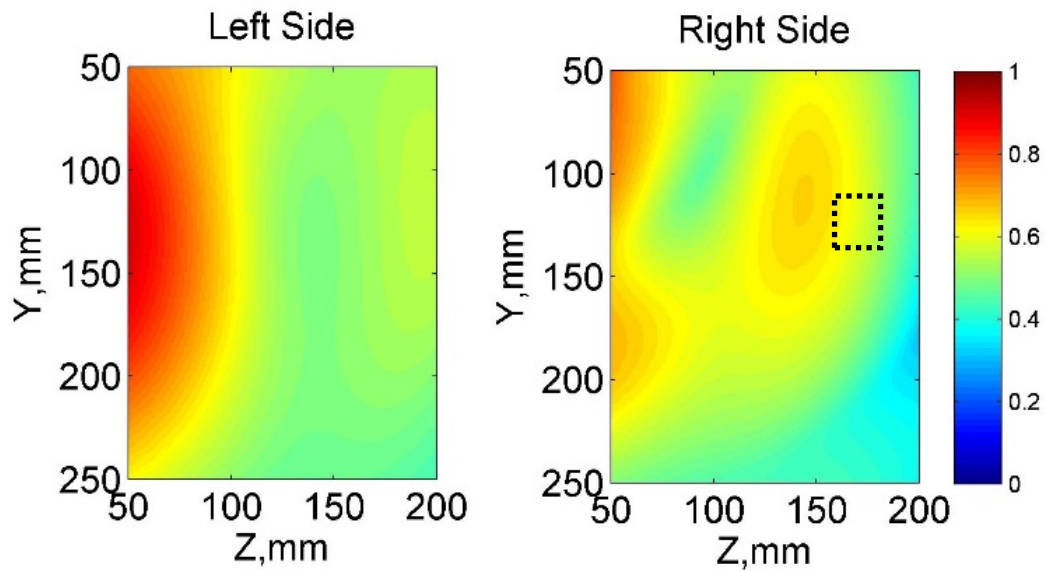


Fig. 5.4. Images from a phantom representing (a) healthy case, and (b) early stage heart failure with fluid accumulated at the left lung.

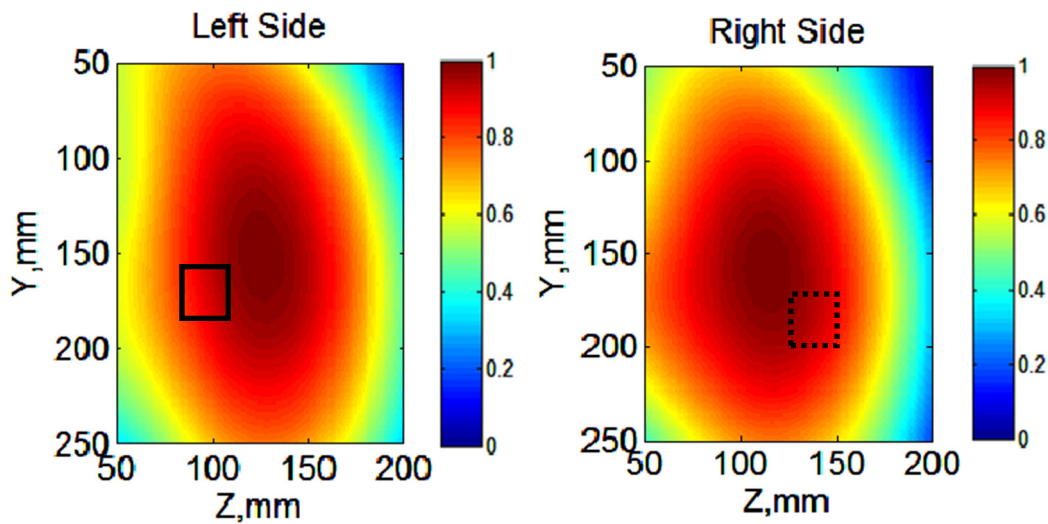
### 5.2.3 Effect of Antenna Characteristics on Imaging Results

To investigate the effectiveness of using the proposed directional antenna, it was replaced with a bidirectional antenna, which is its planar structure, and the same previous measurements and processing procedure were repeated. The attained results are depicted in Fig. 5.5. As it can be seen, the obtained image shows a strong reflection on the right side, which would indicate fluid accumulation. This happens due to the fact that the antenna receives strong reflections both from the torso and the surrounding objects causing a positive false decision. Therefore, a unidirectional radiation is necessary to reduce and ideally cancel the effect of surrounding objects especially behind the antenna, e.g. stand or wall or any possible object in the real scenario.

To verify the importance of using wide frequency band in the detection system, the previous procedure using the proposed antenna was repeated, but this time using the lower 50% of the band. The results depicted in Fig. 5.5 (b) reveal that the fluid can still be detected; however, its location cannot be identified due to the presence of a ghost target (shown as dashed rectangle) in the other healthy lung. Therefore, utilizing unidirectional and wideband antenna is of vital importance to obtain meaningful and precise detection results.



(a)



(b)

Fig. 5.5 (a) Images using a bidirectional for a healthy case, and (b) images using the proposed antenna with reduced bandwidth for an early heart failure affecting the left lung (black rectangle depicts actual detection of location of water and dashed rectangle shows false detection).

### 5.3 Automated Linear Scanning System Using Image Subtraction Method

This part of the thesis presents the design of an automated and operational system, which provides a novel solution to detect and locate the presence of fluid inside the lungs.

#### 5.3.1 Introduction

The first novelty of the system is the design and implementation of a fully automated platform and data acquisition procedure. This is of great importance in terms of speeding the data capturing

and reducing vertical movement as well as exact positioning of the antenna. Secondly, the applied method utilizes the frequency dependent scattering profile obtained by sending and capturing a wideband signal into the torso over a scan area. As stated before, the basis of the used techniques is the fact that lungs' tissues and accumulated fluid have a large difference in their electrical properties; as shown in section 5.2, these changes can be revealed in the scattering profile of a monostatic-radar approach. However, the scattering profiles themselves are small compared to the total reflection caused by other parts of the body. So, to visualize them clearly, a differential technique that compares the scattering profile of the left and right side lungs is used. Based on a parameter study of healthy and varying levels of unhealthy cases, a threshold is proposed to differentiate between healthy and unhealthy cases. Using this threshold, the lowest detectable amount of fluid is determined (system limitation).

### 5.3.2 System Design

The block diagram of the system is shown in Fig. 5.6. The system is controlled by a laptop which is connected to N7081A microwave transceiver via a USB cable on one side, and to a stepper motor via an Ethernet cable on the other side. Using a coaxial cable, the microwave transceiver is connected to an antenna that is attached to the automated vertical scanning platform in the form of a linear rail that is moved by the afore-stated stepper motor. The antenna, which is designed using folding technique, operates between 0.77 GHz and 1 GHz and is located at a certain distance " $d$ " from the torso phantom.

The designed system operates in a way that the transceiver with the antenna operates as monostatic radar. It sends microwave signals towards, and receives the backscattered signals from, the torso. The frequency dependent backscattered signals are converted to time domain signals and then visualized as radargram images. These images show the intensity of scattering within different regions in the torso and can be used to assess the health condition of the torso.

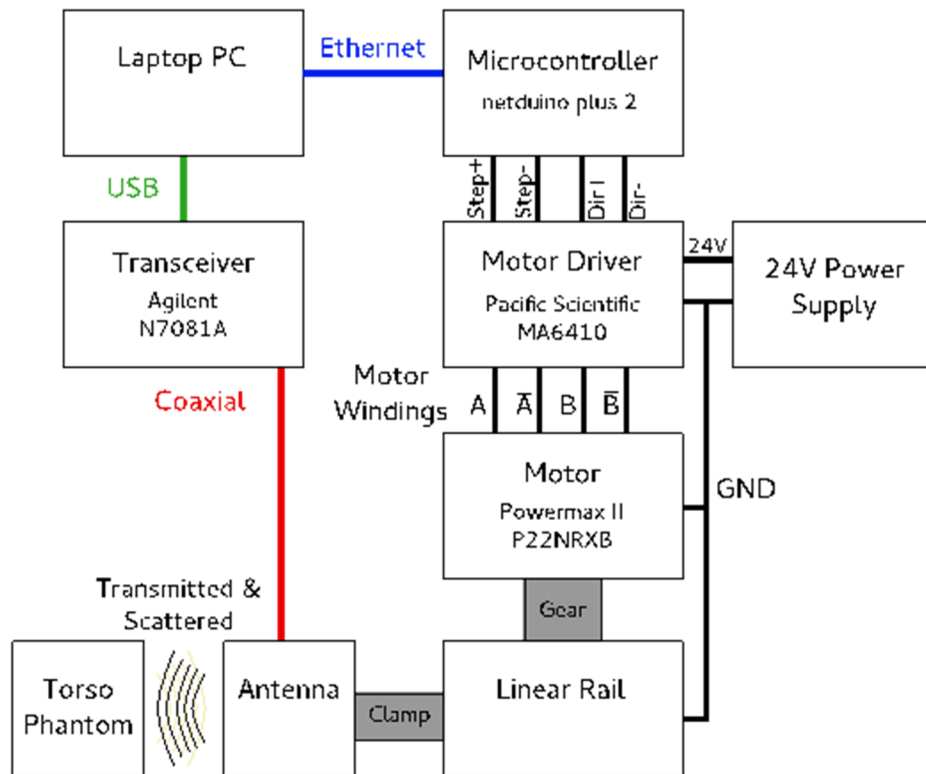


Fig. 5.6 Block diagram of the system.

### 5.3.3 Platform Details

The measurement mechanism is controlled by a laptop with MATLAB installed. It controls both the data acquisition device as well as the automatic antenna positioning. Data acquisition is performed using the Keysight N7081A microwave transceiver connected via USB. In this system, the device is used to gather the frequency dependant scattering parameters over the operating frequency band of the antenna, which is from 0.77 GHz to 1 GHz.

The automatic antenna positioning is performed using a linear rail which is driven using a stepper motor. The stepper motor is a Powermax II P22NRXB, which has a step size of 1.8 degrees and a maximum speed of 1500 RPM. The stepper motor is an eight-pin motor and is connected using series windings. A Pacific Scientific 6410 Step Drive controls this motor using a 2.5 Amp output mode. The step drive converts step and direction inputs from an embedded processor to the required motor winding currents for the stepper motor. The embedded processor providing these inputs is a netduino plus 2, which features an ARM Cortex M4 based platform running at 168 MHz and has 100 kB of RAM and 384 kB of flash storage. This embedded processor is connected to the laptop via an Ethernet based network connection, and is controlled using transmission control protocol (TCP) network packets.

The positioning of the antenna on the linear rail was found to require 85 motor steps per millimetre, meaning that for each measurements the motor is stepped 850 times to achieve 10 mm motion between measurements.

### 5.3.4 Data Acquisition

The data acquisition process is performed using a single script inside MATLAB which is depicted as flowchart in Fig. 5.7. The process begins with calibrating the microwave transceiver using a standard 1-port calibration procedure of open, short and load at the end of the coaxial cable which feeds the antenna. This calibration process is done to eliminate the undesired signals such as internal reflections of the antenna and antenna-air signal distortions.

Next, the data acquisition process is performed which involves the acquisition of 21 measurements in the vertical (y) direction, each separated by 10 mm and totalling to a scan distance of 210 mm. For each measurement, the data is first acquired by the microwave transceiver, and then a command is sent to embedded system to move the linear rail 10 mm. To synchronize the position with measurements, status packets are requested by the laptop to ensure that the motor has finished moving before the measurement is taken and subsequent motion commands.

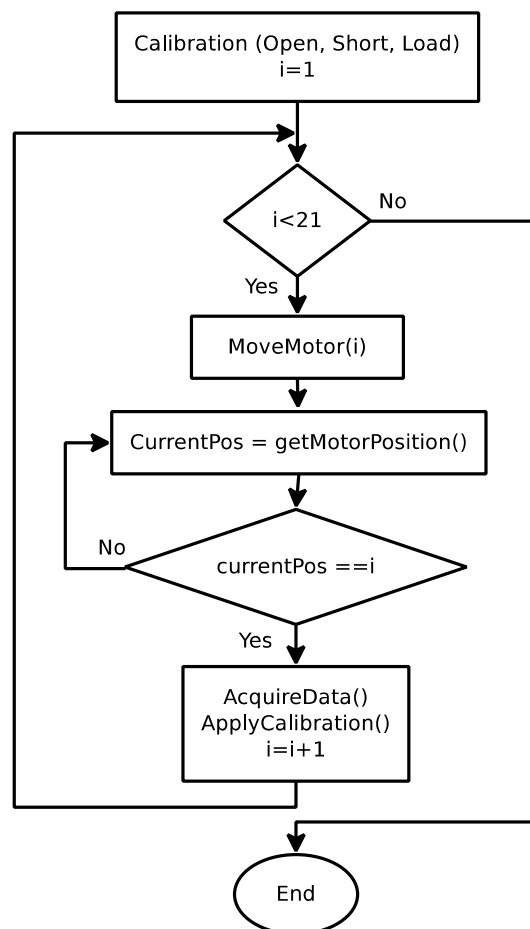


Fig. 5.7 Flowchart of data acquisition procedure

### 5.3.5 Data Processing

In the proposed system, the acquired data (backscattered signals) is recorded as frequency dependent scattering parameters. The first step of processing involves the conversion of each measurement to time domain using an inverse Fourier transform. It should be noted that as the scattering parameters are normalized unit-less quantities, the inverse Fourier transform is also normalized unit-less quantities that correspond to the correlation between the transmitted and scattered pulses. In the experimental results presented in this section, the inverse Fourier transform has been scaled to propagation distance in millimetres. Each of these time domain measurements overlaid on top of each other is shown in the top part of Fig 5.7. By combining the time domain measurements, or traces, over a scan distance, the resulting image is a radargram. Such an image, as depicted in the lower part of Fig. 5.8, shows the scattered wave power delay profile along a set of recorded positions. A precise linear scan is performed by using the stepper motor and linear rail. Hence any error in the measurement is dependent only on the noise and the accuracy of phantom positioning relative to the antenna.

To visualize the healthiness of the lungs, the difference between the left and right scan or a difference in the radargrams between the left and right side of the torso, is used. This differential process provides a clearer picture, as the changes, that may exist, are small variations in phase and amplitude compared to the total scattered signal due to the small size of the target (fluid) to be detected in early stage. The resulting difference can be thought of as a likelihood of whether the left or right side has larger reflections or scattering, at different locations in the lung. Where a high positive value (shown in red) is obtained, it depicts a strong scattering on the left side of the lung at that location, whereas a large negative value (shown in blue) indicates the stronger scattering is present on the right side at that location.

In a healthy case, the tissue distributions of the left and right sides are close, and provide a comparable scattering profile. However, small differences are present due to the heart being present on the left side of the body (see Fig. 5.2). Without using sophisticated signal processing, detectable changes in water accumulation need to provide a scattering difference above this level. Consequently, the monitoring and detection time becomes almost instant. It takes less than three minutes to scan single lung, and less than five seconds to obtain the radargrams using a laptop with ordinary processing capability.

To make sure of the safe use of the proposed system when tested on human subjects, the specific absorption rate (SAR) is calculated using the available human body model in HFSS. The maximum attained SAR value is found 0.06 W/Kg which is below the safe threshold defined by IEEE.

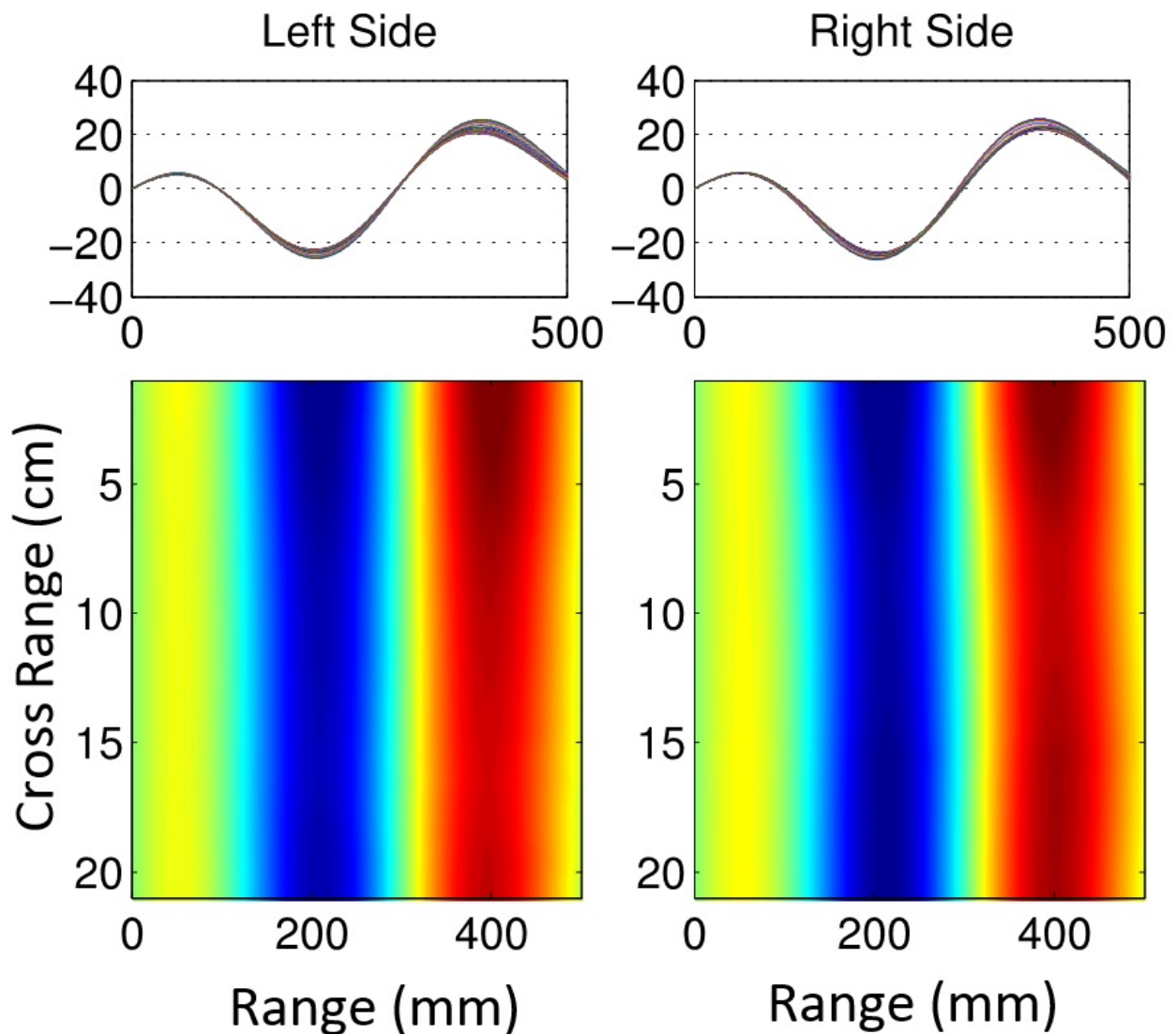
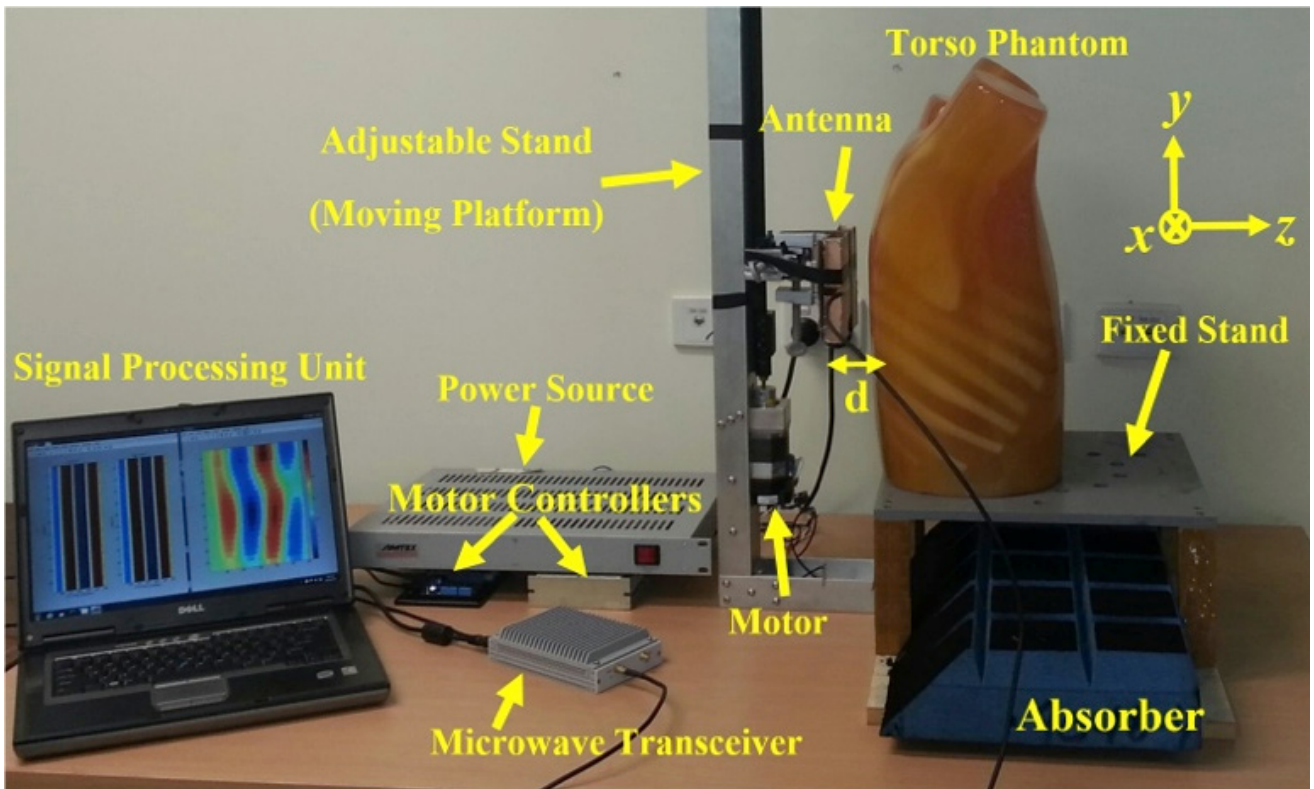


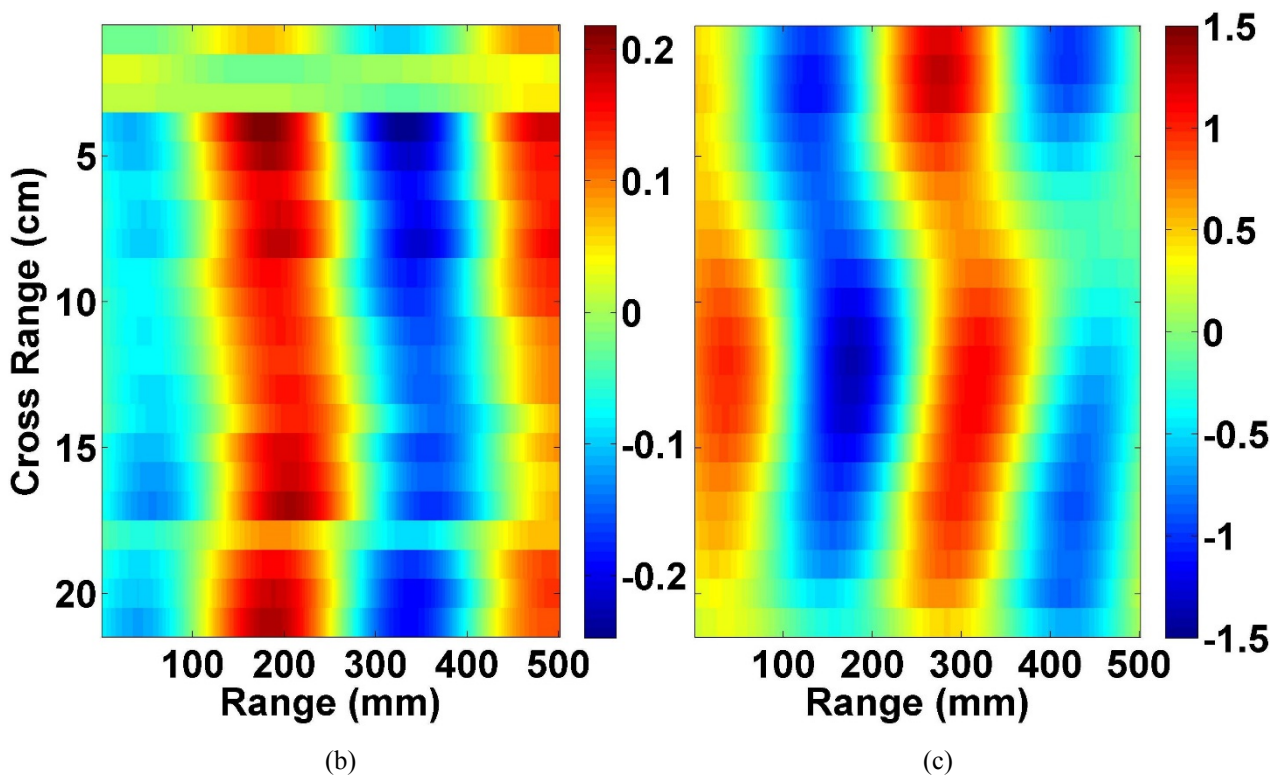
Fig. 5.8 A typical radargram.

### 5.3.6 System Calibration

The complete experimental setup and integrated devices are depicted in Fig. 5.8. As mentioned before, prior to data acquisition, the system is calibrated in the used frequency range of 0.77 – 1 GHz. To start the experiment, the torso phantom is located at a distance  $d = 10$  mm from the antenna. This distance is optimized during the experiment process to obtain the best imaging results. To eliminate any source of error in the detection process, several similar experiments were conducted on the phantom to ensure that the same experiment can be repeated with minimal errors. To that end, the phantom was scanned by the antenna using the automated stand. The same scan was repeated several times. The difference between two consecutive scans is depicted in Fig. 5.9 (a). The maximum error is less than 0.25. This maximum error value will be added to the threshold to obtain rigorous detection decisions. This error value can vary with both the antenna gain and distance separating the



(a)



(b)

(c)

Fig. 5.9 (a) The designed congestive heart failure detection system. Differential scattering profile of (b) measurement error and (c) healthy case.

phantom structure and the antenna. This value is also related to the ratio of transmitted to scattered power and henceforth, is not dependent on the transmitted power. Therefore, the error value is neither a fixed nor standardized value, and is thus specific for the current system. Therefore, it needs to be calibrated and redefined when any system element, e.g. antenna, is replaced. The same would apply to all of the values of the radargrams presented in this section.

Using the differential method, the difference between the scattering profile of left and right side lungs of a healthy case were obtained. In this case, there is no water inserted inside the phantom. As depicted in Fig. 5.9 (b), and as predicted, due to the partial presence of heart inside the left lung, a difference of maximum of 1.5 is observed. This value is verified through several experiments. Therefore, a detection threshold of 1.75 (healthy + error) is designated for the current system.

### **5.3.7 Minimum Detectable Level of Fluid Accumulation**

To determine the minimum detectable level of fluid accumulation in the lungs and to verify whether the designed system is able to detect early fluid accumulation, many experiments using different amounts of fluids inserted inside one, or both of the lungs in plastic bags, were performed. In those experiments, successively smaller amounts of water are located in the top portion of the left lung (arbitrary position) starting with 10 mL. In Fig. 5.10 (a), the difference in the scattering profile for a case of 10 mL has strength of +6. This scattering profile is four times stronger than that of the healthy case (1.5). Rescaling the scattering profile of a healthy case (see Fig. 5.10 (b)) to that of an unhealthy case shows detection of water on the top portion of the torso.

To push the limits of the system, the amount of the emulated water was further reduced. Through extensive experiments, it was found that 4 mL is the smallest detectable amount. As depicted in Fig. 5.10 (c), the strength of the scattered signal from inner tissues of the torso is 2.5, which is 1.7 times stronger than the healthy case. Comparing the differential scattering profile of healthy (Fig. 5.10 (d)) and unhealthy (Fig. 5.10 (c)), a larger change is present at the top portion of the lung, where water was located (arbitrary position). The location of the water is depicted by a black rectangle in this and all upcoming figures. By reducing the amount of water to less than 4 mL, the strength of the reflected signals falls to under the threshold region which is counted as undetectable case. The scattering profile of this case is not depicted due to its similarity to the one of the healthy case.

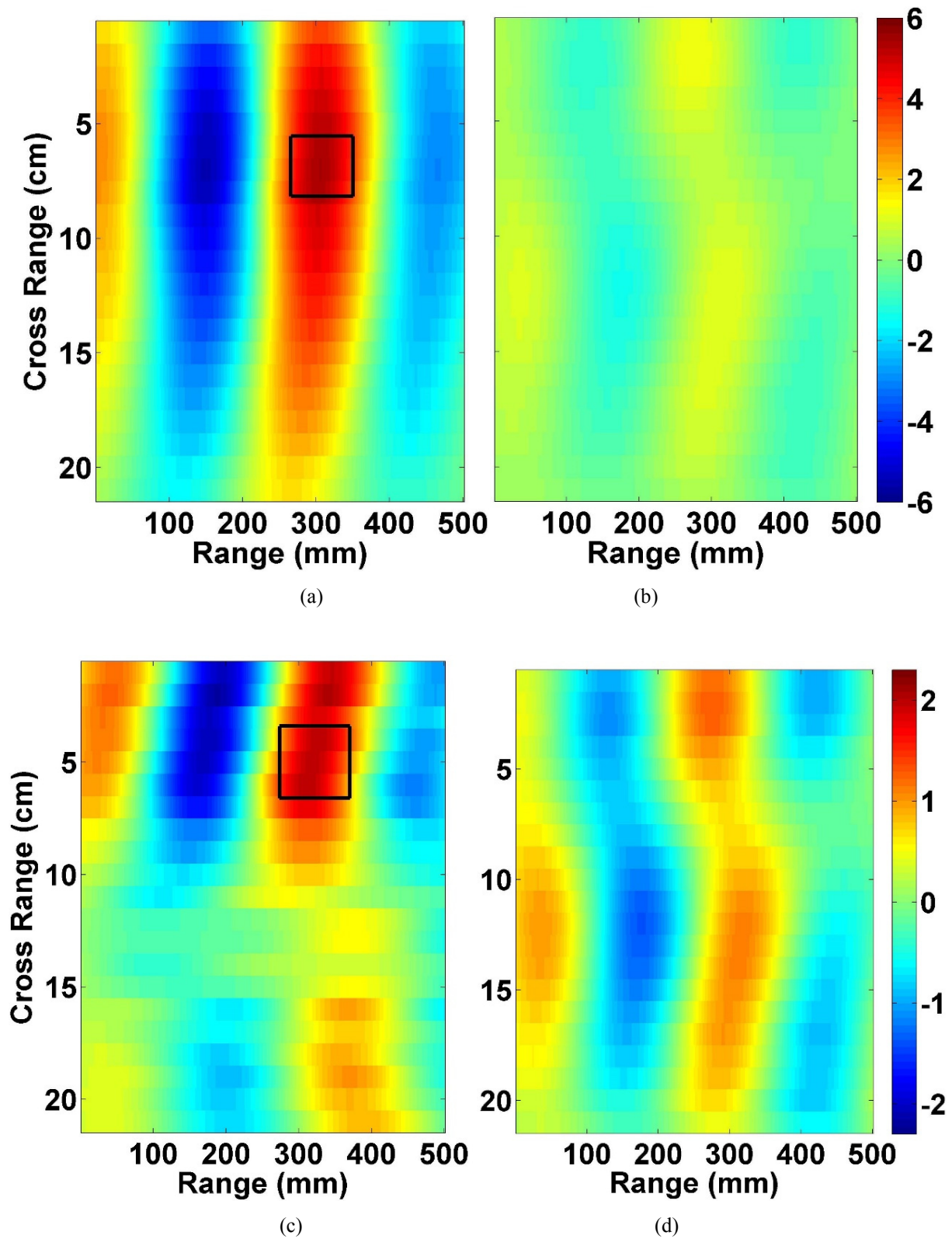


Fig. 5.10 Differential scattering profile of lowest detectable fluid compared to healthy cases with identical scaling, (a) 10 mL water, (b) healthy and (c) 4 mL water, (d) healthy.

### 5.3.8 Fluid Localization

To examine the capability of the system in positioning the accumulated fluid in addition to its detection, another experiment was conducted. A plastic bag containing the smallest detectable water amount (4 mL) was located in the middle of the rear side of the torso phantom. In the second case, the plastic bag is located in the lower front side of the phantom. The differential scattering profiles of investigated cases are depicted in Fig. 5.11. It can be seen that the strength of the signal is analogous to the previously detected 4 mL water content. However, the location of the water varies, which verifies the positioning ability of the system.

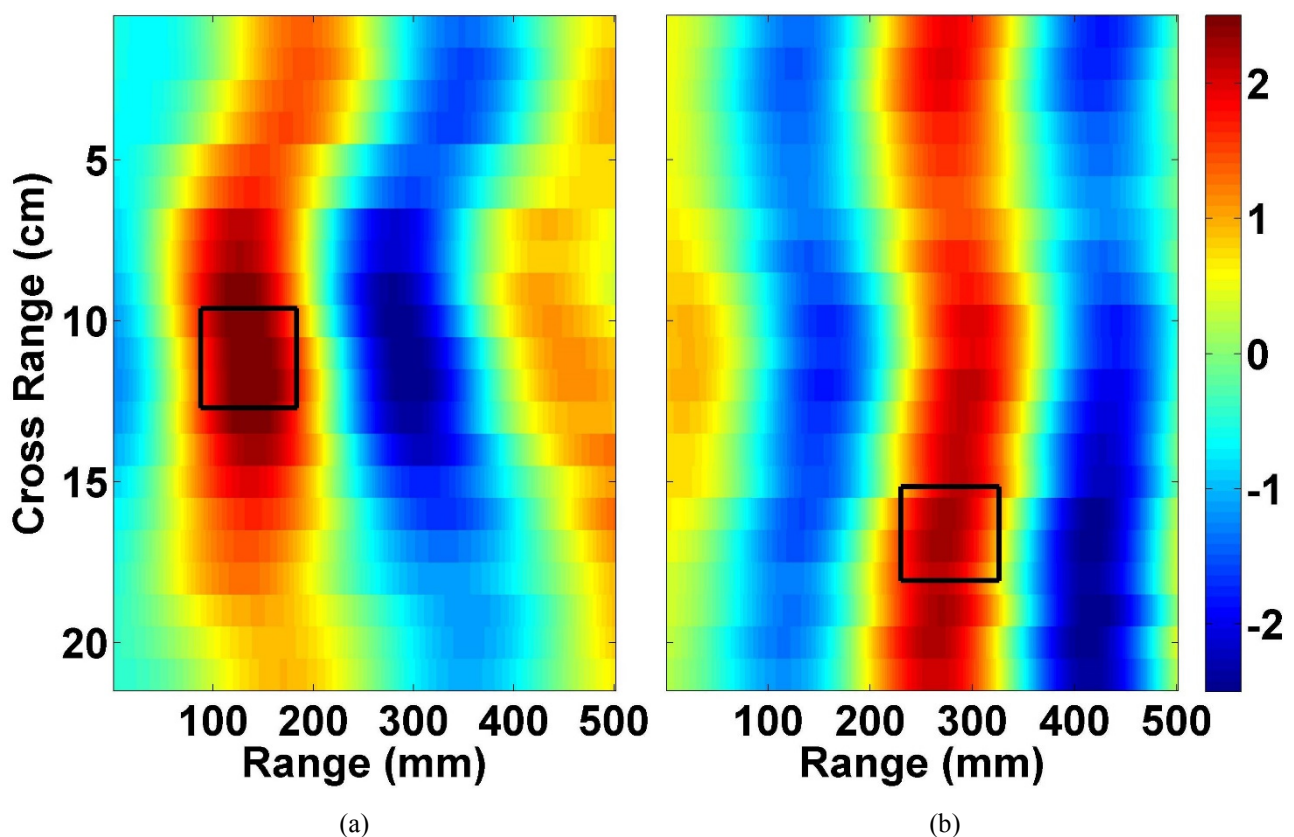


Fig. 5.11 Detecting presence and position of water in two cases, (a) water located at middle rear side of phantom and (b) water located at lower front side of the phantom.

### 5.3.9 Detection in the Case of Presence of Fluid in Both Lungs

One of the cases which has never been investigated before, is the occasion where, there is fluid accumulation in both lungs. This is one of the rarest, yet, possible cases in fluid accumulation manifestation. Considering the fact that due to gravity dependency and lung geometries, the possibility of fluid accumulation in both lungs with exactly the same value is near zero, the current

system can be efficient in detecting the presence of water using similar differential method. In that regard, two plastic bags with two different water contents, 15 and 8 mL, were located in the left and right lungs, respectively. From Fig. 5.12 (a), it can be seen that the scattering profile has a strength of 3.5 which is more than two times stronger than a healthy case. To push the limits of the system, the water content difference was reduced to 4 mL. From Fig. 5.12 (b), one could easily locate the water in the middle of the lungs. The same limit (4 mL) applies for the detection of water in the case of presence of fluid in both lungs.

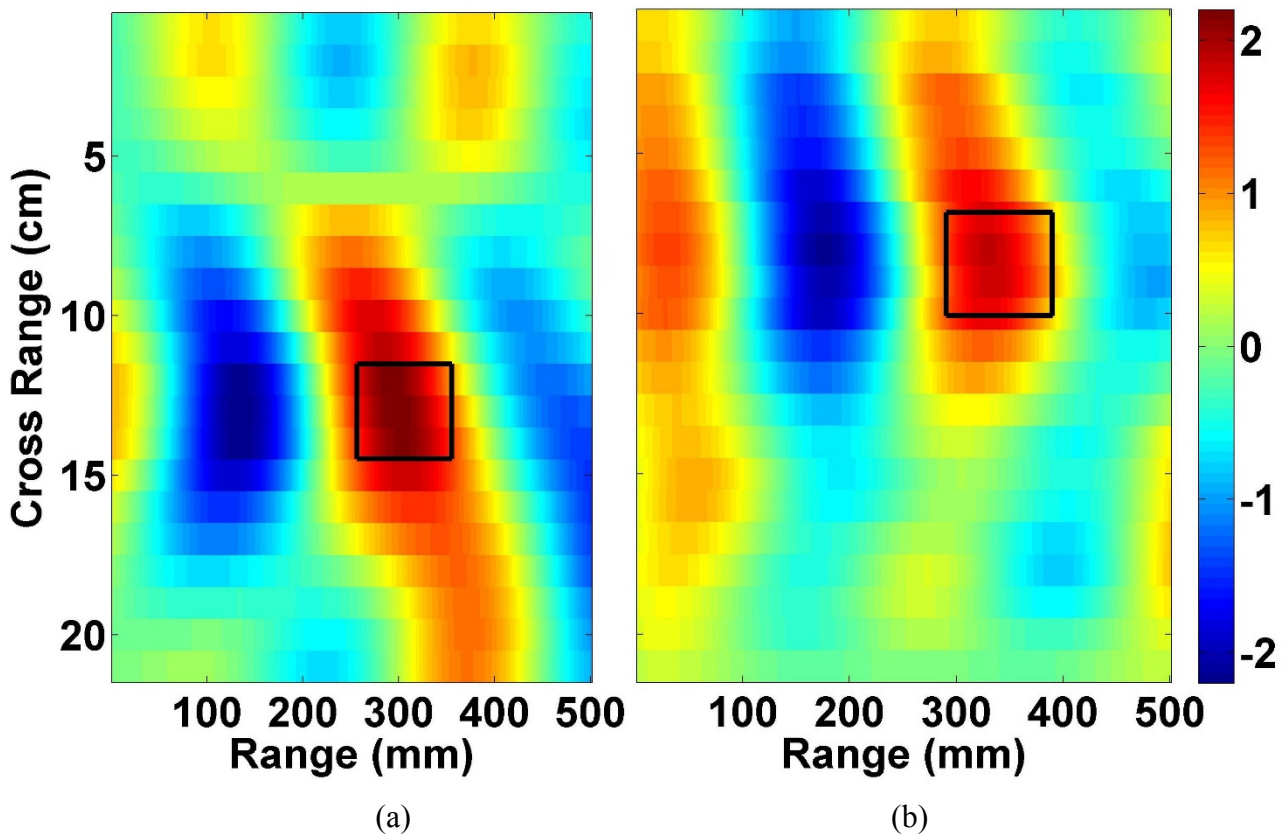


Fig. 5.12 Detecting presence and position of fluid in cases of accumulation inside both lungs, (a) water content with 7 mL difference (b) water content with 4 mL difference.

## 5.4 Automated System Employing Two Antennas for Simultaneous Vertical Scanning

### 5.4.1 Introduction

As can be seen from the above described system, there are two main parameters that can be still improved. The first one is related to the measurement error that exist between the left and right side measurements due to the positioning of the system that needs to be moved and secondly the measurement time that can be reduced. A very simple, yet effective approach to eliminate these

drawbacks is to use two antennas that can scan the torso at the same time. Therefore, firstly, the measurement time is reduced by 50% compared to the previous systems that are using single antennas and the movement error is eliminated. Therefore, the accuracy of the system is increased due to the improved threshold level. Considering the lateral sizes of the proposed antennas and the widest operating bandwidth between them, the three dimensional slot antenna presented in section 3.3 of the thesis is selected. Because of the very simple imaging technique that is intended to be used, building radargrams, this antenna is ideal as its operating bandwidth starts from 0.55 GHz that provides excellent penetration.

In the automated system depicted in Fig. 5.13, two antennas are attached to a linear platform which is used to provide accurate positioning along 21 positions separated by 1 cm along the rear side of the torso in the z-direction. Each movement and measurement takes less than 1 second, with the entire scanning process taking less than one minute. The back-scattered signals are acquired and then converted to time domain signals using an inverse Fourier transform on a laptop. Similar to the previous automated system with single antenna, these signals are normalized as unit less quantities to show the correlation between the transmitted and scattered signals. Combining individual time domain measurements results in the formation of a radargram, which shows the scattered wave power delay profile inside the torso area (Fig. 5.14). The received signals for the rear left and rear right sides of the torso are similar for a healthy case as depicted in Fig. 5.14. Thus, any difference between those two signals is due to fluid accumulation in the lungs.

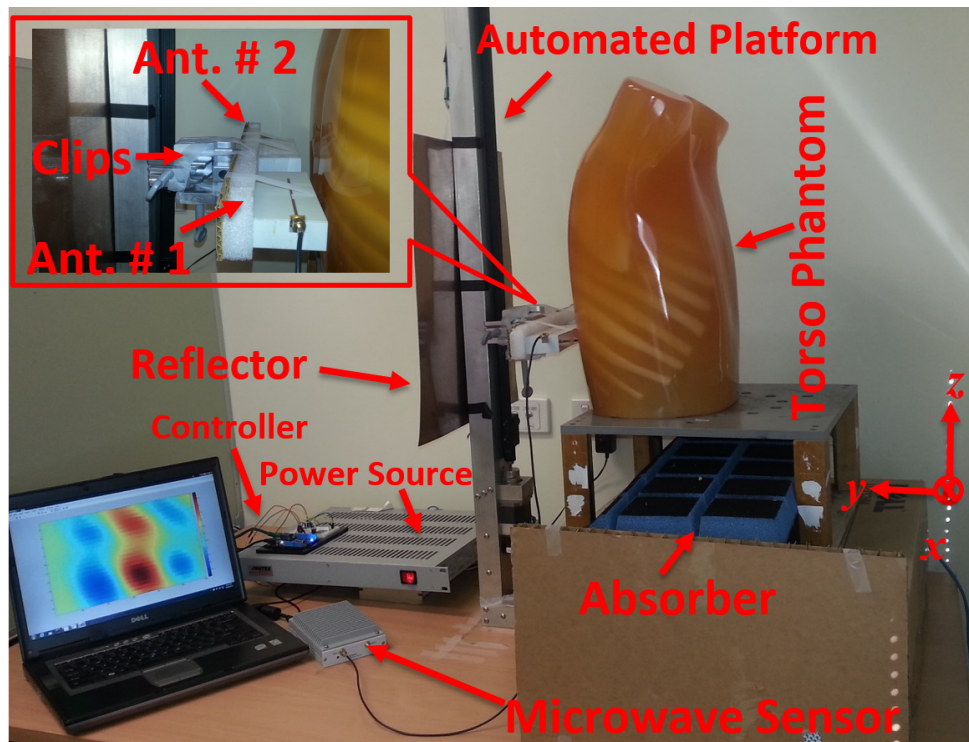


Fig. 5.13 Proposed heart failure detection system using two identical antennas on an automated scanning platform.

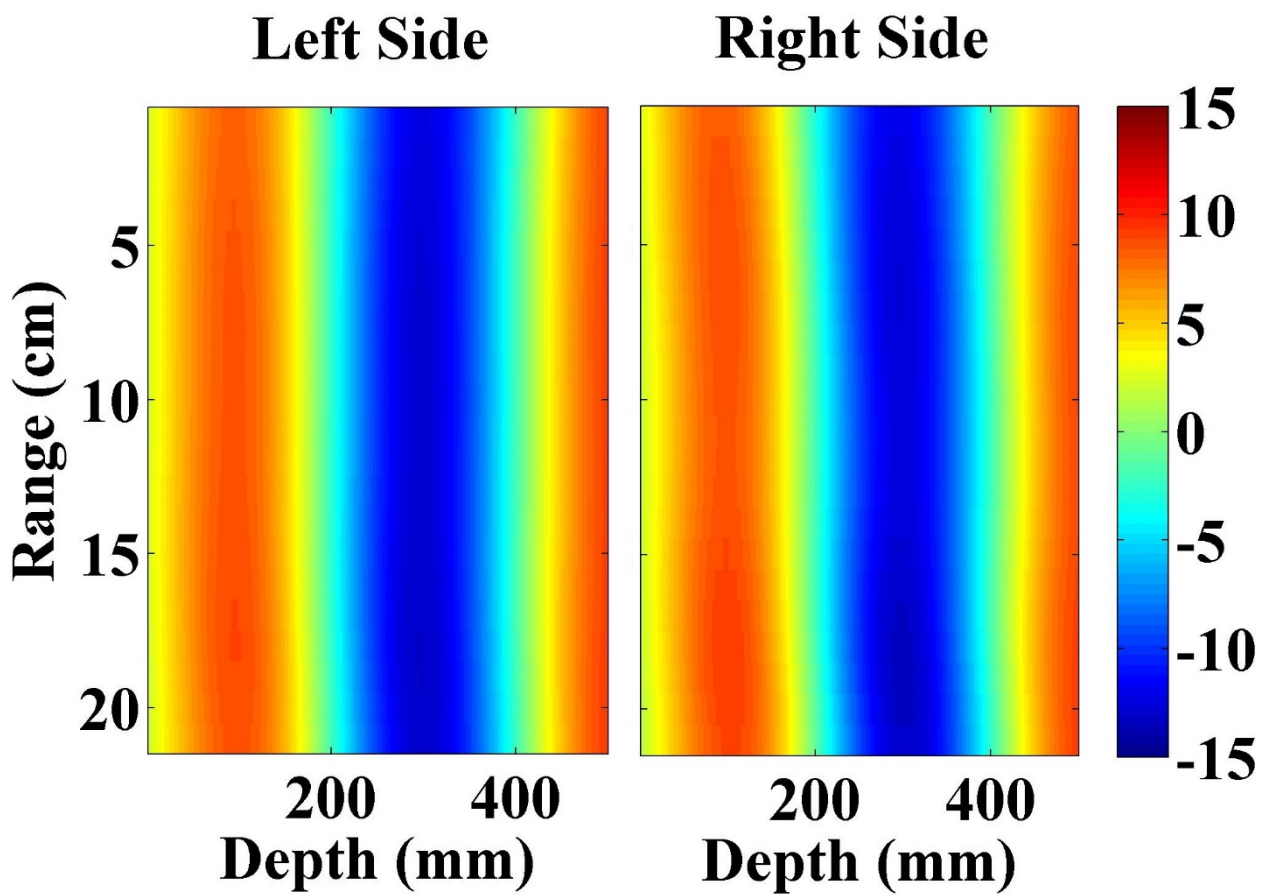
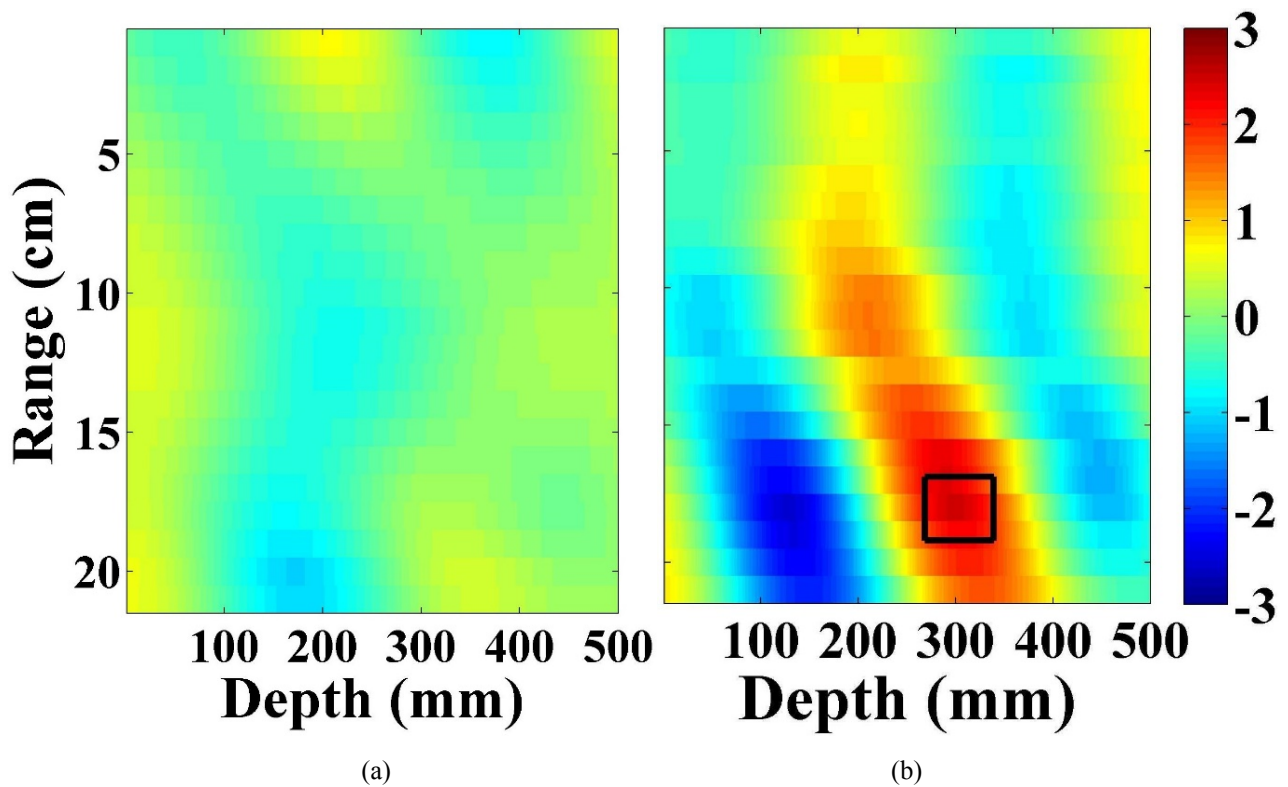


Fig. 5.14 Radargrams of received signals from both sides of the torso.



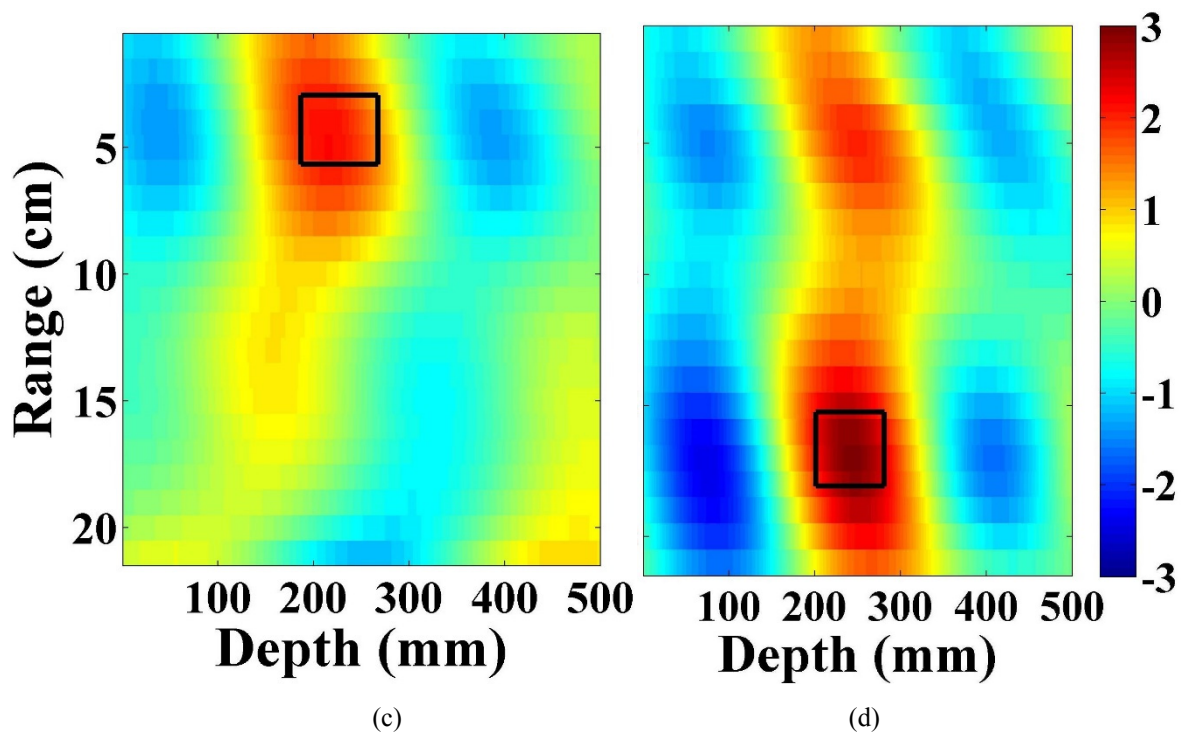


Fig. 5.15 Differential scattering profile of (a) healthy (R-L), and unhealthy cases with fluid accumulated at (b) lower front (R-L), (c) top rear (L-R), where R denotes the right lung and L denotes the left lung.

Like the previous system, differential technique is utilized with 0.1 cm depth pixel resolution to emphasize the changes in the two lungs and define a threshold that can be used to differentiate between healthy and unhealthy cases. To investigate these differences, the aforementioned system is used to scan the torso phantom. The obtained radargrams are then subtracted. The healthy case is shown in Fig. 5.15 (a). The maximum difference in the intensity of the scattering profile of the two sides of the torso is 7%. Before using this as a reference, the system error is also investigated by repeating the scan several times. The largest difference between two scans of the same phantom was found to be less than 3% (not illustrated for brevity). This error, which mainly originates from temperature variations of the transmitter and antenna displacements at various measurements, is added to the afore-obtained value and  $\tau = 10\%$  is defined as a threshold for a healthy case.

To emulate an early stage fluid accumulation, a small amount of water, 10 mL, is located at the rear lower side of the right lung using plastic bags. The same procedure for data acquisition is repeated and the obtained radargrams are subtracted. In the assigned colour bar for Fig. 5.15, the presence of reflections is denoted by intense red and blue regions. The strongest absolute intensity value within the torso area, which is defined at 200 – 400 mm depth, is found. By supposing a fixed subtraction manner, e.g. left side from right side, the strongest red region above the threshold defines the existence of fluid in the right side, whereas the strongest blue colour below the lowest value of threshold defines the existence of water in the left side. However, to have a consistency in the images, the red colour

is used as a sign of presence of water which means that when water is located on the left side, the right side will then be subtracted from the left one. The reflections outside the torso, i.e. between 0 – 200 mm in the results, are caused by the near field interactions of the antenna with the torso and are not considered in the detection decision.

As can be seen from Fig. 5.15 (b), a strong scatterer that has a peak scattering profile more than 3 times the healthy threshold is detected. Unlike previously proposed methods, the location of the accumulation can also be clearly identified with the current technique. To verify that, a plastic bag was located at the top portion of left side and a signal with a peak value of  $2.3\tau$  is identified (Fig. 5.15 (c)). It is worth mentioning that the device can detect fluid volumes as small as 4 mL, which is the detection sensitivity of the system. That value is well below the detectable volume (10 mL) using CT-scan devices.

## **5.5 Automated System Utilizing Two Antennas for Simultaneous Horizontal Scanning**

### **5.5.1 Introduction**

One of the main problems using the previous vertical scanning systems is the presence of the heart that has a large size and considerably higher dielectric constant compared to the lungs, specifically in the inflated case. Therefore, to both facilitate comparable measurement configuration for various body sizes and minimize the effect of heart on detection process, which limits the amount of detectable fluid, a horizontal scanning approach is developed in this section. Moreover, to accelerate the measurement process and reduce the movement errors caused by using a single antenna [4], similar to the previously proposed system, two antennas are utilized to simultaneously scan the top and bottom portions of an artificial torso phantom.

### **5.5.2 Proposed System**

The proposed system, which is depicted in Fig. 5.16, consists of pair of the proposed antenna, an automated platform, a microwave transceiver and a laptop. To simplify the measurement process and eliminate the need for switching networks, a mono-static data acquisition approach is utilized. Therefore, the same antenna is used for both transmitting and receiving. To avoid difficulties with vertical torso scanning, a horizontal scanning approach is adopted in this system. The problem with using vertical scanning is the inadequate spacing/isolation between the two scanning antennas due to the limited space imposed by the limited width of the human torso.

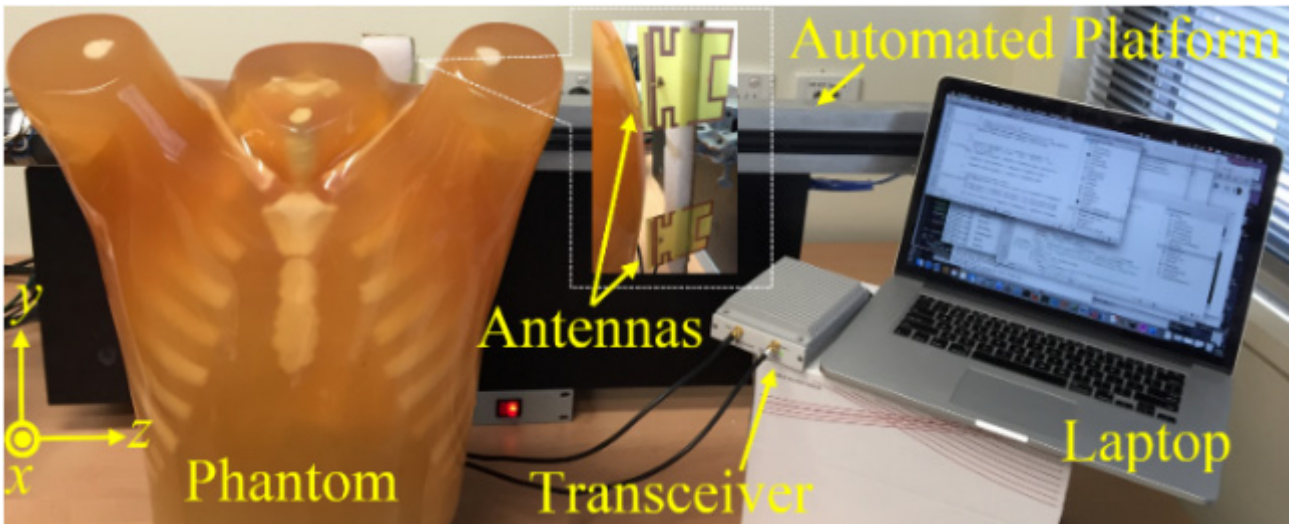


Fig. 5.16 Proposed system for CHF detection.

To accelerate the measurement process, two antennas were utilized to simultaneously scan the torso. To obtain maximum isolation between two antennas without the need for reflector, the antenna designed in section 4.3 is utilized for this system. The antennas were located at 10 cm separation between each other. As the main radiation beam of this antenna is in  $-x$ -direction, a significant change in the orientation of the antenna with respect to the torso results in an adverse effect on the detection accuracy. Therefore, the antennas were fixed on a foam holder ( $\epsilon_r = 1$ ) in the desired positions and alignment. They were then connected to the two ports of a Keysight N7081A transceiver. The performance of the system was tested on the artificial torso phantom. To fully scan the torso's rear top and bottom portions along the width of the torso, the antennas were located at a 2 cm distance from the phantom, and were simultaneously displaced 20 times with 1 cm intervals to horizontally scan the torso at  $z$ - direction.

It is worth mentioning that while the proposed system is not susceptible to variations in the distance between the antennas and the imaged object, knowledge of the distance is needed in the processing and image formation process. The back side of the torso was selected for scanning as it provides a similar structure for both male and female subjects. The backscattered signals were then received by the same antennas and saved in the laptop for processing. The performance of the antenna in front of the torso in the healthy and unhealthy cases in an identical position is depicted in Fig. 5.17 (a). Since the unhealthy case has different effective dielectric properties from those of the healthy case, the scattering/reflections are different and thus, the antenna's reflection coefficient varies between those cases. That variation is utilized as the source of the needed data for image formation. The collected signals are processed using a fast frequency domain imaging algorithm proposed in [137]. The algorithm calculates the intensity of the electromagnetic field inside the torso from the measured fields by the two antennas using the first order Bessel function of the first kind. As a result,

two 2-D images that represent the scattering profiles of different tissues at the upper and lower regions of the torso were obtained. To highlight the differences, and hence distinguish between the healthy and unhealthy cases, a subtraction approach was developed. To that end, the scattering profiles of the top and bottom portions were subtracted from each other to obtain the variances between these areas in a healthy case. This value was then used as a threshold for the detection of unhealthy cases.

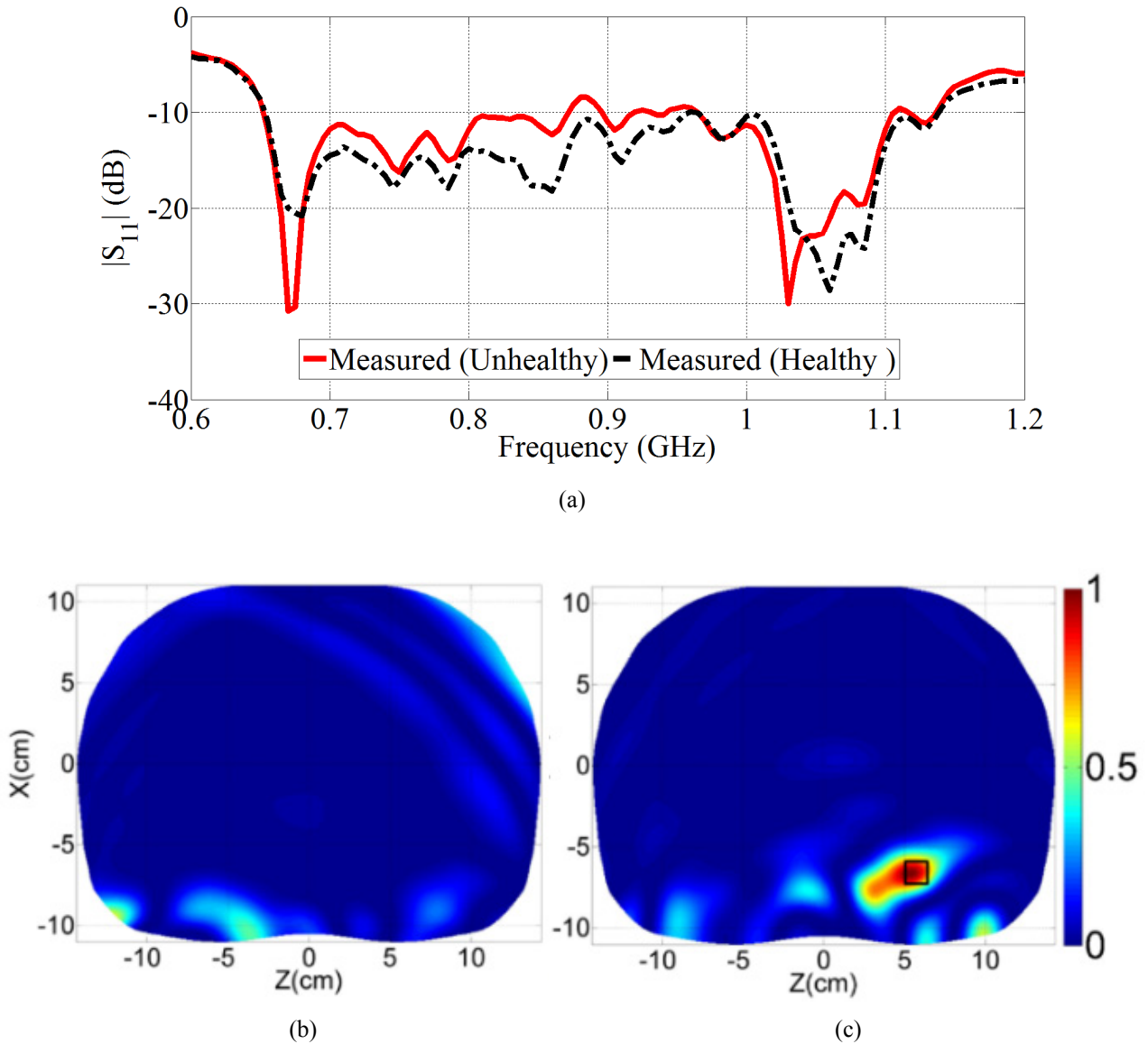


Fig. 5.17. (a) Reflection coefficient samples of the antenna for healthy and unhealthy cases. Obtained images for (b) healthy and (c) unhealthy cases. (Black rectangle shows the location of the inserted fluid inside a lung).

Due to gravity, the fluid always accumulates for CHF affected patients at the lower portions of the lungs. Consequently, the transmitted microwave signal experiences a different reflection compared to the top portion when fluid starts to accumulate inside the lungs (See Fig. 5.17 (a)). Hence, that variation leads to a significantly higher intensity for the scattering profile at the

accumulated fluid location compared to the obtained threshold. To investigate the above-mentioned notion and verify the possibility of detecting early CHF, healthy and unhealthy cases were considered. To imitate an unhealthy case, a small amount of water, e.g. 3 ml, was located at the lower portion of the right lung and positioned towards the middle part of the torso. This is one of the cases that cannot be detected using vertical scanning system used in section 5.3, due to the lack of proper isolation between adjacent antennas. The system was activated, the transceiver generated signals across the band 660-1010 MHz, and the two antennas scanned the torso. The collected data from scanning was then processed and an image that shows the scattering profile inside the torso was generated as depicted in Fig. 5.17. The whole measurement and imaging process was performed within a minute. To better analyse the results, their scales are normalized to the maximum calculated field value. By comparing the intensity of the images, it can be seen that for the unhealthy case, a higher scattering profile that is more than three times stronger in the intensity than the healthy case is achieved. Moreover, the position of the fluid, which is depicted by a black rectangle, is successfully detected by the proposed system.

## **5.6 Multistatic Torso Imaging System Utilizing Expanding Foam**

### **5.6.1 Introduction**

While being extremely successful in detecting small amounts of fluid inside the lungs, the platforms with moving elements such as the ones proposed in previous sections require precise positioning of the patient in front of the platform, and require the patient to remain at the same position for a period of time. This may not be the best option for older people or for people whom have difficulty in being still. Moreover, the measurement time that is required for full scanning needs to be reduced. This purpose was achieved to a great extent by utilizing two antennas and using simultaneous scanning approach, yet, a faster scanning approach would be more convenient.

These problems can be addressed by utilizing several antennas at each side to cover whole lung area, and hence scan whole torso in a short time. However, the issue with utilizing such a system is the great mutual coupling that is experience by the antennas that can mask the target. To that end, a multi static system is proposed in this section. Considering the limited available area at the rear side of the torso and achievable maximum distance between left and right side lungs, an array of four antennas that are embedded in a foam that was presented in section 3.5 is utilized. One of the main advantages of this array is that the height of the foam above the antennas is fixed to a desired value and the patient can lie on the system without any need for antenna adjustments. Moreover, in the

proposed multistatic system in addition to the reflection data there is also a set of each of the transmission coefficients, and hence a multi -static approach provides 2.5 times more data than a mono -static approach for the utilized four -element antenna array.

### 5.6.2 System Realization

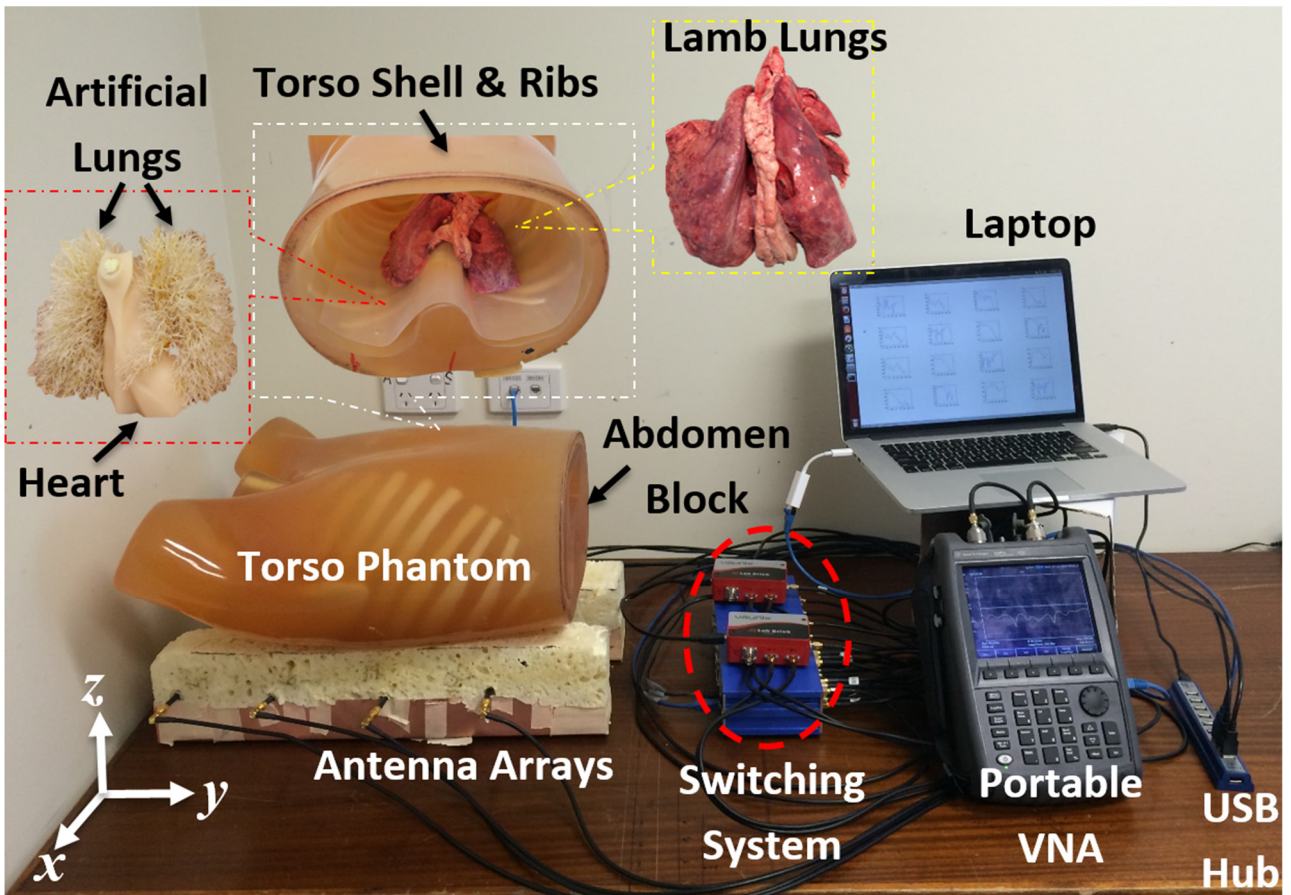
In order to validate the practicality of the antenna array, a portable system with the configuration depicted in Fig. 5.18 (a) is proposed. The system is composed of a pair of antenna arrays each including four antenna elements that are embedded in expanding foam, a switching system using a pair of Mini-Circuits USB-8SPDT-A18 and Lab Brick LSW-502P4T switches, an Agilent N9923A FieldFox portable vector network analyser (VNA), and a laptop. In this arrangement, antenna arrays are connected to the switches to perform multi-static data acquisition that includes  $S_{ij}$  combinations, where  $i, j = 1, 2, 3,$  and  $4$ . Switches are then connected to the ports of the portable VNA. A laptop controls the VNA and switches via a network cable and USB connection, respectively. The whole system is then calibrated using a standard calibration process.

The system validation is done by considering several possible CHF cases. The accuracy of the system was tested by repeating each measurement several times and obtaining analogous results. A full set of measurements that include torso scan and multi-static data acquisition is completed in 31 seconds. The measurements are performed using the artificial phantom. To better mimic human lungs, the lungs in the artificial phantom are replaced with lamb lungs.

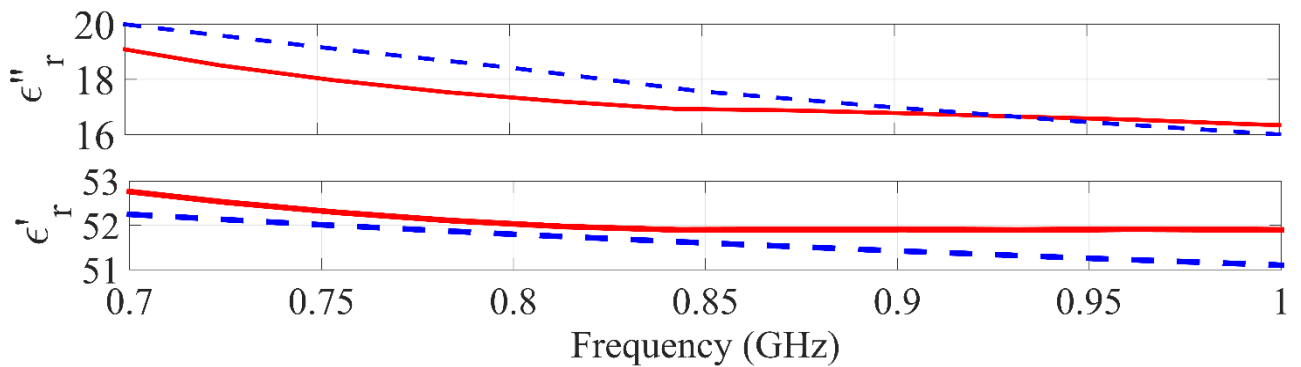
Dielectric properties of the lamb lungs were measured using Agilent's 85070E dielectric probe kit. To that end, several slices were cut from different regions of the lungs and a sample result is depicted in Fig. 5.18 (b). The obtained results, which have less than 5 % variations, indicate that the lamb lungs have very close tissue properties to those of a deflated human lung (average  $\epsilon_r \simeq 51.5$ ) at 700 – 1000 MHz. To facilitate water detection, the designed pair of antenna arrays is located in a horizontal position at a distance of 11 cm from each other. The artificial phantom is then placed on the array such that centre of each lung faces one antenna array.

### 5.6.3 Imaging Algorithm

A multi-static frequency based imaging algorithm is used to map the distribution of the intensity of scattered waves inside the imaged domain/torso. The imaging algorithm consists of four stages, including data calibration, pre-processing, image reconstruction, and post-processing. In the calibration stage, the recorded data without phantom presence is subtracted from the recorded data in



(a)



(b)

Fig. 5.18. (a) Proposed system, and (b) measured dielectric properties of lamb lungs vs human lungs (dashed line: human data, solid line: measured lamb). Human measurement data are obtained from [135].

the presence of the phantom to eliminate the coupling between antenna elements and return losses due to the data acquisition system.

Strong reflections from the skin are mitigated in the data pre-processing step by using an average subtraction method [136], in which the average value of the calibrated signals is subtracted from each signal at each frequency sample. The scattering profile from pre-processed data is then created in the image reconstruction step. The monostatic frequency based technique [137] is extended

here to allow for multistatic data. To that end, an imaging domain is established by dividing into pixels of  $1 \text{ mm}^2$ , with an assumed initial dielectric constant of  $\epsilon$  and magnetic constant of  $\mu$  (Fig. 5.19), and the intensity of energy of each point scatterer/pixel is then estimated [138].

Assuming that an incident wave,  $E_{inc}$ , is transmitted towards an imaged domain, the scattered field  $E_{scat}$  in the distance of  $r$  and angle of  $\varphi$  from the direction of incident wave behaves as a spherical wave [139]:

$$E_{scat}(\rho, \varphi) = f(\rho, \varphi)e^{ik\rho} \quad , \quad (1)$$

where  $\rho = r + R$  is the travelled distance and  $k = 2\pi f\sqrt{\epsilon\mu}$  is the real-valued wavenumber. The amplitude of incident wave,  $|E_{inc}|$  is normalized to one and  $f(\rho, \varphi)$  is the scattering function, which represents the amplitude and phase of the scattered wave from a point-scatterer. The bold characters indicate the complex values. Equation (1) is a solution to Helmholtz equation [140]:

$$\frac{d^2 f(\rho, \varphi)}{d\rho^2} + k^2 f(\rho, \varphi) = 0 \quad , \quad (2)$$

which can be solved using Bessel function of the first kind  $J_1(k\rho)$  [141] :

$$f(\rho, \varphi) = V(\varphi)J_1(k\rho) \quad . \quad (3)$$

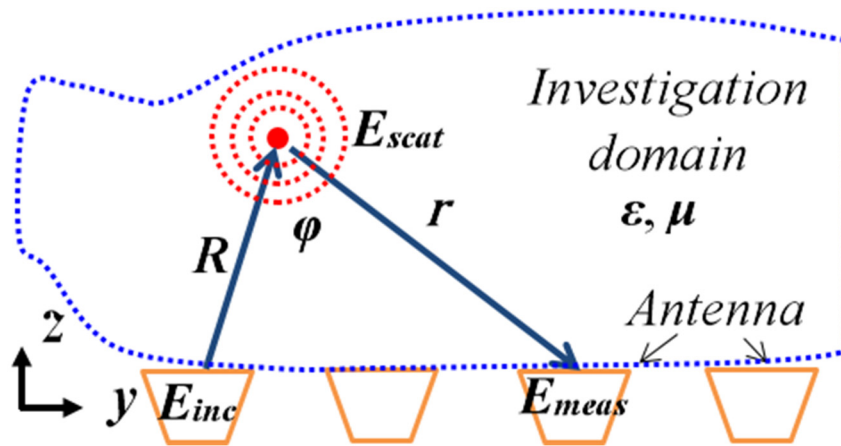


Fig. 5.19 Incident and scattering electric fields in the investigation area.

From the physical point of view,  $V(\varphi)$  shows how the scattered wave varies with  $\varphi$ . Assuming the scattered wave to be spherical,  $V(\varphi)$  in the  $y$ - $z$  plane has a circular shape,  $V(\varphi) = Ae^{i\varphi}$  and consequently, (1) can be rewritten by:

$$E_{scat}(\rho, \varphi) = AJ_1(k\rho)e^{i(k\rho+\varphi)} \quad . \quad (4)$$

Additionally, the measured field in a receiver is composed of a series of scattered waves from different point-scatterers/pixels:

$$\mathbf{E}_{meas} = \sum_s \mathbf{E}_{scat}(\rho, \varphi) = \sum_\varphi \sum_\rho \mathbf{A} J_1(k\rho) e^{i(k\rho+\varphi)} = \sum_\varphi \mathbf{A} e^{i\varphi} \sum_\rho J_1(k\rho) e^{ik\rho} , \quad (5)$$

where  $s$  is the surface of the imaging area ( $y$ - $z$  plane), including all possible distances and angles for the point-scatterers. As the distances and wave number are known the last summation of (5) can be replaced by a constant, represented here by  $B$ :

$$\mathbf{E}_{meas} = \mathbf{B} \sum_\varphi \mathbf{A} e^{i\varphi} = \mathbf{A} \mathbf{B} \sum_{n=0}^{N_{pt}-1} e^{in\Delta\varphi} , \quad (6)$$

where  $N_{pt}$  is the number of defined points in the imaging region and  $\Delta\varphi$  is the angular step between two pixels. The exponential series in (6) can be approximated by

$$\mathbf{E}_{meas} = \mathbf{A} \mathbf{B} \frac{1 - e^{iN_{pt}\Delta\varphi}}{1 - e^{i\Delta\varphi}} \quad (7)$$

By defining very small pixels,  $\Delta\varphi$  tends to 0; then

$$\mathbf{E}_{meas} = \mathbf{A} \mathbf{B} \lim_{\Delta\varphi \rightarrow 0} \frac{1 - e^{iN_{pt}\Delta\varphi}}{1 - e^{i\Delta\varphi}} \approx \mathbf{A} \mathbf{B} N_{pt} . \quad (8)$$

Therefore  $\mathbf{A} \approx \frac{\mathbf{E}_{meas}}{\mathbf{B} N_{pt}}$  and by introducing  $A$  to (4),

$$\mathbf{E}_{scat}(\rho, \varphi) \approx \frac{1}{\mathbf{B} N_{pt}} \mathbf{E}_{meas} J_1(k\rho) e^{i(k\rho+\varphi)} , \quad (9)$$

By calculating the Poynting vector, the directional energy flux density of the scattering wave from one point to the receiver can be obtained by:

$$\mathbf{S}(\rho, \varphi) = \frac{\varepsilon c}{2} \mathbf{E}_{scat}^2(\rho, \varphi) \approx \frac{\varepsilon c}{2 \mathbf{B}^2 N_{pt}^2} \mathbf{E}_{meas}^2 J_1^2(k\rho) e^{i2(k\rho+\varphi)} . \quad (10)$$

where  $c$  is the speed of wave propagation.

The intensity of energy flux inside the imaging region is considered as the final image by superposition of Poynting vectors over all angles of the incident wave (transmitters), observing points (receivers) and frequencies [142]:

$$I(\rho, \varphi) = \left\| \frac{\epsilon c}{2B^2 N_{pt}^2} \sum_{k=1}^{N_f} \sum_{j=1}^{N_a} \sum_{i=1}^{N_a} \mathbf{E}_{meas}^2(tr_i, tx_j, f_k) J_1^2(k\rho) e^{i2(k\rho+\varphi)} \right\| \quad (11)$$

$$, \mathbf{B} = \sum_{\rho} J_1(k\rho) e^{ik\rho}, \quad (12)$$

where  $N_f$  and  $N_a$  are number of frequency samples and number of antennas, respectively. Besides,  $tr_i$  and  $tx_j$  are considered as the receiver and transmitter indices.

In the reconstruction process, a two-dimensional image is created to show the intensity of the scattering energy at each location within the imaged object. The average effective dielectric properties of the imaging domain, including the lung tissues, are used in the calculations. It should be noted that the refractions due to the inhomogeneity of the body are mitigated by the summation process of (11). Due to the utilized approximations, this procedure does not provide the detailed image of the imaged domain; instead, it only shows strong scatterers within the imaged domain as need in medical detection systems. The image quality can be improved by increasing the number of antennas and data samples. The algorithm is valid with  $\pm 10\%$  error in the average dielectric property estimation. Lastly, by utilizing the approximately symmetrical structure of the lungs, a differential approach is used to both eliminate additional clutter and cancel the image similarities in the scattering profiles of the left and right sides of the lungs. In this case, the scattering profile of left ( $I_{left}$ ) and right ( $I_{right}$ ) sides are subtracted (differential approach) to highlight the target intensity and provide higher contrast and easier detection:

$$I_{final}(\rho, \varphi) = \left\| I_{left}(\rho, \varphi) - I_{right}(\rho, \varphi) \right\|^2 . \quad (13)$$

#### 5.6.4 Results

Rear side of the torso is selected for measurements as it provides analogous structure in male and female subjects. Earlier proposed systems were not able to detect fluid amounts lower than 4 mL. To investigate the success of the current algorithm, this amount is reduced to 2 mL in the experiments. In that regard, the artificial phantom in healthy and unhealthy cases is considered. The proposed

imaging algorithm is applied and the obtained images are depicted in Fig. 5.20. To localize the target, an imaging region is considered and segmented into pixels. The intensity of energy flux for each pixel is then calculated using (13). Finally, the calculated values of left and right arrays are subtracted and mapped to a 2-D image. In order to ease the detection process, their scales are all normalized to the highest obtained intensity in each set. The whole process is completed within five seconds. The detection process is based on the fact that as the fluid has higher relative permittivity compared to its surrounding environment and consequently, a higher reflection should be experienced in an unhealthy case. As it can be observed from the images in Fig. 5.20, the case with 2mL of water emulated in the lower right lung at  $(y, z) = (30, 6)$  has a scattering intensity that is over 2.5 times higher than the healthy case. As can be seen, there is a slight discrepancy between the actual and detected location of the water which might be caused by polarization variations of the antenna at different frequencies.

The same process is repeated by replacing the lungs inside the artificial phantom with deflated lamb lungs. This scenario is the most challenging one in CHF detection as it has a lower dielectric contrast with accumulated fluids ( $\epsilon_r \approx 81$ ) in this case compared with the inflated lungs ( $\epsilon_r \approx 22$ ). The above-mentioned procedure is repeated for a healthy case. Then, 2- mL of water is injected to the right lung of the lamb at  $(y, z) = (33, 4)$  and the measurement process is performed. Fluid is injected into the lower side of the lung as it is the case in realistic scenarios. As it can be seen from Fig. 5.21 (a) and (b), the case with fluid has more than twice the intensity of a healthy case.

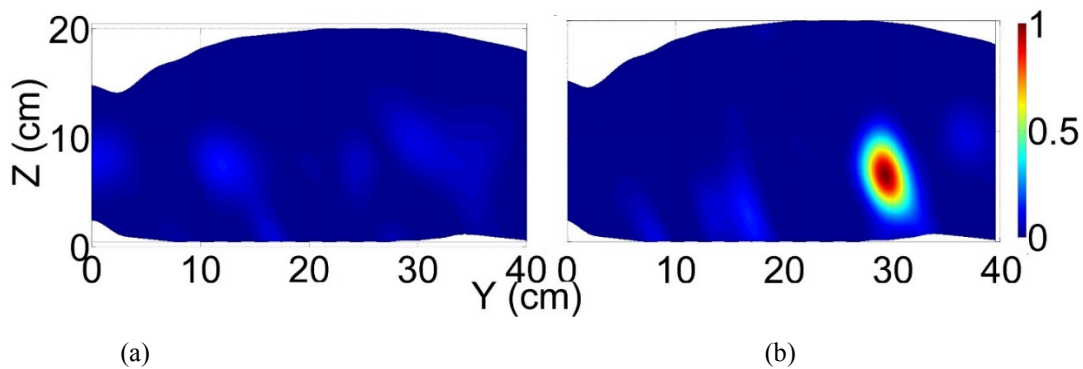


Fig. 5.20. Images for (a) healthy case, (b) 2 mL water injected in right lung.

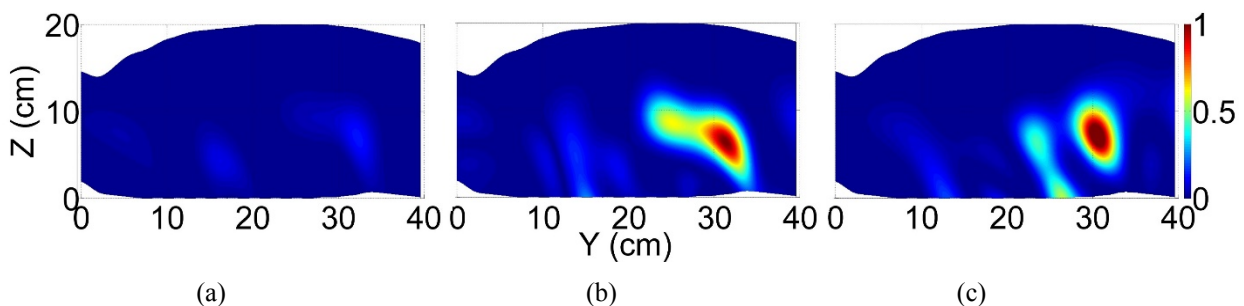


Fig. 5.21. Images for (a) healthy case, (b) 2 mL water injected in right lung and, (c) water injected on both lungs with difference of 2 mL.

There is a chance that CHF causes fluid accumulation in both lungs. Due to the fact that fluid flow depends on the gravity and the chance of equal accumulation on both lungs is small, two different amounts of water e.g. 7 mL and 5 mL representing a 2 mL difference, are injected to the right and left lungs, respectively. The measurement process is repeated for this case and the results are presented in Fig. 5.21 (c). It can be seen that the obtained image has more than three times the intensity of a healthy case. The performance of the system is challenged by locating fluid amounts below 2 mL and fluid differences as small as 1 mL. It is observed that in these cases the intensity of the obtained image is around 1.2 times the healthy case (not depicted for brevity). Therefore, considering this low margin, and to eliminate the chance of error, the sensitivity of the device is defined as 2 mL. It should be stated that, this amount is five times smaller than the lowest amount of water detectable by conventional devices, such as CT-scan.

## **5.7 Semi Elliptical/Circular Scanning Platform**

### **5.7.1 Introduction**

The main reason behind utilizing linear systems in the previous platforms is the similar contact face that the rear side of the torso provides for male and female subjects. However, the main disadvantage of using the rear side of the torso is the fact that if fluid accumulation is present towards the front side of the thorax, there is a chance that it can will not be detected by the linear scanning systems. This is due to the limited power, 0 dBm, which is used by the antennas that are scanning the back side of the torso and hence cannot penetrate deep to the front of the thorax.

However, there are two main points that should be considered before judging the credibility of the proposed linear systems. Firstly, the chance of fluid accumulation in front of the torso is extremely rare due to the physical shape of the lungs and the gravity dependency of the fluid. Secondly, even with the sophisticated X-ray, CT-scan or MRI machines, the patients, even with apparent signs of fluid accumulation, are asked to lay down for a period of time so that the fluid accumulates in a specific region towards the back side of the torso. However, to investigate all possible cases and configurations of a possible detection system, a circular platform is presented in this section.

### **5.7.2 Platform Design**

One of the important aspects that need to be considered in building a circular array is the

number and types of antennas. Generally, imaging algorithms obtain better images with larger number of antennas. However, there are physical limitations regarding the size and type of the antenna and compromises are needed to be made between the possible employable number of antennas and the complexity of utilized imaging algorithm. By investigating the antennas designed in chapters 3 and 4, it can be realized that planar antennas are better options to be used. This is due to the fact that because of their smaller scanning face, which is facing the torso, larger number of planar structures can be placed in a circular/quasi elliptical configuration with less mutual coupling between the antenna elements. Therefore, by considering the ease of feeding structure, the antenna presented in 4.3.

The proposed system is depicted in Fig. 5.22. 16-element array of the designed antenna was arranged to form a quasi-elliptical configuration that encloses the torso area keeping a distance of around 2 cm between the antennas elements and the torso. The antennas are connected to two Mini-Circuits USB-8SPDT-A18 switches (only one is depicted) that are connected to two ports of a portable VNA. The performance of the switches and the VNA are controlled using a laptop that also includes the imaging algorithm.

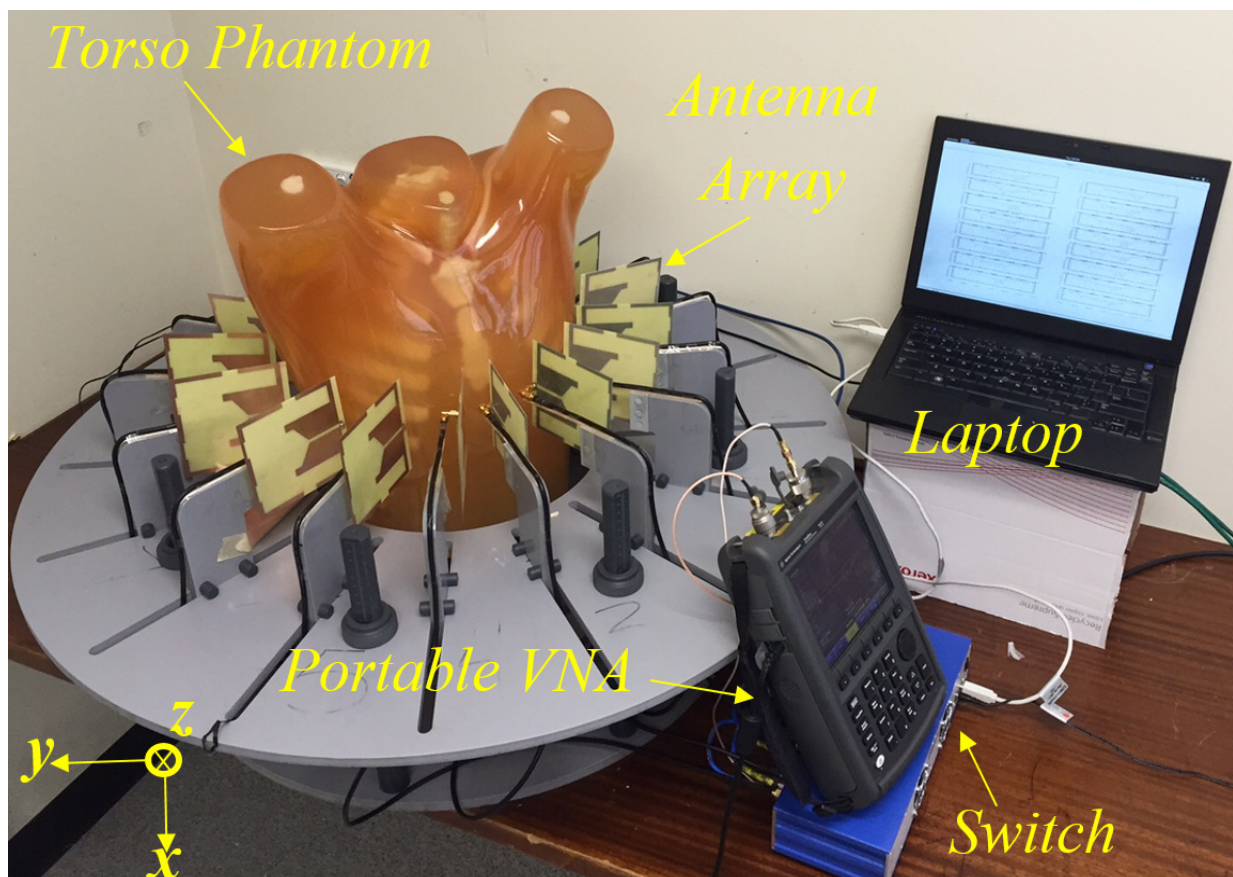


Fig. 5.22 System configuration with quasi-elliptical antenna array.

A small amount of water, 3 mL, is inserted into the lower parts of the lungs in an artificial

torso phantom. The experiment was performed using a monostatic data acquisition approach in which each antenna is used to both transmit and receive sequentially. The previously explained frequency domain based imaging algorithm is then utilized to calculate the intensity of the electromagnetic energy inside the torso and form a two dimensional image using the captured back scattered signals. The obtained images for healthy and unhealthy cases are presented in Fig. 5.23 (a) and (b), respectively. As the algorithm uses the ratio of the received to transmitted power, the intensity scale is normalized to its maximum value in each image and is unit-less. As can be realized, a strong scatterer is observed at the location of the inserted water,  $(y, z) = (3, -2)$ , in the tested pulmonary edema case. The intensity of the detected target is three times higher than the intensity in the healthy case. These results were validated by changing the location of water and repeating it using lamb lungs, which have close tissue properties to that of human beings (Fig. 5.23(c)), and simulation environment using Zubal model [143], which is a realistic three dimensional human phantom (Fig. 5.23 (d)). The obtained results verify the effectiveness of the designed antenna and the whole system in detecting small amount of fluid accumulation inside the torso.

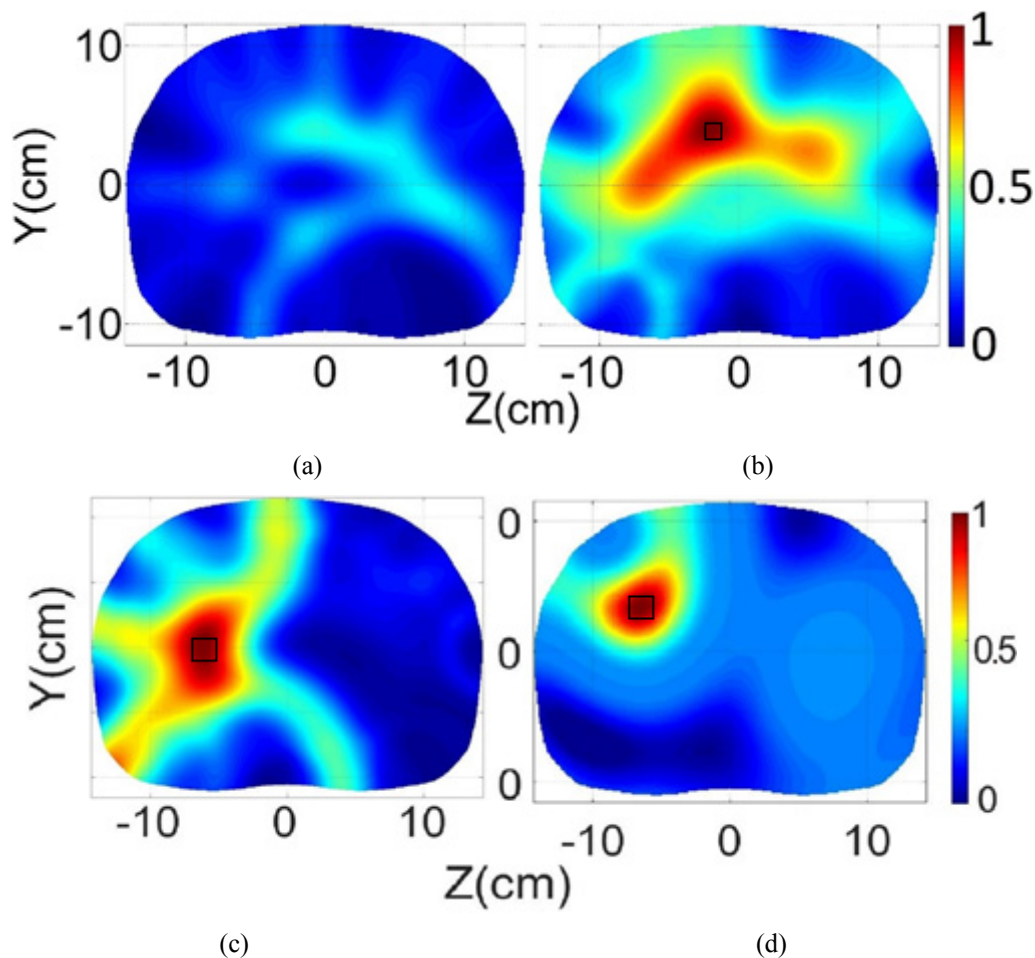


Fig. 5.23. Reconstructed images for (a) healthy case, and pulmonary edema cases using (b) artificial phantom, (c) lamb lungs and (d) Zubal phantom (simulations).

## 5.8 Conclusion

Several linear and a semi-elliptical platforms utilizing all possible configuration for torso imaging are proposed in this chapter. The systems were presented in a systematic manner in which each successive system proposing more beneficiary options compared to the previous one. It was shown that by increasing the number of antennas, systems with faster data acquisition and images with higher accuracy are obtainable. Several challenges, including the interpretation of images with very small differences were addressed utilizing differential detection approach. Additionally, the gravity dependency of the fluid accumulation was utilized to propose horizontal scanning approach that assists in reducing the effect of heart throughout the detection and imaging process. It was shown that despite utilizing a complex hardware configuration, multi static imaging approach provides images with the highest detection accuracy. Finally, the possibility of detecting fluid in any position inside the torso was investigated and successfully proved using a semi-elliptical/circular configuration.

# Chapter 6

## Clinical Torso Imaging Systems

The ultimate aim of this thesis is to propose clinical prototypes for the fluid detection inside the torso that is the cause of miscellaneous diseases. This is of great importance as there is a big gap in building a clinical device. Such devices are already available for breast cancer imaging that is being used by Bristol University, England [144] and McGill University, Canada [145] and for stroke classification that is being used by Chalmers University, Sweden [37]. This chapter will be introducing two clinical systems that are built based on the previously proposed linear and circular platforms. These systems are designed, built and tested on real human beings. As a feasibility study, preclinical tests were conducted on healthy subjects to determinate the type of obtained images, the statistics and threshold levels of their intensity to differentiate between healthy and unhealthy subjects. To test the malignant cases animal tissues were instead used.

### **6.1 Torso Imaging System Embedded in a Clinical Bed**

#### **6.1.1 System Introduction**

The design and realization of a non-invasive and portable microwave system, which has an antenna array platform embedded inside a bed and can be easily used in preclinical and clinical trials, is proposed in this section. This system aims at detecting and monitoring small amounts of fluid inside the lungs that can be caused by various diseases. This system will provide preliminary data for medical staff to pursue further investigations to define the exact cause of the edema. Additionally, it can be used to monitoring the progress of the disease or treatment in pre-hospitalization or rehabilitation process, respectively.

The system consists of a hardware unit for data acquisition and software unit for processing and image formation. The hardware unit comprises of two linear antenna arrays, a switching network, a portable VNA and a laptop which includes the software used for control, processing and image formation. One of the main constrains that have hindered the design of realistic platforms for microwave-based diagnostic systems for fluid detection is the size of the antennas. In order to provide

the required penetration of the signal into the torso area while offering a reasonable image resolution, the 3-D antenna presented in section 3.4 of this thesis is utilized. This antenna provides a wide operating bandwidth, unidirectional radiation and a compact contact face as well as a short height, that allows its integration inside a clinical bed. To monitor the changes inside the lungs and detect fluid accumulation, a frequency domain imaging algorithm, which utilizes backscattered signals from the torso to map the scatterers inside the lungs, is proposed as part of the system. The algorithm is based on the fact that the relation between the measured microwave signals by the utilized antenna array with the scattered signals inside the torso is according to the first order Bessel function of first type. Due to the fact that microwave signals experience higher reflection from fluid compared to the surrounding lungs' tissues, the obtained image shows higher scattered electromagnetic field intensity at the location of the fluid. The presented algorithm does not need solving ill-posed problems of wave path estimation, which is one of the main drawbacks of time-domain techniques.

The experimental results indicate that the proposed system is capable of detecting fluid accumulation inside the lungs as low as 1 mL. Finally, preclinical tests are conducted on five healthy volunteers to establish a threshold level of the expected level of predicted scattered signals inside the lungs. The results of the study, which is conducted in an uncontrolled environment with possible effects of subject movement and breathing, and noise, suggest that the obtained threshold has a certain value for all those cases with 10 % variation. That threshold is needed in the future trials on subjects with and without fluid accumulation.

### **6.1.2 The Proposed Pre-Clinical System**

The proposed system for pulmonary oedema detection is depicted in Fig. 6.1. The utilized antenna arrays are designed and fitted into a series of slots that are cut and trimmed from a radio frequency (RF) transparent foam block, which acts as the base of the bed (platform). As depicted in Fig. 6.1, during tests, the subjects lay on their back so that the antenna array faces the rear side of the torso that provides similar structures in male and female subjects. In order to scan the torso area at the central lines of the two lungs, the platform comprises of two sets of linear antenna arrays. The two arrays are located at a distance of 11 cm from each other, which equals the distance between the center of the left and right side lungs of an average human being. The two antenna arrays are connected to a switching network formed using USB-8SPDT-A18 switches. A portable Agilent N9923A FieldFox RF VNA is used as the microwave transceiver of the system. It generates the required frequency-domain microwave signals, transmits them via the antenna arrays to the torso, captures the received back-scattered signals from the torso, and sends them as digital data to a laptop.

These data are then processed by that laptop using the proposed frequency domain based algorithm, which is also used to generate an image of the scattered field inside the torso.

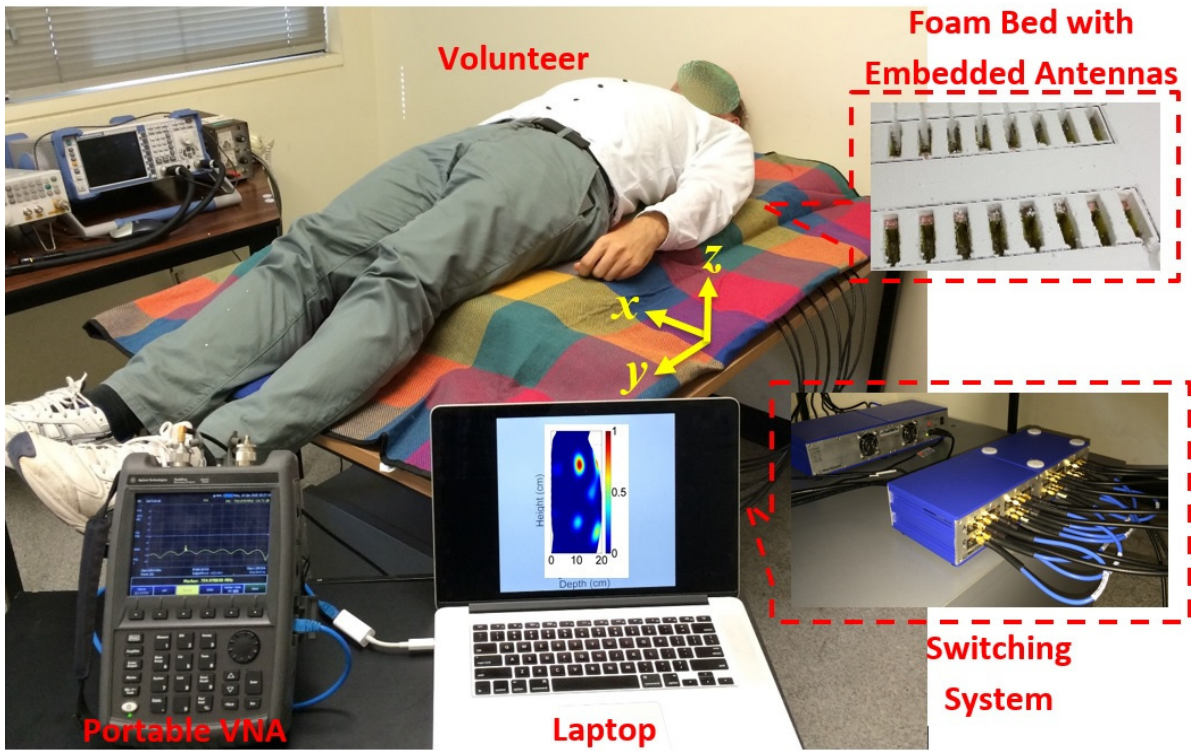


Fig. 6.1 Proposed preclinical microwave imaging system of the torso for fluid accumulation detection.

### 6.1.3 Imaging Process

It consists of pre-processing techniques to eliminate the noise and background reflections from the recorded raw data by the antenna array and an image reconstruction algorithm, which generates an image to help in the fluid accumulation detection system.

If an electromagnetic wave is sent towards the human body, a large portion of that wave is reflected back due to the high permittivity of the skin. The strong reflection represents a clutter that can mask the target, especially if it is small as in the case of early detection of CHF where the amount of accumulated fluid is small. Therefore, a proper pre-processing technique is required to remove or significantly mitigate the skin reflections.

Considering the skin as a dielectric slab with a dielectric constant of  $\epsilon_r$ , the reflection transfer function of the skin can be expressed by [146]:

$$F(\omega) = \frac{-2jR \sin(kd)}{R^2 e^{jkd} - e^{-jkd}}, \quad (1)$$

where  $d$  is the thickness of the skin,  $k=\sqrt{\epsilon_r}\omega/c$  is the wavenumber,  $c$  is the wave speed in vacuum and  $R$  is:

$$R = \frac{\sqrt{\epsilon_r} + 1}{\sqrt{\epsilon_r} - 1} \quad (2)$$

The reflected signal from a layer can be calculated by multiplying the incident wave by (1), which can be strong enough to mask the backscattered wave generated by the target. Therefore, the reflected signal should be removed before applying the imaging method. Although the aforementioned reflection transfer function doesn't provide the reflected signal from a multilayered media, it shows that the reflected wave from each layer depends on its thickness, dielectric properties and frequency. By assuming a uniform thickness of the torso's skin and same distance between the antennas and the skin, the reflected wave behaves in a similar way at each antenna. In this case, the reflection can be removed by subtracting the average value of the received electric field ( $E_{avg}$ ) in an antenna array from the value of each antenna of the array [147]. To do so, the electric field ( $E_{meas}$ ) is extracted from the measured signal, that is S-parameters ( $S_{meas}$ ), for all of the antennas of the array and the average value over the array is subtracted from them:

$$E_{meas}^{n,m} = \sqrt{\frac{2S_{meas}^{n,m}}{\epsilon_0\epsilon_r}} \quad (3)$$

and

$$E_{sub}^{n,m} = E_{meas}^{n,m} - E_{avg}^n \quad (4)$$

where,  $n$  and  $m$  represent the antenna number and frequency step, respectively, and  $\epsilon_0$  is the permittivity of free space. Applying the average subtraction method for all the antennas and frequency steps provides  $N_p \times N_f$  values of subtracted electric field ( $E_{sub}$ ) at each antenna array.

When boundary (skin) reflections are removed, Maxwell's equations can be used to find the scattered electromagnetic fields. However, due to the assumption of homogeneous properties for the imaged region with a constant average dielectric permittivity, calculating the electromagnetic scattered field by Maxwell's equations does not provide the correct field distribution inside the body. Nevertheless, the difference in the dielectric properties of different points within the imaged region can be extracted from the inequality of electric fields at different antenna positions and frequencies. To that end, the imaged area is discretized into square cells and the  $N_p \times N_f$  calculated fields at each

cell are added together to show the distributions of dielectric contrasts within the imaged domain [142].

The torso is a heterogeneous medium that consists of many tissues with different dielectric properties. Thus, to avoid producing images with false positive targets, the intensity of the measured field is enhanced to magnify the dielectric differences and improve the image contrast using

$$E_{norm}^{n,m} = \frac{|E_{sub}^{n,m}|^2}{|E_{inc}|^2} = \frac{|E_{meas}^{n,m} - E_{avg}^n|^2}{|E_{inc}|^2}, \quad (5)$$

where  $E_{inc}$  is the known incident field and is constant for all the antennas. Using the second power operation over the subtracted field and dividing it by the incident field mitigates the effect of low intensity fields scattered from what would be, otherwise, false targets, and magnifies the strong fields scattered by the real target of high dielectric constant.

Maxwell's equations can be applied to the normalized received field ( $E_{norm}$ ) to obtain a map of scatterers within the imaged domain. As depicted in Fig. 6.4, each antenna of a  $N_a$ -element flat array transmits an incident field into the imaging area (a cross section of the torso) and receives the backscattered field. The scattered electric field from each point ( $x, y$ ) inside the imaged area is calculated using Bessel function of the first kind of order zero  $J_1(.)$  [148]:

$$E_{scat}^{n,m}(x,y) = E_{norm}^{n,m} \cdot J_1(k_m \rho) \cdot e^{i(k_m \rho + \phi)}, \quad (6)$$

where  $k_m$  is the wavenumber of  $m$ -th frequency step and ( $\rho, \Phi$ ) represent the distance and the angle of each point within the imaged domain from the antenna position. Applying the summation process to the estimated scattered field, over all the antennas ( $n=1$  to  $N_a$ ) and frequency steps ( $m=1$  to  $N_f$ ) provides the location and intensity of high contrasts of dielectric constants inside the torso for each array:

$$I(x,y) = \sum_m \sum_n^{N_f, N_p} |E_{scat}^{n,m}(x,y)| = \sum_m \sum_n^{N_f, N_p} E_{norm}^{n,m} \cdot |J_1(k_m \rho)| \quad (7)$$

In order to obtain a threshold for healthy and unhealthy cases, the  $I(x, y)$  values of the left and right side arrays are subtracted from each other:

$$I_{sub}(x,y) = |I_{left}(x,y) - I_{right}(x,y)| \quad (8)$$

Due to the fact that the structure of the left and right side lungs have significant similarities, the subtraction process highlights any changes that may have occurred due to the presence of a target (fluid inside the lungs).

In the imaging process, different antennas of a mono-static array are taken into account simultaneously and the electromagnetic equations are solved in frequency domain to not only show the significant scatters' location, but also accelerate the imaging procedure. Additionally, the effect of the system delays and the need for solving ill-posed problems of wave path estimation, which are the major problems in time-domain techniques, are removed by performing the calculations in the frequency domain.

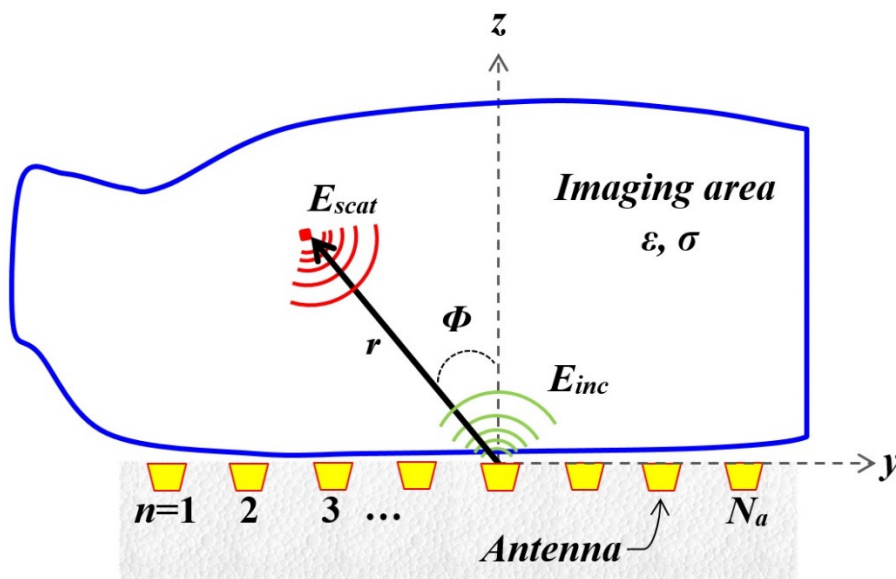


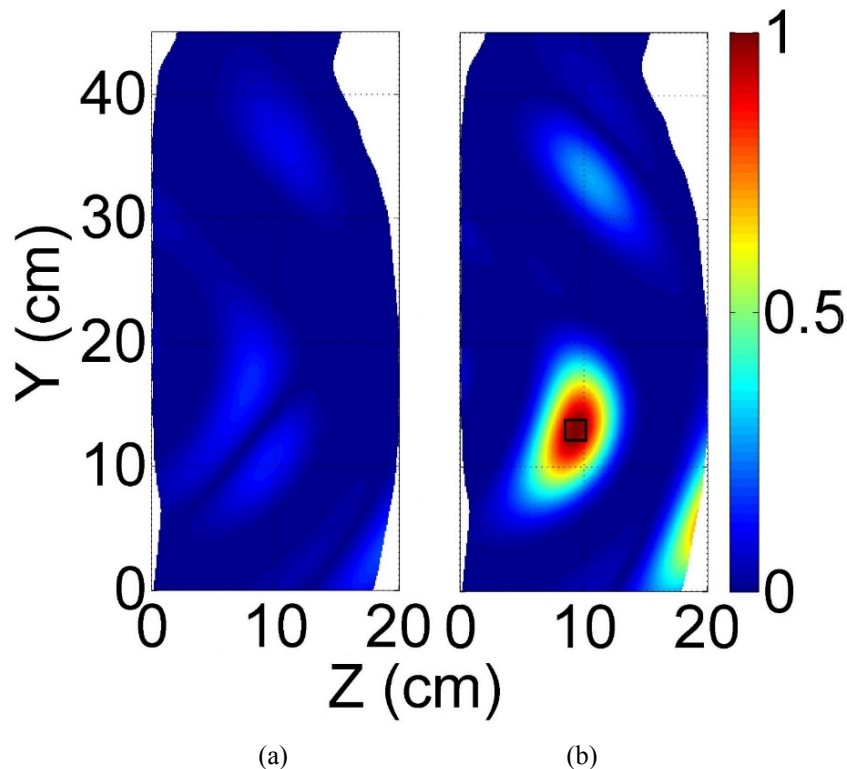
Fig. 6.2 Diagram of the utilized torso imaging domain.

### 6.1.4 Experimental Results

Several experiments were conducted to verify the performance of the presented system. In one of the experiments, eight antennas were fitted in each array with a spacing of 3 cm. The system is tested on the artificial torso phantom. A healthy case was firstly considered when there is no fluid (water) inside the lungs of the phantom. The signals from both arrays are recorded. To emulate a realistic case, various volumes of water were inserted into the lungs of the phantom. In another experiment, the same process is repeated but using four antennas in each array that are located in a 6 cm distance to see whether it is viable to use small number of antennas in the platform. The generated images using the proposed algorithm are depicted in Fig. 6.3. The presented results are the absolute values that are obtained after subtracting the scattering profiles of right and left sides from each other (8). The obtained subtracted images for healthy and unhealthy cases in the first scenario

are shown in Fig. 6.3 (a) and (b). As it can be realized, the maximum normalized intensity of the scattered field inside the torso is around 90 % higher than the healthy one for 1 mL water content located at the lower portion of the lung (black rectangle). This detectable volume of fluid is four times better (lower) than the least detectable amount by recent CHF systems. This system has the potential to detect much smaller volumes of waters than conventional CT-scan devices as reported in [88]. The obtained results for the second setting with only four antenna elements on each array are also depicted in Fig. 6.3 (c) and (d) for healthy and unhealthy cases with 1 mL accumulated water. As it can be seen, the obtained images do not enable an accurate detection of the accumulated water. The successive experimental results revealed that the system with small number of antenna elements is not able to detect water contents lower than 4 mL using this experimental setup. Therefore, the first configuration with larger number of antennas provides better results and therefore, selected for further tests.

To verify the obtained results in a more realistic scenario, the artificial lungs were replaced with a pair of fresh lamb lungs depicted in Fig. 6.4 (a). The dielectric properties of the lungs were measured using Agilent 85070E dielectric probe and an average dielectric constant of 49, which is very close to that of a deflated human lung, is obtained across the operating band of the system. In order to emulate CHF, a 1 mL of water was injected into the lower side of the left side lung. The obtained results depicted in Fig. 6.4 (b) and (c) validate the capability of the system. The imaged profile of the unhealthy case is stronger at the location of the water with a ratio of 2.5:1.



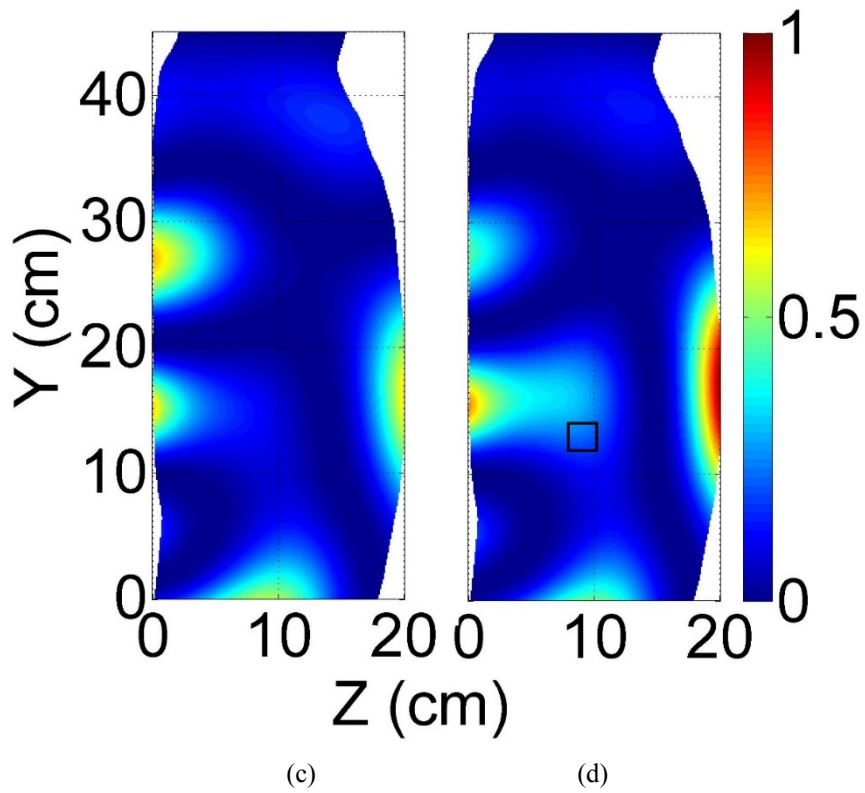


Fig. 6.3 (a) The artificial phantom used in the tests. Images from using  $8 \times 2$  array configuration on artificial phantom: (b) healthy and (c) unhealthy (1 mL inserted water). Images from using  $4 \times 2$  array configuration: (d) healthy and (e) unhealthy (1 mL inserted water).



(a)

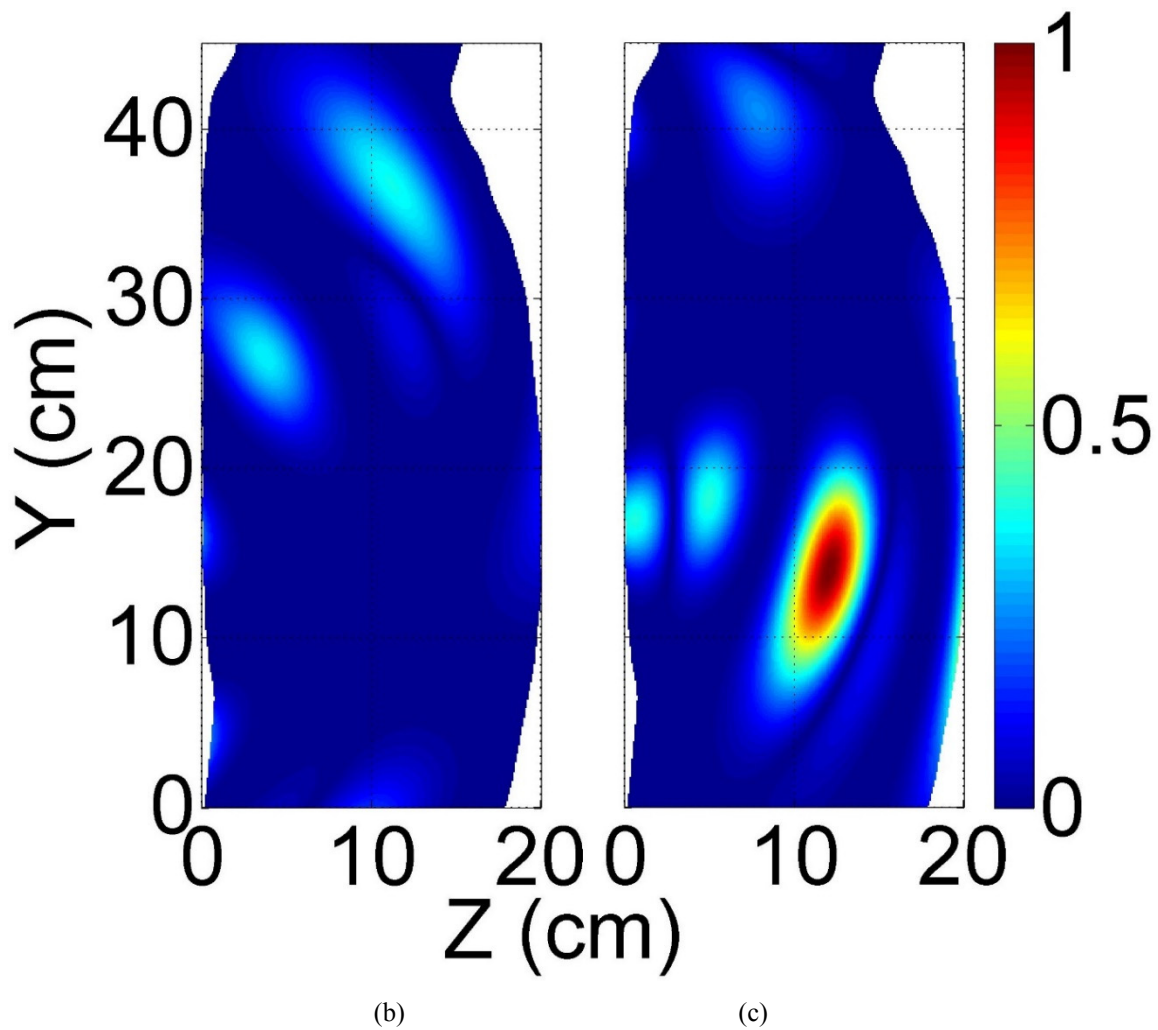


Fig. 6.4 (a) The phantom used in the tests: Lamb lungs inside an artificial torso. Images from using  $8 \times 2$  array configuration on that phantom: (b) healthy lamp and (c) lamb with 1 mL injected water.

Having the reliability of the system attested, a series of preclinical trials were conducted on healthy volunteers. As a common procedure in medical diagnostic applications [149], these studies were conducted with the aim of investigating the possibility of building a data base for healthy and unhealthy people with different physical sizes. The main goal of the study is to investigate whether the obtained intensity levels for the scattering profile of the torso are in a confined range or not. A set of tests were performed according to the protocol approved by the Ethics Committee of The University of Queensland (Australia). The measurements followed the same process explained in the previous experiments. The system is tested on five healthy subjects (four males and one female). The age group of the people were between 26 and 33 years old with skinny, average and fat body types. An example of the images obtained are depicted in Fig. 6.5, with the statistical properties of the upper and lower region of the image shown in Fig. 6.6. The images are normalized with respect to the maximum field intensity obtained over all of the volunteers. In each image, there is a point of high scattering located in the upper region. From to the location of this scatterer and the known dielectric

properties of the torso's organs in the used frequencies, this value can be attributed to the heart, which has a high effective dielectric constant due to the blood inside the heart. This indicates the possibility of detecting strong scatterers inside the torso. In the presence of accumulated water in unhealthy situations, it is expected that the obtained images will show the water inside the lungs as the highest scatterer, because of its higher dielectric constant than the effective dielectric constant of the combination of heart and blood. From the obtained results, the variation of the normalized subtracted electromagnetic field intensity inside the torso is in a confined range with only 10 % variation in all regions of the torso. Although preliminary, the obtained results encourages the possibility of building a global database that can be used as a definite range for healthy people and therefore, can be used as a threshold to detect unhealthy cases.

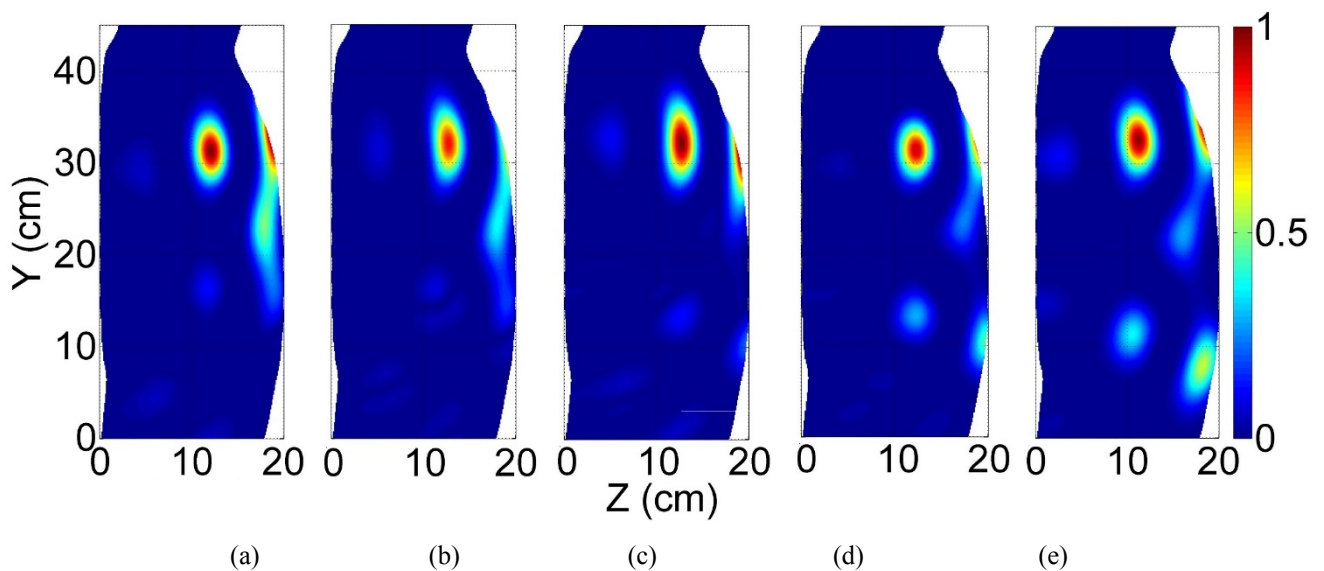


Fig. 6.5 Example of the obtained torso images of healthy volunteers. The high intensity area indicates the location of the heart.

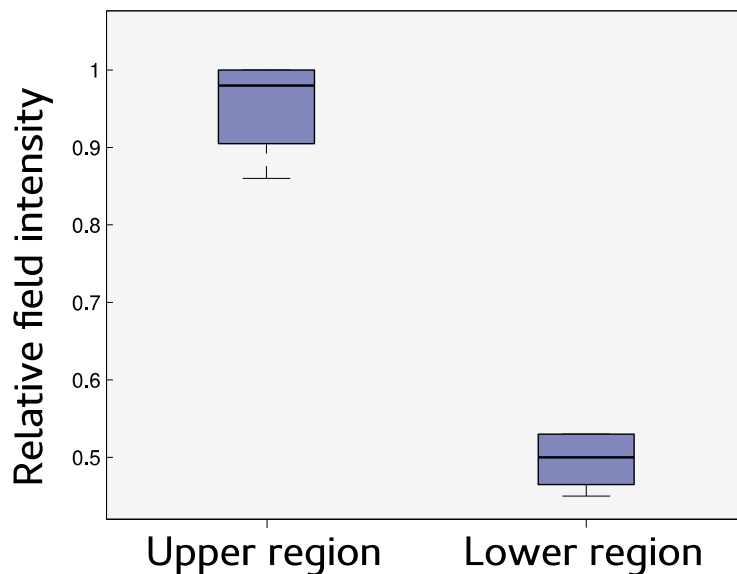


Fig. 6.6 Statistical properties of the field intensity over the subjects.

## **6.2 Microwave Torso Scanner**

This section is dedicated to introduce the second clinical prototype that is designed, fabricated and tested. This system is designed to offer new features compared to the first clinical prototype. As it can be realized from the previous clinical platform while it has proven to be successful in detecting small volumes of fluid, it has limitations in determining the exact fluid position, which is vital in cases where a minimal invasive biopsy is needed to determine the type of oedema causing the fluid accumulation. The limitation of the system in the fore stated system comes from the fact that it uses a linear array configuration to only scan the rear side of the torso. Also, due to the same analogy it cannot detect fluid accumulated in deep positions. To address the abovementioned limitations and enhance the quality of diagnosis in terms of detecting and localizing fluid at any depth, a microwave torso scanner is proposed in this section.

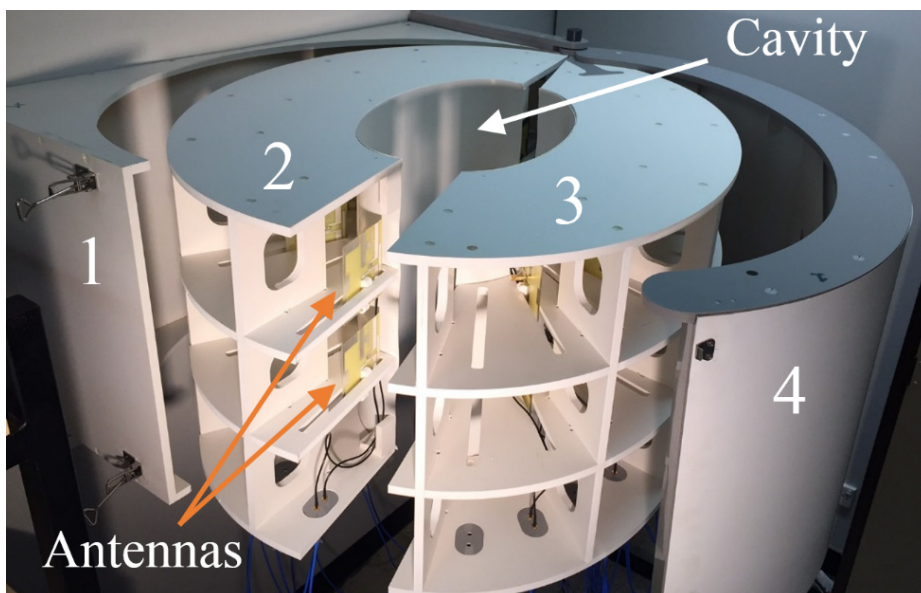
### **6.2.1 Design consideration**

One of the main limitations associated with the detection methods that utilize variations in the amplitude or phase of reflected or scattered signals [11]-[16] as the only detection measure is the lack of defining a real-time reference for the data, i.e. missing a threshold for the correct decision, healthy or otherwise, to be made. While one might argue that a reference database can be built for any individual that reference changes dramatically with time because it is very sensitive to any variation in the human body or the environment of measurements. The only credible reference is the measurements at the moment of scanning but that is obviously not possible as data needs to be compared for the same subject at a healthy and then suspected status. This limitation was partially addressed by utilizing the symmetry between the shapes of the left and right side lungs in the previous clinical system. In that system, a threshold is defined by subtracting the scattering profiles of the two lungs from each other in the healthy case. In the detection process, the presence of fluid is detected if the scattering profile is stronger than the defined value in the differential image. However, the accuracy of detection is restricted by the imperfect symmetry between the left and right lungs due to the presence of the heart in the left side. Studying the structure of the torso reveals that the heart is not present in the upper and lower sections. These regions host very similar tissue types with of course different masses; thus, they are expected to possess similar, yet, not identical scattering profiles. Moreover, due to gravity, any accumulated fluid inside the torso tends to gather inside or around the lower sections of the lungs. Therefore, fluid accumulation at the lower region can be identified by comparing the scattering profiles of the upper and lower regions to that of a healthy case. Therefore,

a system that can scan the upper and lower regions of the torso at the same time is designed and proposed in this section.

### 6.2.2 Proposed System

The dismantled structure of the proposed scanner is depicted in Fig. 6.7(a). The outer layer of the system is designed in a semi-doughnut chamber shape to accommodate the antenna arrays. On the other hand, the inner section of the system, cavity, is designed in an elliptical shape to form similar structure to that of the human torso. It is built using expanded Polyvinyl chloride (PVC) with properties that are radiofrequency (RF) transparent, and therefore, it does not affect the radiation performances of the antennas. The system includes four compartments; the first part is the installation base designed to assist in fixing the system on a clinic wall or base of an ambulance. The second and third compartments are the upper and lower elliptical flanges forming antenna nests that have several slots with equal angles with respect to the centre of the cavity, while the fourth compartment is the cover case of the system. To build the microwave based torso scanner, the system compartments are put together and the antennas are installed inside the designated slots and are fixed using plastic clamps. The antennas are then connected to a switching system to electronically scan the circumference of the torso. The switch network is formed using a Keysight L4491A microwave switch platform [150]. The switching platform is connected to the ports of a Keysight N9923A FieldFox vector network analyser (VNA) [151]. The switching platform is configured with five 87106B-T24 SP6T multiport switches to form a virtual SP24T switch, and thus each of the 24 antennas can be connected to the VNA one at a time.



(a)

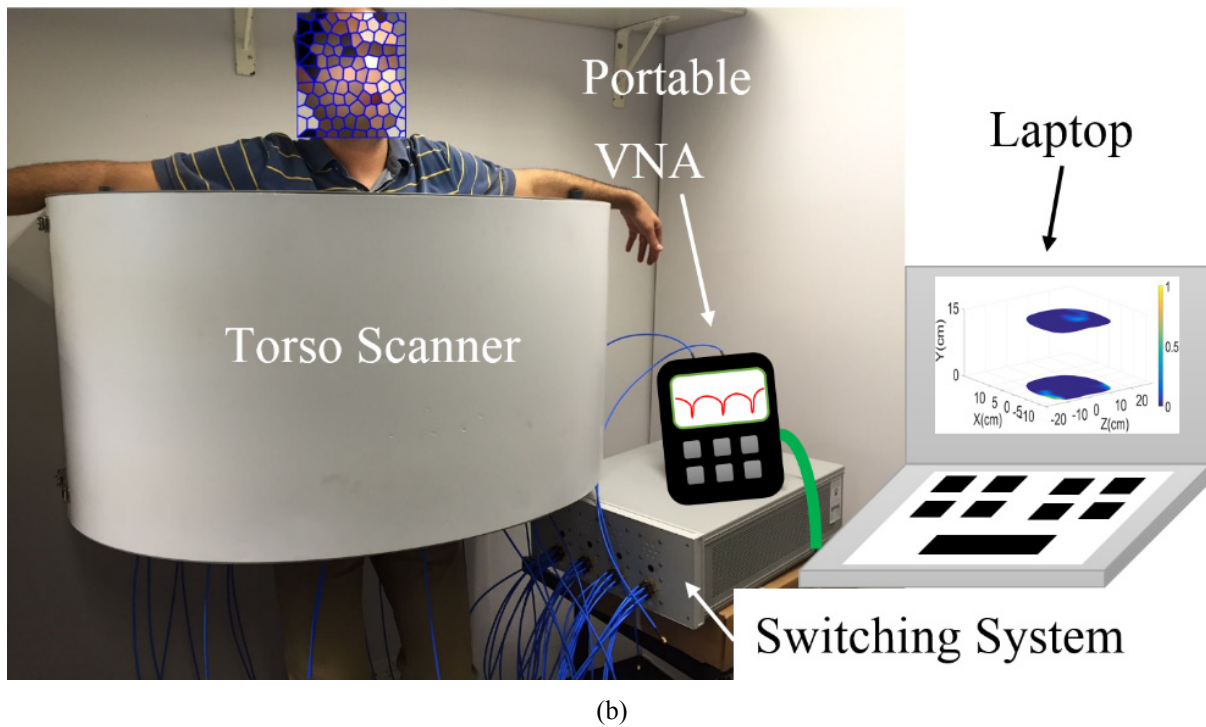


Fig.6.7. (a) Dismantled presentation of the proposed torso scanner installed on a wall. (b) Measurement setup with human subject inside the scanner.

The VNA generates the required microwave signal and measures the frequency response of the connected antenna between 0.5 and 2 GHz. During the experiments, the patient is positioned inside the cavity and the torso is scanned by each of the antennas. Controlling this whole system and saving the data are done by a Python script, which interfaces a laptop to the VNA and the switches via Ethernet and USB connections.

### 6.2.3 System Test Configuration

To verify capability of the system in detecting accumulated thoracic fluids, several test setups were arranged. As mentioned before, in general, two configurations can be used to acquire back scattered signals from torso; monostatic and multistatic. As shown in Fig. 6.8 (a) and (b), in the monostatic approach, the antennas are individually used for both transmitting and receiving signals, while in the multistatic setup, each of the antennas are used as a transmitter while all the others are used to collect scattered signals. This procedure continues till a full scan is completed by all the antennas in the array. Multistatic configuration requires larger number of switches compared to the mono-static scenario, however, it provides much more information that increases the accuracy of the detection. To verify the abovementioned notions and study the accuracy of the system and its detection capabilities, both of the configurations are investigated in this communication.

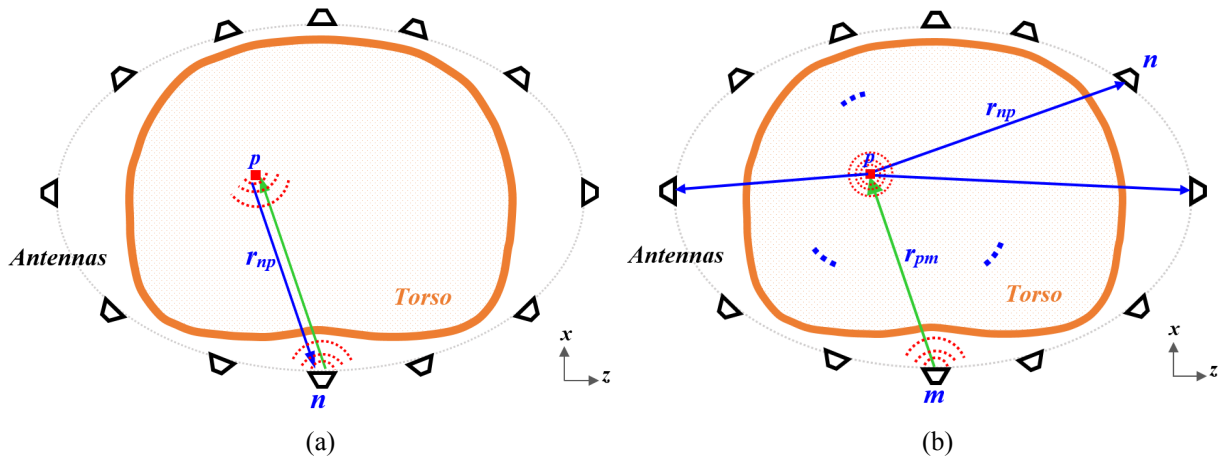
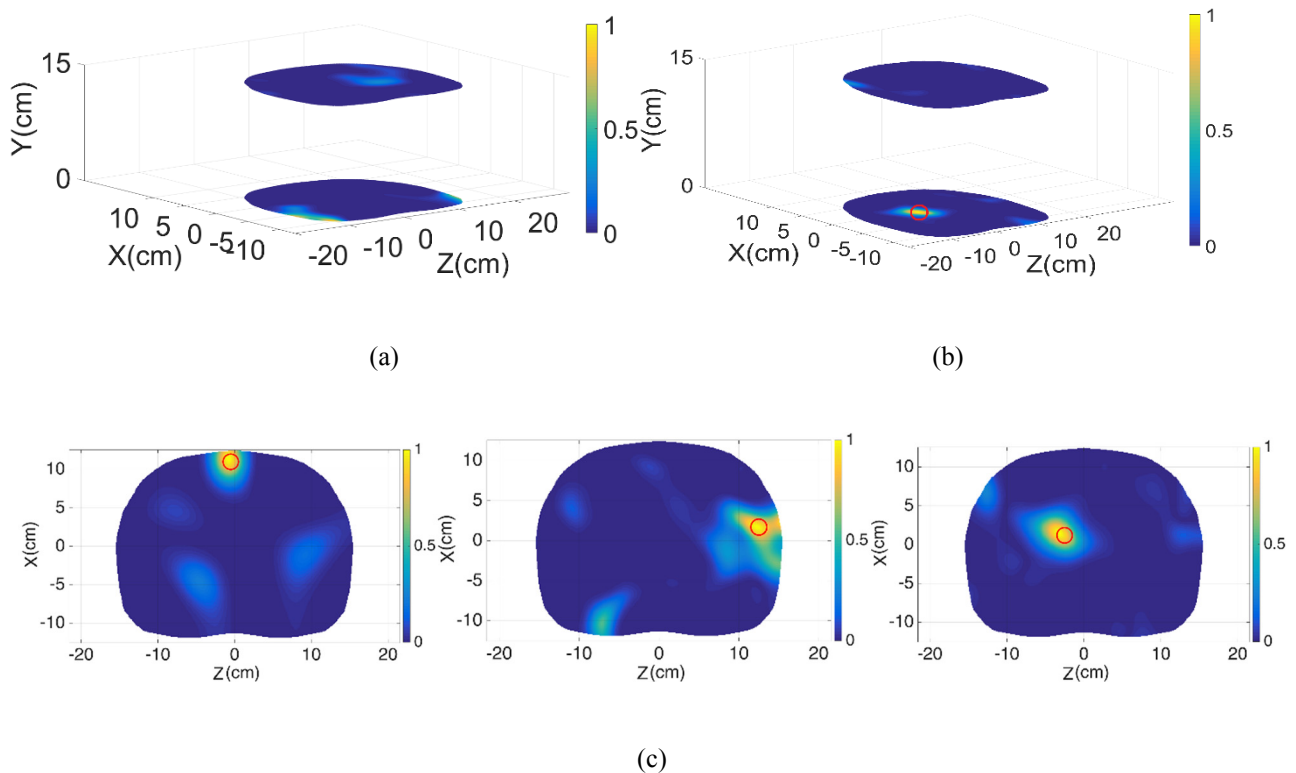


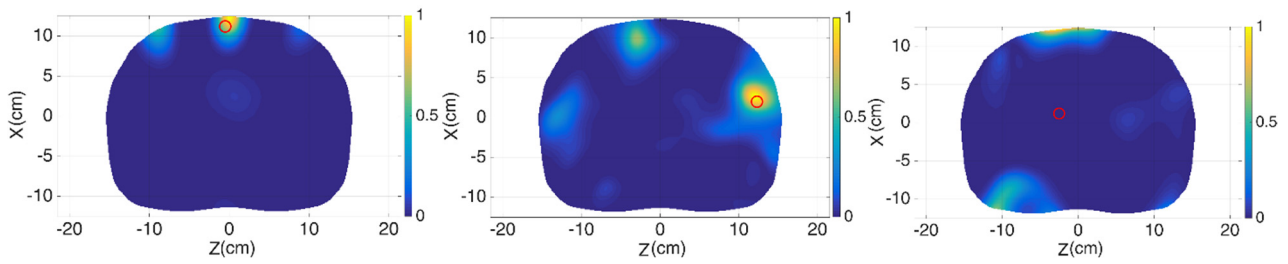
Fig. 6.8. Scattering signal acquisition in (a) mono static and (b) multistatic configurations.

## 6.2.4 Mono-Static Data Acquisition Approach

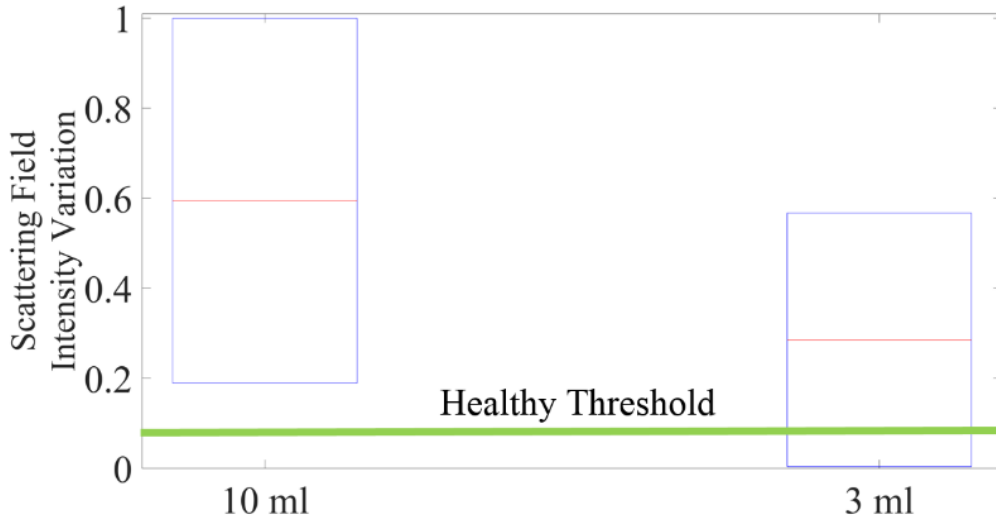
To study different cases of fluid accumulation, the system was tested on the previously explained artificial torso phantom that has exact measures of an average human torso. To calibrate the system and remove the amount of inner reflections of the antennas facing each other with the system's cavity, the system is operated when there is no phantom inside the system and the obtained signals are subtracted from the back scattered signals from torso/human subjects in the subsequent experiments. A full torso scan is performed in less than thirty seconds. To obtain a threshold for detection purposes, the phantom with no fluid inside was firstly scanned and the maximum value of the scattered field was defined as the threshold. The obtained images for the upper and lower regions of the healthy phantom are depicted in Fig. 6.8 (a). As can be realized, there are high levels of similarity between scanning profiles of lower and higher regions of the torso. To analyze the performance of the system, different amounts of accumulated fluid in different positions were investigated. The phantom was located inside the cavity of the scanner and the water was inserted into three different positions. To that end, 10 mL of water was inserted into the right side of the phantom behind thorax ribs, in front of the phantom near the skin (shallow target) and towards center of the phantom (deep target). It is noted that the selected positions for water are the ones that could not be detected using the linear scanner. To magnify the image changes due to presence of fluid (Fig. 6.9(b)), the scattering profiles of upper and lower regions were subtracted from each other and the resultant images are depicted in Fig. 6.9 (c). The exact location of the fluid is defined by a red circle in all images. As seen, the system is capable of detecting the presence and location of the inserted fluid with a high precision. This is an important capability that provides valuable information regarding the exact position of the accumulation to doctors in cases where invasive sampling is required to define the source of fluid leakage by examining the substances present in the fluid.

In order to define the limitations of the system, the injected fluid amount inside the lungs was reduced to extremely low amount of 3 mL, and was inserted at the previously explained positions. The subtracted images are depicted in Fig. 7(d). Analyzing the images reveals the fact that both detection and precision are dramatically deteriorated by reducing the amount of fluid. In the first case where water is located near the skin, the detected position has a shift of around 50% compared to the original position of the inserted fluid, and in the second situation, where fluid is located behind ribs, a relatively strong scatterer is also detected in addition to the identified fluid. Moreover, the system is not able to detect fluid that is located deep inside the thorax. The main reason behind this phenomenon is the strong reflections from the skin that mask the weak reflections from the small amount of fluid inside the torso. To better understand the aforementioned analysis, the scattering field intensity for 10 mL and 3 mL are plotted in Fig. 6.9(e). As realized, in the case of 10 mL, the obtained scattering field intensity is well above the maximum scattering intensity obtained from the subtraction of the upper and lower regions in the healthy case, and hence all cases could be precisely detected. However, in the 3 mL case, some regions have a field intensity that falls below the healthy threshold, thus, the level of the received scattered signal is equal or lower than that of a healthy case, and hence no accurate detection can be realized. Therefore, the system with mono-static configuration is limited in terms of detecting low amounts of fluid in early thoracic fluid accumulation.





(d)



(e)

Fig. 6.9 Reconstructed image of the upper and lower regions of the torso in (a) healthy case and (b) unhealthy case with accumulated fluid inside the thorax area. Subtracted images of the upper and lower regions at three different positions; front side of the torso (left), behind ribs (middle) and deep inside thorax (right) with (c) 10 mL and (d) 3 mL injected water. (e) Scattering field intensity variation diagram for 10 mL and 3 mL inserted water compared to the healthy threshold.

## 6.2.5 Multi-Static Data Acquisition Configuration

To cover the limitations of the mono-static system, the switching system was changed to perform multi-static scanning (See Fig. 6.10(a)). In the multi-static system, each antenna array is connected to the switching platform which can sequentially select any antenna to be the transmitter while all the other antennas form the multistatic receiver. The switch network was configured using two Mini-circuits USB-8SPDT-A18 switches and the Keysight L4491A microwave switch platform. To compare the obtained results with those of the monostatic configuration, 3 mL of water was inserted at the same previous positions and measurements were conducted. With the multistatic switching system, it takes less than six minutes, which is obviously longer than the time needed in monostatic scanning, to complete the scanning process. The obtained data is then processed using the

frequency domain imaging algorithm to generate the differential images depicted in Fig. 6.10 (b). As can be realized, increasing the amount of the received data from different paths inside the thorax significantly improves the quality of images in addition to the accuracy of diagnosis. It is evident that with the multi-static configuration, the system is capable of the accurate detection and localization of the fluid even when it is small and located deep inside the torso. This is also evident from Fig. 6.10 (c), where the intensity of the back scattered signals are compared to that of healthy one. In contrast to the case with mono-static approach, the intensity of the signals are well above the healthy threshold.

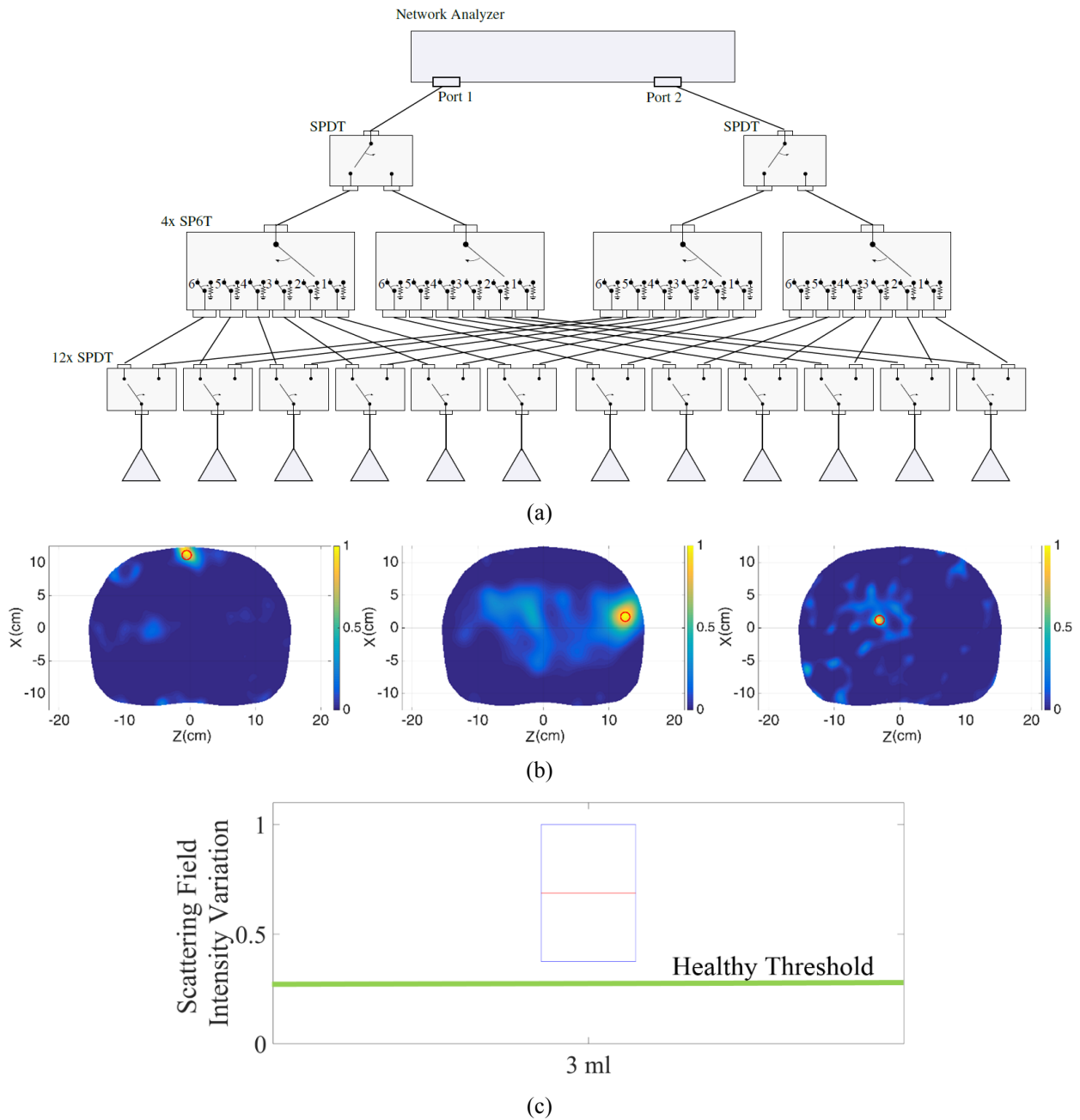
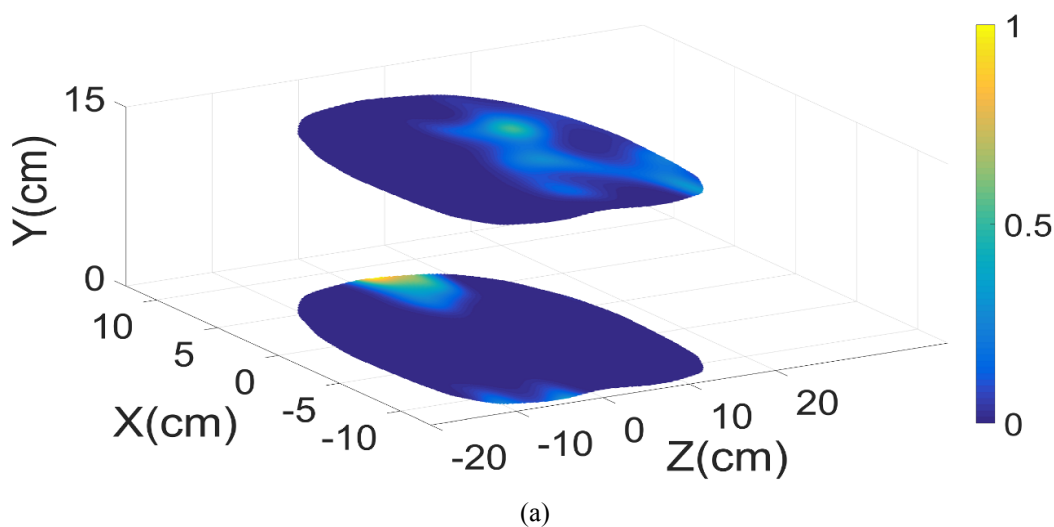
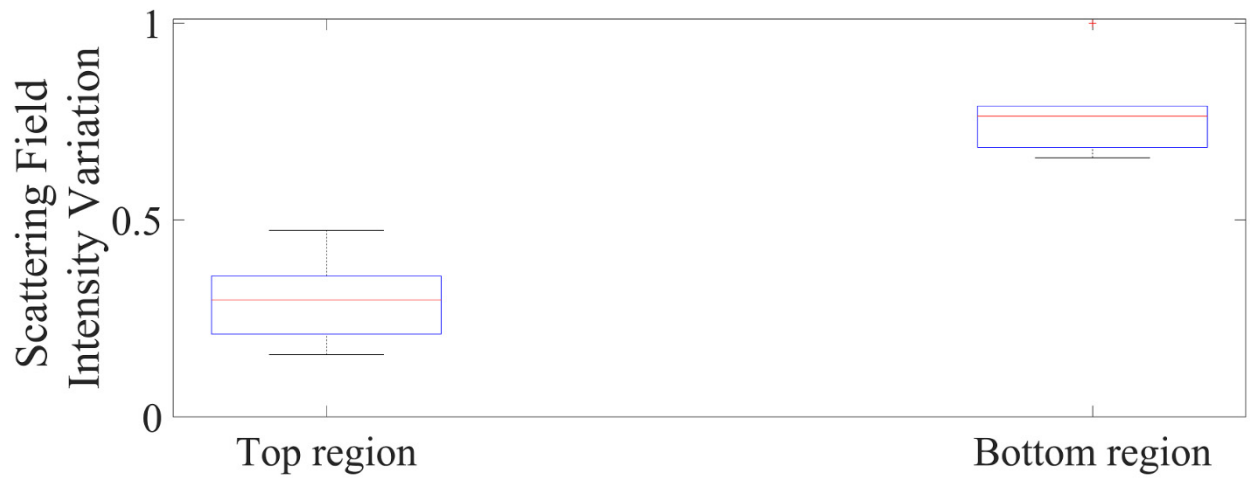


Fig. 6.10. (a) Switching configuration for multi-static data acquisition. (b) Subtracted images of the upper and lower regions at three different positions; front side of the torso (left), behind ribs (middle) and deep inside thorax (right) with 3 mL injected water. (c) Scattering field intensity variation diagram in case of 3 mL inserted water compared to the healthy threshold.

## 6.2.6 Human Test Results

After confirming capability of the system in detecting small amounts of fluid inside the thorax using artificial phantom, it was tested on healthy subjects as an important step in defining the threshold of image intensity for healthy cases. To that end, an informed consent was obtained from all the subjects involved in the study. All of the tests were conducted in accordance with the guidelines and protocols approved by the Ethics Committee of The University of Queensland (Australia). It was assured that the subjects under study do not have any known cardio vascular or related disease. Six subjects with different body sizes and genders were tested. The tests were conducted without controlling the body movements or breathing. These tests were mainly conducted to verify the notion that the upper and lower portions of torso possess relatively similar scattering profiles in addition to investigate the variation range in the image intensity of these two regions with different subjects. Considering that the presence of fluid significantly changes the similarity in the intensity of the scattered field, unhealthy subjects can be identified if their scattering profile is well above the defined range. To de-identify the studied cases, the obtained results from a random human subject is depicted in Fig. 6.11 (a). As can be realized, there is a meaningful similarity between upper and lower regions with no strong scatterers inside the torso. An analysis on the variations between levels of the signals at upper and lower slices of all the cases is depicted in Fig. 6.11 (b). It is realized that the signal levels received from the upper region of the torso are slightly stronger than those from the lower region due to the slightly shorter upper antenna array-body distance than the distance between the lower antenna array. However, the variation between the upper and lower regions of six different cases with different genders and body sizes are in a very confined range. Therefore, this system shows the potential for preclinical tests on a wider range of people and at final stages on subjects with accumulated thoracic fluid.





(b)

Fig. 6.11. (a) Reconstructed images for top and bottom regions of the torso of one of the tested healthy subjects. (b) Scattering field intensity variation range for top and bottom regions for all of the six cases.

# Chapter 7

## Conclusion and Future Work

### 7.1 Conclusion

This thesis presented a comprehensive study of the design and verification of several configurations and resultant systems and clinical scanners for diagnosis and monitoring of fluid accumulation inside lungs as the sign of several malignant diseases such as cardiovascular diseases. These illnesses are the cause of death for more than 31% of the world population. The main motivation of the thesis was the fact that more than 75% of these mortalities are occurring in developing and poor countries where there is limited access to modern diagnostic tools such as CT-scan or MRI. There has been great effort on organizing this thesis in a manner that represents a systematic procedure of understanding the diseases associated with fluid accumulation, explain the weaknesses of the available techniques and suggest feasible solutions that would yield to the build of a clinical platform that can be readily used by non-specialists at a click of a button. It should be noted that the main contribution of this thesis can be categorized as:

- 1) The design of a wide range of wideband and unidirectional antennas that meet the requirements of the wideband microwave imaging systems for torso imaging.
- 2) Proposing detection algorithms that would provide a meaningful, reasonable and real time comparison reference for the paramedics or doctors for diagnostic purposes.
- 3) Design of several initial prototypes of torso scanning systems to test the feasibility of proposed detection algorithm and practicality of the proposed antenna designs.
- 4) Proposal, design, fabrication and preclinical tests of two complete clinical units for fluid accumulation detection purposes in the form of a clinical bed and a doughnut shaped chamber.

To that end, several types of three dimensional and planar antennas are proposed and explained in chapters 3 and 4, respectively. Regarding three dimensional antennas, it is shown that by combining several simple and well know antenna structures wideband antennas can be attained. It is shown that back radiation of a loop antenna can be cancelled if it is folded. To overcome the narrow bandwidth of the loop antenna, it is fed by dual-monopole structures that would both excite the loop and create an additional resonance that would enhance the operating bandwidths. To cancel the effect of folding, which is a great capacitive coupling between the arms of the loop, short ended slot line technique is

utilized to tune the input impedance of the antenna. To lower the main resonance of the antenna while keeping the substrate area of the antenna fixed, meandering technique in addition to capacitive coupling a parasitic strip is utilized in certain designs. Regarding planar antennas, several designs utilizing composite loop-dipole structures and metamaterial loaded structures are proposed. One of the main novelties introduced in the field of loop-dipole composite structures, was the use of offset broadside coupled feeding that resulted in a great range of freedom in terms of controlling radiation characteristics of the antennas as well as independent control of each resonance. On the other hand, a non-periodically loaded metamaterial antenna is introduced as a first of its kind in the literature. It is shown that by non-periodic loading of a loop antenna with mu-negative metamaterial structures, a unidirectional radiation in addition to a wide operating bandwidth is achievable.

Chapters four and five are devoted to design of preliminary platforms and systems that provided a test environment to verify the proposed detection algorithms and their practicality. The initial platforms were designed in linear array form and the symmetry between lungs and consequently similarity in their scattering profiles is used as the threshold to diagnose presence of fluid. However, later on it was shown that linear arrays are not able to detect fluid accumulation if it is located in deeper positions. This was due to the fact that limited microwave power is allowed in medical diagnostic applications and limited number of antennas that are scanning only the rear side of the torso. To overcome this problem, circular array structures that are surrounding torso area were proposed. It was shown that the new configuration is extremely successful in identifying the presence as well as location of the accumulated fluid.

In chapter six, two clinical platforms that were designed and fabricated for preclinical tests were introduced and their performances were verified under different test scenarios. Based on the tests that were performed on artificial phantom, lamb lungs and healthy human subjects, it was found that both systems are capable of detecting small amounts of fluid inside torso, however, as mentioned before, linear scanner system that is embedded inside a clinical bed has limitations in detection of deep targets as well as exact position of the fluid. These shortcomings are covered by the doughnut shaped system that surrounds the torso area.

As a result of the investigations made throughout this thesis it was found that the scattering profile of left and right sides of the lungs have similar scattering profiles, yet, left side lung's scattering profile is always higher than the left ones due to the presence of heart, which is a strong scatter. The same explanation is also true for the upper and lower regions of torso where lungs are positioned. Human tests revealed that these scattering profiles are similar in different human subjects with different body

shapes and genders. Therefore, by defining a confined range that includes numerous number of tests of different people in different time periods, a global database can be formed to define a confined range as a threshold for healthy subjects. Hence, more tests are required to prove the hypothesis that it is expected that due to the great change in the dielectric properties of and unhealthy lung, the scattering profile of unhealthy cases would be out of this range.

Compared to the existing literature, the final clinical product presented in this thesis can clearly identify the exact location of the fluid that could not be identified using previously reported works [11]-[17], [20]-[21]. Furthermore, this thesis introduces novel types of data acquisition systems and algorithms that fill the gap of not having a real time threshold for healthy and unhealthy case identification [11]-[17].

## **7.2 Future work**

Considering the fact that there is never a perfect product in the science, the following work can be done in future:

- 1) Obtaining the required safety certificates required for medical devices and placing the torso scanner in a hospital for initial tests of unhealthy people in different stages of fluid accumulation in different diseases.
- 2) Building a phantom with more realistic and complete tissue properties that also includes the full vein system for blood circulation.
- 3) Design of a wearable elastic antenna array that does not require matching medium with the body and take the shape of the body. This would solve the unequal distance of the antennas to body at different positions and thus imaging algorithms can be simplified.

# Bibliography

- [1] G.W. Bradley, "History of Medical Imaging". *Proc. American Philosophical Society*, vol. 152, no.3, pp. 349-361, 2008.
- [2] *Science Learning*, Available at: <http://sciencelearn.org.nz/Contexts/See-through-Body/Timeline>, 2014. Accessed 15 December 2015.
- [3] World Health Care Fact Sheet on Cardiovascular diseases (CVDs). (2015)  
Available at: <http://www.who.int/mediacentre/factsheets/fs317/en/>. (Accessed: 11th March 2016).
- [4] L. Cardinale, A.M. Priola, F. Moretti, G. Volpicelli, "Effectiveness of chest radiography, lung ultrasound and thoracic computed tomography in the diagnosis of congestive heart failure," *World J. Radiol.*, vol. 6, pp. 230-237, 2014.
- [5] C.M. Yu, et al. "Intrathoracic impedance monitoring in patients with heart failure correlation with fluid status and feasibility of early warning preceding hospitalization," *Circulation*, vol. 112, pp. 841-848, 2005.
- [6] P.B. Adamson, et al. "Ongoing right ventricular hemodynamics in heart failure: clinical value of measurements derived from an implantable monitoring system," *Journal of the American College of Cardiology*, vol. 41, pp. 565-571, 2003.
- [7] W.T. Abraham, et al. "Wireless pulmonary artery haemodynamic monitoring in chronic heart failure: a randomised controlled trial," *The Lancet*, vol. 377, pp. 658-666, 2011.
- [8] A.L. Bui & G.C. Fonarow, "Home monitoring for heart failure management," *Journal of the American College of Cardiology*, vol. 59, pp. 97-104, 2012.
- [9] R.C. Bourge, et al. "Randomized controlled trial of an implantable continuous hemodynamic monitor in patients with advanced heart failure: the COMPASS-HF study," *Journal of the American College of Cardiology*, vol. 51, pp. 1073-1079, 2008.
- [10] C. Susskind, "Possible use of microwaves in the management of lung disease," *Proceedings of the IEEE*, vol. 61, no. 5, pp. 673-674, May 1973.
- [11] P.C., Pedersen, C.C., Johnson, C.H., Durney, D.G., Bragg, "An investigation of the use of microwave radiation for pulmonary diagnostics," *IEEE Trans. Biomed. Eng.*, vol. BME-23, no. 5, pp. 410-412, Sept. 1976.
- [12] P.C., Pedersen, C.C., Johnson, C.H., Durney, D.G., Bragg, "Microwave reflection and transmission measurements for pulmonary diagnosis and monitoring," *IEEE Trans. Biomed. Eng.*, vol. BME-25, no.1, pp. 40-48, Jan. 1978.
- [13] M. F. Iskander, C. H. Durney, D. J. Shoff, and D. G. Bragg, "Diagnosis of pulmonary edema by a surgically noninvasive microwave technique," *Radio Sci.*, vol. 14, no. 6S, pp. 265-269, 1979.
- [14] M. F. Iskander, R. Maini, C.H. Durney, D.G. Bragg, "A Microwave method for measuring changes in lung water content: numerical simulation," *IEEE Trans. Biomed. Eng.*, vol. BME-28, no. 12, pp. 797-804, Dec. 1981.
- [15] N. Celik, R. Gagarin, H.-S. Youn, M.F. Iskander, "A noninvasive microwave sensor and signal processing technique for continuous monitoring of vital signs," *IEEE Antennas Wireless Propag. Lett.*, vol. 10, pp. 286-289, 2011.
- [16] N. Celik, R. Gagarin, G.Ch. Huang, M.F. Iskander, B.W. Berg, "Microwave stethoscope: development and benchmarking of a vital signs sensor using computer-controlled phantoms and human studies," *IEEE Trans. Biomed. Eng.*, vol. 61, no. 8, pp. 2341-2349, Aug. 2014.
- [17] K. Mulligan, A. Adler and R. Goubran, "Detecting regional lung properties using audio transfer functions of the respiratory system," *EMBC*, pp. 5697 – 5700, 2009.
- [18] L. Beckmann, D. van Riesen, S. Leonhardt, "Optimal electrode placement and frequency range selection for the detection of lung water using bioimpedance spectroscopy," *IEEE Intl. Eng. Medicine and Biology Soc.*, pp. 2685-2688, Aug. 2007.
- [19] X. Li, E. Pancera, L. Zwirello, H. Wu & T. Zwick, "Ultra wideband radar for water detection in the human body," *Microw. Conference*, pp. 150-153, March 2010.
- [20] M.F. Iskander, C.H. Durney, T. Grange, C.S. Smith, "Radiometric technique for measuring changes in lung water (short papers)," *IEEE Trans. Microw. Theory Tech.*, vol. 32, no. 5, pp. 554-556, May 1984.

- [21] S. Salman, Zh. Wang, E. Colebeck, A. Kiourti, E. Topsakal, J.L. Volakis, "Pulmonary edema monitoring sensor with integrated body-area network for remote medical sensing," *IEEE Trans. Antennas Propag.*, vol. 62, no. 5, pp. 2787-2794, May 2014.
- [22] R.H. Bayford, "Biomedical impedance tomography (electrical impedance tomography)," *Annu. Rev. Biomed. Eng.*, vol. 8, pp. 63–91, 2006.
- [23] M. Menolotto, S. Rossi, P. Dario, L.D. Torre, "Towards the development of a wearable electrical impedance tomography system: a study about the suitability of a low power bioimpedance front-end," *IEEE Intl. Eng. Medicine and Biology Soc.*, pp.3133-3136, Aug. 2015.
- [24] M. Arad, S. Abboud, "Electrical impedance tomography vs whole thoracic impedance for monitoring lung fluid content in congestive heart failure patients," *Computing in Cardiology Conference (CinC)*, pp. 465-466, 22-25 Sept. 2013.
- [25] Sh. Zhang, et.al., "Computation of a 3-D model for lung imaging with electrical impedance tomography," *IEEE Trans. Magnetics*, vol. 48, no. 2, pp. 651-654, Feb. 2012.
- [26] J.L. Mueller, S. Siltanen, D. Isaacson, "A direct reconstruction algorithm for electrical impedance tomography," *IEEE Trans. Medical Imaging*, vol. 21, no. 6, pp. 555-559, June 2002.
- [27] E.J. Woo, P. Hua, J.G. Webster, J.W. Tompkins, "Measuring lung resistivity using electrical impedance tomography," *IEEE Trans. Biomed. Eng.*, vol. 39, no. 7, pp. 756-760, July 1992.
- [28] A. Zamani, A. Abbosh, "Hybrid clutter rejection technique for improved microwave head imaging," *IEEE Trans. Antennas Propag.*, vol. 63, no. 11, pp. 4921-4931, Nov. 2015.
- [29] X. Yun, R.H. Johnston, E.C. Fear, "Radar-based microwave imaging for breast cancer detection: tumor sensing with cross-polarized reflections," *IEEE Intl. Symp. Antennas Propag. Soc.*, vol.3, pp. 2432-2435, June 2004.
- [30] R. Chandra, H., Zhou, I., Balasingham, R.M. Narayanan, "On the opportunities and challenges in microwave medical sensing and imaging," *IEEE Trans. Biomed. Eng.*, vol. 62, no. 7, pp. 1667-1682, July 2015.
- [31] U. Weinstein, B. Assaf, C. Eyal, "Microwave monitoring of heart function." *U.S. Patent Application 12/759,715*.
- [32] J.A. Walsh, J.T. Eric & S.R. Steinhubl, "Novel wireless devices for cardiac monitoring," *Circulation*, vol. 130, pp. 573-581, 2014.
- [33] M. Xia, et al. "Research of dose-effect relationship parameters of percutaneous microwave ablation for uterine leiomyomas - a quantitative study," *Sci. Rep.*, vol. 4, no. 6469, 2014.
- [34] G. Shafiq, & K.C. Veluvolu, "Surface chest motion decomposition for cardiovascular monitoring," *Sci. Rep.*, vol. 4, no. 5093, 2014.
- [35] S. Brovoll, et al., "Time-lapse imaging of human heart motion with switched array UWB radar," *IEEE Trans. Biomed. Circuits Systems*, vol. 8, pp. 704-715, 2014.
- [36] M.J. Burfeindt, J.D. Shea, B.D. Van Veen & S.C. Hagness, "Beamforming-enhanced inverse scattering for microwave breast imaging," *IEEE Trans. Antennas Propag.*, vol. 62, pp. 5126-5132, 2014.
- [37] M. Persson, et al., "Microwave-based stroke diagnosis making global prehospital thrombolytic treatment possible," *IEEE Trans. Biomed. Eng.*, vol. 61, pp. 2806-2817, 2014.
- [38] S.W. Qu, J.L. Li, Q. Xue, C.H. Chan, S. Li, "Wideband and unidirectional cavity-backed folded triangular bowtie antenna," *IEEE Trans. Antennas Propag.*, vol. 57, no. 4, pp. 1259-1263, Apr. 2009.
- [39] G.M. Zhang, J.S. Hong, B.Z. Wang, G. Song and P. Zhang, "Compact wideband unidirectional antenna with a reflector connected to the ground using a stub," *IEEE Antennas Wireless Propag. Lett.*, vol. 10, pp. 1186-1189, 2011.
- [40] J. Wu, Z. Zhao, Z. Nie and Q.H. Liu, "A broadband unidirectional antenna based on closely spaced loading method," *IEEE Trans. Antennas Propag.*, vol. 61, no. 1, pp. 109-116, Jan. 2013.
- [41] S.A. Rezaeieh, A. Abbosh, "Compact UHF wide slot antenna for microwave stethoscope designed for heart failure detection," *IEEE Asia-Pacific Microwave Conference (APMC)*, pp. 1136-1138, Nov. 2013.
- [42] W.-J. Lu, W.-H. Zhang, K. F. Tong, H.-B. Zhu, "Planar wideband loop-dipole composite antenna," *IEEE Trans. Antennas Propag.*, vol. 62, no. 4, pp. 2275-2279, April 2014.
- [43] C. Tang, Q. Xue, "Vertical planar printed unidirectional antenna," *IEEE Antennas Wireless Propag. Lett.*, vol. 12, pp. 368-371, 2013.
- [44] J. Shi, et. al., "A Compact differential filtering quasi-Yagi antenna with high frequency selectivity and low cross polarization levels," *IEEE Antennas Wireless Propag. Lett.*, vol. 14, pp. 1573-1576, 2015.

- [45] T. Tuovinen, M. Berg, K.Y. Yazdandoost, J. Iinatti, "Ultra wideband loop antenna on contact with human body tissues," *IET Microw. Antennas Propag.*, vol.7, no.7, pp. 588–596, 2013.
- [46] X. Li, M. Jalivand, Y. Sit, T. Zwick, "A compact double-layer on-body matched bowtie antenna for medical diagnostics," *IEEE Trans. Antennas Propag.*, vol. 62, no. 4, pp. 1808–1816, 2014.
- [47] A. Sabban, A., "New wideband printed antennas for medical applications," *IEEE Trans. Antennas Propag.*, vol. 61, no.1, pp. 84–91, 2013.
- [48] EM Phantoms. Available at: <http://www.speag.com/products/em-phantom/whole-body-2/posable-phantom-popeye-3/>. Accessed: March 24, 2016.
- [49] W. T. Joines et al., "The measured electrical properties of normal and malignant human tissues from 50 to 900 MHz," *Med. Phys.*, vol. 21, no. 4, pp. 547–550, Apr. 1994.
- [50] E. Salerno, "Microwave tomography of lossy objects from monostatic measurements," *IEEE Trans. Microw. Theory and Tech.*, vol.47, no.7, pp.986-994, Jul 1999.
- [51] A.M. Abbosh, B. Mohammed & K.S. Bialkowski, "Differential microwave imaging of the breast pair," *IEEE Antennas Wireless Propag. Lett.*, vol. 15, pp. 1434-1437, 2016.
- [52] M. Ostadrahimi, A. Zakaria, J. LoVetri, L. Shafai, "A near-field dual polarized (TE–TM) microwave imaging system," *IEEE Trans. Microw. Theory and Tech.*, vol. 61, no. 3, pp. 1376-1384, March 2013.
- [53] V. Zhurbenko, T. Rubæk, V. Krozer, P. Meincke, "Design and realisation of a microwave three-dimensional imaging system with application to breast-cancer detection," *IET Microw. Antennas Propag.*, vol. 4, no. 12, pp. 2200-2211, December 2010.
- [54] S.Y. Semenov, et. al., "Microwave tomography: two-dimensional system for biological imaging," *IEEE Trans. Biomed. Eng.*, vol.43, no.9, pp.869-877, Sept. 1996.
- [55] C. Furse, "Basic introduction to bioelectromagnetics," *CRC Press (2nd Edition)*, 2009.
- [56] Dielectric properties of body tissues in the frequency range 10 Hz - 100 GHz. Available at: <http://niremf.ifac.cnr.it/tissprop/>.
- [57] J. Li, T. Jiang, C. Wang, and C. Cheng, "Optimization of UHF Hilbert antenna for partial discharge detection of transformers," *IEEE Trans. Antennas Propag.*, vol. 60, no. 5, pp. 2536–2540, May 2012.
- [58] S. Genovesi, S. Saponara, and A. Monorchio, "Parametric design of compact dual-frequency antennas for wireless sensor networks," *IEEE Trans. Antennas Propag.*, vol. 59, no. 7, pp. 2619–2627, Jul. 2011.
- [59] J. C. Soric, N. Engheta, S. Maci, and A. Alu, "Omnidirectional metamaterial antennas based on -near-zero channel matching," *IEEE Trans. Antennas Propag.*, vol. 61, no. 1, pp. 33–44, Jan. 2013.
- [60] C. H. Lin, K. Saito, M. Takahashi, and K. Ito, "A compact planar inverted-F antenna for 2.45 GHz on-body communications," *IEEE Trans. Antennas Propag.*, vol. 60, no. 9, pp. 4422–4426, Sep. 2012.
- [61] H. Y. Lin, M. Takahashi, K. Saito, and K. Ito, "Performance of implantable folded dipole antenna for in-body wireless communication," *IEEE Trans. Antennas Propag.*, vol. 61, no. 3, pp. 1363–1370, Mar. 2013.
- [62] M. Zheng, H. Wang, and Y. Hao, "Internal hexa-band folded monopole/dipole/loop antenna with four resonances for mobile device," *IEEE Trans. Antennas Propag.*, vol. 60, no. 6, pp. 2880–2885, Jun. 2012.
- [63] C. H. Kang, S. J. Wu, and J. H. Tarnq, "A novel folded UWB antenna for wireless body area network," *IEEE Trans. Antennas Propag.*, vol.60, no. 2, pp. 1139–1142, Feb. 2012.
- [64] C. M. Kruesi, R. J. Vyas, and M. M. Tentzeris, "Design and development of a novel 3-D cubic antenna for wireless sensor networks (WSNs) and RFID applications," *IEEE Trans. Antennas Propag.*, vol. 57, no. 10, pp. 3293–3299, Oct. 2009.
- [65] I. T. Nassar and T. M. Weller, "Development of novel 3-D cube antennas for compact wireless sensor nodes," *IEEE Trans. Antennas Propag.*, vol. 60, no. 2, pp. 1059–1065, Feb. 2012.
- [66] H. Kanj and S. M. Ali, "Compact multiband folded 3-D monopole antenna," *IEEE Antennas Wireless Propag. Lett.*, vol. 8, pp. 185–188, 2009.
- [67] H.-D. Chen, "Broadband CPW-fed square slot antennas with a widened tuning stub," *IEEE Trans. Antennas Propag.*, vol. 51, no. 8, pp. 1982–1986, Aug. 2003.
- [68] A. M. E. Safwat, S. Tretyakov, and A. V. Raisanen, "Defected ground and patch-loaded planar transmission lines," *IET Microw. Antennas Propag.*, vol. 3, no. 2, pp. 195–204, Mar. 2009.

- [69] Q. X. Shao, W. L. Jian, and H. Xu, "A differentially-driven dual-polarized magneto-electric dipole antenna," *IEEE Trans. Antennas Propag.*, vol. 61, no. 1, pp. 425–430, Jan. 2013.
- [70] H. L. Jui and T. Z. Gao, "Planar broadband tag antenna mounted on the metallic material for UHF RFID system," *IEEE Antennas Wireless Propag. Lett.*, vol. 10, pp. 1405–1408, 2011.
- [71] L. Ge and K. M. Luk, "A wideband magneto-electric dipole antenna," *IEEE Trans. Antennas Propag.*, vol. 60, no. 11, pp. 4987–4991, Nov. 2012.
- [72] J. L. Hyung, K. L. Ford, and R. J. Langley, "Independently tunable low-profile dual-band high-impedance surface antenna system for applications in UHF band," *IEEE Trans. Antennas Propag.*, vol. 60, no. 9, pp. 4092–4101, Sep. 2012.
- [73] S. C. Wen and C. Yu, "A novel CP antenna for UHF RFID handheld reader," *IEEE Antennas Propag. Mag.*, vol. 55, no. 4, pp. 128–137, Aug. 2013.
- [74] G. A. Casula, G. Montisci, and G. Mazzarella, "A Wideband PET Inkjet-Printed Antenna for UHF RFID," *IEEE Antennas Wireless Propag. Lett.*, vol. 12, pp. 1400–1403, 2013.
- [75] Technical Information Statement on Human Exposure to Microwaves and Other Radio Frequency EM Fields IEEE Committee on Radiation [Online]. Available: [http://ewh.ieee.org/soc/embs/comar/rf\\_mw.htm/](http://ewh.ieee.org/soc/embs/comar/rf_mw.htm/)
- [76] Y.-S. Wang and S.-J. Chung, "A short open-end slot antenna with equivalent circuit analysis," *IEEE Trans. Antennas Propag.*, vol. 58, no. 5, pp. 1771–1775, May 2010.
- [77] C.-K. Hsu & S.-J. Chung, "Compact antenna with U-shaped open-end slot structure for multi-band handset applications," *IEEE Trans. Antennas Propag.*, vol. 62, no. 2, pp. 929–932, Feb. 2014.
- [78] R. Karimian, H. Oraizi, S. Fakhte, and M. Farahani, "Novel F-shaped quad-band printed slot antenna for WLAN and WiMAX MIMO systems," *IEEE Antennas Wireless Propag. Lett.*, vol. 12, pp. 405–408, 2013.
- [79] S. K. Sharma, L. Shafai, and N. Jacob, "Investigation of wide-band microstrip slot antenna," *IEEE Trans. Antennas Propag.*, vol. 52, no. 3, pp. 865–872, Mar. 2004.
- [80] Y. Cao, B. Yuan, and G. Wang, "A compact multiband open-ended slot antenna for mobile handsets," *IEEE Antennas Wireless Propag. Lett.*, vol. 10, pp. 911–914, 2011.
- [81] W. Liu, Y.-Z. Yin, W.-L. Xu, and S.-L. Zuo, "Compact open-slot antenna with bandwidth enhancement," *IEEE Antennas Wireless Propag. Lett.*, vol. 10, pp. 850–853, 2011.
- [82] S. A. Rezaeieh and A. M. Abbosh, "Wideband and unidirectional folded antenna for heart failure detection system," *IEEE Antennas Wireless Propag. Lett.*, vol. 13, pp. 844–847, 2014.
- [83] S. A. Rezaeieh, A. Abbosh, and Y. Wang, "Wideband unidirectional antenna of folded structure in microwave system for early detection of congestive heart failure," *IEEE Trans Antennas Propag.*, vol. 62, no. 10, pp. 5375–5381, Oct. 2014.
- [84] S. Abadi and N. Behdad, "An electrically small, vertically polarized ultrawideband antenna with monopole-like radiation characteristics," *IEEE Antennas Wireless Propag. Lett.*, vol. 13, pp. 742–745, 2014
- [85] C.H. Lee, Y.H. Chang & C.E. Chiou, "Design of multi-band CPW-fed antenna for triple-frequency operation," *Electron. Lett.* vol. 48, pp. 543–545, 2012.
- [86] S.A.Rezaeieh, K.S. Bialkowski & A. Abbosh, "Three-dimensional open-ended slot antenna for heart failure detection system employing differential technique," *IEEE Antennas Wireless Propag. Lett.*, vol. 13, pp. 1753–1756, 2014.
- [87] S.A. Rezaeieh, A. Zamani, A.M. Abbosh, "3-D Wideband antenna for head-imaging system with performance verification in brain tumor detection," *IEEE Antennas wireless Propag. Lett.*, vol. 14, pp. 910–914, 2015.
- [88] Y.H. Yun, S.H. Ham & Y.H. Lee, "The electromagnetic radiation with phase difference in rectangular loop antenna or rectangular loop circuit," *IEEE Intl. Sym. on Electromag. Compatibility*, vol. 1, pp. 381–386, 1998.
- [89] A.T. Mobashsher & A. Abbosh, "CPW-fed low-profile directional antenna operating in low microwave band for wideband medical diagnostic systems," *Electron. Lett.*, vol. 50, pp. 246–248, 2014.
- [90] Federal Communications Commission Office of Engineering & Technology. Guidelines. (2001) Available at: [http://transition.fcc.gov/Bureaus/Engineering\\_Technology/Documents/bulletins/oet65/oet65c.pdf](http://transition.fcc.gov/Bureaus/Engineering_Technology/Documents/bulletins/oet65/oet65c.pdf). (Accessed: 21st January 2015).
- [91] W.-T. Hsieh and J.-F. Kiang, "Small broadband antenna composed of dual-meander folded loop and disk-loaded monopole," *IEEE Trans. Antennas Propag.*, vol. 59, no. 5, pp. 1716–1720, May 2011.

- [92] R. W. Ziolkowski and A. Erentok, "At and below the Chu limit: passive and active broad bandwidth metamaterial-based electrically small antennas," *IET Microwaves Antennas Propag.*, vol. 1, no. 1, pp. 116-128, February 2007.
- [93] P. Karstädt and A. Gupta, "Radiation efficiency measurement of communication antennas with Wheeler Cap method," *International Students and Young Scientists Workshop "Photonics and Microsystems"*, Cottbus, 2011, pp. 64-67.
- [94] C.-H. Chang and K.-L. Wong, "Printed  $\lambda/8$  -PIFA for penta-band WWAN operation in the mobile phone," *IEEE Trans. Antennas Propag.*, vol. 57, no. 5, pp. 1373-1381, May 2009.
- [95] S. M. Aguilar, M. A. Al-Joumayly, M. J. Burfeindt, N. Behdad, and S. C. Hagness, "Multiband miniaturized patch antennas for a compact, shielded microwave breast imaging array," *IEEE Trans. Antennas Propag.*, vol. 62, no. 3, pp. 1221-1231, Mar. 2014.
- [96] Sika Australia. (2014). Sika Boom-AP expanding foam [Online]. Available: [http://aus.sika.com/en/solutions\\_products/02/02a008/02a008sa30/02a008sa30100/02a008sa30101.html](http://aus.sika.com/en/solutions_products/02/02a008/02a008sa30/02a008sa30100/02a008sa30101.html), Accessed on: Dec. 1, 2014.
- [97] M. Li, K.-M., Luk, "A Differential-fed magneto-electric dipole antenna for UWB applications," *IEEE Trans Antennas Propag.*, vol. 61, no. 1, pp. 92-99, Jan. 2013.
- [98] K. He, S.-X. Gong, F. Gao, "A wideband dual-band magneto-electric dipole antenna with improved feeding structure," *IEEE Antennas Wireless Propag. Lett.*, vol. 13, pp. 1729-1732, 2014.
- [99] H. W. Lai, H. Wong, "Substrate integrated magneto-electric dipole antenna for 5G Wi-Fi," *IEEE Trans Antennas Propag.*, vol. 63, no. 2, pp. 870-874, Feb. 2015.
- [100] S. Yan, P. Soh, G.A.E. Vandenbosch, "Wearable dual-band magneto-electric dipole antenna for WBAN/WLAN applications," *IEEE Trans Antennas Propag.*, vol. 63, no. 9, pp. 4165-4169, Sept. 2015.
- [101] W.-J. Lu, G.-M. Liu, K.F. Tong, H.-B. Zhu, "Dual-band loop-dipole composite unidirectional antenna for broadband wireless communications," *IEEE Trans Antennas Propag.*, vol. 62, no. 5, pp. 2860-2866, May 2014.
- [102] P.W. Chan, H. Wong, E.K.N. Yung, "Unidirectional antenna composed of dipole and loop," *Electron. Lett.*, vol. 43, no. 22, Oct. 2007.
- [103] T.-Y. Shih, N. Behdad, "A compact, broadband spiral antenna with unidirectional circularly polarized radiation patterns," *IEEE Trans Antennas Propag.*, vol. 63, no. 6, pp. 2776-2781, June 2015.
- [104] R. Sammeta, D.S. Filipovic, "Quasi frequency-independent increased bandwidth planar log-periodic antenna," *IEEE Trans. Antennas Propag.*, vol. 62, no. 4, pp. 1937-1944, Apr. 2014.
- [105] X.-T. Wu, W.-J. Lu, J. Xu, K.F. Tong, H.-B. Zhu, "Loop-monopole composite antenna for dual-band wireless communications," *IEEE Antennas Wireless Propag. Lett.*, vol. 14, pp. 293-296, 2015.
- [106] H. Kamoda, S. Kitazawa, N. Kukutsu, K. Kobayashi, "Loop antenna over artificial magnetic conductor surface and its application to dual-band RF energy harvesting," *IEEE Trans Antennas Propag.*, vol. 63, no. 10, pp. 4408-4417, Oct. 2015.
- [107] J. Wu, Z. Zhao, Z. Nie, Q. Liu, "A printed unidirectional antenna with improved upper band-edge selectivity using a parasitic loop," *IEEE Trans Antennas Propag.*, vol. 63, no. 4, pp. 1832-1837, Apr. 2015.
- [108] J. Wu, Z. Zhao, Z. Nie, Q.-H. Liu, "Bandwidth enhancement of a planar printed quasi-Yagi antenna with size reduction," *IEEE Trans Antennas Propag.*, vol. 62, no. 1, pp. 463-467, Jan. 2014.
- [109] D.M. Pozar, B. Kaufman, "Increasing the bandwidth of a microstrip antenna by proximity coupling," *Electron. Lett.*, vol. 23, no. 8, pp. 368-369, Apr. 1987.
- [110] F. Croq, D.M. Pozar, "Millimeter-wave design of wide-band aperture-coupled stacked microstrip antennas," *IEEE Trans. Antennas Propag.*, vol. 39, no. 12, pp. 1770-1776, Dec. 1991.
- [111] Ch.-J. Lee, K.M.K.H. Leong, T. Itoh, "Composite right/left-handed transmission line based compact resonant antennas for RF module integration," *IEEE Trans. Antennas Propag.*, vol. 54, no. 8, pp. 2283-2291, Aug. 2006.
- [112] M.A. Antoniades, G.V. Eleftheriades, "A folded-monopole model for electrically small NRI-TL metamaterial antennas," *IEEE Antennas Wireless Propag. Lett.*, vol. 7, pp. 425-428, 2008.
- [113] M.A. Antoniades, and G. V. Eleftheriades, "Multiband compact printed dipole antennas using NRI-TL metamaterial loading," *IEEE Trans. Antennas Propag.*, vol. 60, no. 12, pp. 5613-5626, Dec. 2012.
- [114] E. Forati, G.W. Hanson, D.F. Sievenpiper, "An epsilon-near-zero total-internal-reflection metamaterial antenna," *IEEE Trans. Antennas Propag.*, vol. 63, no. 5, pp. 1909-1916, May 2015.

- [115] W. Liu, Z.N. Chen, X. Qing, "Metamaterial-based low-profile broadband aperture-coupled grid-slotted patch antenna," *IEEE Trans. Antennas Propag.*, vol. 63, no. 7, pp. 3325-3329, July 2015.
- [116] A.L. Borja, P.S. Hall, L. Qing, H. Iizuka, "Omnidirectional loop antenna with left-handed loading," *IEEE Antennas Wireless Propag. Lett.*, vol. 6, pp. 495-498, 2007.
- [117] B.-J. Niu, Q.-Y. Feng, P.-L. Shu, "Epsilon negative zeroth- and first-order resonant antennas with extended bandwidth and high efficiency," *IEEE Trans. Antennas Propag.*, vol. 61, no. 12, pp. 5878-5884, Dec. 2013.
- [118] Sh. Xiao, R.B.V.B. Simorangkir, Y. Lee, "A planar dual-band periodic leaky-wave antenna based on a mu-negative (MNG) transmission line," *IEEE Trans. Antennas Propag.*, vol. 63, no. 5, pp. 2370-2374, May 2015.
- [119] K. Wei, Zh. Zhang, Z. Feng, M.F. Iskander, "A MNG-TL loop antenna array with horizontally polarized omnidirectional patterns," *IEEE Trans. Antennas Propag.*, vol. 60, no. 6, pp. 2702-2710, June 2012.
- [120] M.A. Antoniadou, H. Mirzaei, G.V. Eleftheriades, "Transmission-line based metamaterials in antenna engineering", *Springer*, 2016.
- [121] J.-H. Park, Y.-H. Ryu, J.-H. Lee, "Mu-Zero resonance antenna," *IEEE Trans. Antennas Propag.*, vol. 58, no. 6, pp. 1865-1875, June 2010.
- [122] C. Caloz, T. Itoh, "Electromagnetic metamaterials: transmission line theory and microwave applications," *John Wiley & Sons*, 2005.
- [123] A. Grbic and G.V. Eleftheriades, "Experimental verification of backward-wave radiation from a negative refractive index metamaterial," *Journal of Applied Physics*, vol. 92, no. 10, pp. 5930 – 5935, Nov. 2002.
- [124] H. Tolani, M.A. Eberspacher, T.F. Eibert, "Composite right/left-handed leaky wave antenna with structurally non-periodic unit cell arrangement," *Antennas Propag. Conference (LAPC)*, pp. 165-168, Nov. 2010.
- [125] R.L. Li, et.al, "Unidirectional printed loop antenna," *Proc. 6th Int. Symp. Antennas Propag. EM Theory*, pp. 104–107, 2003.
- [126] Oscar T.-C. Chen, Ch.-Y. Tsai, "CPW-fed wideband printed dipole antenna for digital TV applications", *IEEE Trans. Antennas Propag.*, vol. 59, no. 12, pp. 4826-4830, 2011.
- [127] S.X. Ta, I. Park, R.W. Ziolkowski, "Circularly polarized crossed dipole on an HIS for 2.4/5.2/5.8-GHz WLAN applications," *IEEE Antennas Wireless Propag. Lett.*, vol. 12, pp. 1464-1467, 2013.
- [128] O.O. Olaode, W.D. Palmer, W.T. Joines, , "Characterization of meander dipole antennas with a geometry-based, frequency-independent lumped element model," *IEEE Antennas Wireless Propag. Lett.*, vol. 11, pp. 346-349, 2012.
- [129] Y.-J. Chi, F.-Ch. Chen, "On-body adhesive-bandage-like antenna for wireless medical telemetry service," *IEEE Trans. Antennas Propag.*, vol. 62, no. 5, pp. 2472-2480, May 2014.
- [130] Ch. Liu, Y.-X. Guo, Sh. Xiao, "Capacitively loaded circularly polarized implantable patch antenna for ISM band biomedical applications," *IEEE Trans. Antennas Propag.*, vol. 62, no. 5, pp. 2407-2417, May 2014.
- [131] Chest X-ray. Available at: <http://radiopaedia.org/play/1819/entry/24196/case/31525/studies/32390>.
- [132] Multipurpose Chest Phantom. Available at: [https://www.kyotokagaku.com/products/detail03/pdf/ph-1\\_catalog.pdf](https://www.kyotokagaku.com/products/detail03/pdf/ph-1_catalog.pdf).
- [133] Keysight N7081A Microwave Tranceiver. Available at: <http://literature.cdn.keysight.com/litweb/pdf/N7081-90002.pdf?id=2547904>.
- [134] Y. Wang, A. M. Abbosh, B. Henin and P. T. Nguyen, "Synthetic bandwidth radar for ultra-wideband microwave imaging systems," *IEEE Trans. Antennas Propag.*, vol. 62, no. 2, pp. 698-705, Feb. 2014.
- [135] An Internet resource for the calculation of the dielectric properties of body tissues in the frequency range 10 Hz - 100 GHz. Available at: <http://niremf.ifac.cnr.it/tissprop/>. Accessed 28 June 2016.
- [136] E. C. Fear, S. C. Hagness, P. M. Meaney, M. Okoniewski, and M. A. Stuchly, "Enhancing breast tumor detection with near-field imaging," *IEEE Microw. Mag.*, vol. 3, no. 1, pp. 48–56, Mar. 2002.
- [137] A. Zamani, S. A. Rezaeieh, and A. M. Abbosh, "Lung cancer detection using frequency-domain microwave imaging," *Electron. Lett.*, vol. 51, no. 10, pp. 740–741, 2015.
- [138] M. Fallahpour, J. T. Case, M. T. Ghasr, and R. Zoughi, "Piecewise and Wiener filter-based SAR techniques for monostatic microwave imaging of layered structures," *IEEE Trans. Antennas Propag.*, vol. 62, no. 1, pp. 282–294, Jan. 2014.

- [139] A. Ishimaru, "Chapter 2: Scattering and absorption of a wave by a single particle," *Wave Propagation and Scattering in Random Media*, New York, USA, 1978.
- [140] J. W. Goodman, "Introduction to Fourier Optics," *McGraw-Hill*, 2nd ed., pp. 38–40, 1996.
- [141] D. G Kurup and A. Koithyar, "New expansions of Bessel functions of first kind and complex argument," *IEEE Trans. Antennas Propag.*, vol. 61, no. 5, pp. 2708–2713, May 2013.
- [142] A. Zamani, S. A. Rezaeieh, and A. M. Abbosh, "Frequency domain method for early stage detection of congestive heart failure," *IEEE Proc. IEEE MTT-S Microw. Workshop*, pp.1-3, 8-10 Dec. 2014
- [143] I. G. Zubal et al., "Computerized three-dimensional segmented human anatomy," *Med. Phys.*, vol. 21, no. 2, pp. 299–302, 1994.
- [144] M. Klemm, J. A. Leendertz, D. Gibbins, I. J. Craddock, A. Preece and R. Benjamin, "Microwave Radar-Based Breast Cancer Detection: Imaging in Inhomogeneous Breast Phantoms," *IEEE Antennas Wireless Propag. Lett.*, vol. 8, pp. 1349-1352, 2009.
- [145] E. Porter, M. Coates and M. Popović, "An early clinical study of time-domain microwave radar for breast health monitoring," *IEEE Trans. Biomed. Eng.*, vol. 63, no. 3, pp. 530-539, March 2016.
- [146] R. Scharstein, "Transient electromagnetic plane wave reflection from a dielectric slab," *IEEE Trans. Educ.*, vol. 35, pp. 170–175, 1992.
- [147] R. Solimene & A. Cuccaro, "Front wall clutter rejection methods in TWI," *IEEE Geosci. Remote Sens. Lett.*, vol. 11, pp. 1158–1162, 2014.
- [148] H.C. Strifors & G.C. Gaunaud, "Scattering of electromagnetic waves by a perfectly conducting cylinder with a thin lossy magnetic coating," *IEEE Trans. Antennas Propag.*, vol. 48, pp. 1528–1532, 2000.
- [149] P.M. Meaney, M.W. Fanning, D. Li, S.P. Poplack & K.D. Paulsen, "A clinical prototype for active microwave imaging of the breast," *IEEE Trans. Microw. Theory Tech.*, vol. 48, pp. 1841–1853, 2000.
- [150] Keysight L4490A/91A RF Switch Platform Catalogue. (2014). Available at: <http://literature.cdn.keysight.com/litweb/pdf/5989-7857EN.pdf?id=1365742>. (Accessed: 11<sup>th</sup> March 2016).
- [151] N9923A FieldFox Handheld RF Vector Network Analyzer Datasheet. (2014). Available at: <http://literature.cdn.keysight.com/litweb/pdf/5990-5363EN.pdf?id=1856098>. (Accessed: 11<sup>th</sup> March 2016).